

Thermodynamic and kinetic instability of inorganic solid electrolytes at lithium and sodium metal electrodes

dem Fachbereich Biologie und Chemie
der Justus-Liebig-Universität Gießen

vorgelegte
Dissertation
zur Erlangung des akademischen Grades
Doktor der Naturwissenschaften
– Dr. rer. nat. –

von
Sebastian Wenzel
geb. 21.09.1987
in Wetzlar

Dean : Prof. Dr. Volker Wissemann
1st Reviewer : Prof. Dr. Jürgen Janek
2nd Reviewer : Prof. Dr. Philipp Adelhelm

Eidesstattliche Erklärung

Die vorliegende Arbeit wurde im Zeitraum vom 18.01.2013 bis 29.02.2016 am Physikalisch-Chemischen Institut der Justus-Liebig-Universität Gießen unter Betreuung von Prof. Dr. Jürgen Janek angefertigt.

Ich erkläre: Ich habe die vorgelegte Dissertation selbständig und ohne unerlaubte fremde Hilfe und nur mit den Hilfen angefertigt, die ich in der Dissertation angegeben habe. Alle Textstellen, die wörtlich oder sinngemäß aus veröffentlichten Schriften entnommen sind, und alle Angaben, die auf mündlichen Auskünften beruhen, sind als solche kenntlich gemacht. Bei den von mir durchgeführten und in der Dissertation erwähnten Untersuchungen habe ich die Grundsätze guter wissenschaftlicher Praxis, wie sie in der „Satzung der Justus-Liebig-Universität Gießen zur Sicherung guter wissenschaftlicher Praxis“ niedergelegt sind, eingehalten

Niederwetz, 28. April 2016

Sebastian Wenzel

Table of Contents

1	Introduction	1
2	Survey of solid electrolytes and conductivity mechanisms	5
2.1	Basics of ion conduction	6
2.2	How to affect ionic conductivity	7
2.3	A short overview about solid electrolytes and their respective conduction mechanisms	8
2.4	All-solid-state batteries	10
3	Interface or interphase? – Stability of solid electrolytes in contact with alkali metal	13
3.1	Introduction	13
3.2	Classification of interfaces/interphases	14
3.3	Stability of solid electrolytes – a literature survey	15
3.4	General considerations and basic principles	17
3.4.1	Stability of solid electrolytes	17
3.4.2	Kinetics of solid state reactions	18
3.4.3	Percolation pathways	22
3.5	Combined approach to study interphase formation	23
3.5.1	Limitations of cyclic voltammetry for stability investigation	23
3.5.2	Combined approach	25
3.5.3	Electrochemical approach	26
3.5.4	Overview of the expectations and results for the electrochemical methods	27
3.5.5	The in situ XPS technique	30
3.6	Mixed conducting interphases	32
3.6.1	$\text{Li}_{0.35}\text{La}_{0.55}\text{TiO}_3$	32
3.7	Solid electrolyte interphases	35
3.7.1	$\text{Li}_7\text{P}_3\text{S}_{11}$	35
3.7.1.1	Interphase formation between Li metal electrode and LPS	35
3.7.1.2	Behavior of the interphase	39
3.7.2	$\text{Li}_{10}\text{GeP}_2\text{S}_{12}$	41
3.7.3	Na_3PS_4	46
3.7.4	Interphase formation described as classical solid state reactions	49
3.8	Stable solid electrolytes	52
3.8.1	Na- β ”-aluminum oxide	53
3.8.2	$\text{Li}_7\text{La}_3\text{Zr}_2\text{O}_{12}:\text{Al}$	54
3.9	Thermodynamic assessment and evaluation of stability	56
3.10	Volume effects of SEI formation	57
3.11	Summary and Conclusion	59

4	Interface protection concepts and their limitations	63
4.1	Introduction and literature survey	63
4.2	LiPON on LLTO	63
4.3	Cu ₃ N as sacrificial film	64
4.4	Content classified by JLU	64
4.5	Limitations of protecting concepts	65
5	Kinetic effects of interfaces under current load – a model case	67
5.1	Introduction	67
5.2	Literature survey	68
5.2.1	Silver based interfaces	68
5.2.2	Sodium based interfaces	71
5.2.3	Lithium based interfaces	72
5.3	Plating and stripping of sodium metal	74
5.4	Cell setup for proper interface characterization	75
5.5	Interface formation between sodium metal and beta-alumina	76
5.6	Pressure dependence of metal/solid electrolyte interfaces – an overview . . .	77
5.7	Pressure dependence of metal/solid electrolyte interfaces – a detailed study	79
5.8	Simulation of battery cycling and its effect on the alkali metal electrodes . .	84
5.9	Summary and conclusion	87
6	Kinetic effects of interphases and interfaces under current load	91
6.1	Introduction	91
6.2	SEI forming solid electrolytes – LGPS vs. LPS	91
6.2.1	The interface Li/LGPS	91
6.2.2	The interface Li/LPS	93
6.3	The interface Na/NPS	95
6.4	LLZO, an ideal lithium ion conductor?	96
6.5	Cycling across the interface alkali metal/solid electrolyte	98
6.6	Electrochemically induced interphase growth	100
6.7	Summary and conclusion	103
7	Summary, conclusion and outlook	105
8	Appendix 1 – Synthesis and characterization of solid electrolytes	109
8.1	Perovskites	111
8.2	Garnet type materials	113
8.3	NASICON type materials – LATP	117
8.4	LPS, LGPS, NPS and beta-alumina	119
8.5	Argyrodite	123
8.6	Content classified by JLU	124
9	Appendix 2 - Technical approaches and in situ XPS	125
9.1	Technical approaches	125
9.1.1	DC resistance measurements	125
9.1.2	CV for determination of the polarization resistance	126
9.2	In situ XPS technique – additional information	127
9.3	Additional information about interphase forming materials	129
9.3.1	LLTO	129
9.3.2	LSTZO	130

9.3.3	LATP	132
9.3.4	LPS and LGPS	134
9.3.5	Argyrodite	137
9.3.6	NPS	141
9.3.7	Tantalum containing garnet type structures	142
9.3.8	NaSICON – NZSPO	143
10	Appendix 3 – Supporting results on the interface of sodium metal and beta-alumina	147
10.1	Interface preparation via hot pressing	147
10.2	Limitation of SEM techniques	147
10.3	IR-drop determination	148
10.4	Pressure dependence of the conductivity	149
10.5	Interface relaxation	149
10.6	Galvanostatic experiments for higher current densities	150
10.7	Additional information on the pressure dependent contact loss model	151
10.8	Oscillation of the interface sodium metal/beta-alumina	151
10.9	Reversion of polarity	152
10.10	Dislocation relaxation process	153
11	Appendix 4 – Supporting results on the interface of lithium metal and solid electrolytes	155
11.1	Cycling of lithium metal electrodes on LPS	155
11.1.1	Cycling of sodium metal electrodes on NPS	156
11.1.2	Simulation of the enhanced interphase growth	156
12	Appendix 5	159
12.1	List of abbreviations	159
12.2	List of symbols	161
12.3	List of conference contributions	163
12.4	List of publications	163
13	Bibliography	174

Abstract

In this thesis the question will be discussed and evaluated, whether the application of solid electrolytes will enable the use of alkali metal electrodes in all-solid-state batteries. Different lithium or sodium ion conducting materials were synthesized, bought or delivered by corporation partners. Using these materials, the stability in contact with the respective alkali metals was investigated by a combined approach, using common electrochemical analysis methods like impedance spectroscopy and a during this project developed in situ photoelectron spectroscopy technique. The results led to a classification of stable, mixed conducting and solid electrolyte interphases. Interphases of promising materials like the garnet type $\text{Li}_7\text{La}_3\text{Zr}_2\text{O}_{12}$, Na- β'' -alumina (stable), $\text{Li}_{0.35}\text{La}_{0.55}\text{TiO}_3$ (MCI), $\text{Li}_7\text{P}_3\text{S}_{11}$ and $\text{Li}_{10}\text{GeP}_2\text{S}_{12}$ (SEI) were studied. The SEI formation process was found to show a parabolic behavior and was thus treated like a classical solid state reaction, leading to a long time assessment of the interphase behavior and growth. Thus, insight into interphase formation and the instability of solid electrolytes were gained.

In the second part, the interface between sodium metal electrodes and the solid electrolyte β'' -alumina was investigated under current load, resulting in a strongly increasing voltage for current densities in the range of a few mA/cm^2 due to contact loss (caused by metal dissolution). Thus, the pressure dependence of galvanostatic experiments was investigated. As a result the proper cycling of large amounts of alkali metal and the complete dissolution of a macroscopic metal electrode was realized. Transferring the same techniques and experiments to SEI forming materials led either to short circuits (for $\text{Li}_7\text{P}_3\text{S}_{11}$) or an electrochemical enhanced interphase growth (e. g. for $\text{Li}_{10}\text{GeP}_2\text{S}_{12}$). At the end, the results will be discussed in the context of the initially raised question.

Zusammenfassung

In dieser Arbeit wird die Frage diskutiert, ob die Verwendung von Festelektrolyten die Anwendung von Alkalimetallelektroden ermöglichen kann. Dafür wurden verschiedene Festionenleiter synthetisiert, gekauft oder von Kooperationspartnern zur Verfügung gestellt. Damit wurde zuerst die Stabilität der Materialien in Kontakt mit den jeweiligen Alkalimetallen mithilfe einer kombinierten Methode untersucht, bestehend aus geläufigen elektrochemischen Analysemethoden wie Impedanzspektroskopie und der in dieser Arbeit entwickelten in situ-Photoelektronenspektroskopie. Die Ergebnisse mündeten in der Zusammenstellung einer Klassifizierung dreier Grenzflächen/Grenzphasen, der stabilen Grenzfläche, der gemischt-leitenden (mixed conducting interphase, MCI) und der Festelektrolytzwischenphase (solid electrolyte interphase, SEI). Dabei wurden Festelektrolyte wie $\text{Li}_7\text{La}_3\text{Zr}_2\text{O}_{12}$, Na- β ''-Aluminiumoxid (stabil), $\text{Li}_{0.35}\text{La}_{0.55}\text{TiO}_3$ (MCI), $\text{Li}_7\text{P}_3\text{S}_{11}$ und $\text{Li}_{10}\text{GeP}_2\text{S}_{12}$ (SEI) untersucht. Der Prozess und das Wachstum der SEI-Bildung wiesen dabei ein parabolisches Zeitgesetz auf, was mittels klassischer Modelle für Festkörperreaktionen erklärt werden konnte. Durch die Nutzung dieses Modells wird die Abschätzung des Grenzphasenwachstums und -verhaltens für lange Zeiträume möglich. Damit wurden Einsicht und Informationen über das Verhalten und die Bildung von Grenzphasen insgesamt gewonnen.

Im zweiten Teil wurde der Materialtransport unter Strombelastung zwischen Natriummetallelektroden und dem Festelektrolyten Na- β ''-Aluminiumoxid für Stromdichten im Bereich von ein paar mA/cm^2 untersucht. Dabei zeigte sich ein starkes Ansteigen der Spannung aufgrund von Kontaktverlust an der Grenzfläche, welches durch das Auflösen von Alkalimetall resultierte. Daher wurde die Druckabhängigkeit der galvanostatischen Experimente untersucht. Aufgrund der Resultate wurden dann Zyklisierungsexperimente durchgeführt, wobei signifikante Mengen an Natriummetall transportiert werden konnten, inklusive der Auflösung einer makroskopischen Metallelektrode. Die Anwendung derselben Techniken und Experimente auf die grenzphasenbildenden Materialien führte entweder zu häufigem Auftreten von Kurzschlüssen (für $\text{Li}_7\text{P}_3\text{S}_{11}$) oder zu elektrochemisch verstärktem Grenzphasenwachstum (z. B. für $\text{Li}_{10}\text{GeP}_2\text{S}_{12}$). Zusammenfassend wird dann die ursprüngliche Frage diskutiert, ob Festelektrolyte zur Anwendung von Alkalimetallelektroden in Festkörperbatterien führen können.

Danksagung

Mein Dank gilt allen, die zum Gelingen dieser Arbeit beigetragen haben, insbesondere

- Herrn Prof. Dr. Jürgen Janek für das Anvertrauen dieser Arbeit und die hilfreichen Anleitungen.
- Herrn Prof. Dr. Philipp Adelhelm (Universität Jena) für die Übernahme des Gutachterpostens und die interessierte Verfolgung meines Arbeitsfortschrittes.
- Dr. Joachim Sann für die objektive Bewertung meiner Ergebnisse, die ideenreichen Diskussionen und für die Möglichkeit mich an der XPS auszutoben. Weiterhin danke ich dafür, dass er eine der wenigen Konstanten im Jobkarussell Universität war.
- Dr. Dominik A. Weber (dieses mal habe ich an das A. gedacht!) für die Unterstützung bei und die Durchführung der Rietveld-Verfeinerungen.
- Dr. Thomas Leichtweiss für die guten Gespräche über XPS und die gute Zusammenarbeit bei den XPS-Messungen.
- dem XPS-Team, namentlich Thomas Leichtweiss, Joachim Sann, Carsten Fiedler und Bene Kramm, für die reibungslose Zusammenarbeit an der XPS.
- den Mitarbeitern der Werkstätten für die Konstruktion meiner verschiedenen Apparaturen und Messaufbauten. Besonders zu nennen sind hier Gerd Pfeiffer, Harry Heidt und Harald Weigand.
- Dr. Wolfgang Zeier für die Unterstützung während des Schreibens meiner letzten Publikationen und das kritische Lesen meiner Publikationen.
- Dr. Boris Mogwitz für die FEM-Simulationen.
- Dr. Alexander Schmidt (BELLA, KIT) für die Kapillaren-XRD-Messungen.
- Dr. Stefan Sedlmaier (BELLA, KIT) für die Lieferung der Argyrodite.
- Zhizhen Zhang (Key Laboratory for Renewable Energy (E01), Institute of Physics, Chinese Academy of Sciences, Beijing) für das zur Verfügung stellen der NaSICON-Verbindungen.
- John Blackburn (Ionotec Ltd.) für die unkomplizierte Herstellung und Lieferung der Beta-Alumina-Scheiben.
- Dr. Pascal Hartmann, Dr. Joern Kulisch, Johan ter Maat, Dr. Klaus Leitner (BASF SE) und Dr. Heino Sommer (BELLA, KIT).
- Simon Randau für die Zusammenarbeit bei der Synthese von LGPS.
- Martin Rolf Busche für die Einweisung in die Software RelaxIS.
- Neal Fairley für die Software CasaXPS, die mir die Auswertung der XPS-Daten unendlich viel einfacher gemacht hat.
- Rhd instruments für die Software RelaxIS, die mir bei der Auswertung der EIS-Daten viel Zeit gespart hat.
- dem LOEWE STORE-E Projekt des Landes Hessen und der BASF SE für die Finanzierung meiner Promotion.

- der Chemiker-Fußballgruppe für die vielen spannenden Duelle auf dem Platz.
- meinen Bürokollegen Carsten "MEEEP" Fiedler, Conrad Bender und Patrick Schichtel für das allseits angenehme Arbeitsklima.
- meinen Laborkollegen Benjamin Bergner, Jochen Reinacher, Carsten Fiedler, Patrick Schichtel, Simon Randau, Thomas Leichtweiss, Dominik Weber und Yannik Schneider für ein katastrophenfreies und angenehmes Arbeiten.
- meiner Schwester Carolin für die Hilfe im Kampf gegen den typischen Verwaltungs- und Behördenwahnsinn.
- meiner Familie für die Unterstützung meines Studiums, besonders meinem Vater Martin für das kritische Lesen meiner Arbeit.

1 Introduction

The storage of energy in so-called galvanic cells or more common secondary batteries is a well-established technique. Today's applications range from energy supply for mobile devices like smartphones, laptops or portable music players to starting assistances for car engines. The principles of this technique are quite old and first experiments were already conducted by Luigi Galvani in 1780, using metal electrodes and frog legs. Alessandro Volta then built the first human-made battery, the so-called Volta pile, consisting of alternating layers of silver and zinc metal electrodes and electrolyte soaked fabrics. The fundamental setup has not changed since then, today's batteries still consist of two electrodes that are separated by the electrolyte^[1]. In this setup, the chemical energy is stored in the electrodes and converted to electrical energy during discharge. The electrical power is then obtained by the product of the voltage, which is the electric potential difference between both electrodes, and the discharge current, which corresponds to the battery capacity.

Today, batteries are mostly used in handheld electronics or in cars (to start the engine). In the course of the *energiewende*¹ the focus extends from portable to automotive applications of batteries in order to reduce the carbon dioxide emission. For a medium-size car approximately 16.5 kWh are required for a range of 100 km (165 Wh/km). Considering an energy density of around 120 Wh/kg for lithium ion batteries, the battery will weight approximately one ton for a range of 800 km^[3], which corresponds to one filling of a common gasoline tank. Thus, the overall weight of the car will be approximately doubled, leading to the result that the energy density of the batteries has to be notably increased.

For this purpose higher energy densities are required, either by improving the battery capacity and/or the cell voltage. Potential solutions are concepts like lithium-air or lithium-sulfur batteries, which were intensively investigated in the past, still not leading to industrial applications. In order to increase the current densities, the application of low and high potential materials, respectively, and decreasing the cell volume and weight by decreasing the amount of electrolyte plays an important role. The all-solid-state battery would in principle fulfill all of these requirements. The lowest potential is found for lithium metal, leading to an increased battery performance if it will ever be applied in batteries, as might be seen in Fig.1.1, where the lithium metal electrode notably increases the overall volumetric and gravimetric energy density^[4]. Tarascon et al. already marked in Fig. 1.1 that the application of alkali metal electrodes generally is seen as "unsafe". One reason for this is dendrite growth and resulting short circuits that may lead to cell failure and fire/explosion hazards. These issues basically pertain for batteries with liquid electrolytes.

¹This term is mostly adopted by English media^[2].

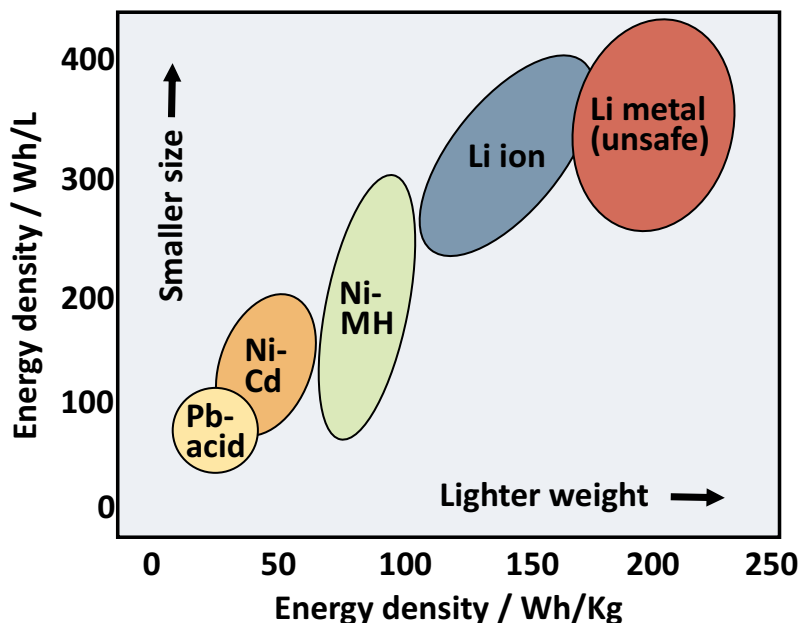


Figure 1.1: Summary of the specific and volumetric energy densities of different battery systems (taken with modifications from Tarascon et al.^[4]).

Thus, the question might be raised, if the application of solid electrolytes will enable the use of alkali metal electrodes in batteries in general and in all-solid-state batteries in particular. An answer for this question will be partly given in this PhD thesis for common well-known and experimental solid electrolytes. At the beginning the principles of ion conduction are shortly reviewed and connected with structural units and material composition. A few examples from literature are given for common and experimental solid electrolytes. The literature surveys and general considerations are given at the beginning of the respective section for the sake of clarity.

The results of this thesis are divided in four sections, three major and a minor section. The first major section covers the stability of common solid electrolytes in contact with alkali metal electrodes and the resulting effects caused by the type of decomposition products. Therefore a combined approach was used by applying established electrochemical methods like impedance spectroscopy and a newly developed in situ photoelectron spectroscopy experiment, which will also be described in this chapter. Additional information about this technique and further investigations concerning additional solid electrolytes are then given in the appendix. Thus, a first hint towards the compatibility of alkali metal electrodes and solid electrolyte is obtained. The results of this part were mostly published or submitted for publication and are consequently marked with the respective citation.

In order to improve the impact of interphase formation or totally prevent it, a few interface protection concepts and their potential limitations are described in the minor part. An outlook and preliminary results for a more suitable interface protection material are reported, too.

In the second main part, the dissolution and deposition² of sodium metal electrodes on the stable solid electrolyte sodium β'' -aluminum oxide (as a model system) are reported for technical relevant current densities. Corresponding to the results, the pressure effects

²In the literature often described as plating and stripping.

on the interface are studied and extensively discussed. In order to transfer the knowledge of the second main part to lithium ion conductors, similar experiments were conducted. Unfortunately, only the unstable and interphase forming solid electrolytes could be used in this current density range. The properties of the interphase (solid electrolyte interphase) and the solid electrolyte then induced effects that showed the strong increase of the interphase resistance, which will be explained by an internal metal deposition model. Additionally, the cell failure due to dendrite formation was a major issue during the experiments for a few materials.

In the end, the results are summarized leading to a conclusion and an answer to the question raised in this introduction.

2 Survey of solid electrolytes and conductivity mechanisms

In this section a short review about common solid electrolyte (SE) materials and their conducting mechanisms and properties will be summarized. Solid electrolytes generally exhibit a higher ionic transference number compared to liquid electrolytes, which is more than two times higher. One reason for this is the relatively high transference number for negatively charged counter ions in liquid electrolytes. In solid electrolytes the electronic conductivity is obviously smaller than the ionic leading to an ionic transference number of approximately unity^[5]. Miniaturization and improved safety is believed to be provided by substitution of liquid with solid electrolytes.

A few criteria are important for the use of solid electrolytes in all-solid-state batteries, which will be listed below. Note that this list is not necessarily comprehensive and might be modified according to the field of application.

1. For the long time stability of the cell performance, the SE should be thermodynamically stable.
2. A sufficiently high ionic conductivity. For most solid electrolytes this criterion is fulfilled, as summarized in section 2.2.
3. Low electronic conductivity to prevent self discharge of the battery. The transference number of ions should be near unity.
4. Chemical inertness against electrode materials. Results concerning the stability in contact with alkali metals will be given in section 3.
5. According to this a wide electrochemical window is favorable as it would enable the use of both low and high voltage electrode materials.
6. A low transfer resistance between the electrode and the solid electrolyte is required. This will be described and discussed in section 3, 5 and 6.
7. The prevention of dendrite formation and growth (and mechanical destruction) is essential. Again, parts of this will be described in section 5 and 6.
8. For industrial application, an easy and cost-efficient synthesis route, abundant starting materials and non-toxic products are favorable.

In the following the principles for ion conduction will be described, governing a physical-chemical and more structural insight into ion conduction. Then, a survey about chosen solid electrolytes will be given, followed by a short introduction of all-solid-state battery concepts. A survey concerning the stability of solid electrolytes in contact with alkali metal electrodes and interfacial properties under current load will be described in section 3 and 5, whereas this section concentrates on the conducting properties and mechanisms.

2.1 Basics of ion conduction

Ionic conductivity in solids is often described as the transport of ions between energetically favorable positions in the crystal lattice. Generally the overall conductivity can be described as shown in equation 2.1, where σ_i denote the partial conductivity.

$$\sigma_{\text{total}} = \sum \sigma_i \quad (2.1)$$

In principle the partial conductivity can be described by the concentration of charge carriers c_i , the Faraday constant F , the charge number z_i and the mobility u_i , assuming that only one charge carrier is transported:

$$\sigma_i = z_i \cdot F \cdot c_i \cdot u_i \quad (2.2)$$

In general, the diffusion coefficient D_i can be described as the product of the squared jump distance a_i and the jump frequency ω_i :

$$D_i = \frac{1}{6} \cdot a_i^2 \cdot \omega_i \quad (2.3)$$

The mechanical mobility b_i , the fraction of the absolute values of the speed \vec{v}_i and the applied force \vec{F} , is directly connected to the diffusion coefficient, which is shown in equation 2.4. T and k denote the temperature and the Boltzmann constant, respectively.

$$b_i = \frac{|\vec{v}_i|}{|\vec{F}|} = \frac{D_i}{k \cdot T} \quad (2.4)$$

The mechanical and the electrical mobilities are then connected via the charge number:

$$u_i = |z_i| \cdot e_0 \cdot b_i \quad (2.5)$$

Inserting equation 2.5 in 2.2 and rearrangement leads to equation 2.6.

$$\sigma_i = (z_i \cdot e_0)^2 \cdot b_i \cdot N_i = z_i^2 \cdot e_0 \cdot F \cdot b_i \cdot c_i \quad (2.6)$$

Insertion of the correlation of the mechanical mobility and the diffusion coefficient (equation 2.4) in equation 2.6 and under application of equation 2.3, directly results in equation 2.7

$$\sigma_i = (z_i \cdot e_0)^2 \cdot b_i \cdot N_i = (z_i \cdot e_0)^2 \cdot \frac{D_i}{k \cdot T} \cdot N_i = z_i^2 \cdot F^2 \cdot \frac{\frac{1}{6} \cdot a_i^2 \cdot \omega_i}{R \cdot T} \cdot c_i \quad (2.7)$$

Thus, the conductivity is a function of the jump distance, the jump attempts and the fraction of charge carriers. The diffusion coefficient is directly connected to conductivity and mobility. In general the diffusion coefficient shows an Arrhenius behavior that is denoted in the following equation:

$$D = D'_0 \cdot \exp\left(\frac{-\Delta G^\ddagger}{R \cdot T}\right) \quad (2.8)$$

Rearrangements and insertions lead to equation 2.9. Note that the entropic term of the Gibbs free energy is combined with the geometric factor (which is then combined and replaced by D_0). This equation is often used for the Arrhenius diagrams by plotting the logarithm of product $\sigma \cdot T$ against the reciprocal temperature and for the derivation of activation energies^[6] (neglecting the activation entropy).

$$\sigma = \frac{D_0 \cdot z^2 \cdot F^2 \cdot c}{R \cdot T} \exp\left(\frac{-E_A}{R \cdot T}\right) \quad (2.9)$$

Thus, the conductivity can be influenced by the amount of charge carriers, the activation energy and diffusion coefficient, which includes the attempt frequency, jump distance and a geometrical factor.

2.2 How to affect ionic conductivity

In this section, the influence of structural and binding state changes on the conductivity will be shortly and qualitatively discussed. For ion conduction, face sharing polyhedra are essential, as the transport often occurs via tetrahedral and octahedral sites, which will be described for a few solid electrolytes in the next section. Generally, the conductivity is affected by the binding states, the structure (framework), composition, temperature, pressure, doping and non-stoichiometry. As already stated above, the conductivity depends on the concentration of charge carriers. Thus, increasing the fraction of mobile charge carriers would in principle improve the ionic conductivity. However, the implementation of additional charge carriers also decreases the number of vacant equivalent crystal sites, which might also affect the attempt frequency. The mobility u is proportional to the diffusion coefficient, which is proportional to a geometrical factor, the attempt frequency and the jump distance (see equations 2.3 - 2.5 in the previous section). Thus, u can be influenced by the jump distance (distance between polyhedral sites), the ratio between vacant to filled sites and the geometry itself. The vacancy or more general the defect concentration can often be increased by aliovalent doping. The interactions of the ions with the lattice are influenced by the bonding states for the framework and the polarizability of the lattice. "Softer" materials are more polarizable and the framework is displaced with lower energy cost, influencing the activation energy^[7]. The activation energy strongly depends on the diffusion pathway and therefore on the polyhedra connectivity. Increasing the polyhedral volume decreases the activation energies. In general, bcc-like anion frameworks allow direct ion hops because of adjacent tetrahedral sites, which is desirable for high conductivities. Against this, fcc and hcp frameworks show a more than two times higher barrier in general^[8].

2.3 A short overview about solid electrolytes and their respective conduction mechanisms

Quite a number of solid electrolytes with different structures, compositions and properties are known. This survey is focused on the ion conductors $\text{Li}_{10}\text{GeP}_2\text{S}_{12}$ (LGPS), $\text{Li}_7\text{La}_3\text{Zr}_2\text{O}_{12}$ (LLZO, garnet type material), $\text{Li}_{1.2}\text{Al}_{0.2}\text{Ti}_{1.8}(\text{PO}_4)_3$ (LATP, NaSICON type material), $\text{Li}_{0.35}\text{La}_{0.55}\text{TiO}_3$ and $\text{Li}_{3/8}\text{Sr}_{7/16}\text{Ta}_{3/4}\text{Zr}_{1/4}\text{O}_3$ (LLTO and LSTZO, both perovskite type materials), $\text{Li}_7\text{P}_3\text{S}_{11}$ (LPS), Na_3PS_4 (NPS), Na- β'' -aluminum oxide (beta-alumina)¹ and argyrodite type materials like $\text{Li}_6\text{PS}_5\text{X}$ (with X= Cl, Br, I). All these materials are promising solid electrolyte materials and were widely used for experiments in this thesis. A literature survey about stability in contact with alkali metal and interfacial properties will be given in the respective sections.

A classical lithium ion conductor is Li_3N , which shows conductivities up to 0.12 mS/cm. Li_3N exhibits a layered structure of hexagonal Li_2N -layers and pure Li-layers that are responsible for the high ionic conductivity. In this structure, jumps between octahedral and tetrahedral sites are responsible for ionic transport. The layered structure implies that Li_3N is an anisotropic ion conductor, which is shown by a two order of magnitude smaller conductivity along the c-axis. By hydrogen doping (0.5 to 1 atom-%), NH_2 -units are formed in the layers, resulting in a weakened Li-N-bond and a Frenkel pair defect or charged vacancies mediated conduction mechanism. Thus, the conductivity is enhanced to 0.3 mS/cm. In principle this material would be a promising solid electrolyte but unfortunately it already decomposes at voltage of 0.44 V against Li/Li^+ , which prevents the use of positive electrode materials in combination with this ion conductor^[9–11].

A promising solid electrolyte with high ionic conductivity of more than 10 mS/cm is LGPS ($\text{Li}_{10}\text{GeP}_2\text{S}_{12}$), which partly belongs to the class of LiSICON² materials³. In this material, the lithium ions are transported via zigzag pathways along the c-axis, through jumps between tetrahedral sites composed of LiS_4 -tetrahedra^[12]. Adams et al. suggested that LGPS is rather a 3D ion conductor than 1D, as the conduction chains are cross-linked^[13,14].

The synthesis of $\text{Li}_2\text{S-P}_2\text{S}_5$ glass materials and the fact that these compounds are ion conductors was reported early by Eckert et al., the reason for the increased conductivity of $\text{Li}_2\text{S-P}_2\text{S}_5$ glasses was found to be the less localized negative charge of the non-bridging sulfur-groups^[15]. In the triclinic $\text{Li}_7\text{P}_3\text{S}_{11}$ (LPS)^[16–18] the difference in activation energy for vacancy and interstitial transport are only slightly different, enabling both conduction pathways. However, the conduction is mainly caused by interstitial transport^[19].

In order to prepare similar ion conducting compounds for sodium, the cubic Na_3PS_4 (NPS) was found, showing conductivities of around 0.46 mS/cm^[20]. Conduction occurs through the Na1 and Na2 sites leading to three dimensional conduction, which is generally missing in the tetragonal modification^[21]. The argyrodite type compound $\text{Li}_6\text{PS}_5\text{X}$ (with X= Cl, Br, I) exhibits conductivities of more than 1 mS/cm^[23] and lithium ion transport occurs via face sharing tetrahedra^[24].

The electronic partial conductivity of these compounds (LGPS, LPS and NPS) was gen-

¹Na- β'' -aluminum oxide is often a mixture of the β'' and β -aluminum oxide phases.

²Abbreviation for Lithium Super Ionic Conductor.

³LGPS is often seen as an independent material class. Sometimes it is assigned to the class of thio-LiSICONs.

erally found to be in the range of a few nS/cm^[22]. One of the biggest disadvantages of these materials is the formation of H₂S in contact with water^[25].

The perovskite type materials (ABO₃) are a further group of lithium solid electrolytes. The most prominent material is Li_{0.35}La_{0.55}TiO₃ (LLTO)^[26,27] or in a more general notation Li_{3x}La_(2/3-x)TiO₃. In this material class, the ionic conductivity mainly depends on the size of the second A-site ion (in this case La³⁺), the vacancy concentration and the inter atomic bond strength of Ti-O^[28], which leads to the conclusion that a vacancy transport (a-site vacancy) mechanism is responsible for the conductivity. The structure exhibits stackings of lithium and lanthanum rich layers. Ionic conductivities up to hundreds of μS/cm could be reached and the bulk material conductivity is found to be in the range of 1 mS/cm. The main reason for this was found to be the grain boundaries, where strong deviations from the perovskite structure were found. Deformation of the Ti-O polyhedra, a lanthanum and lithium decrease are the main findings, leading to strongly decreased ion conductivity^[29]. Li_{3/8}Sr_{7/16}Ta_{3/4}Zr_{1/4}O₃ is another perovskite type solid electrolyte with a similar conduction mechanism and an overall conductivity of around 0.2 mS/cm^[30].

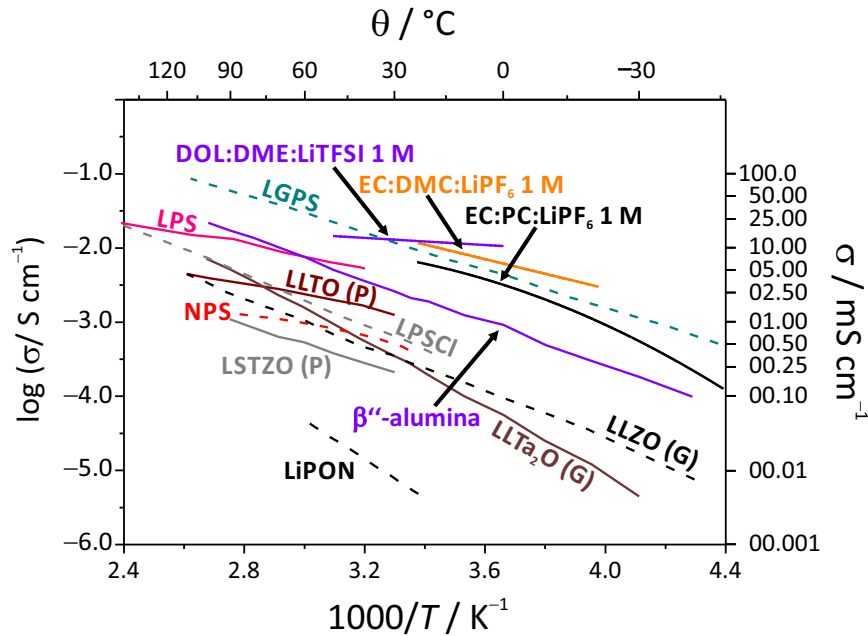


Figure 2.1: Summary of the temperature dependence of the ionic conductivities for different solid and liquid electrolytes. The data for LGPS^[12], LPS^[18], LLTO^[27], LPSCl^[23], LLZO^[34], LLTa₂O^[33], LSTZO^[30], NPS^[20], LiPON^[40] (all SEs), DOL:DME:LiTFSI 1M^[41], EC:DMC:LiPF₆ 1M^[42] and EC:PC:LiPF₆ 1M^[42] (LEs) were taken from literature. LiPON is mostly used in thin-film ASSBs and is drawn as reference. For β''-alumina the data reported in this thesis and by Wenzel et al.^[43] were used.

One of the most prominent lithium ion conductors are the class of the garnet type materials with the general formula of A₃B₂(XO₄)₃. In this structure, lithium conduction occurs between corner sharing octahedral sites that are face sharing with tetrahedral sites^[31]. The sites of lithium ions are three dimensionally connected and Li ions can hop from one edge sharing octahedral site via a tetrahedral site to another octahedral site. Different substitutions were studied for this structure type, the most prominent are Li₇La₃Zr₂O₁₂ (LLZO, Al-doped) and Li₅La₃Ta₂O₁₂. The materials with different substitutions (and

therefore with different lithium contents) show conductivities ranging from 10^{-6} S/cm to 10^{-3} S/cm^[32-34].

The NaSICON type lithium ion conductors ($AM_2(PO_4)_3$ with A = alkali and M = Ge, Ti, Zr, e. g. $Li_{1.2}Al_{0.2}Ti_{1.8}(PO_4)_3$) consist of corner sharing TiO_6 octahedra and PO_4 tetrahedra, leading to a 3 dimensional open framework⁴. In the parent structure $Li_1Ti_2(PO_4)_3$, lithium occupies the position denoted as M(I). Through Al or more general trivalent doping, lithium ions are found at a second position, denoted as M(II), which is an irregular eight-fold coordinated site. The lithium ion migration path, often also called the bottle neck, is described as M(I)-M(II)-M(I). The narrowest parts of the bottle neck channels are widened by Al-doping so that the lithium ion transport can occur without severe lattice distortions, resulting in an overall conductivity increase from 10^{-6} S/cm to 10^{-4} S/cm^[35]. Regarding the sodium conducting NaSICON compounds, the conductivity mechanism is similar and the conductivity is increased by increasing the occupancy of the Na sites to the half. More sodium decreases the conductivity by decreasing the jump frequency, as the neighboring sites are already blocked by sodium ions. An extended review of differently substituted NaSICON materials is given by Guin et al.^[36] and Anantharamulu et al.^[37].

The most prominent sodium conducting solid electrolyte is the so called sodium- β "-aluminum oxide (β "-alumina), with a general composition of $Na_2O \cdot (5-7) Al_2O_3$ ^[38]. The structure exhibits loosely-packed layers containing the sodium ions, which are responsible for the conductivity and are thus called the conduction planes. Likewise, β "-alumina is a two dimensional ion conductor. Between the conduction planes, spinel layers containing the aluminum (in both the octahedral and tetrahedral sites) and oxygen are found^[39]. Doping with lithium or magnesium (on the tetrahedral sites) is necessary to stabilize the β "-modification and to relieve local strain. The ion transport occurs via vacancy, interstitial and interstitialcy jumps, depending on the specific phase. For β - and β "-alumina it is found that the interstitialcy and vacancy diffusion mechanism are dominating^[7].

A summary of temperature dependent conductivities is given in Fig. 2.1, showing that some solid electrolytes can already keep up with common liquid electrolytes. Considering that the Li^+ transference numbers for solid electrolytes are virtually unity and for the liquid electrolytes are mostly less than 0.5, as already stated above, solid electrolytes can show considerably higher conductivities than liquid electrolytes. Regarding Fig. 2.1, it is obvious that only a few solid electrolytes show conductivities that are higher than 1 mS/cm, including LPSCl, LLTO (only bulk conductivity), β "-alumina, LPS and LGPS.

2.4 All-solid-state batteries

All-solid-state batteries (ASSB) are generally regarded as superior compared to common LIBs, concerning safety (non-flammable materials), durability and performance. A Li metal/LiPON/LNMO ASSB (thin film) in comparison with a similar cell using liquid electrolytes revealed remarkable capacity retention for 10,000 cycles, whereas the LIB with liquid electrolyte showed aging effects and capacity decay^[44]. In the following, two ASSB concepts are described and a short overview of the results will be given. The first type of ASSB is entirely composed of thin films. Thus, thin film preparation methods are used, e. g. sputtering and pulsed laser deposition, which requires expensive vacuum setups and are only suitable for smaller cells as the size of deposition chambers is limited.

⁴Abbreviation for Na Super Ionic Conductor, which was adopted for lithium (see LiSICON).

An illustration of the cell setup is shown in Fig. 2.2a. Another preparation method is doctor blading, which was used for fabricating a thin film $\text{TiS}_2/\text{LPS}/\text{Li-In}$ battery^[45].

The second battery type is the so-called thick-film ASSB, which is prepared by pressing of powder materials and schematically shown in Fig. 2.2b^[46]. One example for this cell type was reported recently by Kato et al., using a LiNbO_3 -coated LiCoO_2 (LCO) positive electrode, LGPS as solid electrolyte and $\text{Li}_4\text{Ti}_5\text{O}_{12}$ (LTO) and carbon mixture as negative electrodes. For the positive electrode a ratio of 70:30 wt% for active materials to LGPS and for the negative electrode a ratio of 30:60:10 wt% for LTO, carbon and LGPS was chosen. Reasonable capacities of around 100 mAh/g were obtained at a high current density of $1.15 \text{ mA}/\text{cm}^2$. However, the cyclability and capacity retention was not reported. Main problems for this cell type are voids in the solid electrolyte, volume changes, strain formation and the instability of the solid electrolytes against the electrode materials. This problem will be partially covered in section 3, 5 and 6. LiNbO_3 -coating was necessary to prevent interfacial reactions and mutual diffusion of Co, P and S, which was proven for the interface between LCO and $\text{Li}_2\text{S-P}_2\text{S}_5$ solid electrolyte^[48].

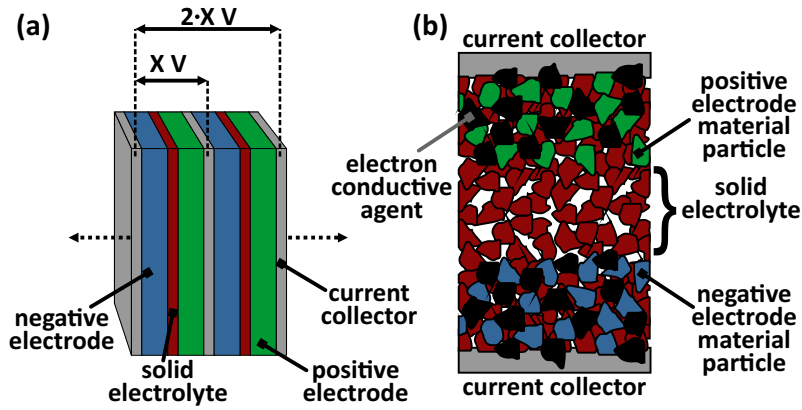


Figure 2.2: Illustration of the two different ASSB cell concepts, in (a) the thin film and the scheme of a battery package^[47] and in (b) the thick-film (powder) ASSB^[46] are displayed.

Another ASSB prepared by powder pressing was reported by Shin et al. using TiS_2 as positive electrode material, LGPS as solid electrolyte and Li-In alloy as negative electrode material. Cycling was conducted between 1.5 V to 3 V resulting in capacities of 240 mAh/g at 0.2 C with reasonable durability. Still capacity fading was observed. The application of higher C-rates resulted in polarization and capacity decrease^[49]. The cycling of a LCO/ $\text{Li}_6\text{PS}_5\text{Cl}$ /LTO cell resulted in a capacity of 27 mAh/g and the growth of a resistive layer was observed, leading to the conclusion that the interface is the most critical part of the cell^[50]. The notion that interfacial reactions and effects are critical for proper cell function was also raised by studying a $\text{Cu}/\text{Li}_6\text{PS}_5\text{Br}/\text{In-Li}$ cell. A capacity of 650 mAh/g was initially obtained which decreased to 90 mAh/g after 20 cycles at C/50. One reason for the capacity fading was reported to be the incorporation of Cu^+ into the solid electrolyte, leading to a volume and resistivity change. This effect was found to be reversible but strongly affected the battery performance.

Another work stated that the use of sulfide solid electrolytes, e. g. $\text{Li}_2\text{S-P}_2\text{S}_5$, only worked at low current densities and the use of garnet type materials completely prevented the battery from working. Thus, Han et al. prepared an ASSB containing the solid electrolyte LGPS (as both electrodes and electrolytes) and carbon as conductive agent, which showed

to be cyclable^[51]. Kotobuki^[52] et al. found that garnet type materials could be used in ASSB, which is in contrast to the report of Han et al.^[51]. Using $\text{Li}_5\text{La}_3\text{Ta}_2\text{O}_{12}$, lithium metal and LCO for negative and positive electrode material, respectively, a capacity of 83 mAh/g (56% of the theoretical value) was obtained. Thus, the knowledge about lithium metal containing ASSBs is generally quite limited, leading to a number of important questions concerning material stability and interfacial properties. A few of these issues concerning alkali metal electrodes in ASSBs will be studied and clarified in this work, which might additionally be assigned to the positive electrode site.

3 Interface or interphase? – Stability of solid electrolytes in contact with alkali metal

3.1 Introduction

The application of alkali metal electrodes in ASSBs would lead to a significant increase in volumetric and gravimetric energy densities^[53–55]. Therefore, solid electrolytes with high ionic conductivities that can keep up with the values for liquid electrolytes were already developed (see section 2.2). By assuming an electrode area of 1 cm^2 , an electrolyte thickness of $2\text{ }\mu\text{m}$ and a conductivity of 2 mS/cm , which are realistic values for new materials like $\text{Li}_7\text{P}_3\text{S}_{11}$ (LPS) or LGPS, a low area resistance of $0.1\text{ }\Omega\cdot\text{cm}^2$ for the solid electrolyte is obtained. The interface properties of the material might then be the limiting factor, as a low interfacial or interphase resistance of $1\text{ }\Omega\cdot\text{cm}^2$ already increases the overall cell resistance to the tenfold. As the kinetics of interphases and interfaces in LIBs are essential for liquid electrolyte based systems^[56], it may likewise be crucial for solid state batteries, too. Thus, the compatibility between solid electrolytes and electrode materials plays a critical role for the proper function of ASSBs, as extensively pointed out by some industry researchers^[57], and is a mostly neglected research topic. Most research is focused on the development and optimization of materials, but the ionic transport properties are already higher compared to liquid electrolytes so that the interfacial properties are getting more important, as described above. Industry representatives strongly suggest to have a look at interfaces and interphases^[57,58].

The investigation of interphases and interfaces – the difference will be explained in the following section – is often cumbersome and laborious, as standard methods cannot be applied. X-ray diffraction techniques often fail due to the small volume and buried character of the interphases (interfaces could not be investigated as no reaction has taken place). The same pertains for SEM and other microscopic techniques. Hence, information about interphase or interface formation is mainly obtained by electrochemical techniques which only give phenomenological and chemical unspecific insights. As the interpretation of the obtained data is often difficult, researchers tend to use more simple methods that do not regard the interphase or interface formation. Often cell cycling at very low current densities is used as method to test the stability and interfacial properties of a material. Cyclic voltammetry (CV) is often used^[59,60] as an alternative technique. The data obtained by these methods are of limited use and even more unspecific, which will be shown and discussed extensively in this chapter.

For the proper investigation and evaluation of material stability (and interphase/interface formation), a classification of the three interphase types is discussed in section 3.2. Then, a literature survey on solid electrolyte stability is given in section 3.3 and the already published results of this thesis are included into this overview for comparison. General

considerations and basic principles are given in section 3.4, which will be needed later on as quantitative interphase models are developed. In section 3.5.1, the limited use of CV results will be discussed and proven by showing example data obtained for several solid electrolytes. In order to clarify the stability of solid electrolytes in contact with alkali metals, a combined approach is described in section 3.5.2, including two electrochemical methods and a newly developed in situ photoelectron spectroscopy technique, altogether leading to chemical and quantitative information about the interphase/interface formation (stability). An overview and comparison of the expected and obtained results for the different electrochemical techniques of the combined approach and a detailed description of the setups and requirements are then given in section 3.5.3 and 3.5.4. In section 3.6 to 3.8 the results for all three interface/interphase types are discussed and a quantitative model for SEI formation and growth is developed. The results for further materials are displayed and described in section 9.3. According to the results reported in this chapter and thermodynamic calculations, synthesis recommendations for stable solid electrolytes are given in section 3.9, directly followed and concluded by an assessment of mechanical stability of interphases. The results of this chapter are then summarized in section 3.11 and a short outlook is given, resulting in a valuation for the use in alkali metal containing ASSBs.

3.2 Classification of interfaces/interphases

In this section a classification of all common interface and interphase types is given, which is already reported by Wenzel et al.^[61], according to the physical properties of the product phases. Three different types of interface/interphase can be distinguished and are schematically shown in Fig. 3.1.

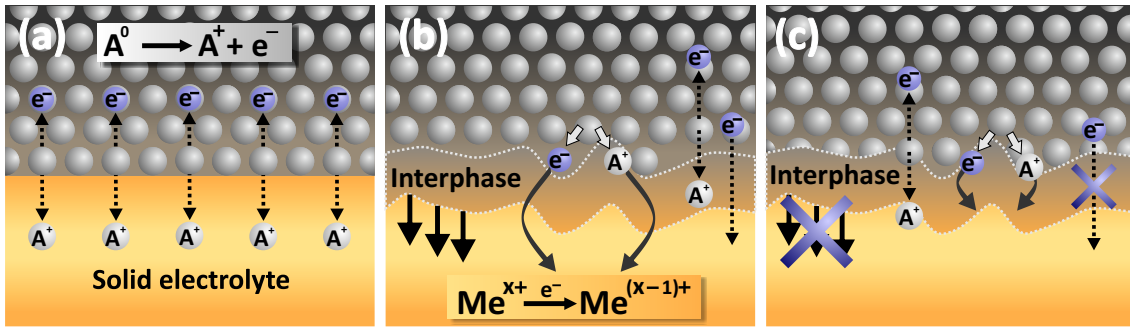


Figure 3.1: The three different interphase/interface types between alkali metal and a solid alkali ion conductor. (a) Thermodynamically stable interface; (b) a reactive and mixed-conducting interphase (MCI); (c) metastable, kinetically stabilized solid electrolyte interphase (SEI). Figure from^[61].

Fig. 3.1a exhibits a sharp two-dimensional interface, as the electrolyte is not reacting and forms a thermodynamically stable interface (2D). It requires that both phases, the alkali metal and the solid electrolyte in contact, are in thermodynamic equilibrium *a priori*. Considering the high reactivity of lithium and sodium metal, this surely will be the minor group of interfaces/interphases. In Fig. 3.1b, a three-dimensional interphase is formed, proposed as mixed conducting interphase (MCI)^[62] due to the physical properties of the decomposition products. The reaction between the electrode and the electrolyte leads to products which are ionic and electronic mixed conductors. An MCI is often formed when

reducible transition metals (TM) are incorporated in the structure, as the reduction of TMs from the insulating highest to lower oxidation states induces electronic conduction, and the decomposition products may become electronic and ionic conducting. Both values are approximately in the same order of magnitude and support a steady and rapid growth of the interphase through the material and significantly alter the properties of the material. MCIs, by growing through the solid electrolyte, will then lead to short circuiting and self-discharge of the battery.

The interphase displayed in Fig. 3.1c shows a different behavior, as the growth of the interphase is kinetically hindered after formation. The growth limitation is caused by either complete insulating character or very low electronic conductivity of the products. Thus, the film growth is limited to very small rates. This interphase type is called solid electrolyte interphase (SEI). Both, MCI and SEI formation are characterized by a thermodynamic driving force for the reaction between alkali metal and solid electrolyte. The difference of both is then only found by the transport properties of the decomposition products.

3.3 Stability of solid electrolytes – a literature survey

The stability of solid electrolytes in contact with alkali metal has been a topic of minor interest in the past. Indeed, there are far more works concerning the conductivity than the stability of the solid electrolyte. In most synthesis procedures, cell assembling and cycling publications, cyclic voltammetry is used as a fast and easy method for stability investigations^[59,60]. Whether this approach is valid or not will be discussed in this chapter. Whiteley et al.^[63] stated that CV is not the method of choice for investigations of chemical stabilities. In general, every material is stated to be stable in contact with alkali metals, often without a real proof, or it is stated to react and the decomposition products are assumed but not proven unequivocally^[59]. Likewise CV is used to investigate the electrochemical stability¹.

For MCI forming materials, a lot of research was focused on lithium lanthanum titanates (LLTO), which were interestingly described both as solid electrolyte and electrode material. Mostly electrochemical methods showed the instability of the LLTO^[64–67,69–71], but also ex situ XPS proved the formation of Ti^{3+} ^[68]. All articles report that only Ti^{3+} is formed during reaction with lithium metal. Wenzel et al.^[61] showed by means of in situ XPS that even titanium metal is formed (see section 3.6.1). The term "mixed-conducting interphase" (MCI) was used first by Hartmann et al.^[62] and the classification of three different interphase/interface types was then composed and summarized by Wenzel et al.^[61] and is described in section 3.2. The classification was later on adopted by Zhu et al.^[72], who tried to classify the results of their stability simulation results. Hartmann et al. showed that NaSICON type lithium ion conductors, e. g. lithium aluminum germanium phosphate (LAGP) and lithium aluminum tantalum titanium phosphate (LATTTP), are not stable against lithium metal, and due to the reduction of germanium, tantalum and titanium an MCI is formed. This article was one of the first experimental studies of interphase formation, except for LLTO. MCIs are often formed when multivalent cations are part of the lattice, as those are prone to reduction. Stable components are MgO ^[73]

¹There is no difference in the thermodynamics concerning the electrochemical and chemical stability. Both are often falsely distinguished in literature.

and La_2O_3 ^[68] for example.

A very interesting finding concerning solid electrolyte stability was reported by Schwoebel et al.^[74], showing that the widely used material LiPON is not stable in contact with lithium metal but instead decomposes into three binary compounds (Li_3N , Li_3P and Li_2O). For this, an elaborated UHV cluster tool was used. A more simple approach was then reported by Wenzel et al.^[61] afterwards and is described in section 3.5.5. Using a standard lab scale photoelectron spectrometer, the decomposition of LLTO was investigated, showing the formation of titanium metal, as already stated above. Another promising class of solid electrolytes is found in the system Li_2S - P_2S_5 , with $\text{Li}_7\text{P}_3\text{S}_{11}$ as one important phase, which is reported to be stable in contact with lithium metal^[75] and only shows changes of the overpotential for three cycles^[5]. Simulations by Zhu et al.^[72,76] and Richards et al.^[77] suggested the instability of the material, which was proven by Wenzel et al.^[78] in parallel by using the combined approach described in section 3.7.1. Simulations and experiments both showed that binary compounds were formed (Li_2S and Li_3P). The results are described in section 3.7.1 in detail. Richards et al.^[77] simulated different types of solid electrolytes, including fluorides, chlorides, bromides, phosphates, oxides (LiSiCON), garnet type materials, LGPS, Li_3PS_4 , hydrides, and nitrogen containing components. All simulations stated that only the binary compounds are stable in contact with alkali metals. LGPS and Li_3PS_4 for example are only stable above 2 V vs. Li/Li^+ and only in a narrow voltage window (< 0.5 V)^[77]. Additionally, reduction and oxidation potentials were calculated for LATP ($\text{Li}_{1.3}\text{Al}_{0.3}\text{Ti}_{1.7}(\text{PO}_4)_3$), LAGP ($\text{Li}_{1.5}\text{Al}_{0.5}\text{Ge}_{1.5}(\text{PO}_4)_3$), $\text{Li}_{0.33}\text{La}_{0.56}\text{TiO}_3$, $\text{Li}_7\text{La}_3\text{Zr}_2\text{O}_{12}$ (LLZO), LiPON, $\text{Li}_7\text{P}_3\text{S}_{11}$, LGPS and argyrodites, suggesting that all materials are not stable against lithium metal and mostly form binary compounds^[76]. Similar calculations were shown for cathode materials in contact with solid electrolytes^[76].

$\text{Li}_{10}\text{GeP}_2\text{S}_{12}$ is one of the known solid electrolytes with the highest ionic conductivity and was reported to be stable in contact with lithium metal, as only the dissolution and deposition current peaks were observed in the CV^[12]. However, it is well known that lithium metal reduces LGPS and forms Li_2S ^[49,79], again reliable results on the decomposition are missing. In this material class the author found that germanium in the structure facilitates the growth rate of the SEI and thus strongly contributes to the interphase formation^[80]. The hypothesis states that Li_2S , Li-Ge-alloy and some Li-P-S compounds are formed during decomposition^[80] in contact with lithium alloy electrodes (Sn-Li and Si-Li). Whiteley et al.^[63] showed by means of impedance spectroscopy that the silicon analogue to LGPS is not stable in contact with lithium metal and forms a growing interphase, but the decomposition products were not investigated. Simulations^[72,76,77,81] suggested that the material will decompose to Li_2S , Li_3P and $\text{Li}_{15}\text{Ge}_4$ alloy. The latter work (Ong et al.) reported also the instability of different composition of LGPS, e. g. substitutions of germanium or sulfur by silicon, tin and aluminum or selenium and oxygen, respectively. All were proposed to react with lithium metal. Again, the decomposition products for LGPS in contact with lithium metal were experimentally proven by Wenzel et al.^[82]. The simulations, mentioned in this survey, only give information about the thermodynamic stability of the material. Kinetic information was not obtained. The experimental work by Wenzel et al.^[43,78,82], which is described in section 3.7, exhibits chemical and kinetic information about interphase formation and growth. In the literature, the growth rate of the SEI is often neglected, e. g. Zhu et al. stated, that the decomposition of the materials is not continuing as there is no thermodynamic driving force inside the bulk^[76] for further growth. The results in this work (and the respective articles^[43,61,78,82]) clearly show that the interphase is still growing as there is always a driving force given by the

different potentials of the electrodes. Sakuma et al.^[80] reported by means of impedance spectroscopy that LGPS is not stable during cycling, when Sn-Li or Si-Li alloy electrodes are applied, too.

The garnet type compound LLZO is generally regarded to be one of the stable materials. Nevertheless, in contact with molten lithium a coloration is observed that is attributed to trapped electrons at an oxygen site^[84]. With XPS, no changes for La, Zr and Al were seen and the formation of a new phase could be excluded^[84]. Another garnet type compound, $\text{Li}_{6.75}\text{La}_3\text{Zr}_{1.75}\text{Nb}_{0.25}\text{O}_{12}$ showed a gradually increasing grain boundary and interface resistance^[85] in contact with lithium metal at room temperature. The results for a similar material will be described in section 9.3.7.

Interfaces and interphases show far more effects than simple reactions. One example for this is band bending, which occurs by contacting a metal (e. g. Li) and a semiconductor^[86] or by contacting two semiconductors^[87]. Thus, depletion and accumulation layers form at the interface. For example a decrease of the lithium ion concentration near the electrode interface might occur^[56,88], even for lithium metal electrodes^[87].

For sodium solid electrolytes, the stability is only reported for insertion type compounds (electrode materials) and Na_3PSe_4 ^[89]. It should be noted that polymer electrolytes are reported to be unstable, too^[90–94].

Thus, the experimental results reported in literature are mainly limited to theoretical simulations or to mere electrochemical studies. Experimental results for some of the materials mentioned above will be summarized in this chapter and are partially published.

3.4 General considerations and basic principles

In this section some general considerations concerning solid electrolyte stability are discussed, including a discussion of the thermodynamics of solid electrolytes, the profile of the chemical potential of the alkali metal in the solid electrolyte, the interphase, in the metal and during reaction. Furthermore, a solid state reaction model is described, which is then applied in section 3.7.4 to solid electrolyte decomposition reactions. The effect of percolation and the percolation threshold are introduced as this phenomenon may play an important role for solid state reactions. This section will not cover all real cases but will show and explain a few principles that facilitate the understanding of interphase formation and growth.

3.4.1 Stability of solid electrolytes

In principle, only few solid electrolytes will be stable in contact with alkali metals, as lithium and sodium are highly reactive (reducing). For stable materials, a simplified view to the band structure is schematically shown in Fig. 3.2a. If the material is stable in contact with alkali metal, the conduction band of the solid electrolyte should be found at a higher energy compared to the Fermi level of the alkali metal. Thus, the transfer of electrons from the Fermi level of the alkali metal to the conduction band of the solid electrolyte is prevented.

The case of instability is shown in Fig. 3.2b, where the Fermi level of the alkali metal is

higher in energy compared to the conduction band of the solid electrolyte and consequently, electrons are transferred (arrows). Likewise, the Fermi level of the positive electrode material should be at higher energies compared to the valence band of the solid electrolyte so that the electron transfer from the valence band of the solid electrolyte to the Fermi level is prohibited. Again, the reacting case is displayed in Fig. 3.2b, where the Fermi level of the positive electrode material is lower in energy than the valence band of the solid electrolyte and hence electrons are transferred. Additionally, the ionic species (the electrochemical potential of lithium ions $\tilde{\mu}_{\text{Li}^+}$) also play a major role (as a contribution to the chemical potential μ_{Li}). Thus, both electrodes are reacting with the solid electrolyte, leading to changing conduction properties and consumption of active material (which equals a capacity loss). The potential difference in Fig. 3.2 is equivalent with the open circuit voltage (OCV) of the cell and is calculated from the energy difference between the Fermi levels of the alkali metal and the positive electrode material. The electrochemical stability window (W_{EC}) is defined as the difference between the conduction and valence band of the solid electrolyte. For stable materials, the OCV should generally be smaller than W_{EC} .

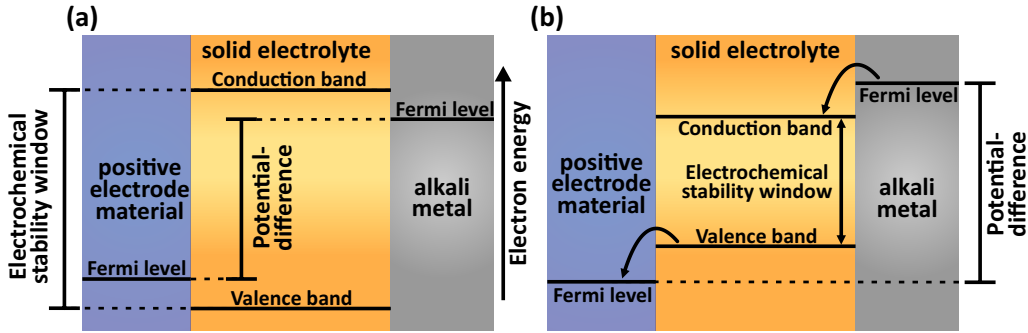


Figure 3.2: The schematic band structure for a solid electrolyte that is stable in contact with the positive electrode material and alkali metal is shown in (a). In (b), the unstable solid electrolyte is shown, which reacts with both electrodes.

3.4.2 Kinetics of solid state reactions

In the following, SEI formation is described by the Wagner model diffusion-controlled solid state reactions^[96,97], as we assume diffusion to be mostly limiting for SEI growth². This model is common for corrosion processes. A few assumptions are necessary for this model, including that the thermodynamic equilibrium at the phase boundary is maintained locally during the entire process (local thermodynamic equilibrium). At the beginning, the flux equations for the charge carriers are required:

$$\begin{aligned} j_{\text{el}} &= -L_{\text{el}} \cdot \nabla \tilde{\mu}_{\text{el}} \\ j_{\text{ion}} &= -L_{\text{ion}} \cdot \nabla \tilde{\mu}_{\text{ion}} \end{aligned} \quad (3.1)$$

L are the respective transport coefficients, j is the molar flux, $\nabla \tilde{\mu}$ the chemical potential gradient of the ions and electrons. The chemical potential gradient of the (neutral) component A is defined as:

²Convection is excluded in the solid state.

$$\nabla\mu_A = \nabla\tilde{\mu}_{\text{ion}} + z_{\text{ion}} \cdot \nabla\tilde{\mu}_{\text{el}} \quad (3.2)$$

Multiplication of equation 3.1 with the opposing transport coefficients results in equation 3.3.

$$\begin{aligned} L_{\text{ion}} \cdot j_{\text{el}} &= -L_{\text{el}} \cdot L_{\text{ion}} \cdot \nabla\tilde{\mu}_{\text{el}} \\ L_{\text{el}} \cdot j_{\text{ion}} &= -L_{\text{ion}} \cdot L_{\text{el}} \cdot \nabla\tilde{\mu}_{\text{ion}} \end{aligned} \quad (3.3)$$

Multiplication with z_{ion} leads to equation 3.4.

$$\begin{aligned} z_{\text{ion}} \cdot L_{\text{ion}} \cdot j_{\text{el}} &= -L_{\text{el}} \cdot L_{\text{ion}} \cdot z_{\text{ion}} \cdot \nabla\tilde{\mu}_{\text{el}} \\ L_{\text{el}} \cdot j_{\text{ion}} &= -L_{\text{ion}} \cdot L_{\text{el}} \cdot \nabla\tilde{\mu}_{\text{ion}} \end{aligned} \quad (3.4)$$

Addition of both equations in equation 3.4 leads to equation 3.5.

$$L_{\text{el}} \cdot j_{\text{ion}} + z_{\text{ion}} \cdot L_{\text{ion}} \cdot j_{\text{el}} = -L_{\text{el}} \cdot L_{\text{ion}} \cdot (\nabla\tilde{\mu}_{\text{ion}} + z_{\text{ion}} \cdot \nabla\tilde{\mu}_{\text{el}}) \quad (3.5)$$

Regarding equation 3.2 and 3.5, leads to equation 3.6.

$$L_{\text{el}} \cdot j_{\text{ion}} + z_{\text{ion}} \cdot L_{\text{ion}} \cdot j_{\text{el}} = -L_{\text{el}} \cdot L_{\text{ion}} \cdot \nabla\mu_A \quad (3.6)$$

Considering charge neutrality, in equation 3.7, results in equation 3.8.

$$\begin{aligned} \sum (z_i \cdot F) \cdot j_i &= 0 \\ (z_{\text{ion}} \cdot F) \cdot j_{\text{ion}} - F \cdot j_{\text{el}} &= 0 \end{aligned} \quad (3.7)$$

$$\begin{aligned} L_{\text{el}} \cdot j_{\text{ion}} + z_{\text{ion}} \cdot L_{\text{ion}} \cdot (z_{\text{ion}} \cdot j_{\text{ion}}) &= -L_{\text{el}} \cdot L_{\text{ion}} \cdot \nabla\mu_A \\ j_{\text{ion}} \cdot (L_{\text{el}} + z_{\text{ion}}^2 \cdot L_{\text{ion}}) &= -L_{\text{el}} \cdot L_{\text{ion}} \cdot \nabla\mu_A \end{aligned} \quad (3.8)$$

The resulting transport equation for coupled transport of ions and electrons is shown in Eq. 3.9. L are the respective transport coefficients, j_A is the molar flux of the neutral component, $\nabla\mu_A$ the chemical potential gradient of the neutral component, F the Faraday constant, ξ the film thickness, μ_A^0 the chemical standard potential for the alkali metal A and σ the respective average conductivities.

$$j_{\text{ion}} = j_A = -\frac{L_{\text{el}} \cdot L_{\text{ion}}}{L_{\text{el}} + z_{\text{ion}}^2 \cdot L_{\text{ion}}} \cdot \nabla\mu_A \quad (3.9)$$

Eq. 3.9 is only valid if the electrons and ions are not interacting and the cross coefficients can be neglected. Further rearrangement and insertion of equation 3.10 leads to equation 3.11 (with $z_{\text{ion}} = 1$).

$$\sigma_i = (z_i \cdot F)^2 \cdot L_i \quad (3.10)$$

$$j_A = -\frac{1}{F^2} \frac{\sigma_{\text{el}} \cdot \sigma_{\text{ion}}}{\sigma_{\text{el}} + \sigma_{\text{ion}}} \cdot \nabla \mu_A = -\frac{1}{F^2} \frac{\sigma_{\text{el}} \cdot \sigma_{\text{ion}}}{\sigma_{\text{el}} + \sigma_{\text{ion}}} \cdot \frac{\mu_A^0}{\xi} \quad (3.11)$$

In a first approximation, the gradient of the chemical potential can then be replaced as the chemical standard potential for the alkali metal divided by the film thickness, as displayed in Eq. 3.11. Thus, we assume a much smaller chemical potential of lithium at the cathode side of the SEI. This approach will be used later for modeling interphase growth.

The chemical potential for pure alkali metal is identical with the chemical standard potential of the alkali metals, as the activity a in Eq. 3.12 is 1. Thus, the molar Gibbs energy for the pure alkali metal can be used, which yields 8.5 kJ/mol for lithium and 15.2 kJ/mol for sodium metal (at room temperature and standard pressure).

$$\mu_i = \mu_i^0 + RT \cdot \ln(a_i) \quad (3.12)$$

Fig. 3.3a shows a sketch of the interphase growth according to Eq. 3.9. Thus, the most important condition is the charge neutrality. Nevertheless, Eq. 3.11 also states that the flux is limited by the conductivity of the minor charge carriers, which is again a consequence of the charge neutrality. If the electronic conductivity of the interphase is significantly smaller than the ionic conductivity, the transport term in Eq. 3.11 is approximately only affected by σ_{el} , as the sum of the ionic conductivity and the significantly smaller electronic conductivity roughly yields the ionic conductivity that is then reduced with the numerator, as displayed in equation 3.13.

$$j_A \cong -\frac{\sigma_{\text{el}}}{F^2} \nabla \mu_A \quad (3.13)$$

$$\sigma_{\text{el}} \ll \sigma_{\text{ion}}$$

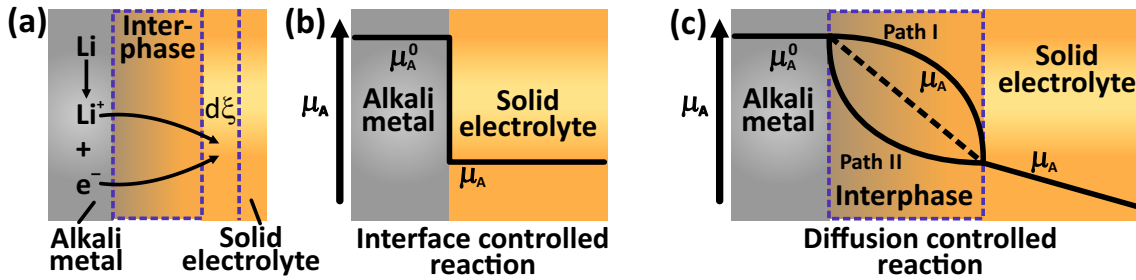


Figure 3.3: Sketch of Wagner's model for tarnishing is displayed in (a). (b) Interface-controlled reaction, the chemical potential difference forms the driving force for the interface transfer. (c) Diffusion controlled growth of SEI.

Directly after contacting, the profile of the chemical potential for the alkali metal shows a steep decrease from the value of the alkali metal to the value of the solid electrolyte. The reaction is then interface controlled (effects like nucleation, charge transfer etc. are the rate determining steps) and only the barrier at the phase boundary is limiting^[97]. The local equilibrium is no longer maintained and a discontinuity in the component activity, a jump in activity, is the driving force for transport through the interface^[97].

After a certain film thickness is reached, the reactions switch to diffusion control, which can then be described by Wagner's model for tarnishing. The chemical potential for the

alkali metal species can show three different profile types. If a nonlinear behavior (Path I and II) is found, the chemical potential gradient is depending on the transport coefficients. A linear progression is only observed if the chemical potential gradient is irrespective of the transport coefficients and constant.

Using Eq. 3.11 (rearranged form of Wagner’s model), an equation that connects the film thickness and reaction time can be obtained. This is shown in the following. In Eq. 3.14, M_{SEI} is the molar mass, ρ_{SEI} the density of the SEI compounds and x the stoichiometric coefficient for the decomposition reaction^[97–99].

$$\frac{d\xi}{dt} = \frac{j_A \cdot M_{\text{SEI}}}{\rho_{\text{SEI}} \cdot x} \quad (3.14)$$

Rearrangement leads to Eq. 3.15:

$$j_A = \frac{d\xi}{dt} \cdot \frac{\rho_{\text{SEI}} \cdot x}{M_{\text{SEI}}} \quad (3.15)$$

Inserting Eq. 3.15 into Eq. 3.11 and further rearrangement leads to Eq. 3.16.

$$\frac{d\xi}{dt} \cdot \frac{\rho_{\text{SEI}} \cdot x}{M_{\text{SEI}}} = -\frac{1}{F^2} \frac{\sigma_{\text{el}} \cdot \sigma_{\text{ion}}}{\sigma_{\text{el}} + \sigma_{\text{ion}}} \cdot \frac{\mu_A^0}{\xi} \quad (3.16)$$

By separation of the variables and indefinite integration, Eq. 3.17 and 3.18 are obtained. The latter shows a parabolic behavior that is often observed for solid state reactions. As only the one dimensional case is regarded here, the absolute value is used³.

$$\int_0^d \xi \, d\xi = \frac{1}{F^2 \cdot \rho_{\text{SEI}} \cdot x} \frac{M_{\text{SEI}} \cdot \sigma_{\text{el}} \cdot \sigma_{\text{ion}}}{\sigma_{\text{el}} + \sigma_{\text{ion}}} \cdot \mu_A^0 \cdot \int_0^t dt \quad (3.17)$$

$$d = \sqrt{\frac{2}{F^2 \cdot \rho_{\text{SEI}} \cdot x} \frac{M_{\text{SEI}} \cdot \sigma_{\text{el}} \cdot \sigma_{\text{ion}}}{\sigma_{\text{el}} + \sigma_{\text{ion}}} \cdot \mu_A^0} \cdot \sqrt{t} = k \cdot \sqrt{t} \quad (3.18)$$

Thus, a square root behavior is obtained, which is in good agreement with the models for SEI formation in liquid electrolyte based systems^[95]. Deviations from the parabolic behavior are observed when the conductivities are not constant during the reaction. Note that this model only applies to diffusion controlled reactions^[96,100]. Additionally, the model is only valid for homogeneous solids, perfect contacts and without phase transfer barriers. A phase transfer limitation cannot be ruled out, too. Nevertheless, by approximating the properties and by assuming that the afore mentioned requirements are valid, the application of this model yields in a qualitative understanding of interphase behavior.

³Equation 3.16 turns positive.

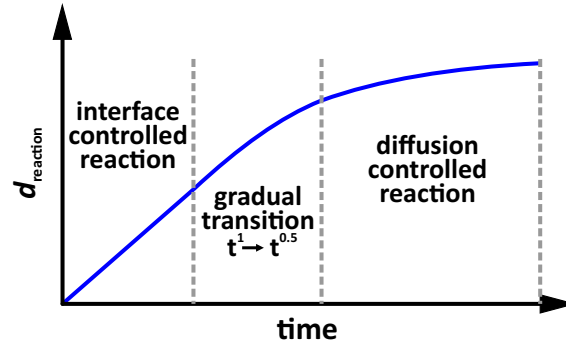


Figure 3.4: Schematic progression of the film thickness for a solid state reaction, showing the transition from an interface to a diffusion controlled reaction.

The film thickness as function of time is sketched in Fig. 3.4. At the beginning, the reaction is interface controlled, as already stated above, and (mostly) exhibits a linear slope. After the film thickness reaches a critical value, the gradual transition from the interface to diffusion control occurs and a parabolic behavior is observed in the end, which can be described by Eq. 3.18. Often, the diffusion control in early states of the reaction is veiled by interface controlled processes. Diffusion control is mostly seen for thicker films ($> 1 \mu\text{m}$) but critically depends on the bulk and interface transport coefficients, which define the transition thickness.

Thus, at the beginning interface processes are limiting and afterwards diffusion is controlling the reaction rate.

3.4.3 Percolation pathways

The Wagner model assumes a homogeneous product phase. In practice, reaction layers are often heterogeneous and may be composed of several different phases with different transport properties.

Then percolation may also influence the interphase growth. It is used to describe transport in inhomogeneous materials, e. g. mixtures of conducting and insulating materials, or homogenous two phase systems with one additional conducting phase^[101]. This is schematically shown in Fig. 3.5a, where a mixture of insulating and conducting materials is formed e. g. during a solid state reaction. The conducting material then may form connecting and/or limited percolation paths. Connecting paths can increase the overall conductivity and limited percolation paths will increase the local transport coefficients^[101].

The percolation limit is defined which is related to the percolation probability. The latter is described as the probability that a region is sufficiently connected to the rest of the material so that it is available for conduction^[101]. A rule of thumb states that approximately 30 vol.% are necessary to ensure 3D percolation^[101]. An example for percolating systems is silver in bakelite powder, that becomes conducting when 30 vol.% are silver metal.

Thus, the overall transport coefficients are enhanced by connecting percolation paths, but also limited paths generate a local increase of the transport coefficients. Additionally, the incorporation of a metal M in an interphase (ionic conducting material), will decrease the potential drop caused by the local transport coefficient increase. Likewise, the elec-

tronic conductivity is increased, which will lead to an increased reaction layer growth rate according to section 3.7.2. The incorporated metal particle will additionally serve as a bipolar electrode^[102] so that the particle shape may change from spherical to a wire.

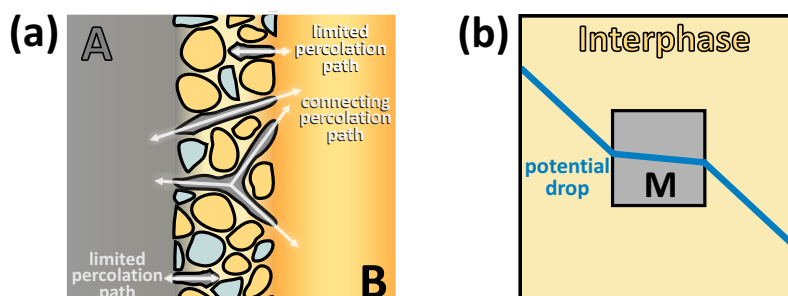


Figure 3.5: Limited and connecting percolation pathways are schematically displayed in (a). The potential drop caused by limited percolating species, with high conductivity compared to the interphase, is shown in (b).

Hence, percolation and formation of metal particles may also play an important role in solid state reactions if a conducting material is formed during reaction.

3.5 Combined approach to study interphase formation

3.5.1 Limitations of cyclic voltammetry for stability investigation

The stability of solid electrolytes in contact with alkali metal electrodes is often investigated by contacting one or two sides of the solid electrolyte pellet with the respective alkali metal and the other with a stainless steel current collector, followed by one cyclic voltammetry measurement^[59,60]. If only a fully reversible signal occurs – the dissolution and deposition of alkali metal – the material is considered to be stable^[59,60]. In fact, most materials are not stable – but show a reversible behavior in CVs^[63]. To clarify this apparent contradiction, cyclic voltammetry was conducted using alkali metal electrodes on both sides (and a alkali metal reference electrode)⁴. The results are shown in Fig. 3.6. All the solid electrolytes – which are shown in Fig. 3.6 – were examined concerning the stability in contact with alkali metal and are described in detail in section 3.6 to 3.8. For better interpretation of the CV data, the knowledge about the stability of the materials in Fig. 3.6 is crucial. Thus, the data were colored according to their stability class, according to the classification in section 3.2. The black, blue and green colored data in Fig. 3.6 mark the stable, the SEI and MCI forming materials, respectively. $\text{Li}_5\text{La}_3\text{Ta}_2\text{O}_{12}$ (garnet type) is colored red as the type of interphase is difficult to determine and a special case.

By comparing the CVs in Fig. 3.6 with the stability data, it is obviously not feasible to gain stability information. The MCI forming materials show a comparable behavior and high currents are measured, for example with LLTO ($\text{Li}_{0.35}\text{La}_{0.55}\text{TiO}_3$) and LSTZO ($\text{Li}_{3/8}\text{Sr}_{7/16}\text{Ta}_{3/4}\text{Zr}_{1/4}\text{O}_3$). In contrast LATP ($\text{Li}_{1.2}\text{Al}_{0.2}\text{Ti}_{1.8}(\text{PO}_4)_3$) is forming an MCI, too, and the currents are not that high compared to LLTO or LSTZO. The MCI formation

⁴Note that some data in literature were obtained by a 2-electrode setup or the setup is not explicitly described.

is then only seen by the direction of the CV, as for MCIs the higher values are obtained for the backward scan (from high to low potentials).

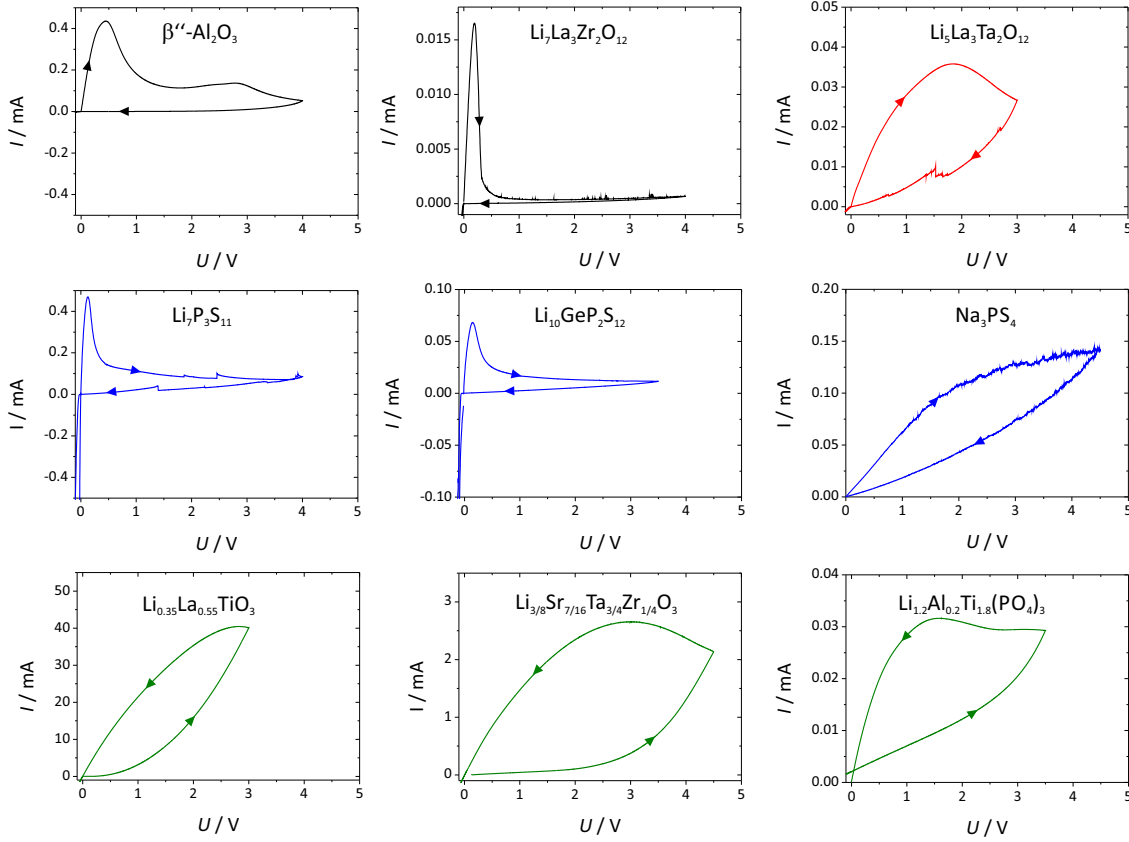


Figure 3.6: Cyclic voltammetry data for a few well-known solid electrolytes, using alkali metal electrodes. The black, blue and green data correspond to the stable, SEI and MCI forming solid electrolytes, respectively. $\text{Li}_5\text{La}_3\text{Ta}_2\text{O}_{12}$ is a special case and therefore marked in red. (Unpublished data).

The data for Na_3PS_4 (NPS) show a similar result, but this time the current values for the backward scan are smaller compared to the forward scan. LATP forms an MCI and NPS an SEI. LGPS ($\text{Li}_{10}\text{GeP}_2\text{S}_{12}$), LPS ($\text{Li}_7\text{P}_3\text{S}_{11}$) and LLZO ($\text{Li}_7\text{La}_3\text{Zr}_2\text{O}_{12}$) show exactly the behavior that is assigned and expected for stable solid electrolytes in literature. LGPS and LPS are in fact not stable (SEI formation), and LLZO is stable. Na- β -alumina (beta-alumina) shows a CV typical for unstable materials, due to the broad signal and the occurrence of a flank connected to the first signal. Nevertheless, β -alumina is stable in contact with sodium metal. $\text{Li}_5\text{La}_3\text{Ta}_3\text{O}_{12}$ shows data which might be assigned to MCI formation. To the contrary it may rather be assigned to an SEI. Thus, CV appears not to be a suitable technique to investigate interphase formation or the stability of solid electrolytes, as the results are too unspecific⁵. The results give rise to the question, whether CV is generally suitable for investigations of chemical degradation processes (reactions) or is only valid for electrochemical reactions.

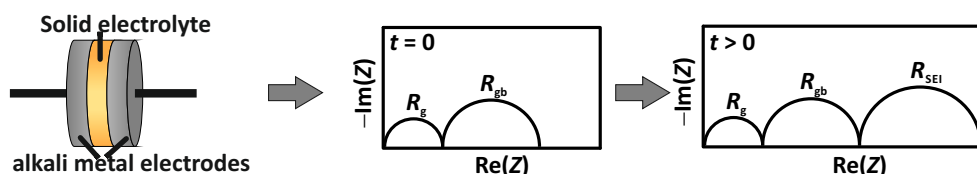
⁵It should be mentioned that changes are seen in the second cycle of the CV. These may either be assigned to material decomposition or contact loss during material dissolution (see section 5).

3.5.2 Combined approach

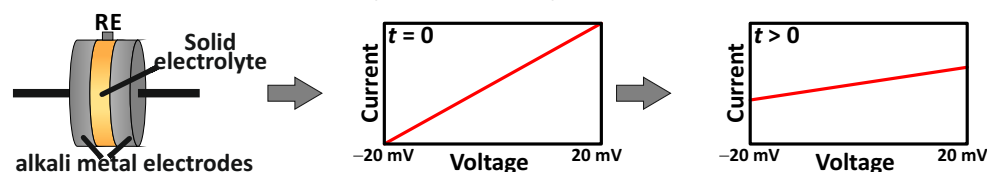
Most analytical techniques, like scanning electron microscopy (SEM), diffraction techniques (e. g. XRD) or energy dispersive x-ray spectroscopy (EDX) either show no results, as the interface is buried, or show no useful results as the interphase volume fraction is too small. For transmission electron microscopy (TEM), which was recently used to investigate solid-state batteries, the sample preparation process is extremely laborious and the interpretation of results for thin samples (lamellae) treated with a high intensity electron beam is critical^[48,103]. Thus, the investigation of interfaces or interphases suffers from severe experimental limitations.

In this section a combined approach is described, which was partially developed during this work or uses common techniques^[33,63] for interface or interphase investigations. The method allows to obtain information about electrolyte stability and provides chemical (thermodynamic) and electrochemical (kinetic) information^[83].

1. Quantification of resistance change by time-resolved impedance spectroscopy



2. Simple stability test by CV / determination of the charge transfer resistance (time-resolved)



3. Determination of reaction products by in situ XPS

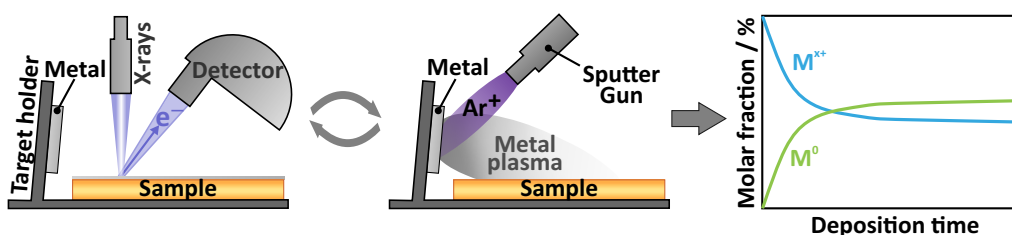


Figure 3.7: The three parts of the combined approach are schematically displayed. The experimental setups and schematic sample data are shown to exemplify the information gained by the respective method. Parts of this figure are already published by Wenzel et al.^[83].

The quantification of interphase formation is achieved by impedance spectroscopy, which is shown in Fig. 3.7.1. Therefore symmetric cells were used and the impedance spectra were recorded as a function of time, to observe resistance changes. The interphase formation is then obtained by proper interpretation of the spectra. The ideal case is shown in Fig. 3.7.1 on the right side. Experimental requirements and more details are given in the next

section. An experimentally more complicated approach is the small range CV technique, which is shown in Fig. 3.7.2. This technique requires the application of a reference electrode, which causes a larger experimental effort. However, the slope changes are easily to be determined and interpreted, which is schematically indicated in Fig. 3.7.2. By this approach, the polarization resistance could be determined, which will be discussed in the following section together with more details about this technique. The third part is the newly developed in situ XPS technique. This approach provides insight into the chemical reaction products of the interphase by application of a standard lab-scale photoelectron spectrometer. In Fig. 3.7.3 the technique is schematically illustrated. By subsequent deposition of alkali metal onto the sample surface followed by XPS measurement, the product phases are identified and changes due to reactions can easily be seen. A detailed description of the method is given in section 3.5.5. It additionally offers insight into the formation of very thin interphases, which are often overlooked by electrochemical methods.

The interphase formation of LiPON was recently investigated by in situ XPS in an elaborated UHV cluster tool^[74]. Before, the instability of LiPON was never reported^[74]. Thus, this combined approach offers a straightforward methodology to study interphase formation and offers a prediction of longtime interphase behavior according to the results.

3.5.3 Electrochemical approach

The electrochemical approach, described in the last section, exhibits some experimental requirements, different to those for the techniques themselves, which are mostly the same for both methods^[83].

- The time span between contacting the alkali metal electrodes with the solid electrolyte and the start of the measurement has to be as short as possible. Otherwise the reaction might already be finished while the data recording has even started. In fact this is the most important issue for stability investigations using vapor deposited alkali metal electrodes. As alkali metal is consumed during the reaction, contact decrease might occur, which will strongly change the impedance spectra or the slope of the CV.
- To ensure proper contacting, which has to be fast, and to keep the interfacial contact, a minimum pressure has to be applied. As the alkali metal hardness is generally low, the pressure magnitude ranges from 10 to 20 bar. These empirical values were determined during this work and will be discussed in section 5 in greater detail.
- The pressure causes plastic deformation of the alkali metal, which directly leads to an increasing electrode area. As a consequence, the data interpretation is extremely challenging and the prevention of the electrode area increase is crucial for the function of both methods and the investigations in section 5.

Hence, the application of a special setup is necessary, which provides fast assembling and the application of pressure and prevents the increase of the electrode area by incorporation of a barrier. More details about this setup are given in section 5.4, as the main purpose for this setup was the investigation of the pressure dependence of the interface alkali metal/solid electrolyte.

In order to obtain information about the interphase formation, the impedance spectroscopy data have to be carefully analyzed. The knowledge of the initial pellet resistance (or con-

ductivity) is important, as it facilitates the data interpretation. Then this technique offers insight in interphase formation and growth. Nevertheless, the sample condition is far from perfect, as grain boundaries, polycrystallinity and impurities (even in high purity starting materials) affect the material decomposition, which leads to small deviations in the results. The same considerations are valid for the CV measurements. For this technique, some more requirements are needed. The most important is the use of a reference electrode. For impedance data, the accuracy is mostly not increased by application of a reference electrode, but the appearance of artifacts is more likely. The fast resistance changes for MCIs induce another issue, as the impedance techniques are too slow and the reaction changes the data during recording (see next section). Thus, a DC technique similar to the CV approach was used (more details can be found in section 9.1).

For the small range CV measurement and the determination of the polarization resistance, sometimes also called charge transfer resistance, the application of a reference electrode positioned as close as possible to the working electrode is necessary. Another important requirement is the use of small overvoltages, which are in the linear range of the I - U -curve^[104] and for which the amount of transported alkali metal is negligible. As the application of a reference electrode in solid electrolytes is a laborious and virtually impossible task, the reference electrode is placed next to the working electrode on the solid electrolyte. The setup and the electrode geometry are schematically shown in section 9.1. Hence, to get the exact polarization resistance the IR drop between reference and working electrode has to be determined via simulations and the potential corrected accordingly. For that, detailed information about the interphase structure and compositions are needed. As the reference electrode consists of alkali metal, too, a reaction should occur at the interface, complicating the IR-drop simulations. Even without, a qualitative interpretation of the interphase or interface resistance is achievable. Thus, a value in the correct order of magnitude is obtained by the inverse slope (which equals the polarization resistance, see equation 3.19)^[104] that allows the evaluation of stability. In equation 3.19, j is the current density, η the overvoltage and R_p the polarization resistance, respectively.

$$dj = \frac{d\eta}{R_p} \quad (3.19)$$

The resulting resistances for both measurement techniques are the interphase resistance (including grain boundaries and bulk of the interphase) R and charge transfer resistance for impedance spectroscopy and one overall resistance (including the overall interphase and polarization resistance) for CV, which is schematically shown in section 9.1. The impedance technique yields in more quantitative results, whereas the results for CV exhibit a more qualitative character.

3.5.4 Overview of the expectations and results for the electrochemical methods

In this subsection, the expectations for the electrochemical methods are compared to the results for real samples. The results are then discussed in detail in sections 3.6 to 3.8, whereas this section primarily serves as an overview^[43,83]. The expectations are shown in Fig. 3.8. For a stable material, the resistance R_P is not changing with increasing contact time and likewise the slope of the CV is not changing, too. Thus, the material might be

seen as stable, if the requirements in section 3.5.3 are carefully kept. The MCI forming materials show a completely different behavior, as the resistance is strongly decreasing to values that approach zero. The degree of the resistance decrease heavily depends on the material properties. The slope of the current-voltage line (CV) is strongly increasing, often to values up to several mA/cm².

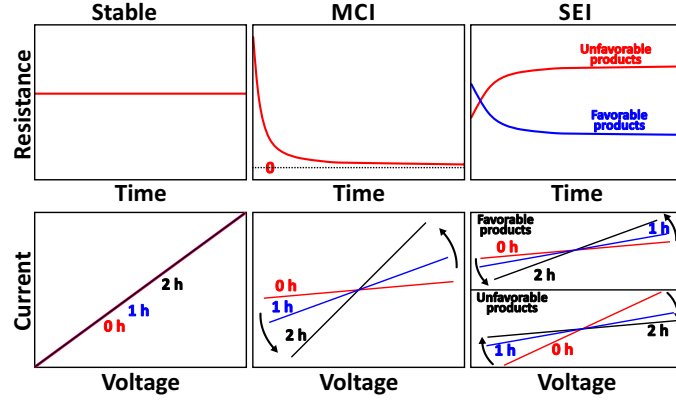


Figure 3.8: The expectations for a stable material and materials which are forming mixed-conducting (MCI) or solid electrolyte interphases (SEI) for the electrochemical techniques^[43,83].

Against this, an SEI may show two different behaviors according to the nature of the decomposition products. If the ionic conductivities of the product phases are smaller than for the solid electrolyte (unfavorable products), the resistance is increasing and shows a more or less parabolic resistance growth after the initial growth (which might be linear, see section 3.4 and 3.7.4 for more information). According to this, the polarization resistance (the inverse slope of the CV) is increasing, as the slope is decreasing. Quite a few samples for this behavior are shown in this work (see section 3.7). The second SEI type might be found when favorable products are found. This might be the case for LiPON, as products with higher conductivities compared to the starting material are partially formed. However, the electrochemical data for this are not reported (or obtained) so far^[74]. This might be caused by experimental difficulties and the small resistance changes. Likewise the slope of the CV data should be increased and the polarization resistance decreased.

The experimental data are summarized in Fig. 3.9. Na- β -alumina, lithium lanthanum titanate (LLTO) and Li₇P₃S₁₁ (LPS) were used as model materials. For the stable solid electrolyte (β -alumina) in Fig. 3.9, the resistance in (a) is not changing with increasing time and the Nyquist plots in (b) show only very small statistically distributed changes (e. g. temperature variations). According to these findings, the slope of the CVs in (c) and the polarization resistance in (d) are not changing with time, which fully agrees with our expectations for stable materials. The results for the MCI forming LLTO are shown in Fig. 3.9 as well. The resistance is strongly decreasing to very small values with time. As mentioned before, the resistance change is too fast to be investigated by impedance spectroscopy for more than a couple of hours. Thus, the DC resistance determination technique is used, which only measures the overall resistance (including charge transfer). Nevertheless, the resistance approaches zero (but evidently never reaches it) and shows conductivities of 0.1 S/cm for a 2 mm thick pellet after 80 h. A few Nyquist plots for LLTO are shown in Fig. 3.9b, showing a change during the measurements, as

the plots show a snail like shape (even for very fast measurements). Both results are matching the expectations in Fig. 3.8. Furthermore, the slopes of the CVs are strongly increasing and current values up to several mA after three hours are observed. Likewise the polarization resistance is heavily decreasing and approaches very small values, which is again in accordance with the expectations.

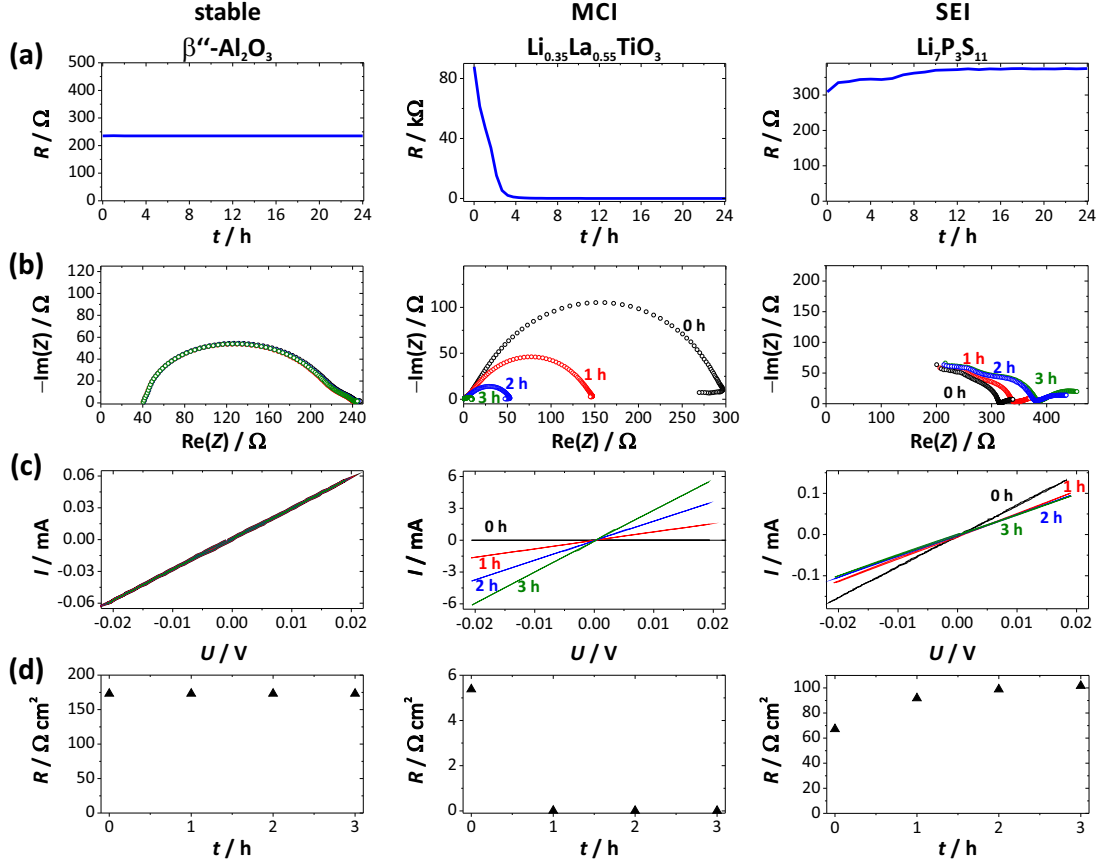


Figure 3.9: Experimental results for a stable, an MCI and an SEI forming solid electrolyte. The resistance change, example Nyquist plots, the CV data and the polarization resistance are shown in (a), (b), (c) and (d), respectively^[83].

The last example is the SEI forming material LPS; the results are shown in Fig. 3.9 as well. For a better comparison, the overall resistance and its change are displayed. In Fig. 3.9a, a resistance increase could be observed that is smaller compared to other materials, but can nevertheless be determined. The corresponding Nyquist plots are shown in Fig. 3.9b, supporting the expectations. In Fig. 3.9c and d, the CVs show decreasing slopes and similarly the polarization resistance is increasing. Note that the changes for the resistance (in Fig. 3.9a) and the CV slope for LPS are both decreasing with time, which is consistent with the expectations.

Thus, the electrochemical methods, when correctly performed, give evidence of interphase formation and additionally prove the type of interphase/interface that is formed. Nevertheless, chemical information about the interphase products is not provided and very thin interphases are hard to determine via this electrochemical approach (e. g. LiPON).

3.5.5 The in situ XPS technique

Chemical information is obtained by applying the in situ XPS technique, which was developed and optimized during this work^[61]. The biggest advantage, beside the chemical information, is that this technique can be applied to every standard lab-scale photoelectron spectrometer equipped with an argon ion gun. Another advantage is that all products could be observed, which is often not the case for ex situ techniques. The schematic setup is displayed in Fig. 3.10, the real setup consists of a simple bend steel plate (see section 9.2).

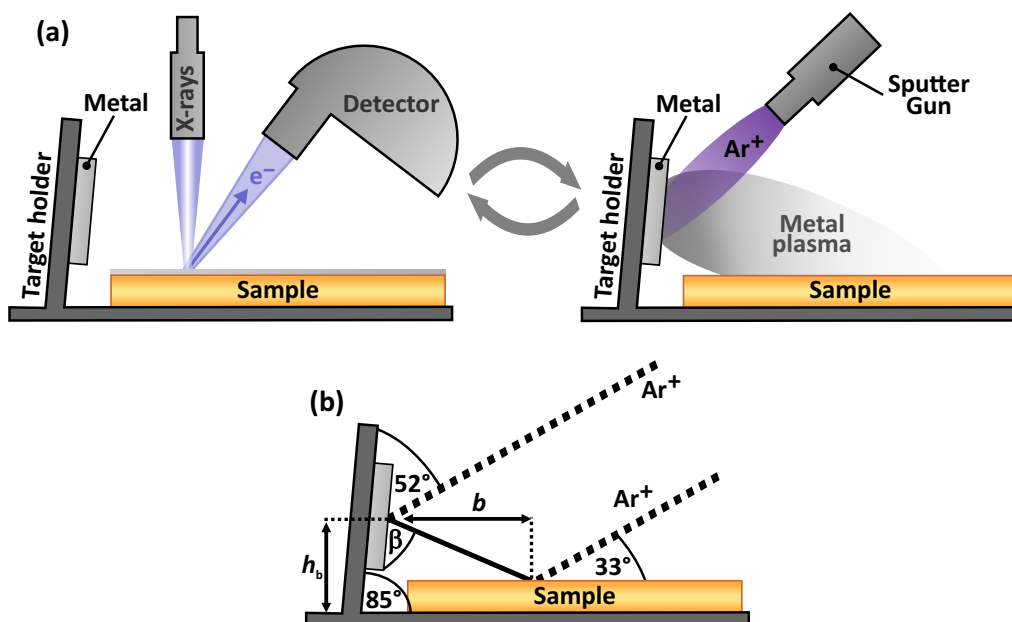


Figure 3.10: The scheme of the in situ XPS technique, the procedure is shown in (a) and involves sequential analysis and deposition steps. The geometrical figure is drawn in (b).^[61]

The angle relative to the sample surface was set to 85°. Smaller angles increase the sputter rate, due to decreasing the distance between sample and target, but sample analysis is no longer possible for geometrical reasons. The main deposition spot is then shielded by the target holder. This might be solved by turning the sample holder, but the intensity of the XPS peaks is then decreased and the method becomes even more surface sensitive^[105]. During the execution of the technique, the sample is measured first and then subsequently covered with alkali metal using the internal ion gun, which is focused on the target holder by simple movement of the sample stage (often involves turning and height adjustment). A similar technique has already been described by Marcus et al.^[106], describing the deposition of aluminum metal onto polymers in a deposition chamber connected to an XPS machine. Similar to the technique described in this section, a bend aluminum plate was used for deposition.

In the following, the procedure to find the best deposition coordinates is described. Starting at the middle position of the sample holder (with already adjusted height and measurement position), which should be identical with the rotation axis, the sample holder is then turned so that the target holder (the target metal) faces the ion gun. Now, the ion gun

is still focused on the sample. The correct height h has to be calculated, as schematically shown in Fig. 3.10b. Therefore, the angle of the ion gun relative to the sample surface (33° in this case), the target height h_b and the distance between the target holder and the measurement position b are needed. The latter is regarded to be constant, as the changes caused by the angle of 85° will be relatively small. Thus, the height difference between the deposition and analysis position is calculated by the sum of the target height h_b and the product of the distance b and the tangent of the ion gun angle. For a PHI Versaprobe II Scanning ESCA Microprobe (Physical electronics) the sputter position is found at the coordinates $x = y = 0$ mm; $z = 12$ mm and a rotation angle of 30° . The analysis position is then found at around $x = y = 0$ mm; $z \approx 18$ mm and a rotation angle of -66° . Slight changes for x and y may occur during adjustment of the analysis position. The deposition leads to a strongly non-uniform metal deposition, caused by the directional cone shaped plasma and the focused ion gun. Nevertheless, the alkali metal spot exhibits a nearly uniform shape with a diameter of at least 1.2 mm. The argon ion current was set to $4 \mu\text{A}$, the acceleration voltage to 4 keV and the beam was not rastered.

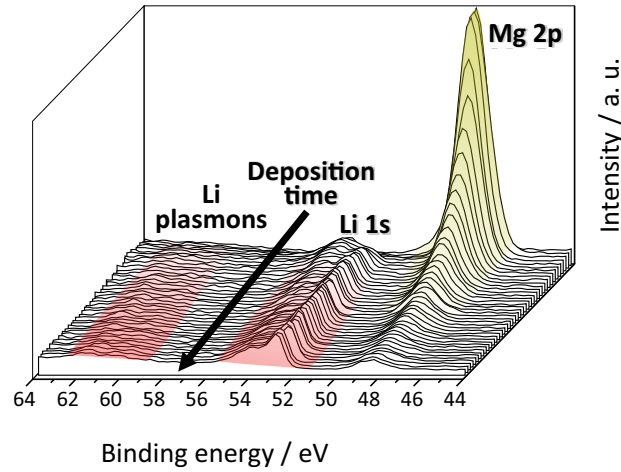


Figure 3.11: XPS spectra of an MgO single crystal deposited with lithium metal. The intensities of the yellow and red colored Mg 2p and Li 1s signals are decreasing and increasing, respectively^[61].

For the determination of the metal film deposition rate, the decreasing signal intensities of stable materials can be used, as the overlayer thickness is increasing. For this, the deposition of lithium metal and sodium metal on an MgO single crystal and a β'' -alumina pellet (see section 3.8.1) was conducted, respectively. MgO is known to be stable against lithium metal^[73] and the stability of β'' -alumina is shown in sections 3.8.1. The spectra in Fig. 3.11 show a decreasing Mg 2p signal, which does not show any changes of the oxidation states. The Mg 2p intensity strongly decays and the Li 1s intensity increases and saturates after a few deposition steps. Unfortunately, some alkali metal oxides are forming during this process caused by oxygen rest gas in the ultra-high vacuum chamber. For the sake of simplicity, a pure metal film was considered. Using the effective attenuation length (obtained by the NIST EAL database^[107,108]), the deposition rates are determined to be 0.25 nm/min for lithium metal and 0.14 nm/min for sodium metal. The standard deposition time was set to 5 minutes, which corresponds to a 1.25 nm thick lithium and a 0.7 nm thick sodium film, respectively. More information about the rate determining procedure

can be found in section 9.2. Thus, a reasonable amount of metal can be deposited, which is enough for investigations of SEI forming or stable materials.

In order to discuss the diffusion limitation of this technique, the diffusion coefficients are assessed using typical measurement times. Therefore, the diffusion coefficient of the minor charge carriers (often the electrons) has to be larger than 10^{-14} cm²/s. For very slow reactions, no changes are observed after deposition. This is the case for a minor charge carrier diffusion coefficient smaller than 10^{-20} cm²/s. Then, no changes are observed, which might be misinterpreted, as the MCI forming materials do not show changes at the beginning (see section 3.6). Nevertheless, slow kinetics then show the formation of an alkali metal film and require waiting steps between deposition and analysis, whereas an MCI requires the deposition of more alkali metal and show no alkali metal film formation on the surface. For reactions with diffusion coefficients in between 10^{-20} and 10^{-14} cm²/s, the reaction is still occurring during the analysis, showing changes during data recording. This might complicate data evaluation.

An advantage of this technique is that virtually any metal (or even material) could be deposited onto various samples, increasing the variability of this technique. The applications range from investigations concerning interphase formation and band offsets in devices^[86] (solar cells, batteries) to studies of space charge layers. Emission depth distribution functions could also be studied. The main purpose is the interphase formation of solid electrolytes and the determination of the reaction products. It may also be possible to determine the SEI thickness, as the slopes (in intensity versus time plots) of the intensity decreases for a reaction and for the burying process should be different. Thus, the thickness could be determined by the deposition time (x-axis) for the slope change, which directly corresponds to an amount of alkali metal. Some more advantages of this technique compared to ex situ methods will become clearer in section 3.7.

3.6 Mixed conducting interphases

As already mentioned in the last section, MCIs are difficult to analyze due to their fast lithium uptake. Very thin samples have to be used. In this section, the results for lithium lanthanum titanate are shown and discussed. More MCI forming materials are LSTZO and LATP; results for both are shown and briefly discussed in section 9.3. Impedance measurements are difficult to interpret, as the resistance is getting to small after the average of 3 hours and changes are occurring during one measurement step. Thus, a DC technique with a much shorter measurement time is used, as mentioned in section 3.5 and shown in section 9.1^[61].

3.6.1 Li_{0.35}La_{0.55}TiO₃

Lithium lanthanum titanate is described as a solid electrolyte and an electrode material (see section 3.3), as well. In fact, it will only be a stable solid electrolyte at a sufficiently low chemical potential of lithium. The photoelectron detail spectra of four deposition steps, obtained by the in situ experiment, for phase pure LLTO are shown in Fig. 3.12. As mentioned above, a very thin sample of approximately 100 µm thickness was used. Changes are observed for the Ti 2p signal; the pristine sample only shows one oxidation

state (4+) and new oxidation states are forming during deposition. These signals at lower binding energies are attributed to the formation of Ti^{3+} , Ti^{2+} and metallic titanium. The latter was never reported in literature, as the material is seldom overlithiated and the contact between the lithium metal and the solid electrolyte is often insufficient. Obviously, titanium is heavily reduced. A waterfall plot for more deposition states is displayed in section 9.3.1.

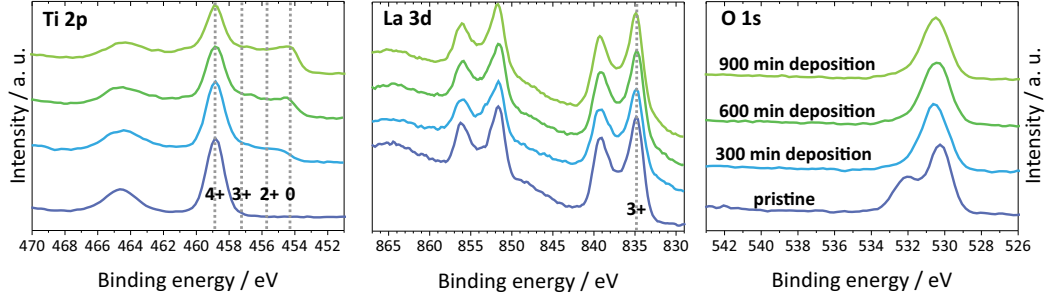


Figure 3.12: Photoelectron spectra for the pristine sample and for deposition times of 300, 600 and 900 minutes for the Ti 2p, La 3d and O 1s signals are shown, respectively (Wenzel et al.^[61]).

The La 3d signal does not show any changes of the oxidation state as the signal is not shifted, indicating the stability of La^{3+} . This is in accordance with previous reports^[68]. Nearly the same applies for the oxygen signal, only the pristine lithium carbonate or hydroxide signals are changed and small shifts to lower binding energies are observed. Consequently, the reduction of titanium must also lead to a decomposition of the material, but does not seem to affect the binding energies of other elements. Most likely the formation of titanium metal and a lithium lanthanum oxide occurs, as the pellet turned from white to dark black. The signal intensities in Fig. 3.12 are only slightly decreasing, as lithium metal is incorporated into the structure. Additionally, the Li 1s signal intensity is not notably increasing and no metal film is found at the sample surface. Both observations lead to the conclusion that lithium metal is rapidly incorporated into the structure.

A quantitative analysis of the Ti 2p detail spectra is then conducted by the development of a peak fit model. This is a challenging task as the Ti 2p_{3/2} and Ti 2p_{1/2} signals show an increasing overlap, caused by the reduction to titanium metal. Various affects like FWHM variations (Ti 2p_{1/2} is generally broader than Ti 2p_{3/2}), the background and asymmetric peak shapes for titanium metal complicate the development of a consistent peak fit model. Thus, a heavily constrained peak model, concerning the positions, the FWHMs and the background was applied to the data. Details about the fit parameters are found in section 9.3.1. The peak models are shown in Fig. 3.13a and b for the pristine and deposited sample, respectively. There, the formation of all three oxidation states is evident. Quantification according to the peak fit model is then shown in Fig. 3.13c. After 300 min, all species have formed and the fraction of the reduced species is increasing, whereas the fraction of Ti^{4+} is decreasing to values of approximately 48 %. The Ti^{3+} fraction reaches saturation around 22 % at about 500 minutes and the amount of Ti^{2+} , which increases more slowly, saturates at less than 7 %. At the end of deposition, the molar fraction of titanium metal yields 23 %. Approximately 250 nm of lithium metal were deposited. For a complete reduction to titanium metal, 160 μm of lithium metal would be necessary. Using the obtained fractions and assuming homogenous distribution

of all titanium species, an MCI thickness of approximately 420 nm is calculated and the amount of inserted lithium could be calculated, which is shown in section 9.3.1.

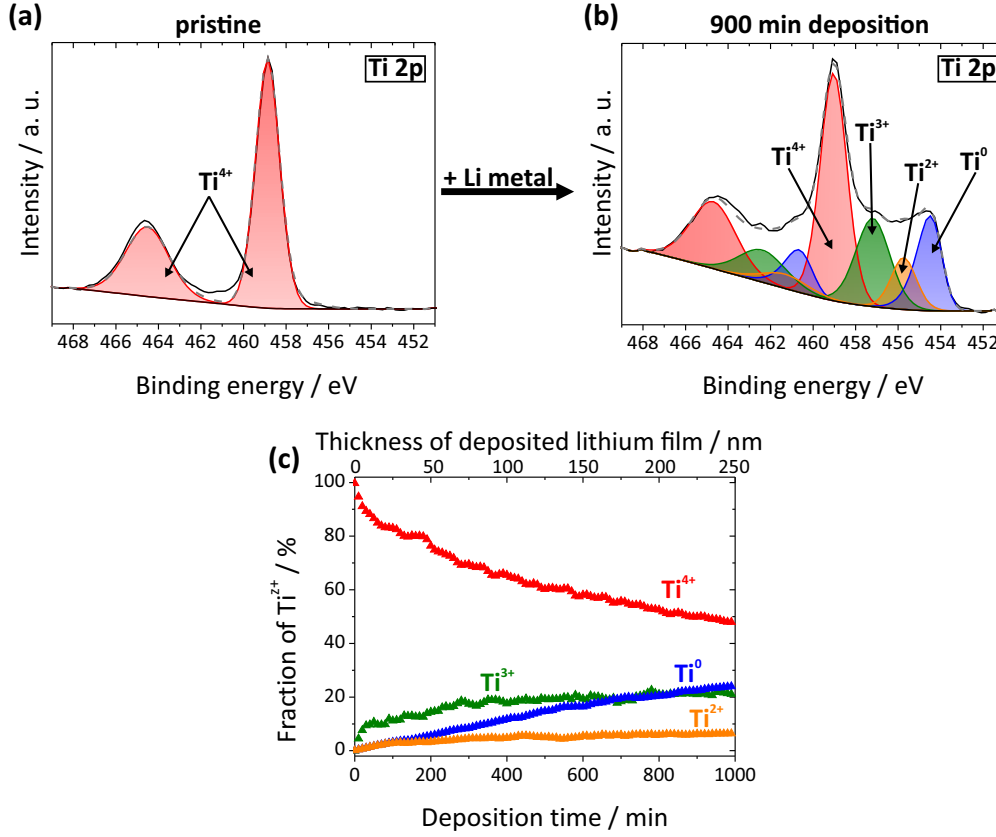


Figure 3.13: XPS fits of the pristine (a) and deposited sample (b) for the Ti 2p signal. Using this peak fit model, the fraction of the titanium oxidation states are displayed in (c) (Wenzel et al. [61]).

At the beginning, LLTO is an excellent ion conductor, with ionic and electronic conductivity of 0.1 mS/cm and 10^{-8} mS/cm, respectively. After the reduction, the electronic conductivity shows values of more than 0.1 S/cm, proving the mixed conducting character of the interphase. The latter was determined by a simple DC polarization technique, after the reduction with lithium metal, using blocking gold electrodes (see section 9.1.1). The temporal evolution of the overall pellet resistance in contact with lithium metal electrodes, using a DC measurement (see section 9.1.1 for more details), is recorded and displayed in Fig. 3.14. As already predicted and shown for MCIs in section 3.5.4, the resistance is strongly decreasing to values near 0 Ω . The CV results were already discussed in section 3.5.4 and show a strong increase of the slope resulting in a decreasing polarization resistance.

The results in this section indicate that LLTO (LSTZO and LATP as well) cannot be used in combination with lithium metal electrodes, as short circuiting and self-discharge of the battery will be the result. The XPS and conductivity results for LSTZO and LATP are shown in section 9.3.2 and 9.3.3, respectively. LSTZO shows a similar behavior like LLTO, whereas LATP shows a significantly smaller resistance increase. Regarding the compositions, this could be caused by the different fractions of reducible components in

the materials and stabilizing effects of the crystal lattice.

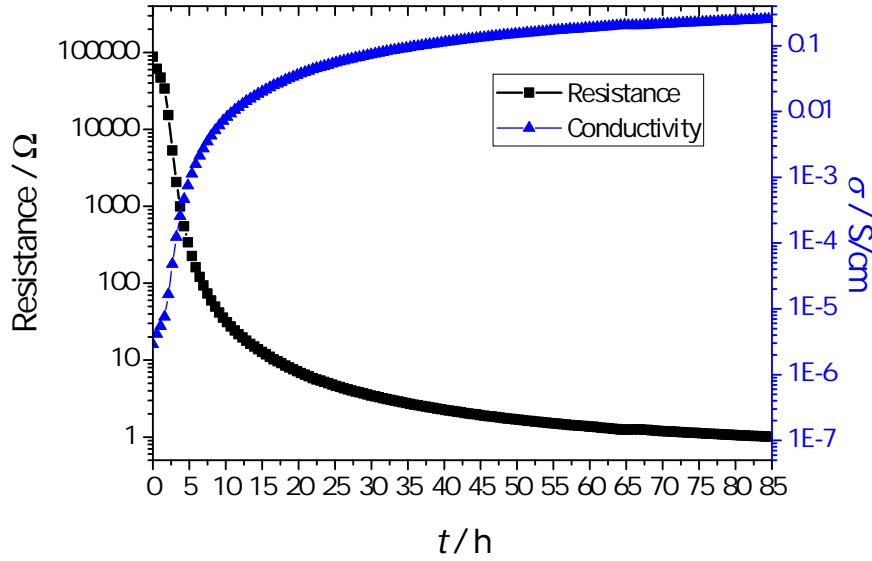


Figure 3.14: Resistance and conductivity changes of an LLTO pellet in contact with lithium metal electrodes (Wenzel et al.^[61]).

Thermodynamic assessments in section 3.9 show that Zr^{4+} , Ta^{5+} and Ti^{4+} containing materials are easily reduced (with the exception of $\text{Li}_7\text{La}_3\text{Zr}_2\text{O}_{12}$).

3.7 Solid electrolyte interphases

Solid electrolyte interphases can easily be analyzed by the in situ XPS approach^[43,78,82,83]. Some samples have to be cooled down to prevent the evaporation of volatile species (e. g. sulfur). The electrochemical analysis is more cumbersome, as small resistance changes are difficult to measure and determine, due to fast reactions. The semicircles obtained by impedance spectroscopy are often strongly overlapping, which creates the need of careful model fitting and data analysis. In this section, $\text{Li}_7\text{P}_3\text{S}_{11}$ (LPS), $\text{Li}_{10}\text{GeP}_2\text{S}_{12}$ (LGPS) and Na_3PS_4 (NPS) are shown. More SEI forming compounds, like argyrodites, and some special interphase types are shown in section 9.3.

3.7.1 $\text{Li}_7\text{P}_3\text{S}_{11}$

3.7.1.1 Interphase formation between Li metal electrode and LPS

For the in situ XPS measurements, the $\text{Li}_7\text{P}_3\text{S}_{11}$ (LPS) samples were cooled to temperatures of $-80\text{ }^\circ\text{C}$ to $-90\text{ }^\circ\text{C}$. Otherwise sulfur is evaporating from the material leading to errors in the analysis, as proven by comparing data of cooled and uncooled samples. The cooled samples show a stable composition over more than 12 h in ultra high vacuum (UHV). The quantification then roughly results in the composition of the material within the uncertainty range of the method. For all investigations, phase pure (see section 8.4)

and highly crystalline material was used^[78]. The amorphous samples show the same results in the XPS analysis, but the recording and interpretation of the impedance data is more challenging, as the overlap between the material and SEI contributions is stronger^[78]. The crystalline LPS samples show a high ionic conductivity of 2 mS/cm, which could be improved to 4 mS/cm by sintering. The electronic conductivity is relatively high and was determined to be in the order of magnitude of 10^{-9} S/cm, which is in accordance to values found for LGPS and NPS in this work and the literature^[22].

The detail spectra of the P 2p and S 2p signals for the pristine and deposited sample are shown in the stack plot in Fig. 3.15. There, the formation of Li_3P is evident and the signal damping due to the formation of a lithium metal overlayer is observed (see section 9.3.4). Similarly, the formation of Li_2S is seen in Fig. 3.15. The ratio of the S 2p signals for Li_2S and the material stays constant, hinting that the reaction is stopped. Signal damping then occurs again by lithium metal overlayer formation.

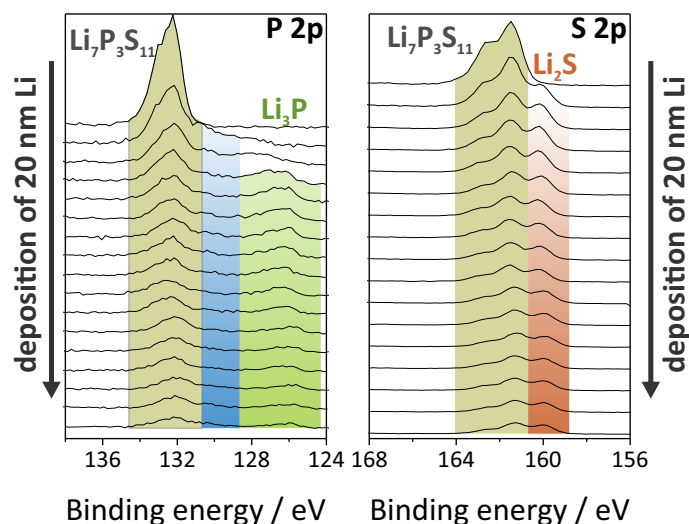


Figure 3.15: Stacked photoelectron spectra for the S 2p and P 2p signals for several lithium metal deposition steps onto LPS. The reaction products are marked and labeled^[78].

A detailed look in the detail spectra for the pristine S 2p and P 2p spectra in combination with reference data obtained for P_4S_{10} , allowed the development of a fit model for this type of compound. The reference spectra for P_4S_{10} and P_4O_{10} are published by Wenzel et al.^[78]. The peak fit model is summarized in section 9.3.4 and is in accordance with the structural composition of the material and is shown in Fig. 3.16a for the pristine sample. For S 2p, three different bonding motives could be separated. The ratio for the P–S–P, P=S and P–S–Li groups was found to be roughly 1:2:7, which matches the theoretical values for this compound. The P 2p signal shows two doublets in the ratio 2:1 that are assigned to the P_2S_7 -ditetrahedra and PS_4 -tetrahedra in the ratio 1:1. After the deposition of lithium metal, the decomposition of the solid electrolyte is observed, as discussed above. Using the peak fit model, the formation of Li_2S in Fig. 3.16b is more evident and can be quantified relatively to the mother compound. Likewise the formation of Li_3P and other reduced phosphorus species can be seen, which are described as two average doublets due to missing reference data. The reduced phosphorus species might be polyphosphides like LiP , LiP_5 and LiP_7 ^[110] or elemental phosphorus. Thus, the results are in good agreement

with the simulations^[72,76,77].

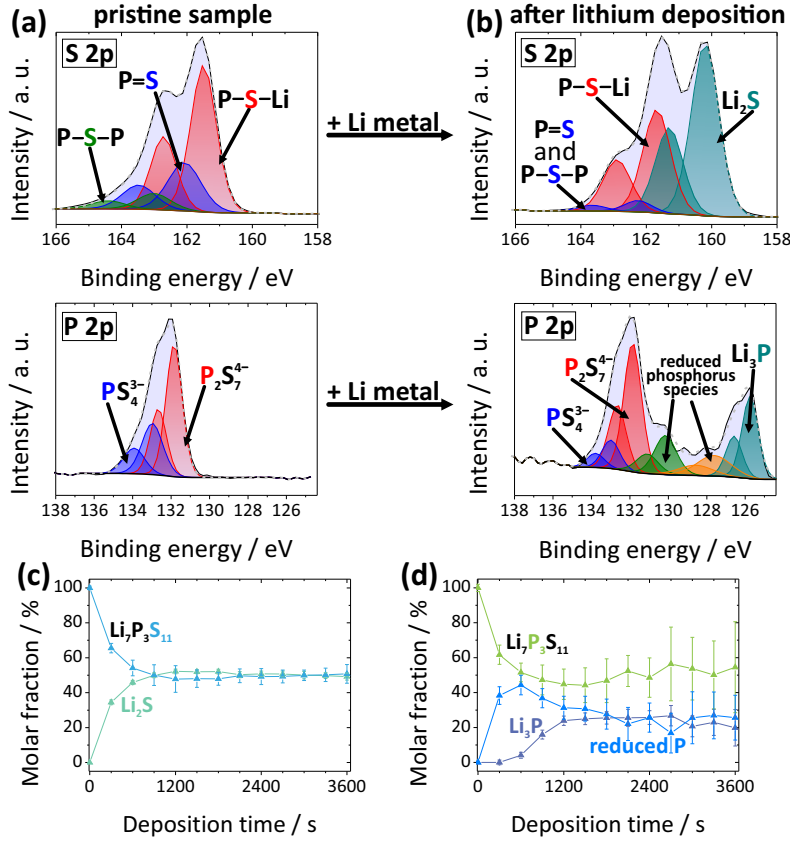
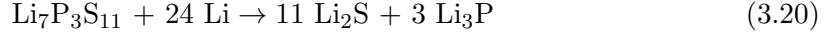


Figure 3.16: The peak fit models for the pristine and the reacted LPS sample are shown in (a) and (b), respectively. In (c) and (d), the resulting molar fractions for the sulfur and phosphorus species are displayed, according to the peak fit model in (a) and (b)^[78].

Using both peak fit models in Fig. 3.16b, the relative molar fractions of all deposition steps could be determined. The results are displayed in Fig. 3.16c and d for S 2p and P 2p, respectively. As shown in Fig. 3.16c, the formation of Li₂S starts with a strong increase and saturates after 900 s of deposition. Likewise the fraction of the pristine sample strongly decreases. Afterwards, the ratios between the sulfur species of the pristine LPS compound and the reaction product Li₂S show approximately equal values, which indicates that the reaction might have stopped at that point. The phosphorus fractions show a more complex behavior. For the first deposition step, reduced phosphorus species are formed and the amount of Li₃P is nearly zero. According to the increase of the reduced phosphorus species, which is composed of the sum of both species, and the formation of Li₃P afterwards, the fraction of the pristine material decreases. After 600 s the fraction of the reduced phosphorus species is decreasing again, corresponding to the formation of Li₃P, which starts at around 600 s of deposition.

This matches well with the assumption that at first the sulfur groups are removed (and form Li₂S) and elemental phosphorus is formed, which is then further reduced to Li₃P in the second step. According to these findings, the overall reaction is proposed as:



The thermodynamic calculations in section 3.9 corroborate this finding although substitution materials had to be used. The deposition time of 3600 s corresponds to a lithium film thickness of 15 nm that, when fully reacted, would result in an SEI thickness of 17 nm. This is actually not the case, as still some pristine sample is observed after 3600 s of deposition. In order to estimate the SEI thickness, coupled XPS peak fits were implemented. Therewith the peak areas of the pristine material, the Li_2S , Li_2O and Li_3P signals (S 2p, O 1s and P 2p) were coupled with the respective area of the Li 1s signal. Thus, the amount of lithium metal, formed lithium oxide and lithium in the pristine material could be separated from the amount of lithium metal that reacted with the LPS (more information on this can be found in section 9.2). The amount of reacted lithium metal was determined to be only 12 at.%. In combination with the amount of deposited lithium metal, an SEI thickness of approximately 2 nm is calculated. Note that this value does not include the polyphosphides so that the value is slightly larger.

In order to provide insight into the kinetic behavior of the interphase, time-resolved impedance measurements were carried out, like described for the combined approach. Using a symmetrical cell and lithium metal electrodes, the impedance data were recorded for 30 h. The results are shown in Fig. 3.17. The equivalent circuit is displayed in the inset in Fig. 3.17a and the Nyquist plots directly after contacting (0 h) and after 12 h are shown. More Nyquist plots and Bode plots are shown in section 9.3.4.

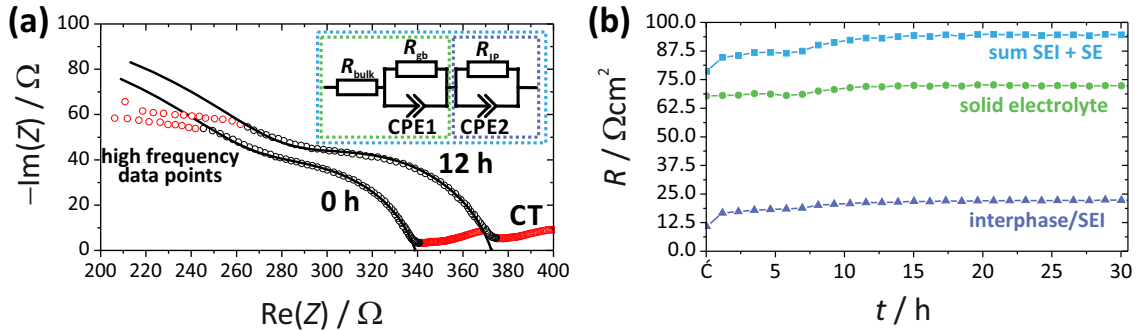


Figure 3.17: Two Nyquist plots directly after contacting and after 12 h hours for a symmetric Li metal electrode/LPS cell are shown in (a). In addition, the fit and the equivalent circuit are displayed. The obtained resistance change for one electrode is then monitored in (b). Modified version of an already published figure (Wenzel et al.)^[78].

For the fit, the unreliable high frequency data points and the charge transfer data at low frequencies were not considered. The resistance change for the sample after 0 h compared to after 12 h is obvious and is assigned to the SEI. Using the equivalent circuit and the initial conductivity of the material, the SEI resistance is calculated and separated from the material resistance⁶. The bulk and grain boundary contributions could not be separated, which is often the case for materials with high conductivities. Thus, only the overall material resistance is obtained. The material resistance and the interphase resistance changes

⁶In agreement with the capacitance values in the order of magnitude^[90,95] of 10^{-9} F.

are monitored in Fig. 3.17b for 30 h for a pellet thickness of 1.5 mm. The highest resistance increase at the beginning could not be recorded, as the reaction is obviously very fast, so that the resistance increase directly after contacting already yields approximately $10 \text{ } \Omega \cdot \text{cm}^2$, which roughly corresponds to half of the resistance increase. After 30 h the SEI resistance has already increased to $22 \text{ } \Omega \cdot \text{cm}^2$. The interphase growth is not finished after 12 h as the still increasing resistance indicates, but the growth rate is decreasing. This is discussed in detail in section 3.7.4. The increase in Fig. 3.17b corresponds to a resistance of $45 \text{ } \Omega$ for an electrode with a diameter of 8 mm. Using the resistance values shown in Fig. 3.17b and 8 nS/cm as conductivity for Li_2S ^[109], which is approved to be the main decomposition product, an SEI thickness of 2.3 nm is calculated. The value obtained by impedance spectroscopy (2.3 nm) is in good accordance to the value gained by in situ XPS (2 nm).

The CV method, already shown and discussed in section 3.5.4, likewise shows the material degradation. Note that the reaction for vapor deposited electrodes will be undoubtedly faster due to better contact (and higher reactivity), a time consuming processing and will consequently not be seen in time resolved impedance measurements. The results for LPS strongly suggest that the interphase formation will strongly influence the battery performance, durability and function, as the charge transfer resistance is deteriorated. In the following section, the behavior of the interphase will be investigated, especially for Li_3P , which is surprisingly not found for ex situ prepared interphases. Furthermore, the limited thickness is shown by depth profiling.

3.7.1.2 Behavior of the interphase

The changes of the chemical surface or interface species (deposition or decomposition profile) in Fig. 3.16d shows a fluctuating behavior for the phosphorus species. In order to get insight into the underlying reactions, the time resolved evolution of the interphase compounds was explored, which is marked as "waiting". The results are shown in Fig. 3.18a.

The S 2p signals do not change during this time, which is not surprising as Li_2S and the buried material are notably stable in UHV under cooling conditions. In contrast the oxygen signal is increasing, as more lithium oxide is formed by reaction of the residual oxygen in the UHV chamber and lithium metal. The strongest changes are seen for the phosphorus compounds, as all reduced species, including Li_3P are vanishing. This might be explained by the moisture and oxygen sensitivity of the phosphide species^[110] and the lack of vacuum stability. The same reason might apply for the lack of Li_3P in ex situ prepared interphases.

In order to show the limited thickness of the interphase and to prove that the material underneath the SEI could still be found, a depth profiling experiment was conducted and the interphase is sequentially removed. The results are displayed in Fig. 3.18b. For S 2p, the Li_2S is removed after 12 min of sputtering (argon ion gun, 2 keV, 2 min steps) together with the residual lithium metal. Afterwards the pristine material is reobtained, indicating the sputter stability of the material. The O 1s signal shows a similar behavior, the lithium oxide film is quickly removed and the oxygen content reduces to values of approximately zero. As the reduced phosphorus species are already removed during the time-resolved

experiment, the intensity of the pristine phosphorus signal is simply increasing. Thus, the material could be fully retained and the interphase is completely removed, indicating the limited thickness of the SEI.

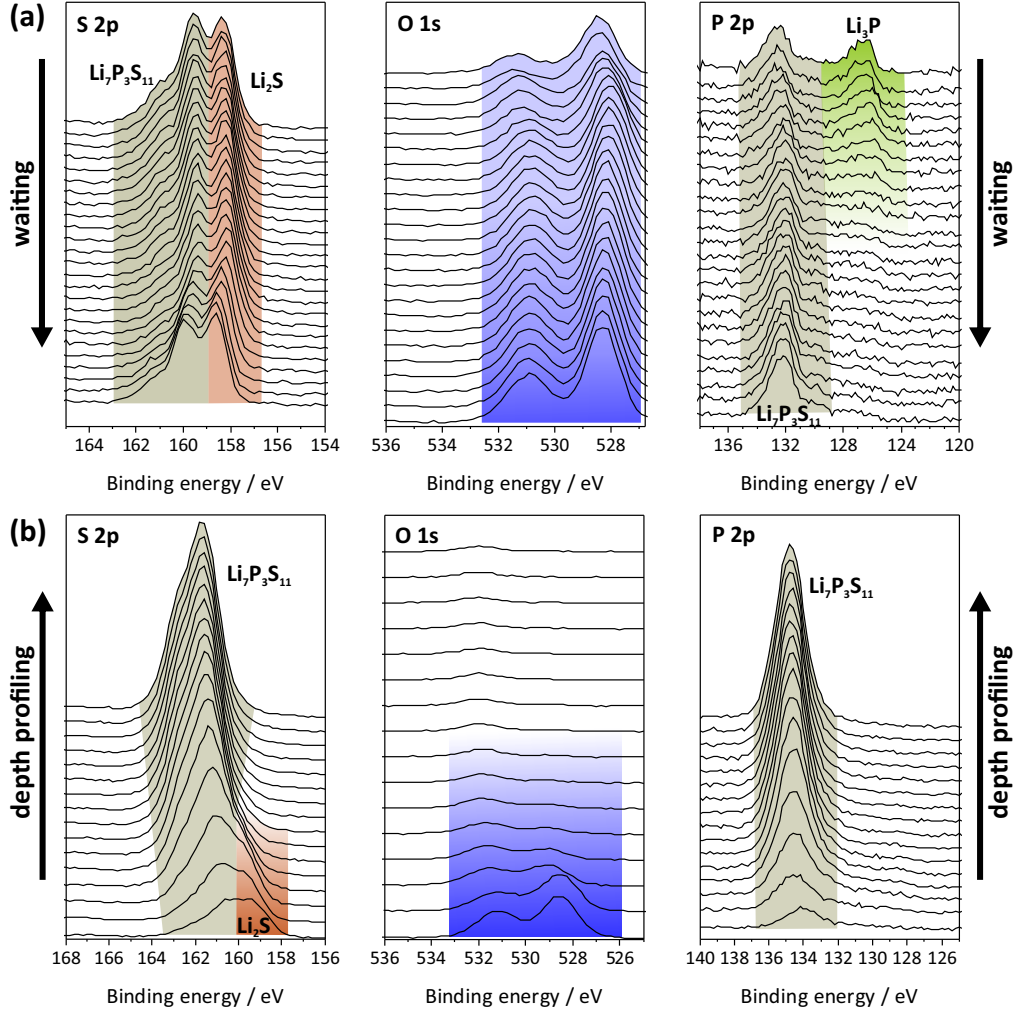


Figure 3.18: Time-resolved photoelectron spectra for S 2p, O 1s and P 2p signals are shown in (a). Depth profiling to remove the interphase was then conducted and the obtained detail spectra are displayed in (b) for the S 2p, O 1s and P 2p signals (Wenzel et al.)^[78].

3.7.2 $\text{Li}_{10}\text{GeP}_2\text{S}_{12}$

In this section the interphase formation between lithium metal and the promising ion conductor $\text{Li}_{10}\text{GeP}_2\text{S}_{12}$ (LGPS) is discussed and partially compared to the results for LPS, as both show similar structural motives but the first contains germanium^[82]. For the in situ XPS analysis, the samples were cooled as described for LPS and sequentially covered with lithium metal by sputter deposition. Stacked photoelectron spectra for the evolution of the S 2p, Ge 3d and P 2p signals for several deposition steps are shown in Fig. 3.19.

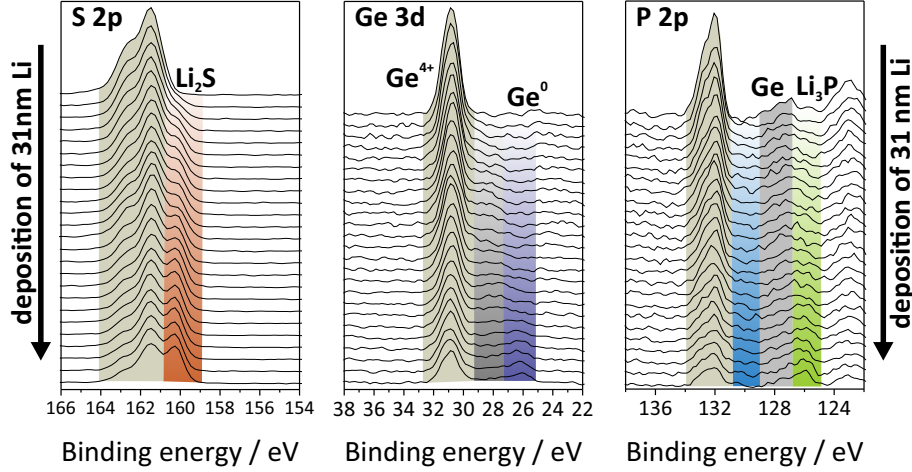


Figure 3.19: Photoelectron detail spectra for S 2p, Ge 3d and P 2p for several lithium metal deposition states. Some products are colored and labeled directly in the figure^[82].

The S 2p signal shows the formation of a new species at lower binding energies during deposition, again assigned to Li_2S . This is in accordance with the findings for LPS. Likewise the signal intensity is damped. The detailed signal analysis will be described later in this section. The Ge 3d signal shows the formation of lower valent Ge species, which will be assigned as Ge metal and reduced $\text{Ge}^{(4-x)+}$ species later, and the decomposition of the GeS_4 -tetrahedra. Consequently, the P 2p signal reveals the reduction of phosphorus, the formation of Li_3P and the decomposition of the PS_4 -tetrahedra. Here, the Ge 3p signals are interfering but can be clearly separated, which is described later in this section. The element quantification of LGPS is again in good agreement with the theoretical values, which is another hint to the phase purity of the sample. To offer a detailed insight into the reduction species and process, peak fit modeling was conducted and is shown in Fig. 3.20.

The model parameters are summarized in section 9.3.4. A look into the spectra and the peak model in Fig. 3.20a for the Ge 3d peak for the pristine sample shows that only one oxidation state for germanium is found, corresponding to Ge^{4+} of the GeS_4 -tetrahedra. After lithium deposition, the formation of germanium metal is obvious and different reduced germanium species have formed as well. The latter were fitted with an average signal, as the separation of the different $\text{Ge}^{(4-x)+}$ species is difficult due to a strong overlap. Thus, the formation of high electronic conducting species is proved. Nevertheless, the germanium content of the sample is relatively small and the impact on the interphase formation and growth will be discussed later in this section.

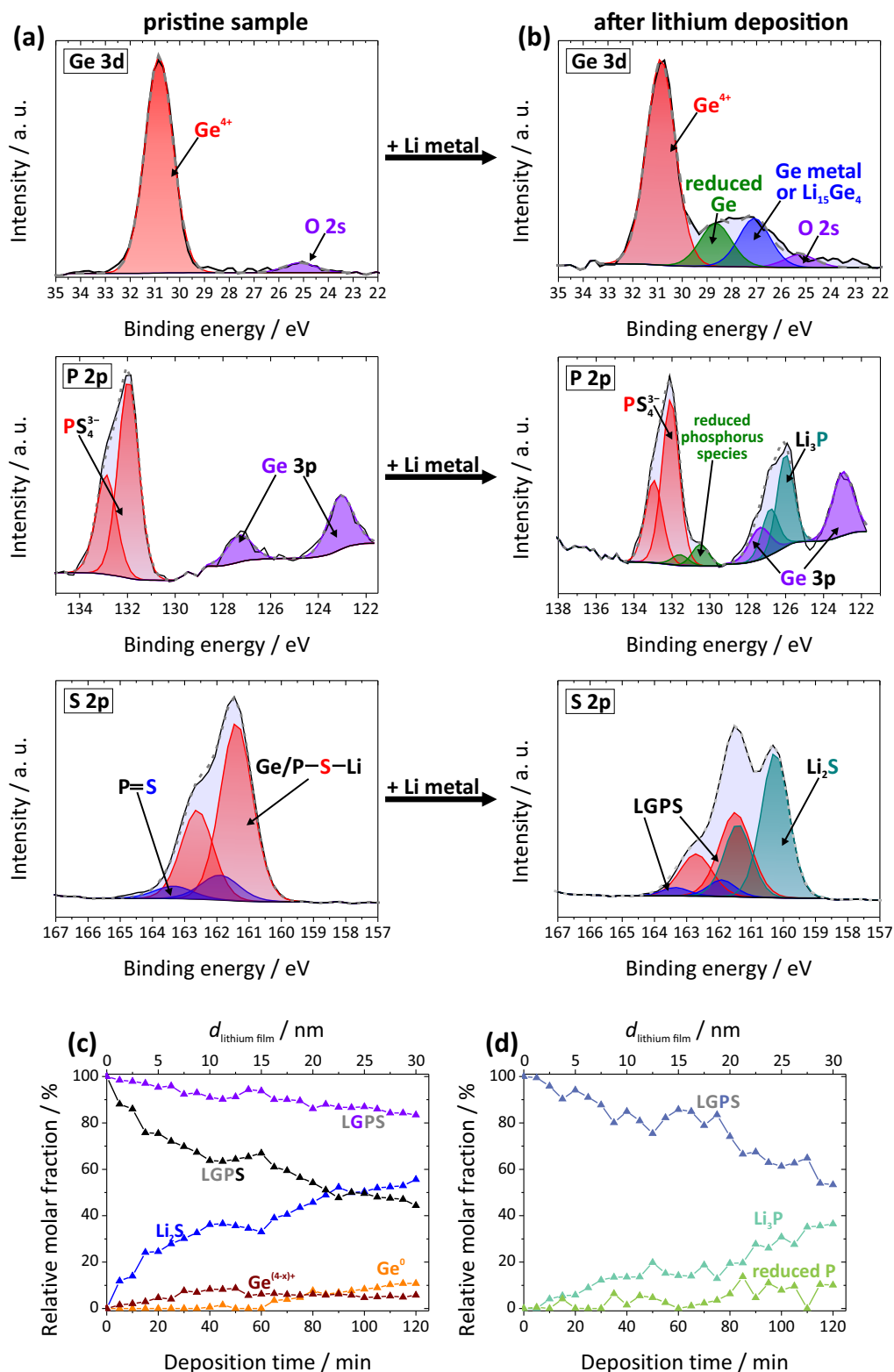
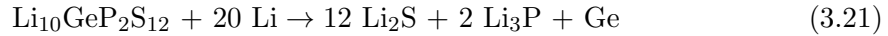


Figure 3.20: The peak fit models for the Ge 3d, P 2p and S 2p signals for the pristine and deposited sample are shown in (a) and (b), respectively. The obtained deposition profiles for the different species are displayed in (c) for the Ge 3d and S 2p species and in d for P 2p species (Wenzel et al.)^[82].

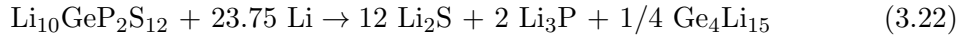
It is possible that a germanium lithium alloy is formed instead of pure germanium metal,

as the Gibbs free enthalpy for alloy formation yields -622 kJ/mol, but the assignment in the XPS data is difficult due to missing references. At the sample surface the alloy formation is more likely, compared to the deeper interphase layers, where the lithium amount is strongly limited by diffusion⁷. The P 2p signal of the pristine sample shows two doublets, the first is assigned to the PS₄-tetrahedra and the second to Ge 3p. The ratio of GeS₄- and PS₄-tetrahedra was found to be 1:2, in good agreement with the theoretical values. After lithium deposition, the signal for the PS₄-tetrahedra can be still found in the P 2p signal, but additionally reduced phosphorus species can be seen, which are difficult to assign as described in section 3.7.1.

Again, the formation of Li₃P is detected. This time, the quantification of the Li₃P signal is more difficult due to the overlap with the Ge 3p_{1/2} signal. However, the Ge 3p_{3/2} signal is not affected so that the intensity of the Ge 3p_{1/2} signal could easily be determined by the ratio of 1:2 for the Ge 3p_{1/2} in relation to the Ge 3p_{3/2} signal according to the ratio of degeneracy. The S 2p signal of the pristine sample shows a significant intensity and the double bound sulfur P=S and Ge/P–S–Li groups could clearly be separated. After lithium metal deposition the formation of Li₂S is observed. Using the results in Fig. 3.20a and b, the following reactions are proposed, assuming complete conversion:



Or in the case of alloy formation:



The decomposition products are again in good agreement with the literature^[72,76,77,81]. Using the peak fit model, the formation of the chemical species could be quantified for all deposition states. The results are displayed in Fig. 3.20c and d.

While the Ge^{(4-x)+} fractions are nearly saturated, the germanium metal fraction is continuously increasing. Likewise the intensity of the pristine germanium species is linearly decreasing. The S 2p species in Fig. 3.20c show a strong increase for the intensity of the Li₂S and a strong decrease for the pristine LGPS sulfur species, which shows a similar trend compared to LPS, this time without saturation. Saturation might be observed for more deposition cycles, but the sluggish kinetics caused by cooling aggravates the further analysis. The P 2p fractions in Fig. 3.20d exhibit a decreasing fraction for the initial P 2p species of the pristine LGPS and strongly increasing fraction of Li₃P, whereas the fraction of the reduced species stays at very low levels, as this compound is further decomposed to Li₃P. Again the analysis of the decomposed phosphorus species is hindered by the instability of the reaction products, as already described for LPS. The amount of deposited lithium metal yields 31 nm, which indicates that the interphase is obviously more extended compared to LPS, as the lithium metal amount is larger and the reaction process is not yet finished during the measurement.

The results for the electrochemical methods are discussed in the following. In Fig. 3.21a two Nyquist plots directly after contacting (0 h) and after 12 h are shown, the fit of the

⁷The same may also apply for the phosphorus species.

data and the equivalent circuit are displayed. The corresponding Bode plots and more Nyquist plots are shown in section 9.3.4. For the data analysis in Fig. 3.21a, the unreliable high frequency region and the low frequency region (the charge transfer resistance) are not considered. The fit results are summarized for 30 h and compared to LPS in Fig. 3.21b. In section 9.3.4, the monotonously changing spectra are shown, suggesting a resistance growth as monitored in Fig. 3.21b. The comparison between LPS and LGPS shows a similar trend, but the values for LGPS are approximately 10 times higher. Both materials exhibit a parabolic resistance behavior, which will be discussed and interpreted in detail in section 3.7.4.

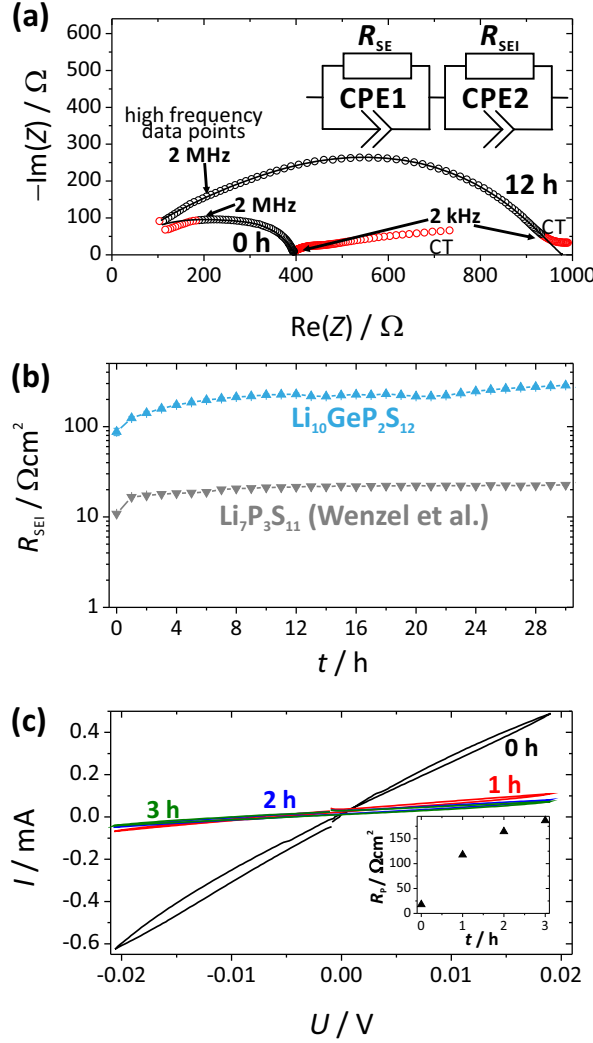


Figure 3.21: Two Nyquist plots, directly after contacting and after 12 h hours for a symmetric Li metal electrode/LGPS cell, are shown in (a). In addition, the fit and the equivalent circuit are displayed. The obtained resistance change for one electrode is then monitored in (b) and the CV data in (c). The inset in (c) displays the polarization resistance evolution^[82]. Again, the capacities are in the range of 10^{-9} F, comparable to Peled et al.^[90,95]

As stated for LPS, only the overall material resistance of LGPS could be monitored; the bulk and grain boundary contributions are not resolved. Again, the major part of the resistance increase could not be observed, as the reaction is notably too fast. The resistance increase is again gradually slowing down, which is attributed to a diffusion

controlled solid state reaction and the formation of an SEI. For a LGPS sample with a thickness of 3 mm, a material resistance of $60 \Omega \cdot \text{cm}^2$ is found, which is very low compared to the interphase resistance of $R_{\text{SEI}} = 250 \Omega \cdot \text{cm}^2$. The higher interphase resistance of LGPS compared to LPS leads to the valid assumption that the cell performance and cyclability are remarkably stronger deteriorated. As both materials exhibit similar bonding motives concerning the PS_4 -tetrahedra, the main reason for a larger SEI thickness might be the reduction of germanium. Germanium metal exhibits a high electronic conductivity but also shows a high lithium diffusivity^[111,112]. Additionally, minor contributions are expected due to the different structure, so that other reaction processes occur. As three dimensional percolation pathways are only expected for phases with 30 vol.% or more (rule of thumb), the formation of connecting percolation pathways could be excluded. Taking germanium metal into account, the volume fraction in relation to Li_2S yields only 4 vol.%. For the $\text{Li}_{15}\text{Ge}_4$ alloy the value is 12 vol.%, which is still far smaller than 30 vol.%. Thus, only germanium metal or alloy subnetworks of partially percolated germanium composites might be responsible for the larger SEI thickness.

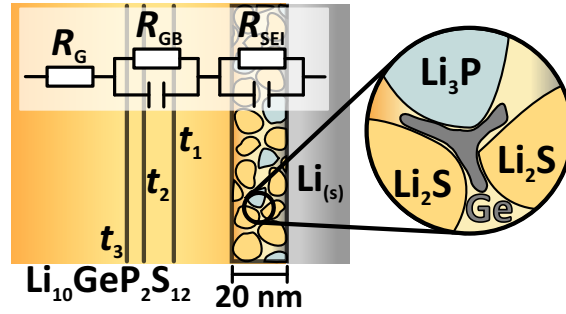


Figure 3.22: Sketch of the SEI between lithium metal and LGPS to illustrate the formation of partial percolating subnetworks^[82].

Indeed the microstructure of the SEI plays an important role, too. This hypothesis is sketched in Fig. 3.22, showing that the local charge transfer is increased, resulting in an increased average lithium transport coefficient. Additionally, the potential slope at a germanium subnetwork is decreased showing a nearly constant trend. Thus, the SEI growth is accelerated. More information about the interphase morphology might be obtained by TEM, but the sample preparation is challenging.

As already shown for LPS, the CV technique to evaluate the polarization resistance was conducted, too, in order to show the possible application and to compare it with the value obtained by impedance spectroscopy. Like expected, the slope in Fig. 3.21c is decreasing and likewise the polarization resistance is increased. Note that the polarization resistance is obtained without IR-drop correction, so that the values are generally higher than the real values. This time the polarization resistance is slightly smaller compared to the one obtained by impedance spectroscopy, but is in the same order of magnitude, which is in the range of the precision or reproduction quality of the interface manufacturing. This technique again proves the instability of the material and the formation of an SEI. Using the resistance increase obtained by impedance spectroscopy and Li_2S as main decomposition component (and an ion conductivity of 8 nS/cm)^[109], an SEI thickness of more than 20 nm is calculated after 30 h, which is ten times larger than for LPS. Nevertheless, as three different phases with different properties are formed a precise assessment is difficult.

3.7.3 Na₃PS₄

Sodium ion conductors are often believed to be more stable in contact with sodium metal than their lithium equivalents, because of the lower reduction potential of sodium compared to lithium metal^[43]. In order to investigate the interphase formation and the stability of Na₃PS₄ (NPS) in contact with sodium metal, the techniques of the combined approach were again applied. For the in situ XPS analysis, the samples were cooled to avoid sulfur evaporation. Again, the experimental composition matches well with the theoretical values. The temporal evolution when sodium metal is deposited for the P 2p, Na 1s and S 2p signal are displayed in Fig. 3.23, showing significant changes.

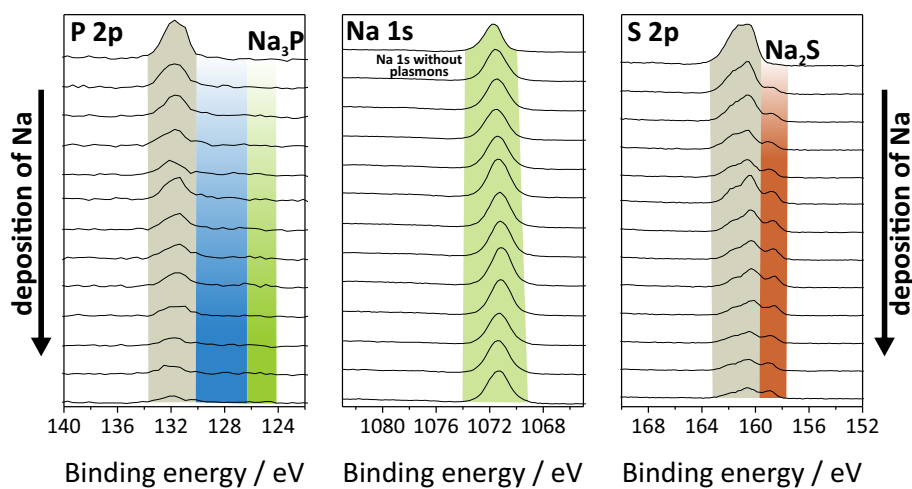


Figure 3.23: Deposition state dependent photoelectron detail spectra for the P 2p, Na 1s and S 2p signals of the NPS sample^[43].

In the P 2p spectra, the formation of Na₃P and reduced phosphorus species is observed, which is in accordance with results found for LPS and LGPS in the sections before. Interestingly, the sequential deposition of sodium metal does not result in the formation of sodium metal or sodium oxide at the surface, as the signal for sodium metal and the plasmons are missing. For stable compounds plasmons could clearly be observed, which is shown in section 3.8 for stable materials. Thus, the Na 1s spectra reveal that a reaction is taking place, too. By casting a glance to the S 2p spectra, the formation of Na₂S is observed which is in accordance to the results for the lithium equivalents.

For a detailed interpretation of the results, a peak fit model was developed, which is shown in Fig. 3.24 for the pristine and reacted sample. Further details and the fit parameters can be found in section 9.3.6. For the pristine sample, two different sulfur species, the double bond P=S and the single bond P–S–Na group, are found. The intensity ratios for both groups are in good agreement with the theoretical values (1:3). After sodium metal deposition, the formation of sodium sulfide is found and quantified by applying the fit model to the spectra of all deposition states. The P 2p spectra show only one doublet (spin orbit splitting) corresponding to the PS₄-tetrahedra. After deposition, a few more species are formed. Again, reduced phosphorus species, which are fitted as two average signals due to the lack of reference data, are identified. Furthermore, the signal at around 125 eV is assigned to Na₃P. Thus, the decomposition products are similar to

those found for LPS. The results indicate that the following reaction equation describes the decomposition process:



Using the fit models in Fig. 3.24a and b, a decomposition profile is obtained by quantification of the reaction species. The results are shown in Fig. 3.24c and d for the sulfur and phosphorus species, respectively.

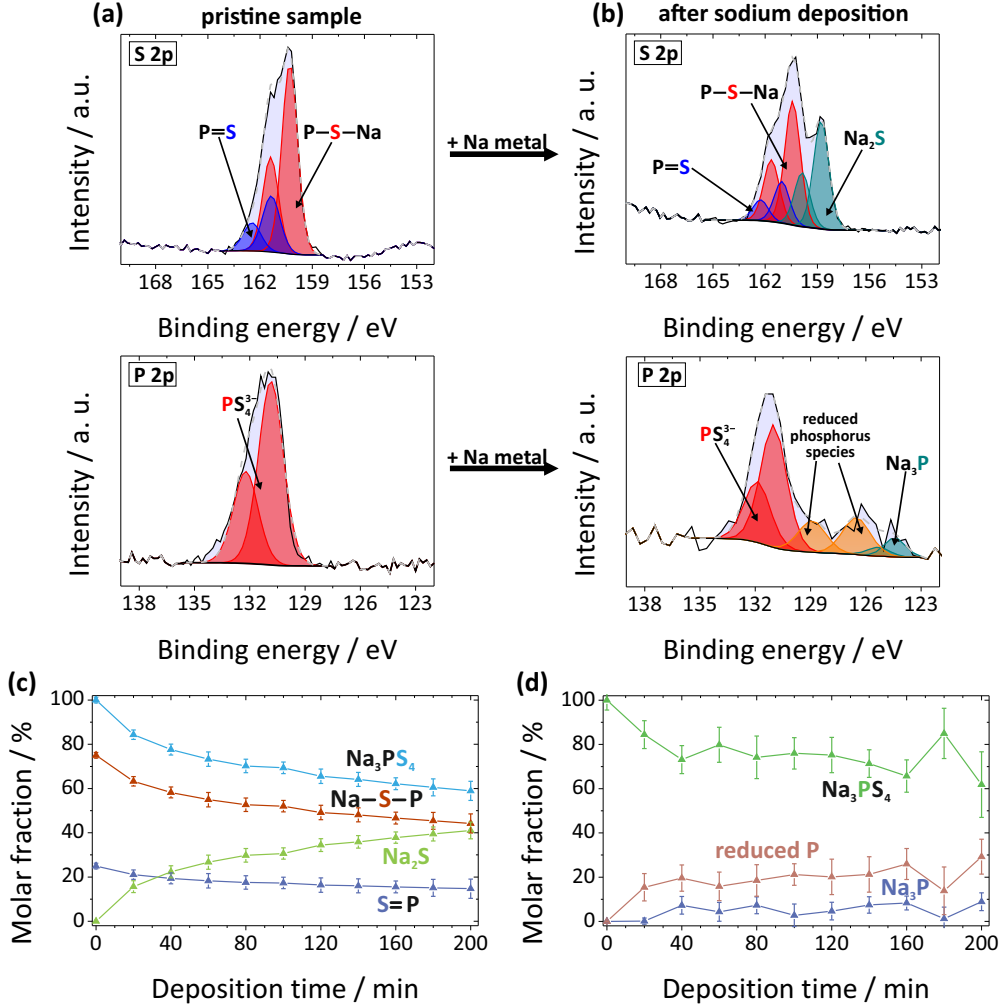


Figure 3.24: The detail spectra of the pristine and the reacted samples including the fit model for the S 2p and the P 2p signal are shown in (a) and (b). (c) and (d) show the evolution of the decomposition products^[43].

As expected, the fraction for the species assigned to Na₃PS₄ is decreasing. A detailed analysis additionally shows that the fraction of the double and single bond sulfur species are decreasing similarly, indicating that a simultaneous decomposition occurs. The profile for Na₃PS₄ and Na₂S seems to approach a boundary value but the point of saturation is not reached during the measurement. This finding might indicate that the decomposition might show a similar behavior like LPS and LGPS. In addition, the fraction of the PS₄-tetrahedra is slowly decreasing and the decomposition product fractions are increasing. This time, the amount of Na₃P is significantly lower than the reduced phosphorus species

compared to LPS or LGPS. Again, a side reaction with residual oxygen and water in the UHV chamber might complicate the data analysis and interpretation.

Using time-resolved impedance spectroscopy of symmetrical Na/Na₃PS₄ cells, the temporal evolution of the resistance is obtained. In Fig. 3.25a, the Nyquist plots directly after contacting and after 12 h are shown altogether with the result for the fit. Bode plots and additional Nyquist plots can be found in section 9.3.6. Again, the high frequency and the low frequency data points were excluded from the fit. The latter shows a partly resolved resistance that is assigned to the charge transfer resistance of the electrode and the solid electrolyte. By simply estimating the resistance increase of 12 h in Fig. 3.25a, the resistance is nearly doubled.

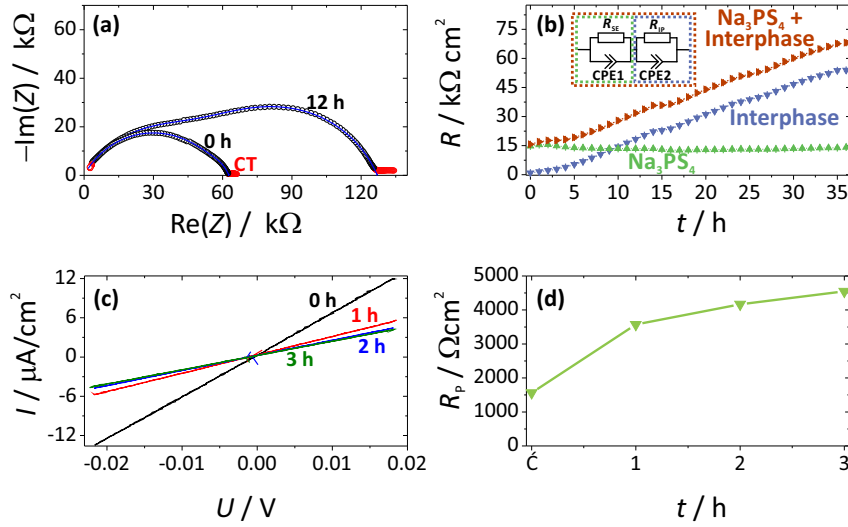


Figure 3.25: Two Nyquist plots directly after contacting and after 12 h hours for a symmetric Na metal electrode/NPS cell are shown in (a). The obtained resistance change is then monitored in (b). In addition, the fit and the equivalent circuit are displayed in (a) and (b), respectively. The CV data are shown in (c) and the thereof determined polarization resistance is plotted in (d)^[43].

A detailed analysis, using the equivalent circuit shown in the inset in Fig. 3.25b leads to the separation of the material and SEI resistance, respectively. The results are displayed in Fig. 3.25b showing a linear increase of the interphase resistance. After 10 h the interphase resistance equals the material resistance and after 36 h the values increase to the fourfold. The values are significantly higher than for LPS or LGPS. Moreover a linear resistance increase is observed, indicating that an interface controlled reaction is taking place, as it does not show a parabolic behavior as found for LGPS or LPS.

The CV data in Fig 3.25c and the resulting polarization resistance in Fig. 3.25d corroborate the resistance increases with time. After 3 h a resistance of 4.5 $\text{k}\Omega \text{ cm}^2$ and 3 $\text{k}\Omega \text{ cm}^2$ are found by CV and impedance spectroscopy, respectively, which are in good agreement. Keeping in mind that the resistance obtained by CV is overestimated, as the IR-drop correction is not considered, the values might be closer to the one obtained by impedance spectroscopy. Note that the polarization resistance in Fig. 3.25d is showing a parabolic behavior because with this technique only the interface and parts of the interphase are considered (see section 9.1).

Nevertheless, the formation of an interphase mainly consisting of Na₂S will lead to a large

resistance increase⁸, which will cause large overvoltages. Thus, the battery performance will be drastically deteriorated.

3.7.4 Interphase formation described as classical solid state reactions

Classical solid state reactions that form a single reaction product can be described theoretically by the Wagner model for tarnishing. A short introduction to the model is given in section 3.4. The diffusion controlled growth of mixed-conducting products can be described by this model. Most materials show a mixed conducting behavior, but often either the electronic or the ionic conductivity is dominant. Unfortunately, the SEI formation results in at least two products with different properties^[78,82,83].

The rearranged equation for Wagner’s model^[96] is given in Eq. 3.24, where $\bar{\sigma}$ and $\nabla\mu_A$ are the average partial conductivities of ions and electrons and the chemical potential gradient between the alkali species of the metal and the solid electrolyte, respectively. F is the Faraday constant and j the molar flux of the neutral component, described by the transport coefficients and chemical potential gradient of the alkali species across the film.

$$|j_A| = \frac{1}{F^2} \frac{\bar{\sigma}_{\text{el}} \cdot \bar{\sigma}_{\text{ion}}}{\bar{\sigma}_{\text{el}} + \bar{\sigma}_{\text{ion}}} \cdot \nabla\mu_A = \frac{1}{F^2} \frac{\bar{\sigma}_{\text{el}} \cdot \bar{\sigma}_{\text{ion}}}{\bar{\sigma}_{\text{el}} + \bar{\sigma}_{\text{ion}}} \cdot \frac{\mu_A^0}{d_{\text{SEI}}} \quad (3.24)$$

As the chemical potential gradient of the alkali species across the interphase and especially the chemical potential in the solid electrolyte are not known, the chemical potential gradient is substituted by the potential difference (divided by the SEI thickness d) and approximated to the values for the pure alkali metal μ_A^0 . Surely, the chemical potential for the alkali species A in the metal is notably larger than in the solid electrolyte, so that this assumption will only lead to small deviations. Using the flux j_A , the average molar mass M of the SEI, the density ρ of the SEI and the stoichiometric coefficient x (moles of alkali metal required for the reaction), the theoretical growth rate r can be assessed by Eq. 3.25 for diffusion controlled reactions.

$$r = \frac{dd_{\text{SEI}}}{dt} = \frac{j_A \cdot M_{\text{SEI}}}{\rho_{\text{SEI}} \cdot x} \quad (3.25)$$

For interphases with two reaction products that exhibit different properties, average conductivities are used as described in the following for LPS. It is assumed that the electronic properties of both decomposition products are similar to each other so that the average electronic conductivity for Li_2S is used for the calculations. To the contrary, the ionic properties are significantly different, as Li_2S shows a low value of 8 nS/cm^[109] and Li_3P a higher value of approximately 0.7 mS/cm^[113]. As only the conductivity of minor charge carriers is really considered in Eq. 3.24 (the conductivity of the major charge carriers is reduced from the fraction), the value for the ionic conductivity does not matter. The results for this model are shown in Fig. 3.26 for different electronic conductivities. Unsurprisingly, the growth rate shows a square root behavior. The data derived from the measurements are drawn in red, showing that this model is qualitatively valid in this range.

⁸Reliable conductivity data for Na_2S were not available. It is assumed that the conductivity of Na_2S is at least comparable to the conductivity of Li_2S .

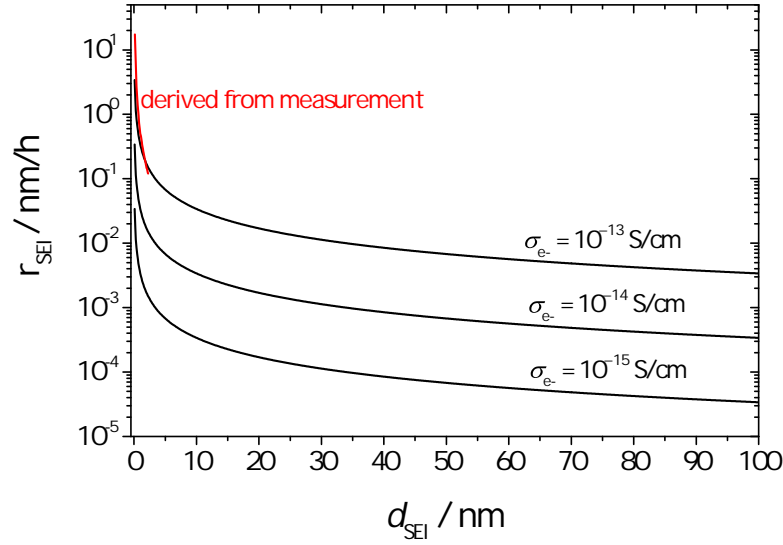


Figure 3.26: Theoretical growth rate of the interphase of Li metal and LPS as a function of the interphase thickness d_{SEI} . Different electronic conductivities were used for the theoretical simulations. The results are compared to the data derived in section 3.7.1^[78].

The theoretical estimates yield in a growth rate of 0.17 nm/h for an interphase thickness of 2 nm, which is rapidly decreasing with increasing interphase thickness. For LGPS the application of this model is difficult, due to the fact that three phases with completely different transport properties were formed, complicating a precise assessment.

Values for the rate constant can be evaluated for diffusion controlled reactions by a plot of the interphase thickness against the square root of time^[96,100], see section 3.4. This is valid for LGPS and LPS, but not for the interface-controlled reaction of NPS⁹.

Using the impedance data of section 3.7.1, 3.7.2 and 9.3.5 and the assumption that Li_2S as main decomposition product determines the resistance increase, an SEI thickness is calculated and plotted against the square root of the time, which is shown in Fig. 3.27a. The resulting linear curves are then fitted, resulting in the parabolic rate constants in Tab. 3.1. The data of the curves do not start at zero, as it should be the case for completely diffusion-controlled reactions.

Table 3.1: The slope (parabolic rate constant k) and d -intercept for the fits in Fig. 3.27 for LPS, LGPS and LPSCI.

	Parabolic rate constant / $10^{-7} \text{ cm/h}^{0.5}$	d -intercept / 10^{-7} cm
LPS	0.23 ± 0.02	0.99 ± 0.05
LGPS	3.61 ± 0.08	6.60 ± 0.19
LPSCI	0.59 ± 0.01	0.59 ± 0.03

Thus, the formation of the first few nm is interface controlled and then enters the range of diffusion control. As the SEI is not a homogenous phase, a deeper analysis of growth kinetics by models for solid state reactions is yet not possible. Nevertheless, the data in

⁹For NPS this approach might be applied when the diffusion-controlled reaction regime is reached.

Tab. 3.1 can be used to extrapolate the SEI growth for a period of ten years, which is often stated as the battery lifetime by the industry.

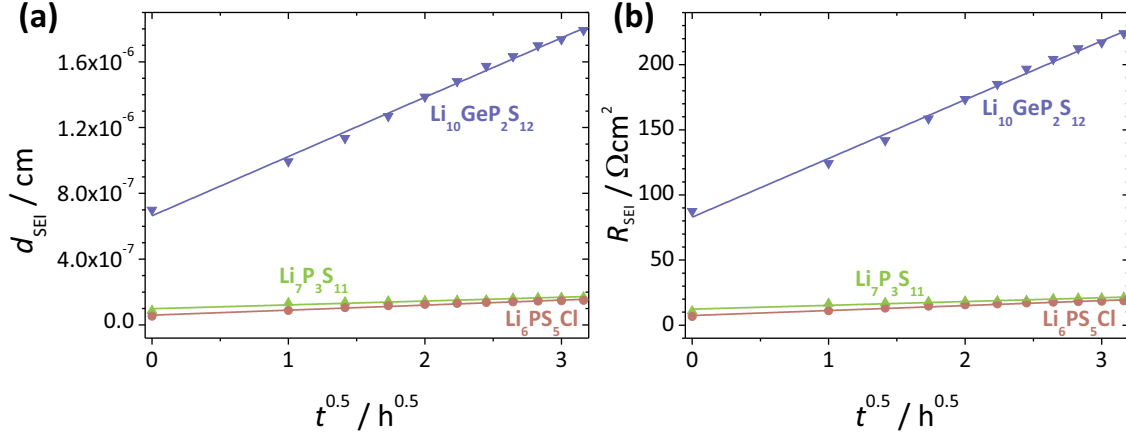


Figure 3.27: The interphase thickness in dependence of the square root of the time is displayed in (a). The parabolic behavior proves the diffusion-controlled growth mechanism. The fit results are summarized in Tab. 3.1^[82]. (b) shows the resistance increase, which was directly obtained by equation 3.26 and the SEI resistance. The fit results are summarized in Tab. 3.2.

The use of Li_2S as a SEI substitute leads to a deviation in the thickness, which is caused by neglecting the influence of Li_3P on the SEI^{10} . Thus, a more correct model can be developed using equation 3.26.

$$\begin{aligned} d_{\text{SEI}} &= k \cdot \sqrt{t} \\ R_{\text{SEI}} \cdot A \cdot \sigma_{\text{SEI}} &= k' \cdot \sqrt{t} \\ R_{\text{SEI}} &= k \cdot A \cdot \sigma_{\text{SEI}} \cdot \sqrt{t} = k' \cdot \sqrt{t} \end{aligned} \quad (3.26)$$

Table 3.2: The slope (parabolic resistance rate constant k') and d -intercept for the fits in Fig. 3.27b for LPS, LGPS and LPSCl.

	Parabolic rate constant / $\Omega\text{cm}^2/\text{h}^{0.5}$	d -intercept / Ωcm^2
LPS	2.9 ± 0.3	12.3 ± 0.6
LGPS	45.1 ± 1.0	83.9 ± 2.3
LPSCl	3.8 ± 0.2	7.4 ± 0.4

The results of the interphase growth simulation are shown in Fig. 3.28a for the interphase thickness and in Fig. 3.28b for the resulting resistance increase. LGPS is showing an interphase thickness of approximately $1 \mu\text{m}$ after 10 years, which is more than ten times higher compared to LPS. Likewise, the resistance increases up to values of $4294 \Omega\cdot\text{cm}^2$, $9500 \Omega\cdot\text{cm}^2$ and $13400 \Omega\cdot\text{cm}^2$ for LGPS and $285 \Omega\cdot\text{cm}^2$, $622 \Omega\cdot\text{cm}^2$ and $874 \Omega\cdot\text{cm}^2$ for LPS after one, five and ten years, respectively.

Thus, the overvoltage should increase similarly and will significantly deteriorate the battery performance, cyclability and lifetime. Solid electrolytes show a similar behavior to

¹⁰Due to the vanishing of the phosphorus species and the unknown microstructure.

liquid electrolytes, as both form solid electrolyte interphases and show a parabolic resistance behavior^[115]. Nevertheless, the SEI of liquid electrolytes may dissolve or disperse in the liquid electrolyte, leading to the formation and growth of a new SEI^[116,117].

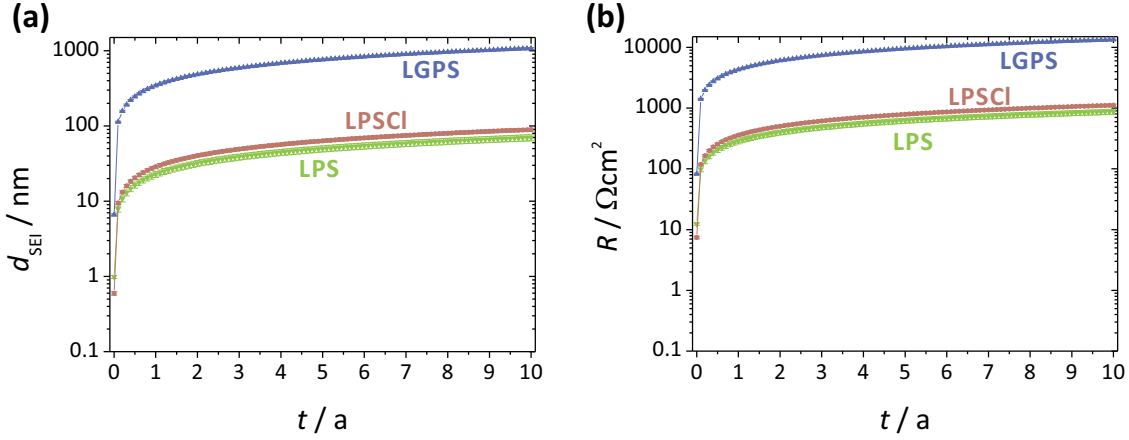


Figure 3.28: Simulated interphase thickness (a) and resistance increase (b) for LGPS, LPS and LPSCI for a battery lifetime of ten years, using the parameter in Tab. 3.1 and 3.2.

Using the combined approach described in section 3.5, the interphase behavior can be assessed in accordance with experimental data and the impact on battery cycling can be predicted. The results clearly show that the battery performance will be deteriorated even without charge and discharge process (cycling).

Recently, Kato et al.^[118] published the use of LGPS in combination with lithium metal electrodes in an ASSB. The observation of a high irreversible capacity of 0.2 mAh in the first cycle, leads to the calculation of an SEI thickness of approximately 2 μm . In this study, an interphase thickness of approximately 20 nm is obtained for the interphase of LGPS and lithium metal. Against that, Kato et al. studied a full ASSB cell, which might additionally show reactions at the cathode side. Further reasons for the different results might be the cycling procedure, which may lead to an enhanced interphase growth, delamination processes, dead lithium metal¹¹, dendrite formation (including voids and cracking) and kinetic limitations. In this work, the pristine LGPS material was still observed after interphase formation in the XPS, which directly excludes interphase thicknesses larger than a few nm.

3.8 Stable solid electrolytes

Stable solid electrolytes are favorable when it comes to the application in batteries, as shown in the last sections, as no degradation of the interface and the material during the contact with the electrode material occurs. This might be different during cycling and the behavior of stable and interphase forming solid electrolytes will be described and discussed in section 5 and 6. In this section, two stable solid electrolytes will be shown and the respective results for the combined approach discussed. The group of stable materials is the smallest interface/interphase type in the classification; as only a few of

¹¹Lithium metal which could not be electrochemically used due to morphological reasons.

all materials are stable in contact with the highly reactive alkali metals. Both materials, Na- β -alumina and LLZO ($\text{Li}_7\text{La}_3\text{Zr}_2\text{O}_{12}$ doped with Al) are stable in contact with their respective alkali metals. The combined approach, which even worked for the formation of very thin interphases, proved the stability. The results are described and discussed in the following^[43,83].

3.8.1 Na- β ''-aluminum oxide

Na- β -alumina is known to be stable in contact with molten sodium metal and is already used in high temperature sodium-sulfur batteries^[38]. Thus, it is no surprise that this component is stable in contact with solid sodium metal, too. In order to show at least one material for every interface/interphase type, stable solid electrolytes should not be missing. Thus, the results obtained by the combined analytical approach are shown and discussed in the following. Detail XPS spectra for several deposition steps for the Al 2p, Na 1s and O 1s signal are shown in Fig. 3.29. The Al 2p spectra do not show the formation of reduced aluminum species. Only the plasmon formation for the Na 2s signal is observed caused by the deposition of sodium metal. These plasmons, which are an undeniable sign for sodium metal film formation are not seen for the reaction with Na_3PS_4 (see section 3.7.3).

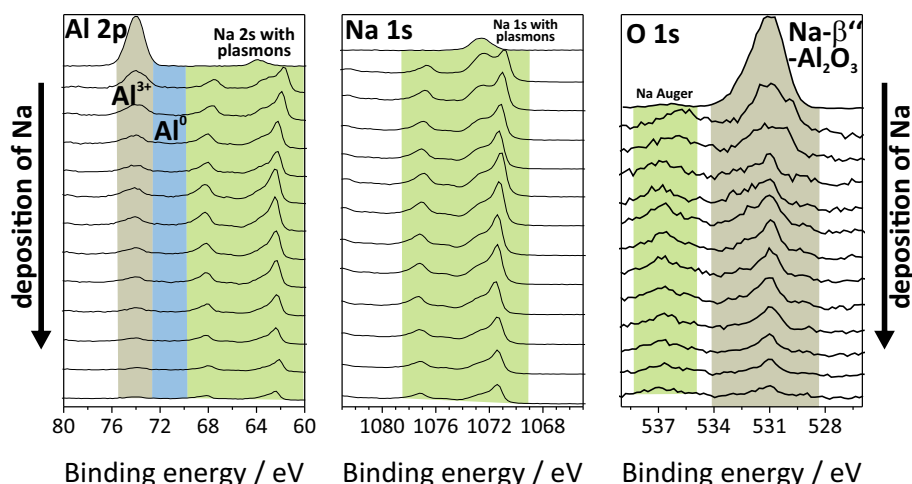


Figure 3.29: Deposition state dependent photoelectron detail spectra for the Al 2p, Na 1s and O 1s signals of the β ''-alumina sample^[43].

Both the missing reduction of aluminum and the plasmon formation are distinct proves for the stability of the material. The signal intensity of the Al 2p peak is decreasing, caused by the burying of the material with sodium metal. In the Na 1s spectra, the formation of plasmons is seen, too, which corroborates the results discussed for the Al 2p spectra. As there is no change observed for the O 1s signals, except for the Na-Augur lines, no chemical reaction occurs during the contact of sodium metal and β ''-alumina.

The results for the electrochemical analysis techniques were already shown in section 3.5.4, but are shown again in Fig. 3.30. The Nyquist plots in Fig. 3.30a only exhibit very small deviations which are easily explained by temperature variations during the measurement. Deviations to slightly larger and slightly smaller values were observed, which correspond to a temperature decrease or increase, respectively. A detailed discussion of an advanced contacting process for β ''-alumina and sodium metal electrodes can be found in section 5.

The time-resolved CV data in Fig. 3.30b corroborate the findings obtained by impedance analysis, as no change in the slope can be determined, which corresponds to a constant polarization resistance.

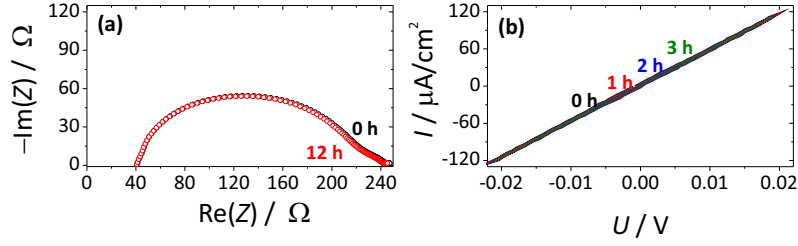


Figure 3.30: Nyquist plots for 0 h and 12 h after contacting the beta-alumina pellet with two sodium metal electrodes are displayed in (a). The CV data are shown in (b) [43].

3.8.2 $\text{Li}_7\text{La}_3\text{Zr}_2\text{O}_{12}\text{:Al}$

The second stable solid electrolyte investigated here is the cubic garnet-type material $\text{Li}_7\text{La}_3\text{Zr}_2\text{O}_{12}$ (doped with Al). Like in many different stability investigations in literature, the stability of LLZO is often proved simply by standard CV experiments.

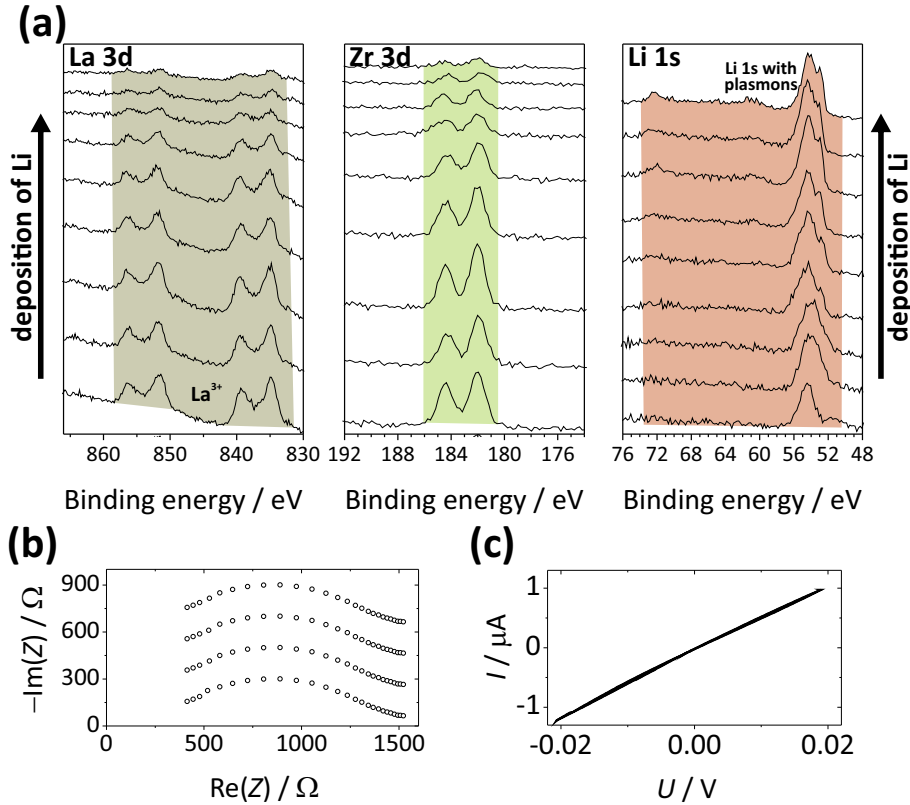


Figure 3.31: Deposition state dependent photoelectron spectra for the La 3d, Zr 3d and Li 1s signals of the LLZO sample are displayed in (a). Note that the data are stacked with a constant value to improve the clarity. The results for the time-resolved impedance and CV analysis are shown in (b) and (c), respectively. Unpublished data.

To really show the stability of the interface LLZO/ lithium metal, the combined approach is used again and the results are summarized in Fig. 3.31.

In Fig. 3.31a, the results for the La 3d and Zr 3d spectra are shown. The only change is the signal intensity, which is decreasing due to the formation of a lithium metal overlayer. No signals at lower binding energies relative to the peaks of the highest oxidized species are found, proving that the material is stable in contact with lithium metal. The Li 1s spectra in Fig. 3.31a then only show the formation of lithium metal plasmons and exhibit for lithium characteristic low intensities. As the impedance data in the stacked plot in Fig. 3.31b and the CV slope in Fig. 3.31c do not exhibit any changes, the material is proven to be stable in contact with lithium metal.

3.9 Thermodynamic assessment and evaluation of stability

In order to support the development of new solid electrolytes and to estimate the stability of different materials, thermodynamic calculations were performed using the HSC Chemistry 7.00 (Outotec Research) software. Due to missing thermodynamic data for the most components, substitution compounds were used. LLZO for example was simulated by the reactions of lithium metal with La_2O_3 , Al_2O_3 and ZrO_2 (as LLZO can be described as a solid solution with the composition of $(\text{Li}_2\text{O})_x(\text{La}_2\text{O}_3)_y(\text{ZrO}_2)_z$). The results of the calculations are sketched in Fig. 3.32 for sodium and lithium metal, respectively. As Al_2O_3 and ZrO_2 are not stable and La_2O_3 is stable in contact with lithium metal, it can be assumed that the compounds up to a Gibbs free energy of approximately -100 kJ/mol can be stabilized by the structure and in combination with stable compounds. Therewith, a rough border range (rule of thumb) is defined, where stable compounds might be found and the material is stabilized by the structure.

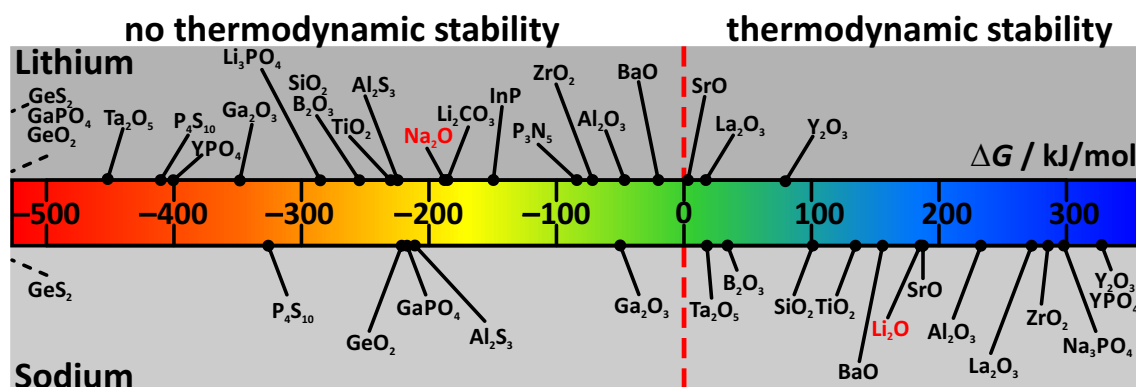


Figure 3.32: The Gibbs free energies for the decomposition of substitution materials are sketched in a diagram to illustrate the stability. All values are normed to the reduction of one mol of elements. For example the reduction of Ta_2O_5 is normalized to the value for the reduction of one Ta^{5+} to Ta^0 . Unpublished data.

The data in Fig. 3.32 vividly illustrate that there are far more materials that are stable against sodium metal than for lithium metal. In the following, the different materials, which were already described in this section and in section 9, are linked to the thermodynamic data. LLTO is containing one stable compound, the lanthanum oxide, and an extremely reducible compound, the titanium oxide. As the value for the reduction of titanium is virtually higher than the border range for structural stabilization (rule of thumb), all compounds containing titanium will not be stable. The same assumptions are valid for tantalum in LSTZO and titanium in LATP as well. All three materials are forming an MCI. The requirements for an MCI or SEI formation, apart from the thermodynamic, will be given later in this section. Interestingly, phosphate compounds also show a very high negative Gibbs free energy, which will lead to decomposition, too, and lithium oxide and lithium phosphide will be formed. This might explain the different decomposition behavior of LATP compared to LLTO or LSTZO. To summarize the thermodynamic assessment for metal ions, almost all metal ions are reduced by lithium metal, with exception of the earth alkali metals, yttrium and lanthanum compounds. Thus, the opportunity to find a stable lithium ion conductor is strongly limited, with the exception of LLZO. For the stability against sodium metal, far more stable compounds can be found, including aluminum-, yttrium-, tantalum- and titanium oxide. The latter is controversially discussed in liter-

ature, as the reduction of TiO_2 by sodium metal is reported^[114]. Surprisingly, sodium phosphates and most likely the sodium analogue to LiPON will be stable. However, the thermodynamic calculations sometimes lead to incorrect values, which is shown for the NaSICON material^[119] in section 9.3.8. ZrO_2 and phosphate should be stable in contact with sodium metal, but Zr is clearly reduced. The reason for this might be inaccurate values in the data base. Nevertheless, thermodynamic assessments can save a lot of time, when the evaluation of stabilities is required. P_4S_{10} for example, as a substitution compound for LPS, LGPS and NPS, shows neither for lithium or sodium positive Gibbs free energies, quite the contrary, large negative values are found. Likewise germanium oxide compounds are not stable against sodium or lithium and the sulfides exhibit even higher negative values. Thus, neither LGPS, LPS, NPS nor similar compounds (e. g. argyrodites) will be stable against their respective alkali metal.

In this work it has been shown that the P–S bonds are not stable and are easily reduced. The same is observed for P–O bonds for example in LiPON^[74]. The stable materials, even for higher voltages compared to the alkali metals, are binary compounds, which unfortunately seldom exhibit high ion conductivities at room temperature or are not stable at higher voltages. Examples are Li_2S , Li_3P , LiI , Li_2O or Li_3N .

To settle the question, whether an MCI or an SEI is formed, different aspects have to be taken into account. If electronic insulating products are formed, the formation of an SEI is observed. By incorporating redox-active metal ions in the structure, the SEI growth can be accelerated, depending on the metal fraction. Higher fractions of highly reducible metals may lead to an MCI when the other decomposition products exhibit high ionic transport coefficients. Interstitial and alkali ion vacancies also play a crucial role. The NaSICON material^[119] (see section 9.3.8) shows the reduction of Zr^{4+} to lower valent oxidation states and a relatively high content of zirconium in the structure. This may lead to the assumption that an MCI will be formed. Nevertheless, the further reduction of the material is most likely prevented by charge neutrality. For every electron used for the reduction of the metal ions, one alkali ion has to be inserted into the structure. Therefore, vacancies and interstitials are required, without them interphase growth is most likely prevented.

Thus, thermodynamic calculations with substitution materials often give a hint about the stability of the material against alkali metals. Very few materials are stable in contact with lithium metal but some more are stable against sodium metal. Whether an MCI or SEI is formed strongly depends on the nature of the decomposition products, the structure of the materials (vacancies and interstitials) and the fractions of the electronic conducting products.

3.10 Volume effects of SEI formation

In this section, an assessment for the interphase morphology, based on the consideration of volume effects will be described. The reaction products of metal corrosion will be porous, when their molar volume is less than that of the reacted metal^[97]. Calculations were conducted in order to evaluate the possible strain or porosity formation, according to the

Pilling-Bedworth ratio PBR ^[120] in equation 3.27, where V_{SEI} and V_{SE} are the volume of the resulting SEI and the solid electrolyte (SE), respectively.

$$PBR = \frac{V_{SEI}}{V_{SE}} \quad (3.27)$$

The procedure is sketched in Fig. 3.33a and b. One mol of solid electrolyte is completely decomposed and the molar volumes of the solid electrolyte are compared to the volume generated by the decomposition products. Thus, a ratio is calculated that describes the volume expansion or shrinkage, respectively. For this, the model in Fig. 3.33a and b is used.

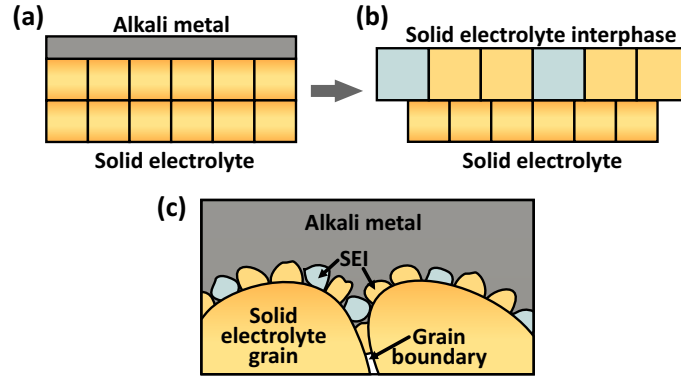


Figure 3.33: The model cases for the volume increase are shown in (a) and (b). A more realistic picture of the interphase is displayed in (c).

For the complete conversion of one mole LPS to the products Li_2S and Li_3P , the volume is increasing to the 2.2-fold of the initial value. The conversion of NPS leads to an SEI volume that is 2.8 times larger compared to the unreacted sample. LGPS can form two different decomposition products, germanium metal and $Li_{15}Ge_4$. The values for both cases lead to a volume increase of the 3.2-fold and 4.4-fold of the starting volume, respectively. For the SEI formation of the argyrodite Li_6PS_5Cl and lithium metal, a relatively small volume increase to the 1.4-fold is calculated. Thus, the interphase formation will lead to strain between the solid electrolyte and the SEI, which may lead to contact loss when the SEI flakes break, which will be notably worse for LGPS, LPS and NPS, whereas the volume expansion for the argyrodite is significantly smaller. Other results of the strain generation might be cracks in the interphase that may lead to further reaction with the alkali metal, as it may be pressed into the void or dendrites grow inside the cracks. Surely the contact area between the interphase and the electrode will also decrease, as no charge transport occurs in the void. A pressure in the cell will most likely not be formed as the overall volume increase will be mostly compensated by the consumption and plastic deformation of alkali metal.

Including the volume of alkali metal to the assessment, the cell volume changes to the 0.83-fold for LPS and NPS, 1.1- and 1.2-fold for LGPS (depending on the alloy formation), according to equation 3.28 and the obtained R_{WS} values.

$$R_{WS} = \frac{V_{SEI}}{V_{SE} + V_A} \quad (3.28)$$

, where V_A denotes the volume of the consumed alkali metal. Thus, the interphase formation generates a mismatch between the solid electrolyte and the SEI, but the cell volume is decreasing in the case of LPS and NPS and increases in the case of LGPS. This might result in contact loss (between the electrode and the solid electrolyte) and mechanical strain formation, which will affect all cell parts. The morphological instability of the interphase was observed during the experiments. During the removal of the alkali electrodes, the SEI is often destroyed and powdered and the electrode is more easily removed compared to directly after contacting. In section 5, the pressure dependence of battery cycling will be described. Assuming that a certain pressure is necessary for proper cycling, the interphase formation, leading to a volume decrease, may decrease the pressure and the cyclability of the battery.

3.11 Summary and Conclusion

The application of alkali metals in all-solid state batteries is often described as the "holy grail", due to the high (volumetric and gravimetric) theoretical capacity and the resulting energy density, and is believed to be one of the potential major advantages of ASSBs compared to LIBs and sodium ion batteries^[54,55]. However, the chemical stability of solid electrolytes in contact with the respective alkali metals is a very important key requirement, as the instability of the materials will either result in short circuits or in a resistance increase of the all-solid state battery. In the literature, the reports on the stability are mostly limited to electrochemical investigations or simulations (see section 3.3). The identification of decomposition products is seldom reported. According to the classification displayed in section 3.2 and published by Wenzel et al.^[61], three different interface/interphase types can be distinguished. The unstable materials show a thermodynamic driving force for the decomposition, whereas the stable materials are in equilibrium a priori. According to the properties of the decomposition products, the interphase is then assigned to an MCI or SEI, depending on the electronic and ionic conductivities of the products. In this work, a combined approach is described that offers chemical information about the decomposition products (by in situ XPS) and kinetic information about the interphase formation and growth (electrochemical methods). The in situ XPS technique was developed during this work and consists of sequential XPS analysis and alkali metal deposition by application of the inbuilt argon ion gun. In order to give a guideline for the investigation of interphase/interface formation, the expectations and the results of the electrochemical methods for all three interphase/interface types are compared. Thus, using the electrochemical methods of the combined approach, the interphase type can be determined and kinetic information about interphase formation and growth are obtained. The in situ XPS technique then gives information about the decomposition products.

All materials that were discussed in this chapter are assigned to one of the interphase/interface classes, which is summarized in Fig. 3.34. The least favorable type is the mixed conducting interphase (MCI) which will lead to short circuits and self-discharge of the battery. MCI forming materials are the perovskite type materials lithium lanthanum titanate (LLTO), lithium strontium zirconium tantalate (LSTZO) and the NASICON-type material lithium aluminum titanium phosphate (LATP). These materials cannot be used in alkali metal containing ASSBs. MCIs were often formed when reducible metal ions are incorporated in the structure in reasonable fractions.

The range of SEI forming materials comprises promising materials like $\text{Li}_7\text{P}_3\text{S}_{11}$ (LPS), $\text{Li}_{10}\text{GeP}_2\text{S}_{12}$ (LGPS), argyrodites (LPSCl, $\text{Li}_6\text{PS}_5\text{Cl}$) and LiPON¹². For LGPS, LPS and LPSCl, the results of the combined approach results in the development of models for the description of interphase growth, according to classic solid state reaction models. For this, the kinetic information about the growth and the identification of the decomposition products (mostly Li_2S and Li_3P) played a crucial role. Together, a parabolic growth rate constant was obtained which allows simulation of the SEI behavior for 10 years, showing that the resistance will be strongly increased and alkali metal will be consumed, resulting in decreasing cyclability and battery capacity. The results also indicate that the SEI thickness for LGPS is larger compared to LPS and LPSCl, which might be assigned to the properties of germanium alloy and metal that is formed during decomposition, as the local transport coefficients are increased. Nevertheless, verification by transmission electron microscopy was not possible.

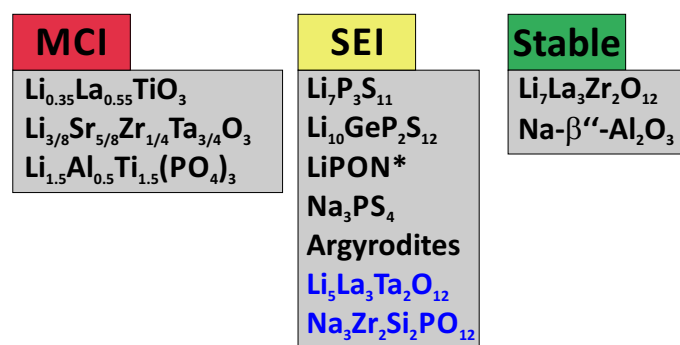


Figure 3.34: The different materials are classified according to the type of interphase/interface that is formed. LiPON is marked with an asterisk, as it is not shown in this work but is nevertheless one of the most prominent ion conductors. $\text{Na}_3\text{Zr}_2\text{Si}_2\text{PO}_{12}$ and $\text{Li}_5\text{La}_3\text{Ta}_2\text{O}_{12}$ are special cases that might be assigned to SEI forming materials.

Na_3PS_4 showed a growth rate that is assigned to an interface controlled reaction and thus, an extrapolation was not possible as the transition from interface to diffusion control was not observed during analysis. The low conductivity of the decomposition products hinted that diffusion control might be reached, but the SEI is notably more extended compared to LPS or LGPS. $\text{Na}_3\text{Zr}_2\text{Si}_2\text{PO}_{12}$ (NaSICON type compound) showed slight reduction of zirconium, but the other components do not seem to be affected^[119] (see section 9.3.8). $\text{Li}_5\text{La}_3\text{Ta}_2\text{O}_{12}$ (LLTa₂O) is a special case, as the in situ XPS experiment revealed the formation of tantalum metal, which may lead to the assumption that LLTa₂O is an MCI forming material. Indeed, the resistance of the pellet is increasing during contact with alkali metal electrodes, which is a characteristic for SEI formation. Thus, this material showed a Janus-faced behavior. SEI formation may cause morphological instabilities (e. g. dendrites) at relatively high current densities, which will be shown in section 6.

Strain formation also plays an important role, as the SEI formation leads to a volume increase compared to the initial material. Compared to the initial cell volume, the volume after interphase formation is slightly decreasing to approximately 0.8-fold (LPS, NPS and LPSCl) and 1 – 1.2-fold for LGPS (depending on the fraction of alloy). Thus, the overall cell volume will be changed, which may lead to a decreasing or increasing mechanical cell pressure. The influence and importance of mechanical pressure on the cycling behavior

¹²Systematic measurements were conducted by Dr. Thomas Leichtweiss.

will be described in section 5.

The last interphase/interface class contains the stable materials, which only consists of two materials: The sodium β'' -alumina and the $\text{Li}_7\text{La}_3\text{Zr}_2\text{O}_{12}:\text{Al}$ (LLZO), that both did not show any changes in the in situ XPS and electrochemical measurements and are thus assigned to be stable in contact with sodium and lithium metal, respectively. According to thermodynamic calculations and the results in this chapter, a synthesis recommendation is given. As only a few materials will be stable in contact with lithium metal, the formation of protecting films and interphases with reasonable conductivity is required, the number of stable materials is mainly limited to LLZO and binary compounds. For sodium ion conductors, more materials will be stable as the reduction potential for sodium is remarkably lower compared to lithium metal. Thus, quite a few materials will be stable, including the promising Na- β'' -alumina.

In order to show the influence of SEI formation the following assessment may help. The interphase between alkali metals and the solid electrolyte showed a resistance increase that ranges from $25 \Omega\cdot\text{cm}^2$ to several hundred $\Omega\cdot\text{cm}^2$. Assuming an $1 \mu\text{m}$ thick solid electrolyte film (with $\sigma = 1 \text{ mS/cm}$, a reasonable value), the interphase and the material resistance will be around $25 \Omega\cdot\text{cm}^2$ and $0.1 \Omega\cdot\text{cm}^2$, respectively, leading to an overall resistance of $25.1 \Omega\cdot\text{cm}^2$. Assuming a conductivity of 0.1 mS/cm and 0.01 mS/cm for a stable, $1 \mu\text{m}$ LLZO thin film, again reasonable resistance values of $1 \Omega\cdot\text{cm}^2$ and $10 \Omega\cdot\text{cm}^2$ are calculated. Thus, the material resistance is not the limiting factor, as the interphase resistance, which will be growing, is significantly larger than the resistance of stable materials with lower ionic conductivity. However, the charge transfer resistance plays an important role, too, and was not considered in the assessment.

Thus, the interphase resistance and growth significantly increase the battery resistance, leading to a significantly decreased battery performance. This directly leads to the conclusion that stable materials will always be favorable in ASSBs. The interphase formation shows a few other significant effects, which will be described in section 6.

4 Interface protection concepts and their limitations

4.1 Introduction and literature survey

In section 3 it was shown that most solid electrolytes are not stable in contact with alkali metal electrodes. The stabilities of further materials are described in section 9. In order to prevent the decomposition of unstable solid electrolytes, a few protection concepts were established. For this, a stable solid electrolyte is deposited onto an unstable solid electrolyte and thus, the decomposition is prevented. The protecting materials range from polymer electrolytes^[121], LiPON^[122] (via sputter deposition), $\text{Li}_6\text{BaLa}_2\text{Ta}_2\text{O}_{12}$ ^[123] (LBLTO, via pulsed laser deposition) to sacrificial layers of Cu_3N ^[124]. According to the experience gained during this project, the stability of polymers against lithium metal is doubtful. LiPON was shown to react^[74] by formation of an SEI and is therefore suitable for protection. The stability of LBLTO is not reported yet, but according to the results in section 9.3.7 and section 3 for LLTa_2O (both garnet type materials, the difference is the barium substitution) LBLTO might not be stable, too. LiPON and sacrificial layers as protection films for solid electrolytes are promising concepts. In this chapter, the experimental results for LiPON-based protecting films on LLTO and the use of Cu_3N as sacrificial protection film are discussed.

At the end, theoretical limitations of protection concepts are described.

4.2 LiPON on LLTO

In order to protect a highly reducible LLTO pellet, LiPON was deposited onto the sample. Fig. 4.1a shows the pristine pellets and b the pellets after deposition. Afterwards, lithium metal electrodes were applied to the protected and the pristine pellet. The instability was easily observed as the pristine pellet turned dark black upon reduction, as seen in Fig. 4.1d. The protected pellet did not change and is displayed in Fig. 4.1c.

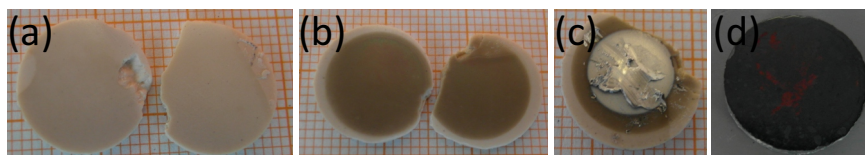


Figure 4.1: The pristine LLTO pellet is shown in (a), after LiPON deposition in (b), with lithium metal in (c) and a reacted sample in (d).

Thus, LiPON protects the LLTO against reduction, as the pellet is not blackened even after

weeks. Unfortunately, the resistance had strongly increased so that it was not possible to measure the conductivity of the samples. Whether this is caused by a large interfacial resistance between LiPON and LLTO or the LiPON itself could not be clarified in the present study.

4.3 Cu_3N as sacrificial film

Cu_3N ^[124] is reported to function as a sacrificial protection film (SPF) and might protect the solid electrolyte against reduction, as the lithium conductor Li_3N is formed, which then protects the solid electrolyte and is not blocking the ion transport. The following reaction is proposed for this:



Unfortunately, copper metal is formed during the reaction so that an electronic conductor is part of the artificial interphase. Thus, an ionic and an electronic conductor are formed. Using the rule of thumb for percolation (see section 3.4), which stated that for volume fractions greater than 30 vol.% percolation will most likely occur and notably increase the electronic or ionic conductivity of the material. The volume fraction for the decomposition of Cu_3N was found to be 45.8 vol.% for copper, which is greater than 30 vol.% and thus, percolation will occur. As one of the products is an ionic conductor and the other an electronic conductor, some kind of mixed conducting interphase (MCI) might have formed. Thus, this protection concept is in principle very promising but might also fail due to percolation. The microstructure of the interphase, i. e. spatial distribution of Cu will be decisive for the protecting function.

4.4 Content classified by JLU

[REDACTED]

 \rightarrow  (4.2)

 \rightarrow  (4.3)

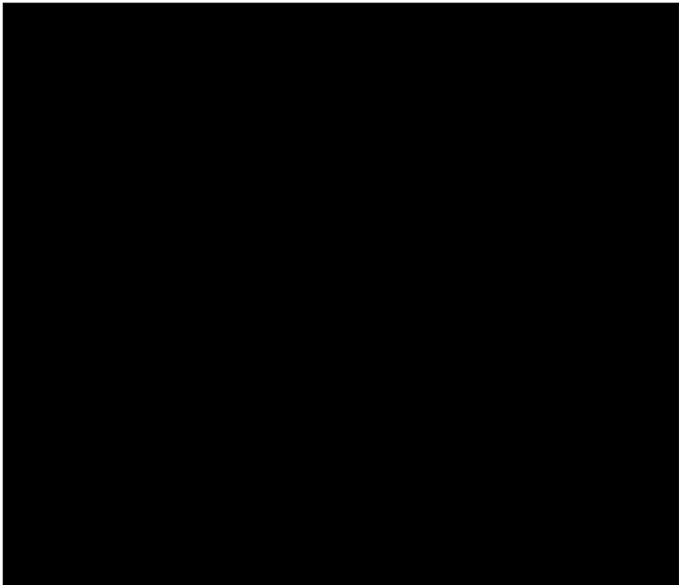
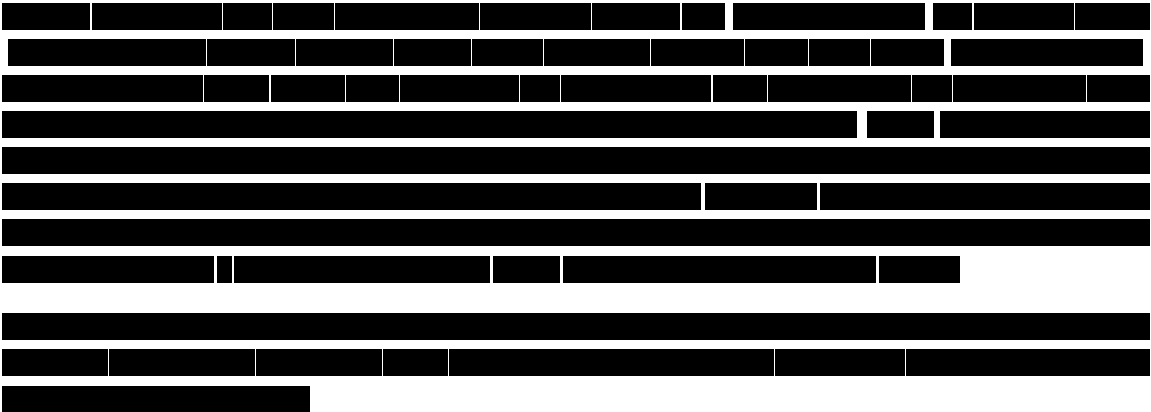


Figure 4.2: Content classified by JLU



4.5 Limitations of protecting concepts

Another issue, except for percolation or finding proper sacrificial materials, is that in theory a stability window gap should form by using sacrificial films. This is schematically shown in Fig. 4.3, using the simulated results of Zhu et al.^[76]. Li_3N , which could also serve as an electrode material, is only stable up to 0.44 V vs. Li/Li^+ . Other promising solid electrolytes, like LPS or LATP are only stable for voltages over 2.28 V and 2.17 V vs. Li/Li^+ , respectively. Thus, there is a stability window gap between the interphase material Li_3N and the solid electrolytes. Whether contacting Li_3N and a solid electrolyte will lead to decomposition of the solid electrolyte or not, is still not clear. It is altogether possible that the interphase products are hindering the growth so that the decomposition

could not be observed. Other unsolved issues are the volume expansion during reaction, voids and insufficient contact of the reaction products.

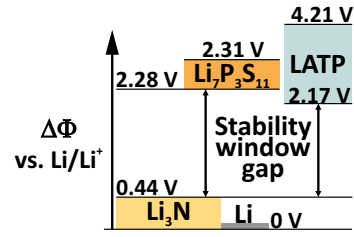


Figure 4.3: Stability window gap diagram. The stability data were taken from Zhu et al. ^[76].

5 Kinetic effects of interfaces under current load – a model case

5.1 Introduction

The stability of solid electrolytes in contact with alkali metal plays an important role for the incorporation of alkali metal electrodes in ASSBs, as already described in section 3 and the interface kinetics will be crucial, too. Beside the resistance increase caused by chemical reactions the transfer between the alkali metal electrodes and the solid electrolyte, either during deposition or dissolution, is of vital importance for the cell function. Space charge layers in the solid electrolyte or SEI for example may hinder the ion transfer^[86,87]. The transfer of ions from one phase to another and the ionization at the interface are thermally activated processes with an activation barrier (activation energy). Other issues are less reported for alkali metal containing cells, but were already studied for Ag/AgX interfaces. An overview is given in the following section. Thus, the results for alkali metal/solid electrolyte interfaces will be compared to the findings for silver metal/solid electrolyte interfaces. The experimental effort to study alkali metal interfaces is higher compared to silver metals, as the handling, storage and cell preparation have to be conducted under inert gas. This might be the most important reason why there are much more reports for silver than for alkali metals.

The difficulties that are described in section 3 for the investigation of interphase formation and solid electrolyte stability are additionally valid for the experimental efforts towards alkali metal dissolution and deposition in all-solid-state systems. Microscopic techniques (SEM, TEM and optical) often fail or could only be used at boundaries (edge between the metal and solid electrolyte) or special cell setups that are far from representing a real battery system. The only exception might be transparent single crystals.

Beside defined interface preparation, effects during metal dissolution and deposition complicate the application of alkali metal/solid electrolyte interfaces. For automotive applications, current densities in the range of a few mA/cm² are required^[127,128]. Thus, current densities between 0.5 mA/cm² and 10 mA/cm² were studied, focused on current densities between 0.5 mA/cm² and 2 mA/cm² according to the results of this section.

In order to study the interface between metal electrode and solid electrolyte the stable ion conductor β'' -alumina was used as model system, as it is already applied in batteries¹. First a literature survey about interfaces between silver, sodium and lithium metal electrodes in contact with the respective solid electrolytes is given. Then, the results of early experiments are shown and discussed in order to define the issues of the interface.

¹In high temperature sodium sulfur cells (with liquid sodium metal).

Further studies required the development of a suitable cell setup that fulfills the requirements generated by the use of soft alkali metals and the results reported in this chapter. This is described in section 5.4. Different techniques to prepare alkali metal/solid electrolyte interfaces are compared and the best preparation technique was determined. The results for pressure dependent galvanostatic experiments are summarized, discussed and connected to the findings in the literature in section 5.5 and 5.6, leading to a quantitative model in the covered parameter range. Cycling experiments were also conducted in order to offer insight into the cyclability and the applicability of the results in this section. The results of this chapter are then summarized and concluded.

The conclusion of this section is that the interface preparation, cell setup and purity of the alkali metal electrodes and solid electrolytes are of vital importance. Drawing a current disturbs the electrode equilibrium, leading to non-equilibrium states at the interface. Deviations from the equilibrium result in time-dependent interface states and non-linear behavior of the system. Consequently, the interface exhibits various effects, which are presented and discussed in this section.

5.2 Literature survey

5.2.1 Silver based interfaces

The interface between silver metal and silver solid electrolytes has been extensively studied in the past. In this chapter an overview about important articles is given that are necessary to explain the behavior of alkali metal based systems in the following sections. An extensive review of works about the interface of silver metal and silver ion conductors is given by Janek^[129].

It is generally acknowledged that the reproducible preparation of incoherent interfaces for kinetic studies is challenging and the preparation of chemically and structurally well-defined interfaces is crucial for kinetic studies^[130]. During galvanostatic experiments, the metal is oxidized at the anode side and reduced at the cathode side.

Considering a non-equilibrium interface, different fluxes j can be formulated, which are schematically shown in Fig. 5.1. During dissolution of metal, metal ions migrate into the solid electrolyte, leading to an increased concentration near the boundary that causes a flux of alkali metal ions j_M from the boundary into the solid electrolyte. The ions might move via interstitial or vacancy sites, depending on the conductivity mechanism and defect type of the solid electrolyte. It follows that vacancies are depleted in the solid electrolyte near the boundary, causing a flux of vacancies towards the boundary (interface). Both, the depletion of vacancies and accumulation of metal ions in the solid electrolyte lead to a relaxation zone ξ_{SE}^{relax} , where defect relaxation (recombination) occurs. The same applies to the metal, where alkali metal ions are incorporated into the solid electrolyte leading to metal vacancy accumulation and likewise metal depletion at the interphase. Thus, a flux j_{V_M} is generated, transporting metal to the interface. Again a relaxation zone ξ_M^{relax} develops^[130].

In the interface or the structural relaxation zone $\xi_{\text{structural}}$ the non-equilibrium defects like pores and vacancies are formed (due to metal dissolution) and annihilated (due to diffusion or plastic deformation)^[130]. Thus, the relaxation of vacancies at the interface controls the interfacial kinetics^[130], as the transport inside the solid electrolyte is often significantly faster.

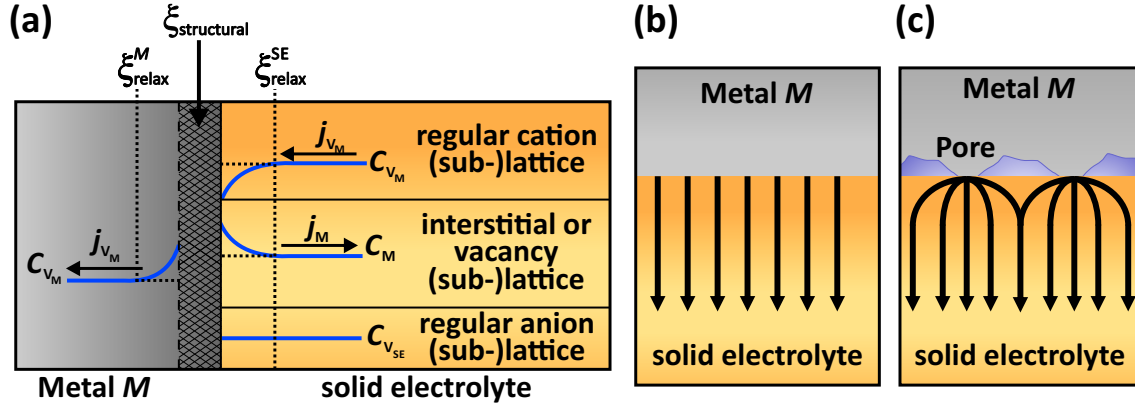


Figure 5.1: Schematic figure to illustrate the interface between a parent metal M and the M^+ conducting solid electrolyte is shown in (a). The concentration gradients are drawn in blue and denoted with C and indices according to the Kroeger-Vink notation. ξ_{relax} denotes the relaxation zones. Modified figure according to Janek and coworkers^[130]. (b) and (c) show the behavior of the fluxes lines before and upon pore (vacancy accumulation) formation, respectively

The dissolution of one metal ion leads to the formation of one vacancy that is injected into the metal^[131]. Due to diffusion, the vacancies may accumulate under formation of pores that lead to a changed metal morphology at the interface and a decreased contact area. This effect is mostly found for high current densities during anodic polarization, where the transport to the interface through diffusion is smaller compared to the transport from the interface (into the solid electrolyte). The morphology change leads to a decrease of contact and a strongly increasing voltage and may also lead to oscillations^[132]. Generally, oscillations depend on the current density, the applied mechanical pressure and temperature. The application of a reference electrode confirms that the oscillations are caused by the anode^[132]. Oscillations are a result of formation and breakdown of pore structures due to the mechanical instability, which was proven by dilatometric experiments^[133] and by SEM of a partially dissolved Ag electrode showing a porous morphology^[132]. Note that SEM experiments could only be conducted as the electrode could be successfully removed from the solid electrolyte without destruction of the morphology and single crystalline electrodes and solid electrolytes with very low roughness were used. Otherwise, the morphology might result from templating of the solid electrolyte surface.

Increasing the pressure above 7 bar, the oscillations disappeared^[132], mainly caused by plastic deformation of the metal^[131]. This is in accordance with the finding that vacancies (and pores) influence the mechanical properties of the metal electrode and that the deformation is accompanied by the formation and diffusion of defects^[131]. According to Fischbach, two processes are rate determining during the dissolution of metal at the interface: the transfer of the metal atom from the electrode to the solid electrolyte and the diffusion of adatoms^[131] (along the pore walls). Screw dislocations also play an important role, as a steady dissolution of metal is maintained, since the re-formation of surface nu-

clei is not required^[131]. Thus, the dislocation density strongly influences the dissolution process^[134]. All processes are occurring simultaneously at different sites, the separation of the different processes by the overvoltage so far was not successful^[131]. According to Janek and coworkers, three processes are occurring at the interface, which were identified by LSV (linear sweep voltammetry) and galvanostatic dissolution experiments: Process one is described as the metal dissolution at small interface areas (with high current densities), whereas the second consist of the transfer of adatoms that are supplied by diffusion along the pore walls. The third process is identified as the decomposition of the solid electrolyte^[130]. According to the findings that lead to oscillations, the bulk diffusion rate of vacancies is not high enough to maintain the interfacial contact area and to deliver sufficient relaxation rates. That is in accordance with the finding that the exchange current density increases with increasing pressure. Thus, the exchange kinetics strongly depends on the mechanical pressure and the plastic properties of metal and solid electrolyte^[135].

According to Rohnke et al., the diffusion of adatoms is the rate determining step in the first sweep of an LSV experiment and in the second sweep the depletion of adatoms is observed due to low formation rates at the pore walls^[134]. Thus, the anodic process mainly occurs at the interface^[134]. Freshly (cathodically) deposited Ag metal shows a memory effect and is dissolved without noteworthy overvoltages^[132,135,136]. An EMF of -3 mV was found between the freshly cathodically deposited silver metal and the counter electrode and a higher activity of cathodically deposited silver is assumed^[135]. The elevated activity is degrading with time, leading again to silver with the properties of the pristine metal. Thus, an aging process was found for cathodically deposited silver^[136].

Especially metal whiskers show high exchange current densities up to 50 mA/cm^2 ^[137]. Whiskers (and dendrites) are often formed when the solid electrolyte is supersaturated with silver ions, resulting in quick precipitation of silver metal in order to release the supersaturation^[138]. At the region of former supersaturation, precipitates with elevated surface energy are formed, e. g. whisker. In addition, the morphology of deposits is voltage dependent^[139], which is in good agreement with the explanations above. Whiskers (and dendrites) may grow into the solid electrolyte^[140], leading to an increased short circuiting probability. By placing both metal electrodes on the same side of the pellet, silver dendrites grow towards the counter electrode, if the solid electrolyte is mixed conducting^[141]. As already stated in section 3 every material shows an electronic conductivity, even if it is extremely small. Thus, this effect surely will also apply for electrodes that were placed on opposite sides of the pellet^[141]. This finding is in agreement with results of Peppler et al., describing that a bipolar electrode, which is not directly electronically connected, is formed due to polarization. The polarization leads to the formation of dendrites at the cathodic and the dissolution at the anodic side of the bipolar electrode. Again the migration speed can be correlated with the voltage^[102], which means that bipolar electrodes are moving faster for higher overvoltages during battery charging and decrease the time until short circuiting.

Bipolar electrodes might be formed by different processes, including SEI formation of metal containing solid electrolytes^[82] (see sections 3.4 and 3.7.2). Other reasons for formation of bipolar electrodes might be internal electrochemical reactions (decomposition) that may lead to metal deposition inside the solid electrolyte (boundary of materials with different transference numbers)^[130].

In order to maintain the contact between the metal electrode and the solid electrolyte, mechanical pressure is applied to the interface, resulting in plastic deformation of the metal. Metals can be described as plastic media with high viscosity. The plastic deformation rate does not linearly change with the mechanical pressure^[142].

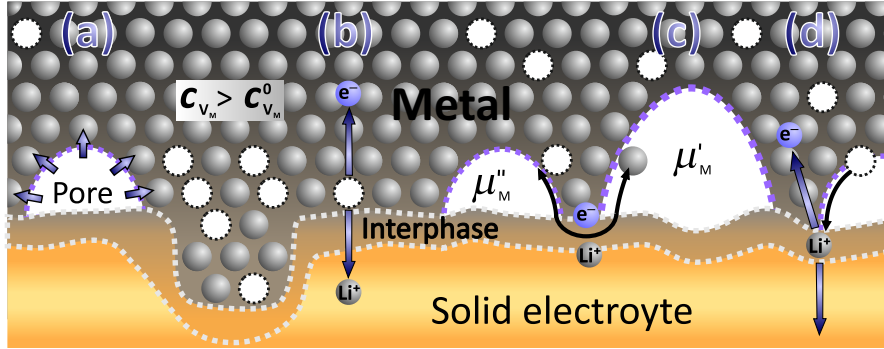


Figure 5.2: Summary of the processes at the interface of a metal and a solid electrolyte during galvanostatic dissolution process. According to Janek et al.^[143].

A summary of the processes that occur at the interface is given in Fig. 5.2. In general the pores are growing during dissolution of metal, which is schematically shown in a. The pores are formed during the initial step of the dissolution process in b, as the vacancy concentration at the interface is increased due to the dissolution. Accumulation of the vacancies then leads to pore formation. In order to minimize the surface energy, a transport between smaller and larger pores through the electrolyte (metal ions) and the metal (electrons) occurs, theoretically leading to pores with the same size² (electrochemical Ostwald ripening^[144]). Along the pore walls, adatoms can then diffuse to a metal column that is still connected to the solid electrolyte and can be dissolved, as seen in d.

5.2.2 Sodium based interfaces

The interface sodium metal/ β'' -alumina was extensively studied for liquid sodium electrodes, as these are used in high temperature sodium sulfur batteries^[38,145]. Beside insufficient wetting of the solid electrolyte, two failure modes are limiting the sodium metal/ β'' -alumina interface. Both are shown in Fig. 5.3. Failure mode³ I consists of liquid sodium metal that fills the pre-existing pores and structural heterogeneities of the ceramic, leading to a path with lower resistance. Thus, sodium metal is discharged at the sodium tips resulting in a flux of sodium metal out of the crack. The following generation of Poiseuille pressure will lead to crack extension. Subsequently refilling and cracking may lead to mechanical failure of the solid electrolyte^[146,147].

Consequently, inhomogeneous deposition may lead to cell failure^[146,147]. For solid sodium electrodes, the freshly deposited sodium metal cannot be removed by establishing a flux, but will surely lead to mechanical strain, too.

Failure mode II degradation is caused by the development (locally change) of partial electronic conductivity in the solid electrolyte, e. g. due to oxygen loss. The gradient of ionic

²Theoretically in this case means that the non-equilibrium state (drawing a current) influences and prevents the adjustment of the equilibrium state and thus will prevent the equilibration of pore sizes.

³The notation was adopted from the literature.

and electronic conductivity causes the internal deposition of sodium metal, which then bends the flux lines and induces strain^[146,147].

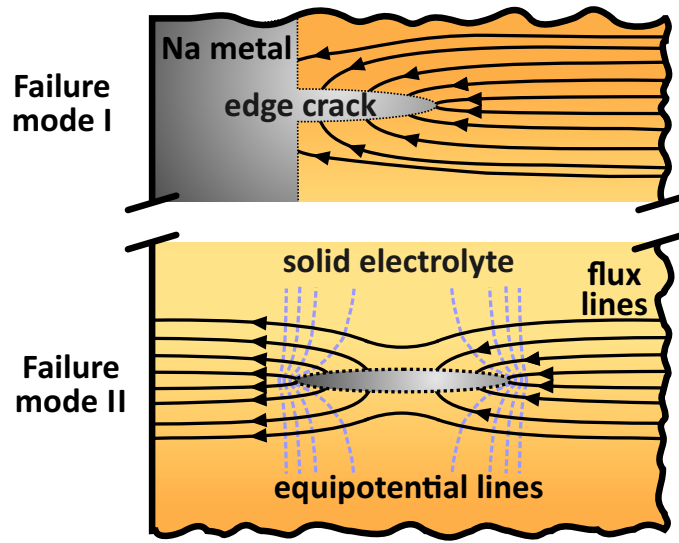


Figure 5.3: The two failure modes for liquid sodium/β''-alumina interfaces according to Virkar and Ansell^[146,147] are illustrated.

In high temperature sodium sulfur cells, the wetting of the solid electrolyte by the sodium metal plays an important role^[148]. Armstrong et al. studied the impedance of a symmetric β''-alumina and liquid sodium cell in the temperature range between 150 °C and 350 °C, finding that for a smooth surface, intimate contact is rapidly formed, whereas rough interfaces lead to poor contacts^[149].

5.2.3 Lithium based interfaces

The interface lithium metal/solid electrolyte has mostly been investigated by cycling only. For this, metal electrodes were placed on both sides and the cell was cycled for one or more current densities (e. g. 0.2 mA/cm² or 4.6 μA/cm²)^[5,150,152–154,159]. In the following survey, the reports that describe the interfacial behavior of the lithium metal electrodes on solid electrolytes are summarized. For interfaces between lithium metal and single crystals of Li₃N, the LSV current density increases with temperature, as the metal is getting softer. Additionally a useful preparation method, by melting and contacting lithium metal and the solid electrolyte is reported^[155]. For investigations of interfaces, mostly microscopic techniques were used. The lithium metal deposition was microscopically studied by a cell consisting of a copper current collector with a viewport on top of a LiPON coated LATP solid electrolyte. For that current densities between 50 μA/cm² to 1 mA/cm² were used. It was found that higher current densities result in smaller precipitations that could be described as adjacent and coalesced islands. For lower current densities, lithium metal grows through the copper current collector due to the formation of rods. During dissolution, hollow rods are remaining^[156]. The growth of lithium metal structures can lead to dead⁴ lithium during dissolution in general, which was investigated by in operando

⁴Lithium metal that can no longer be dissolved as one contact, either to the solid electrolyte or the current collector/electrode, is missing.

TEM with liquid electrolytes^[157]. High current densities suppressed the formation of rods^[156].

Results for microscopy of lithium deposits on LiPON corroborated the findings that higher current densities lead to a decreasing size of lithium metal precipitates. At the beginning of the initial lithium plating, a voltage spike was observed, that was assigned to the nucleation and growth processes^[158].

Morphology changes at the interface of lithium metal and 80-Li₂S–20-P₂S₅ glass were studied in situ by scanning electron microscopy at the edge of lithium metal and the solid electrolyte. Current densities in the range of 0.05 mA/cm² to 1 mA/cm² were used. For high current densities of 1 mA/cm² the deposited lithium metal triggered large cracks (dendrite formation) and led to short circuiting of the cell setup. Lower current densities of 0.05 mA/cm² showed homogeneous deposition of lithium metal^[159].

Devaux et al. observed the partial delamination of lithium metal and polymer electrolyte by x-ray tomography^[160], which is in good agreement with findings for silver metal/solid electrolyte interfaces. As the solid electrolyte is not a free flowing liquid, the vacancies that were formed due to metal dissolution have to be refilled by diffusion. If the discharge rate (current density) is higher than the diffusion rate, voids are formed by vacant sites, leading to a loss of interface contact. High current densities consequently shorten the time until contact loss^[161].

Pressure application to Li/LiI(Al₂O₃)/PbI₂ battery cells led to more pronounced discharge profiles, as the plateau is only seen at pressures higher than 400 kg/cm². Still contact loss and cell failure occurred^[162]. Meyer et al. concluded that contact between lithium metal and Li₃N is decreasing due to a hysteresis observed during CV experiments. Improved contacting was seen for cathodically deposited lithium metal according to linear behavior of LSV curves that directly corresponds to the ohmic resistance^[163]. Additionally, the application of pressure should suppress dendrite growth^[164].

The development of dendrites and short circuits was mentioned before in this section and the following studies are focusing on dendrite formation and prevention. It is generally acknowledged that homogenous solid electrolytes with a shear modulus of at least 6 GPa will prevent dendrite formation^[165,166]. As the lithium metal electrode shrinks by several µm during dissolution, adhesion between the metal electrode and the solid electrolyte is not maintained if the solid electrolyte is a simple solid with a modulus of 6 GPa. The efficiency of adhesion is strongly decreasing when the modulus exceeds a few MPa. Polymer electrolytes showed no hint of delamination and dendrite formation for current densities of 0.17 mA/cm²^[166]. But neither did the solid electrolytes (for low current densities).

Garnet type materials are often believed to be optimal lithium solid electrolytes. Thus, experiments with symmetric Li/Nb-containing garnet/Li cells and current densities between 0.2 mA/cm² and 1 mA/cm² (for 10 s) were conducted, resulting in plateaus with gradually increased overvoltage. A current density of 0.5 mA/cm² led to short circuits after 280 s, but no short circuits were observed for a current density of 0.1 mA/cm² after 41 h^[85]. This is in good agreement with the results of Ren et al. who investigated the dendrite formation for LLZO. Again current densities of 0.5 mA/cm² resulted in short circuiting due to dendrite formation along grain boundaries. Dendrite formation was observed via a strong voltage drop during the galvanostatic experiment and via dark spots in the SEM pictures^[167]. Sudo et al. reported short circuiting after 1000 s for current densities of 0.5 mA/cm² due to dendrite formation^[168].

The dissolution and deposition of lithium metal on a garnet type solid electrolyte was studied by Kotobuki et al., using current densities between 0.01 mA/cm² to 0.05 mA/cm². The voltage strongly increased after 550 s and 90 s for the current densities of 0.02 mA/cm² and 0.05 mA/cm², respectively. For 0.01 mA/cm² a stable plateau (no voltage increase) was observed for 10 minutes^[169]. It is reported that dendrite formation could be prevented by densifying the solid electrolytes, shown for LLZO^[170].

5.3 Plating and stripping of sodium metal

In order to investigate the interface of sodium metal and β'' -alumina, current densities in the technological relevant range were applied^[127,128] (in the range of 0.5 mA/cm² to 2 mA/cm²). Higher current densities were also applied; the limitations are shown in section 10. As β'' -alumina is one of the few stable solid electrolytes (see section 3.8.1), interphase growth will not interfere with the experiments and thus will facilitate the direct investigation of the interface. The basic experiment consists of the application of two sodium metal electrodes onto the electrolyte pellet and the conduction of a galvanostatic experiment afterwards. In order to distinguish the influence of the working and counter electrode on the voltage behavior, a reference electrode was applied in order to separate both contributions. The result can be seen in Fig. 5.4, showing that the reason for the increasing voltage will be found at the working electrode, as the voltage for the counter electrode is not increased and smaller than 0.1 mV. Thus, the stripping process is responsible for the voltage increase.

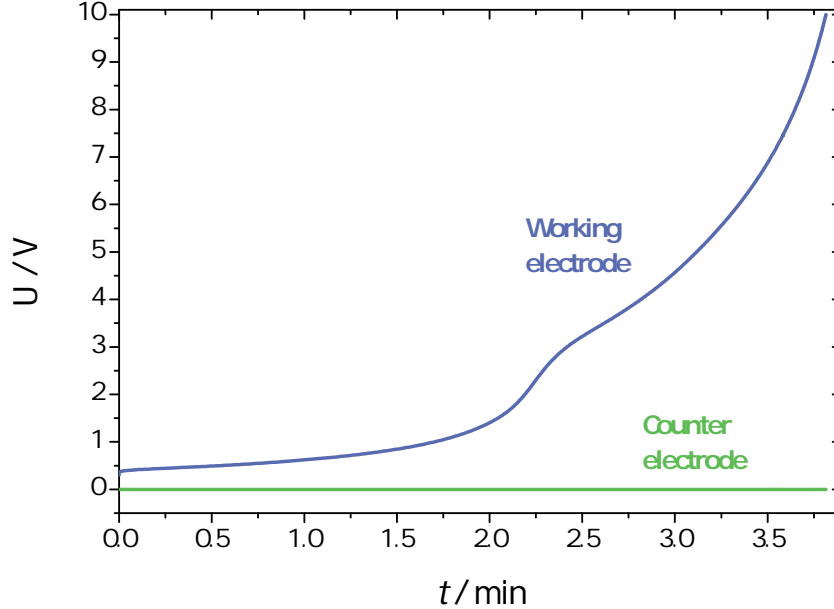


Figure 5.4: Galvanostatic experiment for a symmetric Na metal/solid electrolyte cell with application of a reference electrode is shown. External pressure was not applied and a current density of 1 mA/cm² was chosen.

Fig. 5.4 illustrates that the cell resistance is increasing, as the voltage is rising during the application of constant currents⁵. To find the reason for this, pressure dynamic gal-

⁵Beta-alumina was reported to be stable up to at least 50 V^[174].

vanostatic experiments were conducted. For this, a suitable setup is required, as sodium and lithium metal are very soft materials^[171], so that a few precautions are needed, which will be described in the next section. Under the given assumptions that the voltage is increasing due to contact lost (pore formation due to accumulation of vacancies)^[130,131] is correct, plastic deformation of the metal electrode will increase the transport rate towards the interface. As already described in the introduction, microscopic techniques are often not applicable. Proofs for this are given in section 10, where the morphology of the sodium metal electrode after dissolution might be explained by pore formation due to the dissolution process or the templating of the solid electrolyte morphology.

5.4 Cell setup for proper interface characterization

Sodium and lithium metal exhibit very low Brinell hardness values (0.5 and 0.07⁶)^[171] and are therefore easily deformed, which may lead to maintaining the contact area. By the application of pressure without confining the electrode area, the electrode area is increased which directly leads to a decreasing cell resistance. This issue was solved by insulating PEEK (polyether ether ketone) barriers.

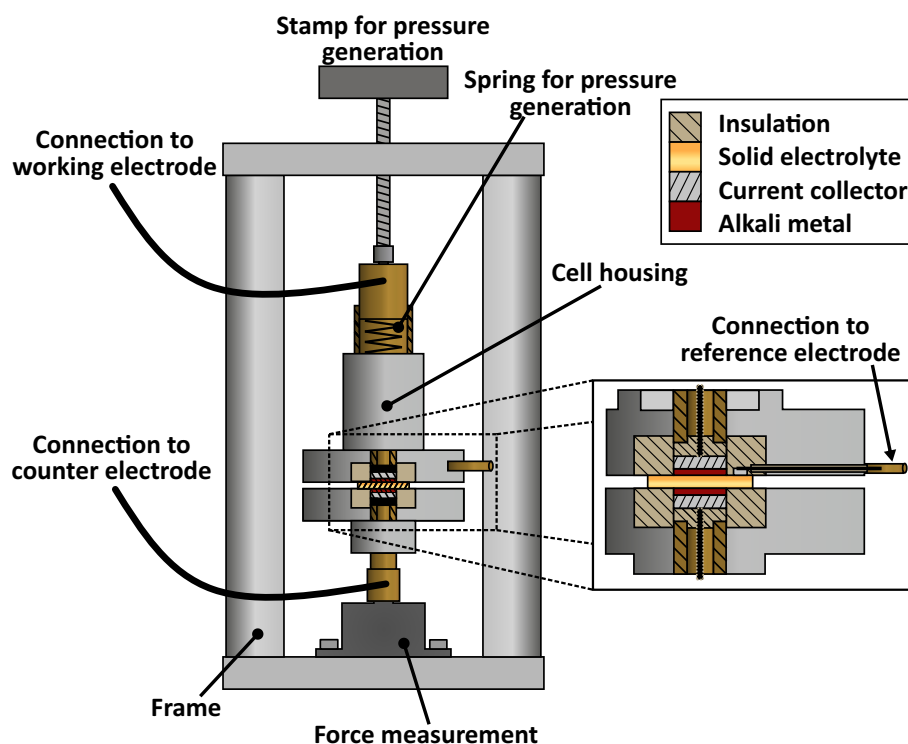


Figure 5.5: The setup for the pressure dependence of galvanostatic plating and stripping of alkali metal electrodes is displayed. The inset shows a magnification of the cell housing.

Furthermore, the void between the table track and pressure applying stamps should be wide enough so that the pressure is not influenced by friction, but small enough that the alkali metal is not pressed into the void. The first will show higher pressures compared to

⁶The unit is not given. The historical and more common unit would be kp/mm^2 (kilopond) and the SI conform unit N/mm^2 .

the pressure that is actually applied to the electrode and the latter will strongly decrease the pressure through decreasing the amount of alkali metal of the electrode. In addition, the incorporation of alkali metal into the void will also increase the friction between the pressure stamp and the table track. Thus, an optimum value of the gap width was found and applied to the setup and to other compressible cell setups. A sketch of the cell setup is shown in Fig. 5.5. The setup was used in an argon filled glove box and therefore a load cell⁷ was used instead of a direct pressure determination, as ambient (air) pressure changes do not influence the force values. The pressure is then obtained by combining the force data with the constant electrode area. The force is generated by a spring that is compressed by screwable stamp and either directly applied to the electrode or with the assistance of the frame. The frame, the spring and the cell housing were built of metal because of the mechanical stability requirements (and the relatively strong forces).

To prevent short circuiting of the cell, the current collectors are insulated with a mechanically and thermally robust plastic (PEEK) and connected to the bridge circuit via a cable. A second insulation was incorporated in order to insulate the solid electrode, the alkali metal electrode and the cell housing. Again, robust plastic was used. Reference electrodes are incorporated next to the working and counter electrodes due to the difficulty to prepare reference electrodes inside the solid electrolyte⁸. This setup was then additionally used for the instability investigations in section 3 and for the pressure dependent measurements under current load (in this section and section 6).

5.5 Interface formation between sodium metal and beta-alumina

The knowledge of interface formation between alkali metals and solid electrolytes is generally small; often vapor deposition techniques were used. Here, different contacting methods were used and evaluated by the slope of the current-voltage curve for small overpotentials, yielding the polarization resistance, as shown in Fig. 5.6a. For this, a finite element method (FEM) analysis was conducted in order to correct the voltage for the IR-drop (see section 10). The vapor deposited electrodes showed the worst contact properties for sodium metal, for lithium metal this technique is reported to guarantee improved contact^[33]. Reason for this might be insufficient wetting or dewetting^[148]. By direct cold pressing of sodium metal electrodes onto the solid electrolyte, the contact is slightly improved compared to the vapor deposition process.

The hot pressed electrode/electrolyte contacts show a more than two times lower polarization resistance after cooling that is comparable to electrochemically deposited sodium metal. This finding is surprising as freshly deposited sodium metal should exhibit the lowest polarization resistance^[135,136].

Fig. 5.6b displays the Nyquist plots for gold and sodium electrodes on β'' -alumina, respectively. Generally, the used β'' -alumina exhibits a pellet resistance of 200 Ω at maximum. As the semicircle for the charge transfer (polarization) resistance is merged with the pellet resistance, the charge transfer resistance could only be distinguished to be in the range of 45 Ω , reasons for this might be space charge layers^[87] or sodium oxide contaminations of the sodium electrode surface.

⁷In order to determine the force applied to the electrodes.

⁸Either the solid electrolyte was too hard or too brittle.

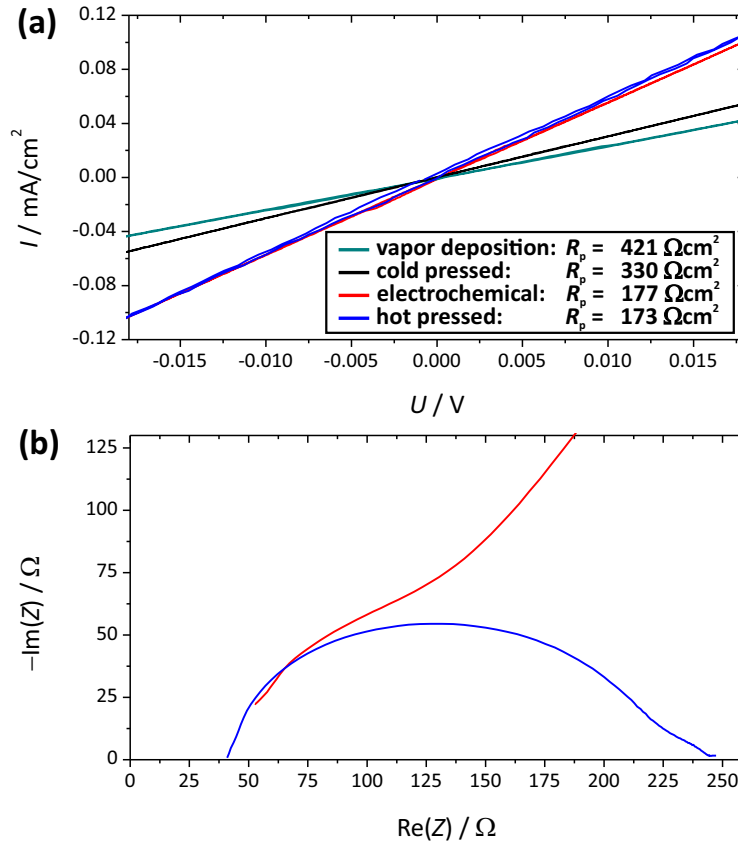


Figure 5.6: The current/voltage curves for cells with differently prepared electrode-electrolyte contacts are shown in (a). In (b), the Nyquist plots of a solid electrolyte with gold and sodium electrodes are displayed for comparison. All data were recorded without externally applied pressure and at room temperature.

Thus, the hot pressing method is a fast and effective method for the preparation of suitable contact between alkali metal electrodes and solid electrolytes. Using this contacting method, the pressure dependence of the alkali metal/solid electrolyte interface under galvanostatic current load was investigated and is discussed in the following section.

5.6 Pressure dependence of metal/solid electrolyte interfaces – an overview

The interface of the sodium metal/solid electrolyte was prepared by the hot pressing technique described in the last section. To get a first overview about the pressure dependence, a constant current was drawn for 20 min, the pressure was stepwise increased and the effect on the voltage was observed. The results for $0.5 \text{ mA}/\text{cm}^2$, $1 \text{ mA}/\text{cm}^2$, $1.5 \text{ mA}/\text{cm}^2$ and $2 \text{ mA}/\text{cm}^2$ are shown in Fig. 5.7a, b, c and d, respectively. Thus, significantly higher current densities were used compared to the literature^[156,159]. Fig. 5.7 serves also as a proof for the proper function of the cell setup.

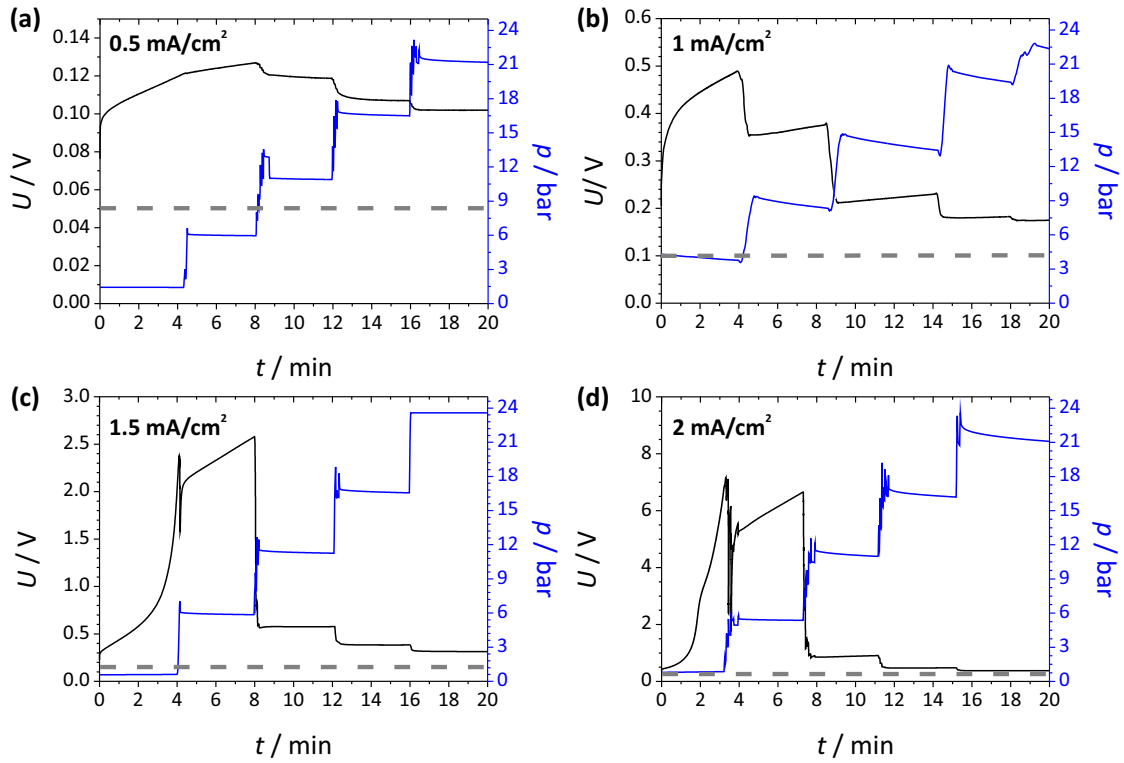


Figure 5.7: The results for pressure dependent galvanostatic measurement (at room temperature) for current densities of 0.5 mA/cm², 1 mA/cm², 1.5 mA/cm² and 2 mA/cm² are displayed in (a), (b), (c) and (d), respectively. The theoretical voltage drop caused by the pellet resistance is shown in dashed gray and the pressure in blue.

For a current density of 0.5 mA/cm², which corresponds to a dissolution rate of 75 nm/min, the overvoltage is more than two times higher than calculated alone from the pellet resistance. The voltage increase in Fig. 5.7a is relatively small and is further decreased by application of pressure, leading to almost no slope after the mechanical pressure exceeds 9 bar. Likewise the overvoltage is decreasing as the pressure is increased. By setting the current density to 1 mA/cm² (dissolution rate of 150 nm/min), the initial voltage is more than 3 times higher than calculated for the pellet resistance. This time, the resistance increase is notably higher compared to smaller current densities. By increasing the pressure, the voltage is erratically decreased and the slope is getting smaller. Further pressure increase leads to smaller erratic voltage steps and changes for the slope. Thus, the changes for pressures larger than 22 bar are very small.

The increase of the current density to 1.5 mA/cm² and 2 mA/cm² (dissolution rates of 225 nm/min and 300 nm/min) leads to even higher voltage slopes and the strongest effect is seen for the first pressure increase. Further pressure increase only leads to smaller voltage decreases, again approaching a limiting value. Note that the pressure is fading after adjustment due to plastic deformation of the alkali metal. In order to show that the pellet conductivity is not influenced by the pressure (caused by lattice comprising)⁹, pressure dynamic impedance experiments were carried out. Using blocking gold electrolytes, the Nyquist plots are not influenced by the pressure in the given pressure range, like shown

⁹This effect should not occur in this pressure range.

in section 10.

Thus, the application of pressure on the interface between sodium metal electrode and β'' -alumina leads to a remarkable voltage decrease. Reason for this is obviously the depletion of vacancy accumulates (e. g. pores) by plastic deformation of the metal electrode. Regarding the data with and without applied pressures, it can be assumed that the plastic deformation becomes the more dominant interface relaxation process. The interface morphology exhibits some kind of self-healing, observed by resting experiments after dissolution that lead to a decreasing resistance. Nevertheless, drawing a current after relaxation results in a strongly increasing voltages and resistances and the termination criterion was abruptly reached (see section 10). It can be concluded that the self-healing rate is negligible compared to plastic deformation relaxation processes.

Oscillations could be observed, too, as displayed in section 10. However, the oscillations could not be reproduced and were found for different and randomly chosen parameters (in a relatively small current density and pressure range). The results in Fig. 5.7 also hint that the lowest voltage value is approximately two times higher than the IR-drop of the pellet. In the next section, a detailed look and quantification of the results will be shown and discussed.

5.7 Pressure dependence of metal/solid electrolyte interfaces – a detailed study

In order to investigate the pressure dependence in detail, impedance spectroscopy measurements were carried out before and after galvanostatic experiments. The voltage-time diagrams for current densities of 0.5 mA/cm², 1 mA/cm², 1.5 mA/cm² and 2 mA/cm² in dependence of the mechanical pressure and the corresponding Nyquist plots are shown in Fig. 5.8. For a current density of 0.5 mA/cm², the voltage increase is relatively low for the pressureless measurement. By increasing the pressure, the voltage is strongly decreased for pressures between 0 bar and 9 bar, afterwards only very small changes are observed. This is in good agreement with the results described in the previous section. The Nyquist plots after end of the sodium metal dissolution process exhibit a notably larger extent, the overall resistance is nearly doubled. A summary of the interface resistances obtained by fitting the impedance data with the equivalent circuit shown in the inset of Fig. 5.8a will be given later. The impedance data suggest that the contact area between the sodium metal electrode and the β'' -alumina pellet is decreased during cycling. The initial cell resistance is reobtained by application of raised pressures for 2 min to 5 min (depending on the applied pressure), which supports the hypothesis. By increasing the current density to 1 mA/cm², displayed in Fig. 5.8b, the voltage slope is increased and exceeds 2 V after 10 minutes, corresponding to a 1.5 μ m thick dissolved sodium metal film. The voltage slope (voltage change divided by the time) is strongly decreased with increasing pressure and remains constant for pressures above approximately 6 bar. This finding is supported by the impedance data in Fig. 5.8b. Without pressure the overall resistance is strongly increased to more than 1400 Ω . The application of the pressure decreases the resistance increase. The same behavior can be observed for 1.5 mA/cm² and 2 mA/cm², but the resistance increase is obviously larger without the application of pressure.

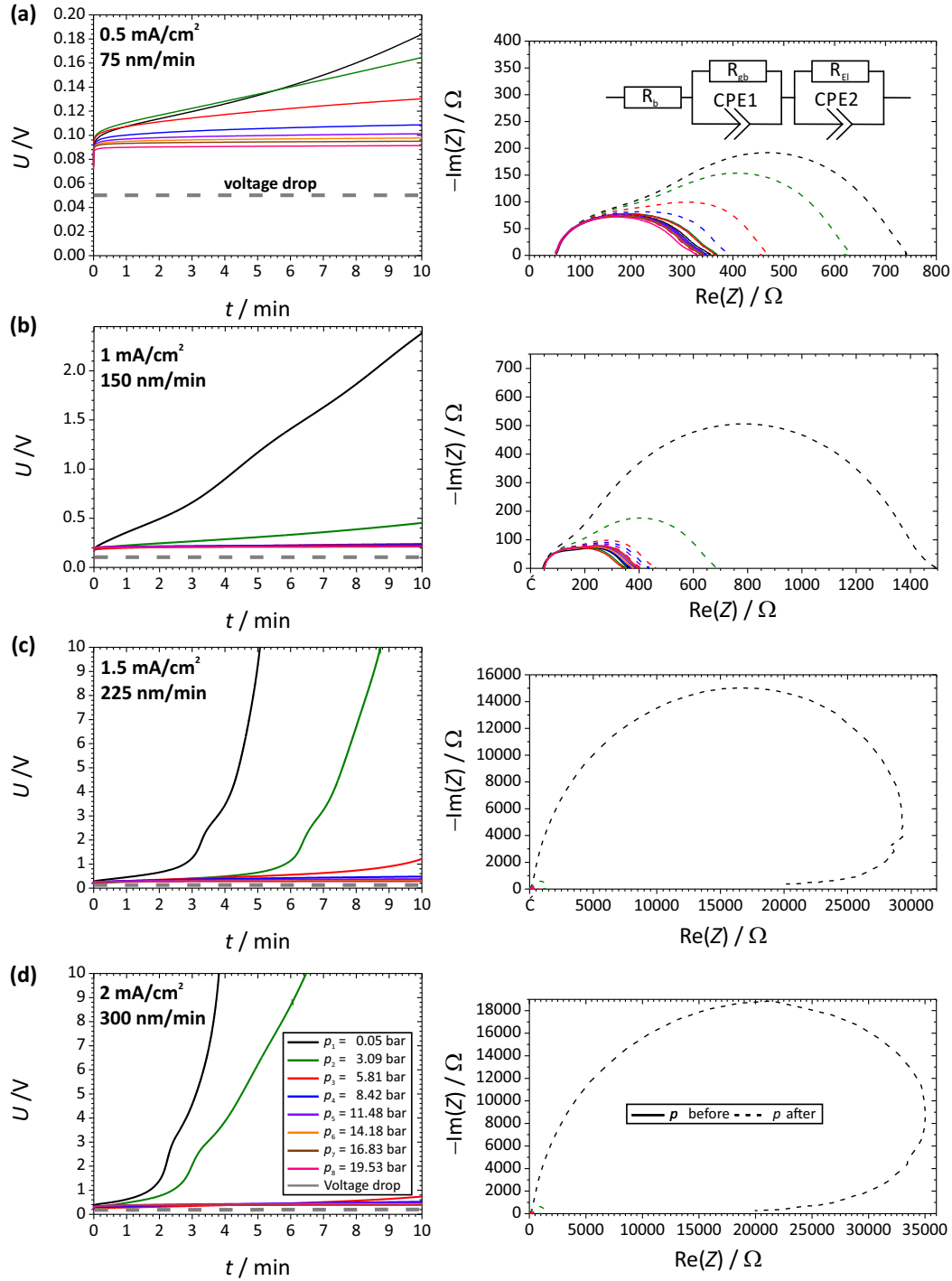


Figure 5.8: The pressure dependent galvanostatic measurements and the corresponding Nyquist plots before and after the measurement are displayed for current densities of 0.5 mA/cm^2 , 1 mA/cm^2 , 1.5 mA/cm^2 and 2 mA/cm^2 in (a), (b), (c) and (d), respectively. For 1.5 mA/cm^2 and 2 mA/cm^2 , the initial resistances and values for high pressures are showing similar behavior as for 1 mA/cm^2 , but are hidden due to the excessively high resistance after the pressureless experiment.

Fig. 5.8 also shows that higher current densities lead a enhanced overvoltage increase, which might be explained with a higher number of vacancies, increased pore volume and a lower contact area. This results in higher voltage slopes and higher resistance values at the

end of the experiment. The Nyquist plots in Fig. 5.8 also show that the initial interfacial state of the interface could be approximately reobtained (with small deviations to higher and lower values) after each cycle of the experiment, even for higher current densities. Thus, it can be assumed that the resistance increase is only caused by the morphological changes of the interface. For current densities of 1.5 mA/cm² and 2 mA/cm², the Nyquist plots in Fig. 5.8 also show a snail like behavior at low frequencies, which is attributed to the interface relaxation (diffusion or deformation).

In the galvanostatic experiments in Fig. 5.4 and 5.8 a characteristic slope change (peak) is observed for all measurements where the externally applied mechanical pressure is not exceeding the border value of approximately 6 bar. This finding may be caused by two different diffusion processes, which will be revisited later on. It should be mentioned that dendrites and short circuiting were not observed in this pressure and current density range. Galvanostatic experiments were also conducted for higher current densities. One example for 10 mA/cm² is shown in section 10, showing that the pressure is not sufficient to maintain the interfacial contact.

In order to obtain quantitative understanding of the process it is assumed that the only changes that are responsible for the resistance increase are the accumulation of vacancies and the resulting contact loss (decrease of contact area). Thus, the contact area is normalized to the maximal macroscopic¹⁰ contact area, which is believed to be established at the beginning of the measurement. The area changes for four different current densities are shown in Fig. 5.9a. For a current density of 0.5 mA/cm² and without the application of a pressure, the area is decreasing to the half of the initial value. By increasing the pressure, the contact area at the end of the measurement is increased and remains nearly constant for pressures up to 12 bar. The same applies to the other current densities, but the area is strongly decreased for measurements without pressure. Applying pressure to the interface slowly increases the contact area preservation, for higher current densities a pressure of at least 20 bar is required. The thicknesses of dissolved sodium metal for current densities of 1 mA/cm², 1.5 mA/cm² and 2 mA/cm² for 10 minutes are 1.5 µm, 2.25 µm and 3 µm, respectively, which correspond to a capacity of 0.32 mAh/cm² for a current density of 2 mA/cm².

The development of a model for the pressure dependent galvanostatic cyclization is challenging, as a quantification of transported material (by plastic deformation, metal) is not reported so far. Furthermore, the use of polycrystalline sodium metal and solid electrolytes complicates the model. Nevertheless, the data in Fig. 5.9a could partially be fitted using an asymptotic function (in equation 5.1) and under disregard of the first two to three data points.

$$A = A_0 - b \cdot a^p = 0.502 \text{ cm}^2 - b \cdot 0.779^p \text{ cm}^2 \quad (5.1)$$

A_0 , b , a and p denote the initial contact area, the response range, the rate and the pressure. The first two to three data points may show a linear behavior. Fitting of the data points in Fig. 5.9a leads to the curves in Fig. 5.9b, the equation is displayed in the inset. As expected, the asymptote corresponds to the initial interface area. Surprisingly, the rate was found to be 0.779 for all four current densities, only the value of the response range b is changing. In order to show the change of the response range as function of the current density, the diagram in Fig. 5.9c was obtained. There, a linear behavior might

¹⁰The microscopic contact area might be different.

be seen, only the value for 1 mA/cm² does not match the progression. Fitting the data with and without the b -value for 1 mA/cm², the intercept is approximately zero and the slope ranges between 0.79 cm²/mA and 0.74 cm²/mA. Using 0.74 cm²/mA for the slope and the assumption that the linear region is also valid for higher current densities, the pressure that is required to maintain 95 % of the contact area is simulated for current densities up to 100 mA/cm². The results are shown in Fig. 5.9d. Even for small current densities of 0.1 mA/cm² a pressure of approximately 5 bar is required to maintain proper contact. For higher current densities of 100 mA/cm² pressures above 30 bar are required. Unfortunately, this pressure range was hardly accessible in the experiments due to the lack of proper springs. Other pressure generating devices could easily reach this range but the exact pressure adjustment is extremely challenging¹¹. Thus, the assessment in Fig. 5.9d might at least offer insight into the required pressure ranges. In the range that was investigated in this work, the simulated data perfectly fit the experimental results, as expected.

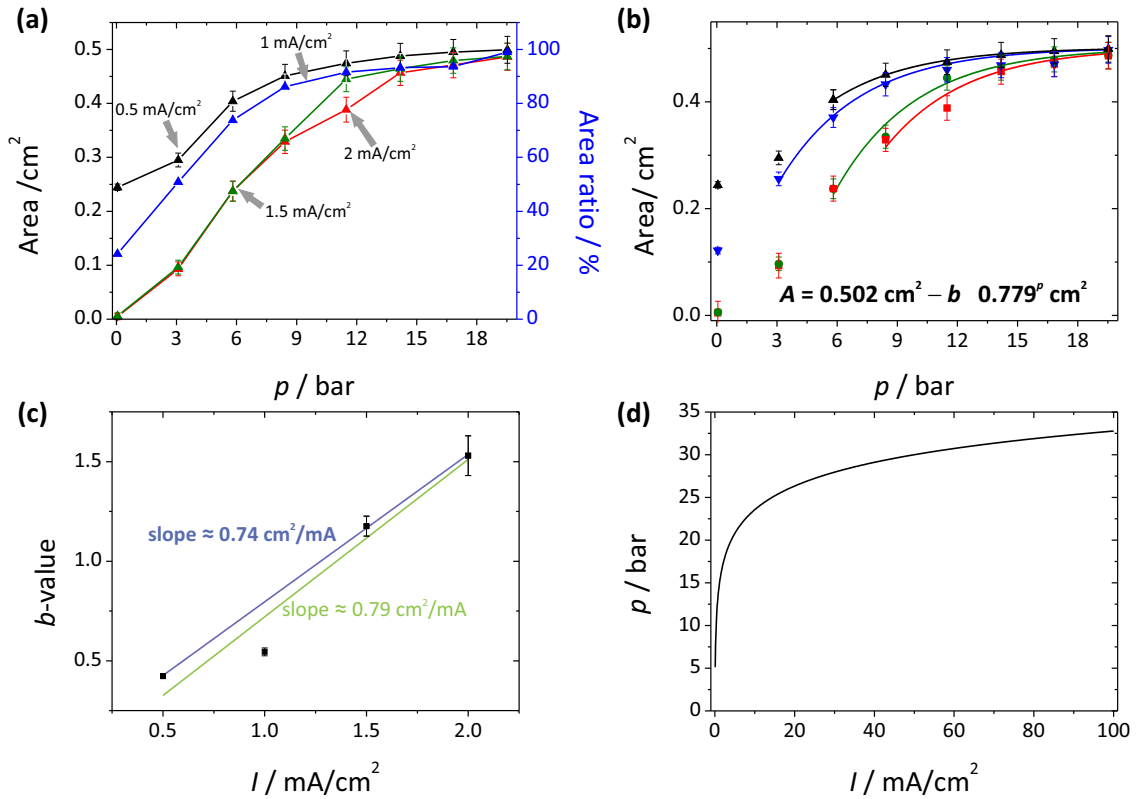


Figure 5.9: The calculated area changes in dependence of the pressure are shown without and with the fit results in (a) and (b), respectively. In (c), the response range value b is plotted against the current density and the slopes are directly given in the figure. According to the results in (c) the current density dependence of the pressure that is required to maintain 95 % of the contact area is drawn in (d).

Summaries of the average voltage slope (dU/dt) and the overvoltage (voltage corrected for the IR-drop of the solid electrolyte) are displayed in section 10. Both are approaching limiting values of 0 V/s and two times the calculated value for the IR-drop (in good agreement with the finding that the voltage seems to be at least twice as large as the IR-drop).

¹¹Pressure determination is challenging, too, as pressure detectors, which were designed for higher pressures, show a critical inaccuracy (and sometimes negative values).

To illustrate the influence of the pressure on the cyclability, linear sweep voltammetry (LSV) was conducted at four different pressures. The results are displayed in Fig. 5.10, showing that the pressureless interface exhibits a maximal current density of approximately 2 mA/cm², whereas the application of higher pressures increases the current density. Two different processes can be seen in the LSV, both are marked (with I and II, respectively). These processes might be correlated to findings for Ag/AgX single crystal experiments^[130]. Process one (I) is described as the dissolution of metal at small interface areas and process two (II) by the diffusion of adatoms. Finding two processes corresponds well with the observation of the slope change (peak) in the galvanostatic experiments.

Increasing pressure then leads to the domination of one process (I) that might cover the minor one (II). By increasing the pressure to 5.76 bar, the maximal current density is nearly doubled. Further pressure increasing leads to higher current densities that are not doubled. At a pressure of 16.92 bar, the LSV exhibits nearly ohmic behavior. The theoretical ohmic behavior is drawn in red. Thus, the pressure obviously improves the contact between sodium metal electrodes and solid electrolytes. The CV in Fig. 5.10 also leads to a good estimation of the maximal usable current densities, hinting that higher current densities might be possible. By decreasing the electrolyte thickness (and therewith the resistance) even higher current densities might be applied. Unfortunately, higher pressures and voltages above 2.5 V lead to short circuiting of the cell, the current density sharply increases to values of several A/cm². Reason for this might be Mode II degradation processes^[146,147] or whisker and dendrite growth through and around the β'' -alumina pellet¹². Galvanostatic experiments for lower current densities do not show a strong pressure dependence compared to higher current densities.

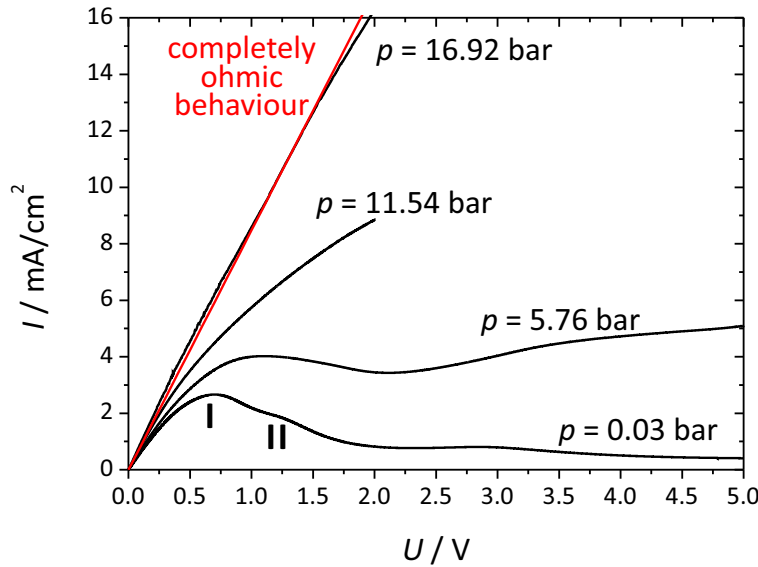


Figure 5.10: The pressure dependent LSV measurements and the simulation of ohmic behavior are displayed for comparison.

In order to evaluate the overvoltage as function of the current density without contact area loss effects, transition current experiments were carried out. The results are displayed in

¹²This is actually observed for high current densities

Fig. 5.11a.

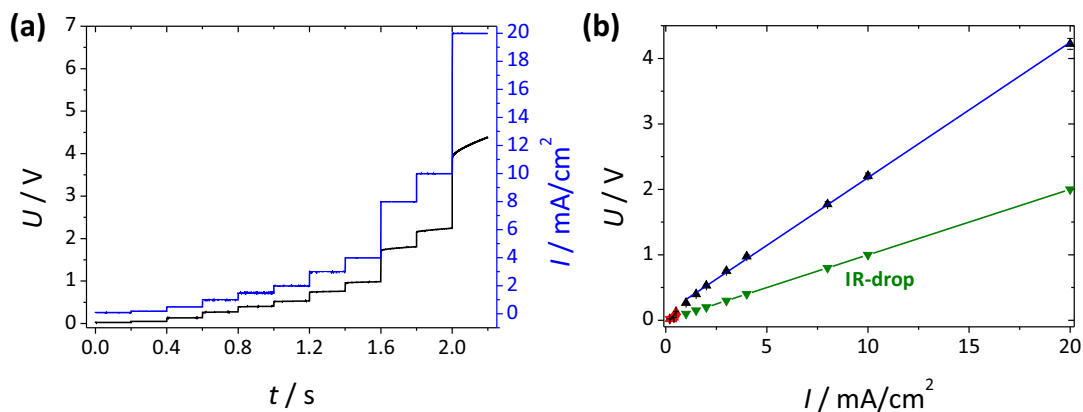


Figure 5.11: The results of the transition current experiment are displayed in (a) and (b) shows the fit of the data obtained for this technique.

Therefore, current densities between 0.25 mA/cm^2 and 20 mA/cm^2 were used, showing that the voltage to maintain the current densities are smaller than 1 V for current densities up to approximately 4 mA/cm^2 . By drawing the voltage of the data in Fig. 5.11a against the current densities, a linear dependence is observed, which is shown in Fig. 5.11b. Using the slope determined from Fig. 5.11b, a starting resistance of $207 \Omega \text{ cm}^2$ is found for the β'' -alumina pellet that is two times higher than calculated for the pellet resistance. This finding is in accordance with the findings in Fig. 5.7, that the voltage is approximately two times higher than the theoretical IR drop.

The reason for this might be sodium oxide contaminations of the metal electrode. Photoelectron spectroscopy experiments show that even high pure and properly stored¹³ alkali metal and freshly prepared electrodes are oxidized at the surface. Another cause might be the polarization resistance of the interface and space charge layers^[87].

5.8 Simulation of battery cycling and its effect on the alkali metal electrodes

In batteries, the deposition and dissolution of alkali metal will take place during use and thus, cycling experiments with focus on the alkali metal electrode were conducted in order to simulate the cycling of a real battery, without the effects caused by positive electrode materials. Cycling without pressure is shown in Fig. 5.12a for a current density of 1 mA/cm^2 . The initial dissolution of sodium metal leads to a relatively strong voltage increase, in good agreement with the results in the section before. However, all following cycles show that the voltage is not increasing and stays constant. Reason for this might be that the freshly deposited sodium metal can be dissolved without noteworthy overvoltage, like it is found for silver/AgX interfaces^[132,135,136]. The results for a simple reversion of polarity experiment is shown in section 10, corroborating the findings in this section. Fig. 5.12a also shows a spike at the beginning of the second cycle, which can be attributed to the initial plating/deposition process, according to Sagane et al.^[158].

¹³For example in a glove box. However, alkali metals are even reacting with oxygen traces in UHV chambers.

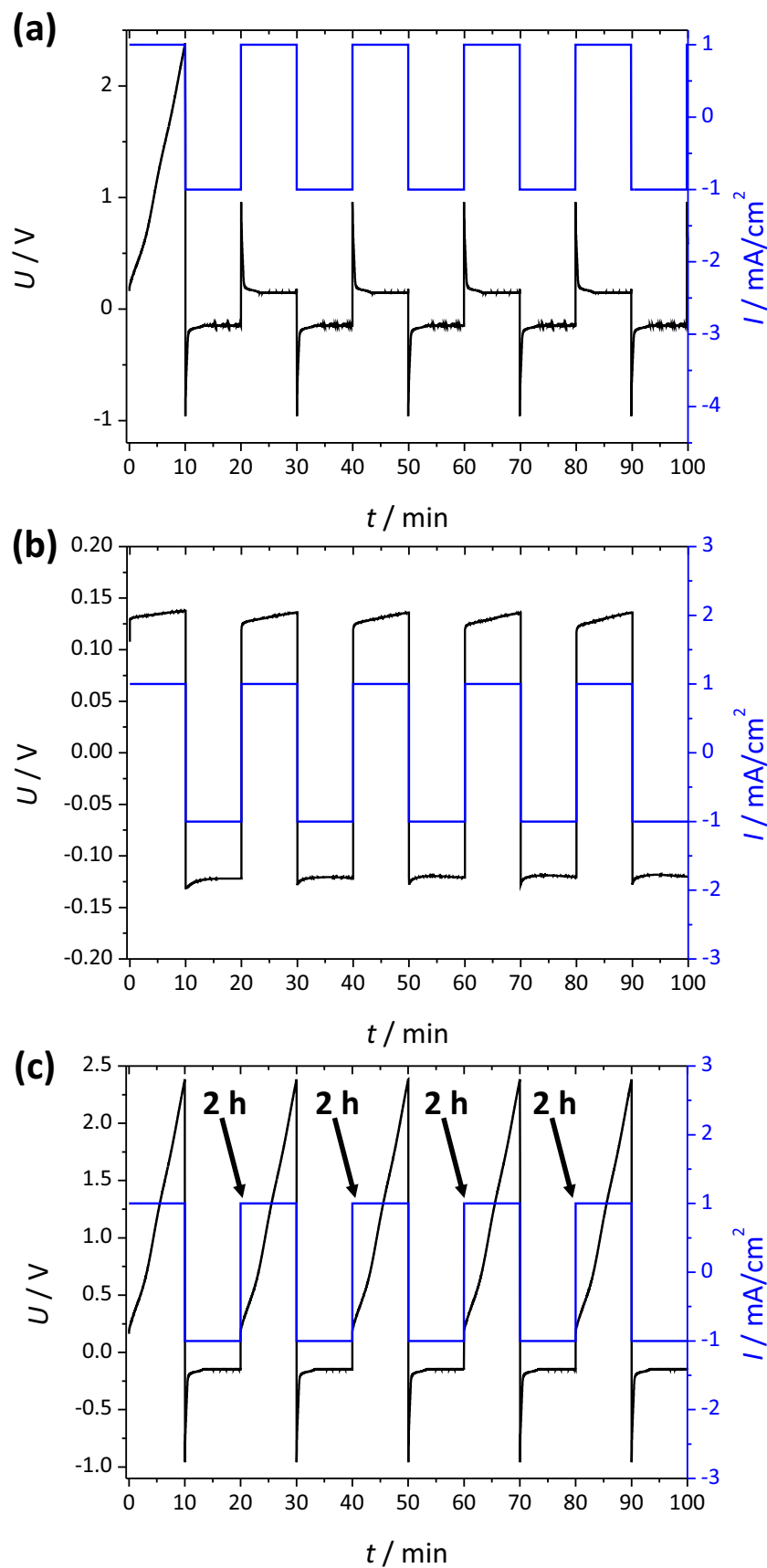


Figure 5.12: Cycling (at room temperature) of a symmetric Na/ β'' -alumina/Na cell without (a) and with (14 bar) (b) the application of pressure is displayed. In (c) the cell rested for 2 h between the cycles.

This finding might be interpreted such that no pressure is required after the initial formation cycle. Results in Fig. 5.12c show that this effect is vanishing with time, again leading to a voltage increase during cycling. The relaxation of freshly deposited sodium metal is in agreement with results for silver^[136]. The application of a certain pressure (around 14 bar) prevents voltage increase, which is shown in Fig. 5.12c. The results also clearly show that the freshly deposited sodium metal might be unaffected by pressure application. In order to clarify this hypothesis, sodium metal was deposited with the halved current density for 10 minutes and then the polarity was reversed with a current density of 2 mA/cm², so that the previously deposited sodium metal is now dissolved again. During cycling the pressure is stepwise increased, like displayed in Fig. 5.13. The voltage is generally low for this current density and unaffected by the pressure. After the initial deposited amount of sodium metal is consumed, the voltage is not increasing due to the high pressure that is applied. Thus, the freshly deposited sodium metal can be dissolved without the application of pressure.

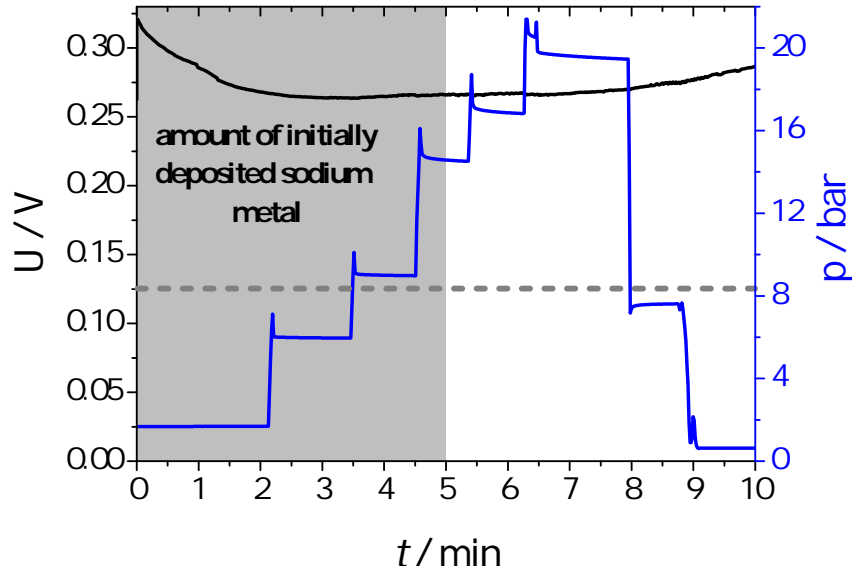


Figure 5.13: Pressure dependent dissolution of initially deposited sodium metal is displayed. The initially deposited amount of sodium metal is marked with gray.

It is shown that the pressure is a crucial parameter for the cyclization of alkali metal containing ASSBs and only pressure application enables the proper cycling of sodium metal electrodes during long time cycling.

Fig. 5.14 displays the result for a current density of 1 mA/cm² and a minimal pressure of 16 bar. An approximately 500 μm thick sodium metal electrode¹⁴ was almost completely dissolved and deposited, respectively. The voltage increase at the end corresponds to contact loss due to the completely consumed sodium metal. Calculation of the capacity leads to a value of approximately 50 mAh/cm².

¹⁴Determination of thicknesses of soft alkali metals is cumbersome and leads to uncertainties in the range of tens of μms .

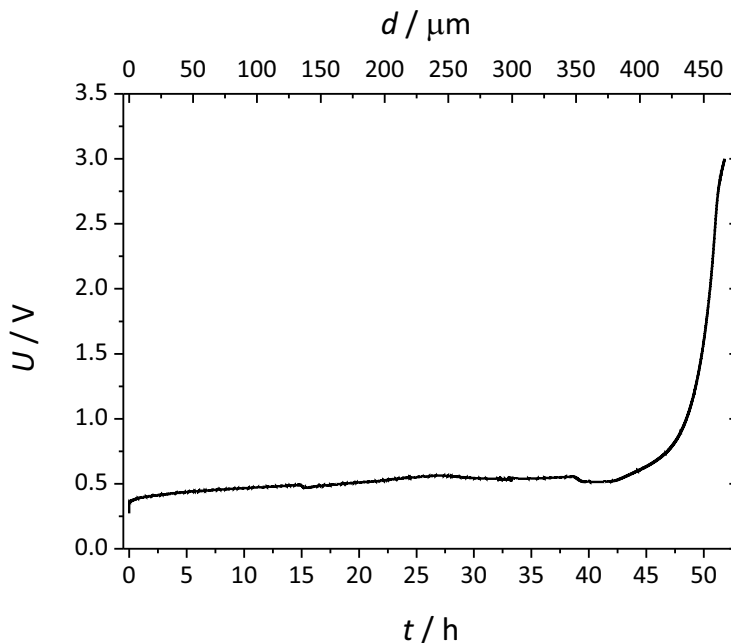


Figure 5.14: The dissolution of a 500 μm thick sodium metal electrode by application of a pressure of 16 bar and a current density of 1 mA/cm^2 at room temperature.

5.9 Summary and conclusion

Generally all results in this section are qualitatively reproducible but quantitative reproduction is not achieved, mainly due to very sensitive interfaces (especially the alkali metals are reacting with small traces of air and water). This finding agrees well with the prediction made in the introduction.

In this chapter, the properties of sodium metal electrodes in contact with the solid electrolyte β'' -alumina were studied and discussed. After the literature survey, the problems caused by current flux and sodium metal dissolution were shown, leading to the assumption that the voltage increase is caused by vacancy accumulation (pore formation) at the anodic side of the cell. The application of a reference electrode corroborates this finding. To guarantee the maximum contact with the lowest polarization resistance, different techniques to attach the sodium metal electrode to the electrolytes were investigated, showing that the freshly electrochemically deposited and the hot pressed sodium metal electrodes exhibited the lowest polarization resistances. Nevertheless, the overall IR-drop yielded at least two times the theoretical IR-drop of the β'' -alumina pellet, even at high pressures.

As the relaxation rate during the experiments was found to be insufficient to maintain the interfacial contact (decrease the pore volume) and resting did only slightly improve the contact for a short time, more efficient relaxation processes were required. One possibility was the application of pressure to the electrodes and to the interface, resulting in material transport due to plastic deformation (via defect and dislocation transport/movement). In order to study the effect on the interface, a suitable setup was developed that limited the contact area to a certain maximum value and allowed the determination and generation

of pressure to the interface in the range between 0 bar and 24 bar.

Using this setup, pressure dependent galvanostatic experiments were conducted, showing that current densities between 0.5 mA/cm^2 and 2 mA/cm^2 required the application of pressures between 9 bar and 24 bar, depending on the experiment time. Otherwise the applied voltage to maintain the current drastically increases and thus will lead to decreased performance in batteries during cycling due to elevated overvoltages. The influence of pressure on the material conductivity (due to lattice compressing) could be experimentally excluded in this pressure range.

Transition current experiments showed that current densities up to 4 mA/cm^2 exhibit acceptable overvoltages for mechanical pressures between 16 bar and 24 bar. A comparison of the results with other ion conductors will be given at the end of the next chapter. Linear sweep voltammetry results also indicated that the application of high pressures (between 16 bar and 24 bar) lead to curves that are approaching the ideal ohmic behavior. Thus, pressure was proven to be one of the most important parameters for maintaining the interfacial contact. Cycling of symmetric sodium metal electrode/ β'' -alumina cells showed that the voltage at the second cycle (after inversion of polarity) was minimized to the initial value of the freshly prepared cell and stayed constant. This finding was explained by the elevated activity of freshly deposited metal and the pressure independence of the dissolution for freshly cathodically deposited sodium metal was shown. However, the freshly deposited sodium metal exhibited a self-healing effect, which changed the electrode behavior back to the properties of the initially prepared sodium metal electrode.

Cycling at elevated pressures resulted in an almost linear voltage behavior during metal dissolution. Long-time cycling experiments will be shown and compared to other ion conductors in the next chapter. Short circuits and dendrite (or whisker) formation were not observed in this pressure and current density range, but were seen for current densities of 10 mA/cm^2 . Thus, the application of pressure to the interface between sodium metal and β'' -alumina, or more general the interface between alkali metal and solid electrolyte, is crucial for proper cycling at high current densities. Using the results of this section, a macroscopic sodium metal electrode (approximately $500 \text{ }\mu\text{m}$, corresponding to a capacity of 50 mAh/cm^2) was dissolved and deposited again without high voltage values.

In Fig. 5.15 the results of this section and the interpretation according to the literature survey in section 5.2 are summarized. At the beginning an almost ideal contact between the alkali metal is established (Fig. 5.15a). During dissolution, vacancies are formed that accumulate under the formation of pores. As the incorporation and oxidation of alkali metal atoms can only happen at the interface, alkali metal atoms have to be transported towards the interface, either by diffusion or by adatom diffusion, which is illustrated in Fig. 5.15b. The application of pressure to the interface, which is displayed in Fig. 5.15c, will decrease the pore size and maintain the contact area. All three relaxation effects are shown in Fig. 5.15d, the adatom diffusion and the plastic deformation of the alkali metal electrode, caused by forced dislocation and vacancy movement. Application of force tends to attract dislocations toward the surface^[172]. A schematic figure illustrating the material transport due to dislocation relaxation is given in section 10.

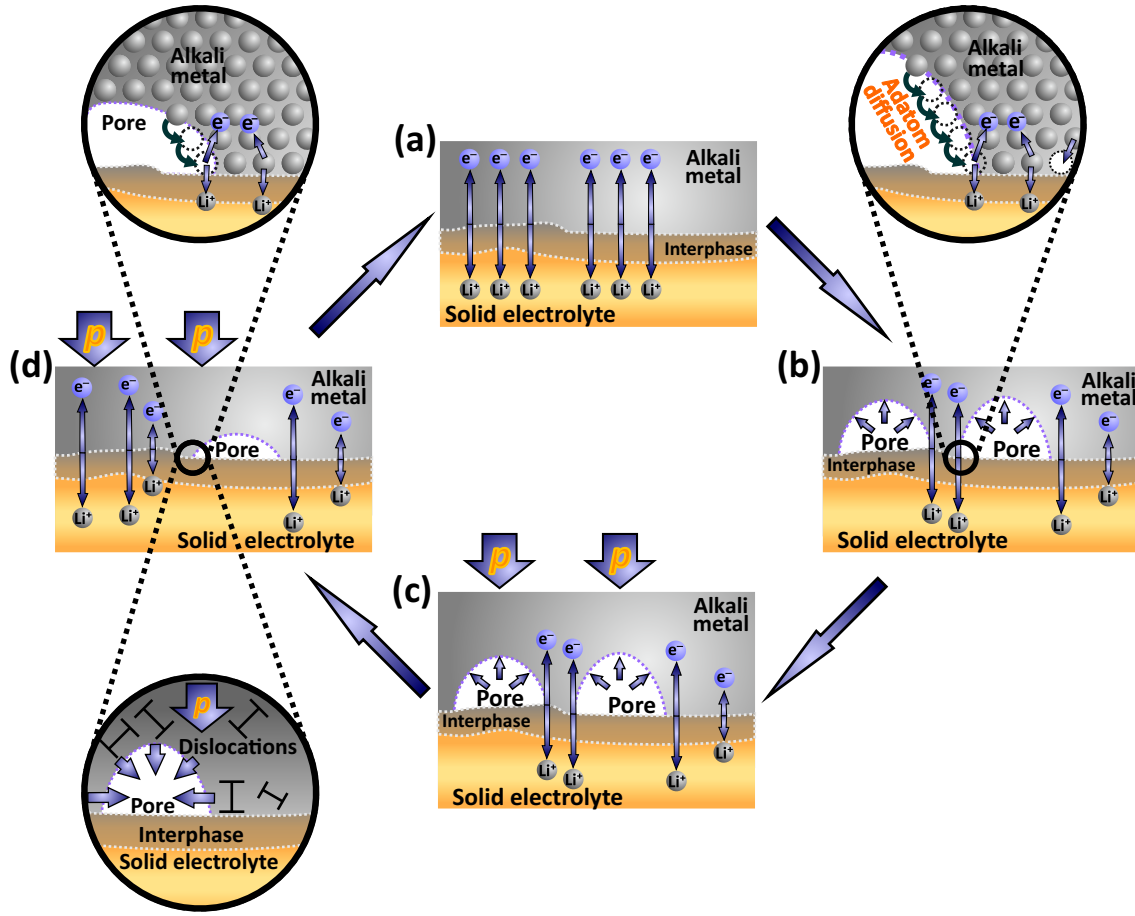


Figure 5.15: Schematic summary of the effects during dissolution at the interface between alkali metal and solid electrolyte is shown according to the results in this chapter and the literature survey in section 5.2.

The results in this section show that β'' -alumina is a suitable solid electrolyte for the incorporation in sodium-based ASSBs. Nevertheless, the application of pressure is highly necessary in order to maintain the interface contact area. Then cycling under transport of large amounts of sodium metal with relatively high current densities is accessible.

6 Kinetic effects of interphases and interfaces under current load

6.1 Introduction

A systematic investigation of lithium metal/solid electrolyte interfaces is quite more challenging than for sodium metal. Reasons for this are the chemical instability (interphase formation) or in the case of garnet type materials, the insufficient interfacial properties. Nevertheless, two promising but unstable lithium ion conductors, LGPS and LPS, were studied in this project. The mechanical and chemical instabilities strongly influence the experiments and thus, only a few results could qualitatively be reproduced. A literature survey can be found in section 5.2.

In this section, the pressure dependence of alkali metal electrodes/solid electrolytes is shown and discussed for LGPS, LPS, NPS and LLZO. The cycling behavior leads to a evaluation of the applicability for this solid electrolytes in combination with alkali metal electrodes in ASSBs. Cycling revealed a critical new effect of electrochemical enhanced interphase growth, which will be shown in this chapter. At the end, a summary and comparison of the interfacial performance will be given and the best solid electrolyte for the application of alkali metals in ASSBs will be discussed.

6.2 SEI forming solid electrolytes – LGPS vs. LPS

6.2.1 The interface Li/LGPS

The interface¹ shows a similar pressure dependence like Na/ β'' -alumina, but the overall resistance is notably higher, which is surprising, especially when the higher material conductivity is taken into account. Results of pressure dependent measurements are shown in Fig. 6.1a and b for current densities of 0.5 mA/cm² and 1 mA/cm². As the LGPS pellets were mechanically destroyed at higher pressures and short circuits were generated (probably due to dendrite formation), the periods between pressure enhancements and the conduction time span of the galvanostatic experiment were chosen smaller compared to β'' -alumina. For LGPS, the voltage starting values and the voltage slope are obviously higher in comparison with the data for β'' -alumina, which may be caused by higher polarization and interphase contributions to the overall resistance.

¹In this case, interphase (Li-SEI-SE) would be the more correct term, but interface is used instead, as only the effect of ion transfer between the electrode and the solid electrolyte is considered.

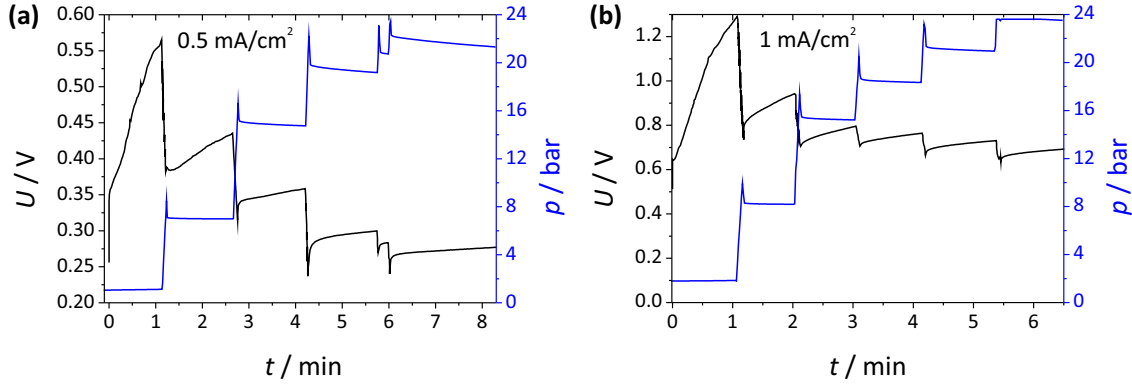


Figure 6.1: Results of the pressure dynamic galvanostatic experiment for a symmetric Li metal/LGPS cell are shown in (a) and (b) for current densities of 0.5 mA/cm^2 and 1 mA/cm^2 , respectively.

Increasing the mechanical pressure to approximately 24 bar, a voltage increase is observed, that is smaller compared to Na/ β'' -alumina interfaces, which is not surprising as the Brinell hardness of lithium is approximately ten times higher than of sodium metal^[171]. Thus, the plastic deformation rate and the pressure dependence of the galvanostatic experiments are far smaller, so that higher pressures are required. Another explanation for this will be described in section 6.6. Detailed insight into the behavior of the lithium metal/LGPS interface will be given in the following. The transition current experiment for a very thin pellet (0.5 mm) is displayed in Fig. 6.2a.

By increasing the current density from 0.1 mA/cm^2 to 20 mA/cm^2 , the voltage increases from values smaller than 0.1 V to 3.5 V. Thus, for current densities above 5 mA/cm^2 , the overall resistance is getting very high, leading to an increased cell overvoltage. The termination condition was set randomly to 4 V, as the real stability window was not known at the time of the experiment. A detailed comparison of the transition current results for all solid electrolytes, which were investigated during this project, will be shown later.

LSV experiments have shown promising results for investigating the pressure dependence of alkali metal/solid electrolyte interface and evaluating the limiting current densities (see section 5). The results for LGPS are shown in Fig. 6.2b. For lower voltages (approximately 1 V), the current increases up to approximately 2 mA/cm^2 , which is comparable to the findings for β'' -alumina. As the LSV results also depend on the conductivity of the respective material, which is higher for LGPS, and the pellet thickness, which is smaller for LGPS, comparing the LSV results is difficult. The comparison of the transition current experiment results is more beneficial and will be discussed later. Nevertheless, the LSV curve that was recorded without pressure, showed a completely different behavior to β'' -alumina. The identification of two different processes and maximum values could not be provided. By increasing the pressure, the current density values are increased but are far from equaling the ohmic behavior. Reasons for this might be the interphase, which was not taken into account since it is difficult to obtain an interphase resistance during a non-equilibrium technique. From the results it may also be concluded that the interphase might grow during galvanostatic experiments, but this finding will be described and discussed later. Another reason might be the approximately ten times higher hardness of lithium compared to sodium metal that leads to a decreased deformation rate of the electrode. Higher voltages then lead to lower current densities than for β'' -alumina.

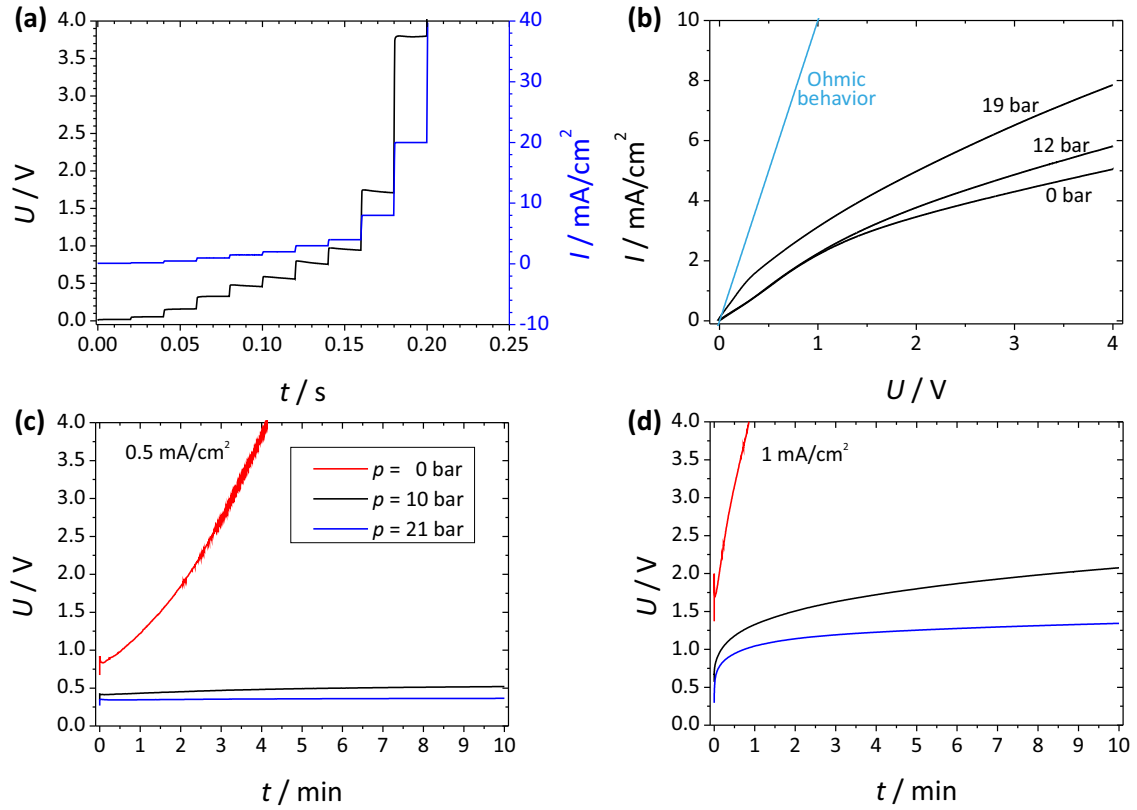


Figure 6.2: The transition current experiment results are displayed in (a) and the pressure dependent LSV data together with the theoretic ohmic behavior in (b). The results of the pressure dynamic galvanostatic experiments are shown in (c) and (d) for current densities of $0.5 \text{ mA}/\text{cm}^2$ and $1 \text{ mA}/\text{cm}^2$, respectively.

In order to show the pressure effect on the interface, galvanostatic experiments were conducted for current densities of $0.5 \text{ mA}/\text{cm}^2$ and $1 \text{ mA}/\text{cm}^2$, both are displayed in Fig. 6.2 c and d. Without the application of pressure, the voltage increases and meets the limiting value for both current densities. Increasing the pressure leads to a nearly linear voltage slope that is obviously higher than for β'' -alumina. Thus, the application of pressure is less effective for LGPS than for β'' -alumina. Whether the interphase thickness is increasing during cycling and a comparison between the different metal/solid electrolyte interfaces will be given later in this section.

6.2.2 The interface Li/LPS

The pressure dynamic galvanostatic experiments for LPS are shown in Fig. 6.3a and b for current densities of $0.5 \text{ mA}/\text{cm}^2$ and $1 \text{ mA}/\text{cm}^2$, respectively. For $0.5 \text{ mA}/\text{cm}^2$, the voltage slope is decreasing with increasing pressure, as expected. Unfortunately, the LPS pellets strongly tended to form short circuits, mainly due to dendrites that grew through the solid electrolyte. Thus, the time span for the experiment was decreased in order to obtain the requested information without short circuiting of the cell. Often the LPS pellets broke by increasing the pressure to values above 20 bar. Thus the pressure range was mostly limited to values below 20 bar. Generally, the starting value is reached again, when the pressure exceeds 16 bar to 24 bar. For LPS at a current density of $0.5 \text{ mA}/\text{cm}^2$ this is not observed, but might be seen for higher pressures. In Fig. 6.3b, the pressure

dependent galvanostatic results for a current density of 1 mA/cm^2 showed a severe slope for a pressure of 0 bar. Increasing the pressure decreases the overall voltage value but the slope is only slightly influenced until a pressure of 12 bar is exceeded. For pressures above 15 bar, the calculated resistance (including SEI) is reached (shown in dotted gray). The initial behavior of the interface strongly depends on the preparation and was quite difficult to reproduce for LPS (and LGPS). For both lithium ion conducting thio-phosphates, the initial cell resistance could not be reobtained after the experiment, which is in contrast to the findings for β'' -alumina (for stable solid electrolytes).

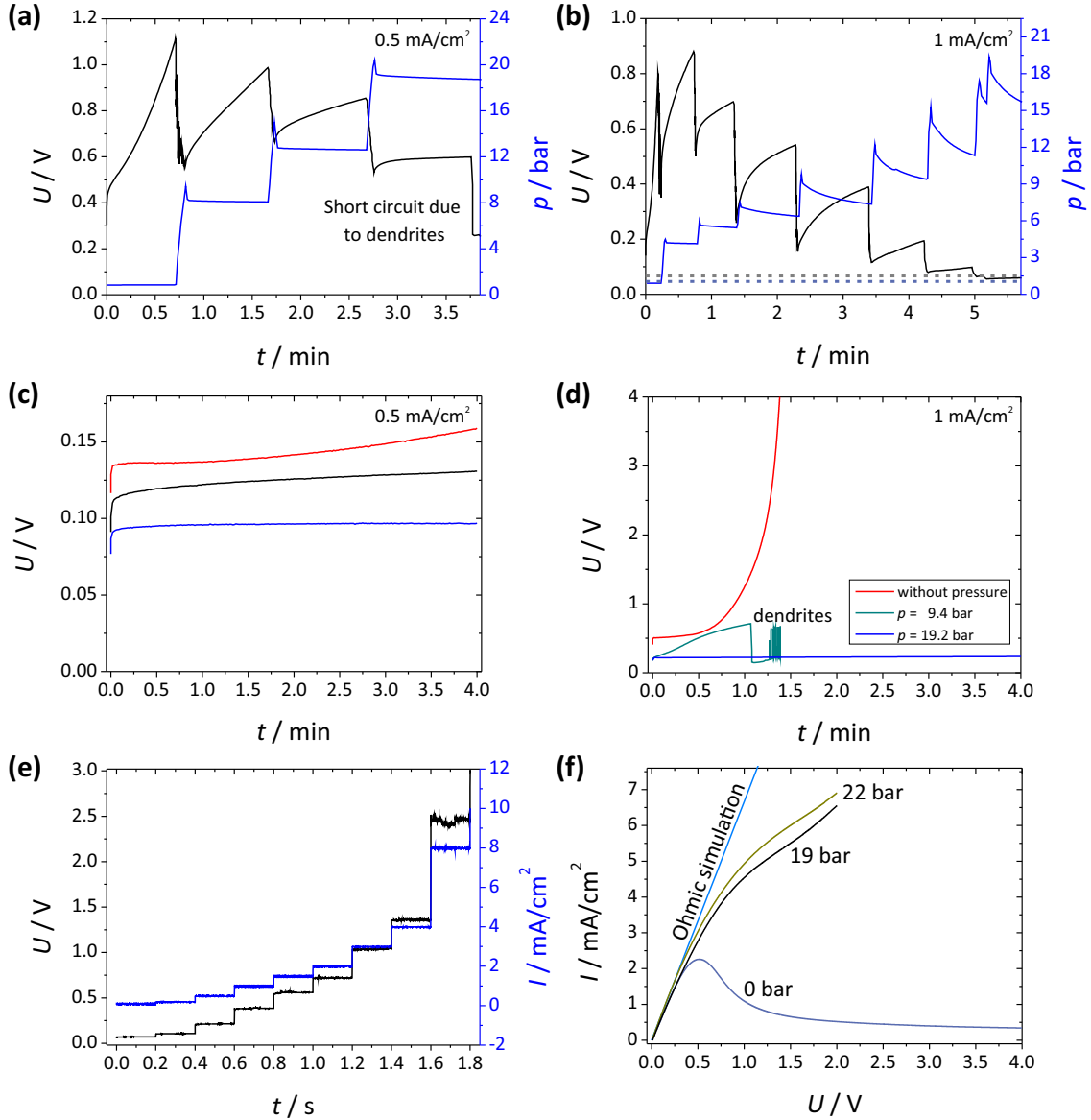


Figure 6.3: Results of the pressure dynamic galvanostatic experiments for a symmetric Li metal/LPS cell are shown in (a) and (b) for current densities of 0.5 mA/cm^2 and 1 mA/cm^2 , respectively. The results of the galvanostatic experiment for different pressures are shown in (c) and (d). The transition current experiment results are displayed in (e) and the pressure dependent LSV data together with the theoretic ohmic behavior in (f).

Fig. 6.3c and d show the galvanostatic experiments for the current densities of 0.5 mA/cm^2

and 1 mA/cm^2 . Generally, the voltage decreases with increasing pressure, which is expected regarding the results for LGPS and β'' -alumina. For 0.5 mA/cm^2 , the slope approaches zero for pressures larger than 19.2 bar. The same applies to the results for a current density of 1 mA/cm^2 . This time, the voltage increase for the pressureless results is virtually higher than for lower current densities. Again the voltage slope could be strongly decreased to approximately zero. Unfortunately, a short circuit was observed after 1 minute for a pressure of 9.4 bar, identified by the voltage drop and the following oscillations, which seems to often occur at higher current densities^[159]. In Fig. 6.3e, the transition current values for different current densities are summarized. Compared to LGPS, the voltage increase is smaller but may again be caused by the different material conductivities, interphase and pellet thicknesses. Thus, a detailed comparison will be given later, taking all effects into account. The results of the LSV experiment are shown in Fig. 6.3f for three different pressures and the theoretical ohmic behavior. For the pressureless measurements, a voltage peak at 0.5 V with a current density of approximately 2 mA/cm^2 is found, which is comparable to the findings for β'' -alumina. This time only one peak and accordingly only one process could be observed. Increasing the pressure to 19 bar and 22 bar, the results approach the ohmic behavior for voltage values smaller than 0.5 V. The differences between the curve for 19 bar and 22 bar are relatively small and strongly deviate from the ohmic behavior. Thus, the lithium metal depletion at the interface is still influencing the current-voltage profiles.

In principle LPS shows promising results concerning the current densities and overvoltage; β'' -alumina shows approximately two times higher current densities for an approximately two times thicker pellet. The application of LPS in lithium metal containing ASSBs will be limited by the densification procedure and the prevention of dendrite formation, the later was responsible for the failure of most experiments. Whether the interphase (mainly Li_2S , see section 3.7) promotes dendrite and whisker formation (and growth) has to be clarified. Assuming that whisker and dendrite formation are caused by oversaturation of the solid electrolyte, which is more than likely for the interface Li_2S /lithium metal, the SEI is mostly responsible for the short circuiting. This hypothesis has to be clarified experimentally. Again, the results in this section hint that a stable solid electrolyte will be more favorable.

6.3 The interface Na/NPS

The interface between sodium metal and NPS is shortly discussed in this section, as the interpretation of the results is not unequivocal. Reason for this is the rapidly increasing interphase thickness (see section 3.7.3) that will strongly influence the results. Fig. 6.4a and b show results of the pressure dependent galvanostatic and the galvanostatic experiment for three different pressures. Generally, NPS shows properties comparable to β'' -alumina, regarding the pressure dependence of the interface, and to LPS, regarding the mechanical instability. By increasing the pressure, the voltage is decreasing and the changes are found to be negligible above 20 bar. Nevertheless, the voltage is relatively high for a current density of 0.1 mA/cm^2 . This results from the low material conductivity and the extended interphase.

Regarding the values for the transition current experiment in Fig. 6.4c, it is clearly observed that 0.2 mA/cm^2 is the maximal current density for NPS. Higher current densities will result in exceeding the voltage termination criterion. The LSV data in Fig. 6.4d

corroborate this finding, as the pressure enhancement from 0 bar to 8.5 bar only slightly increases the current density up to 0.3 mA/cm^2 for 4 V. Raising the pressure to 21.2 bar results in 0.5 mA/cm^2 for 4 V. Note that drawing the ohmic behavior in Fig. 6.4d would not be reasonable, as the interphase growth will lead to strong and unpredictable changes of the pellet resistance².

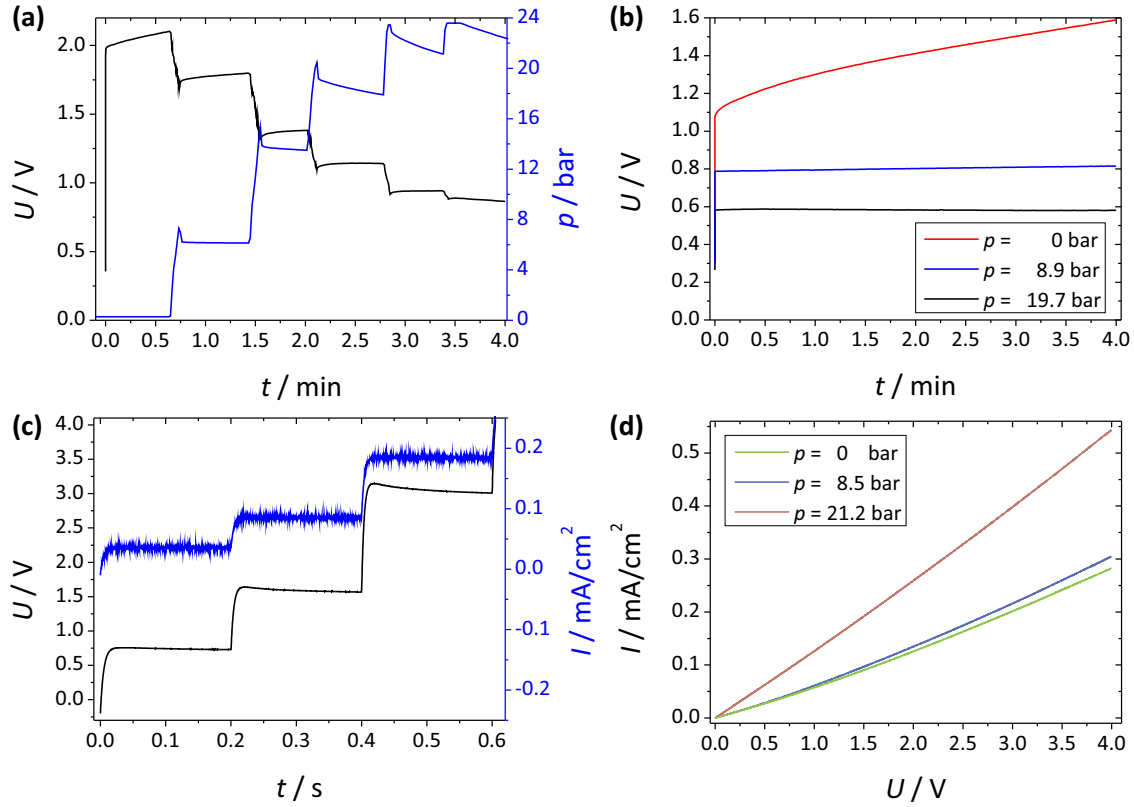


Figure 6.4: The results for the pressure dependent galvanostatic and galvanostatic measurements for three different pressures are shown in (a) and (b) for a current density of 0.1 mA/cm^2 , respectively. In (c) and (d), the transition current measurement and the LSV for three different pressures are displayed.

6.4 LLZO, an ideal lithium ion conductor?

It has often been stated in this work that stable solid electrolytes are more favorable than those that form an SEI. For β'' -alumina this is actually the case. LLZO, another stable solid electrolyte, exhibits a completely different behavior. Regarding the pressure dependent galvanostatic results for a current density of 0.2 mA/cm^2 in Fig. 6.5a, it is obvious that the interface is barely affected by pressure, only the slope is markedly changed, and that the voltage values are relatively high. Reason for this is the five times lower conductivity compared to the LPS and β'' -alumina pellets and the interface. During this project it has not been possible to obtain favorable interfaces. It is generally assumed that lithium hydroxide, oxide and carbonate formation and small particles at the surface strongly decrease the transfer coefficient, which will then lead to an increased interfacial resistance^[173].

²The SEI is more than 10 times thicker compared to LGPS and is still steadily growing, see section 3.7.3.

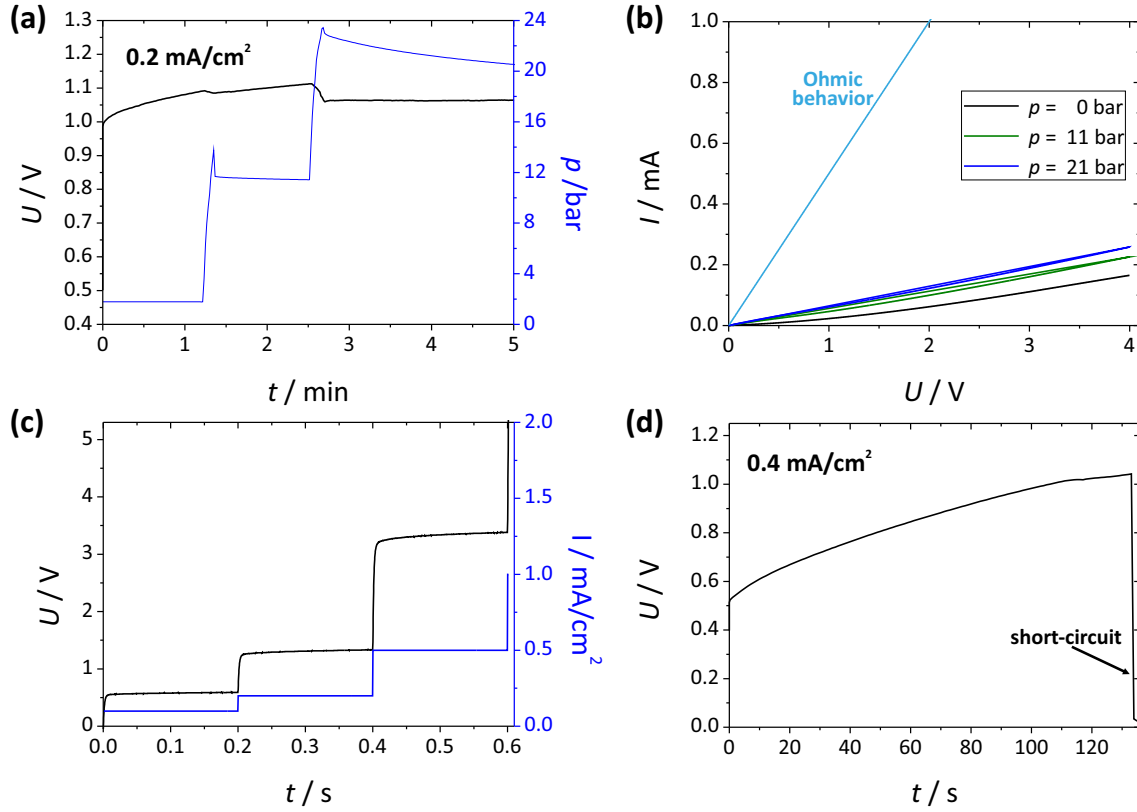


Figure 6.5: The results for the pressure dependent galvanostatic measurements are shown in (a) for a current density of 0.2 mA/cm^2 . In (b) and (c), the LSV data for three different pressures (including the simulated ohmic behavior) and the transition current measurements are displayed. (d) shows a representative voltage profile for a current density of 0.4 mA/cm^2 leading to short circuiting.

This hypothesis is supported by the LSV experiments displayed in Fig. 6.5b for three different pressures. Not surprisingly, the pressure dependence of the LSV slopes is negligible mainly due to the low amount of dissolved lithium metal. Nevertheless, the LSV curves are nearly linear and slightly increasing for enhanced pressures. Resulting from the strong deviation of the LSV curves from the theoretic ohmic behavior, it is concluded that the insufficient interface is the reason for the high overall resistance. The contact between solid electrolyte and lithium metal might be improved by using vapor deposition techniques. In order to maintain the comparability of the results, the same preparation method was used for all interfaces. The transition current experiments in Fig. 6.5c corroborate the findings obtained by LSV, as the elaborately prepared LLZO/lithium metal interface only shows voltage values in the stability range of LLZO up to 0.5 mA/cm^2 , which seems to be the limiting value. It should be mentioned, that short circuiting is a major problem for LLZO at higher current densities like displayed in Fig. 6.5d. For current densities between 0.3 mA/cm^2 and 0.5 mA/cm^2 , the short circuiting times range between 60 s to 240 s, depending on the current and the thickness of the solid electrolyte.

In order to show the performance of symmetric Li/LLZO/Li cells for current densities of 0.2 mA/cm^2 and 1 mA/cm^2 , cycling experiments were conducted. The results are shown in Fig. 6.6a and b. For 0.2 mA/cm^2 , cycling was possible for limited time of 4 minutes with reasonable voltage values. Increasing the current density value to 1 mA/cm^2 results in the voltage time profile in Fig. 6.6b, where one cycle takes less than 2 ms until the

termination criterion is reached.

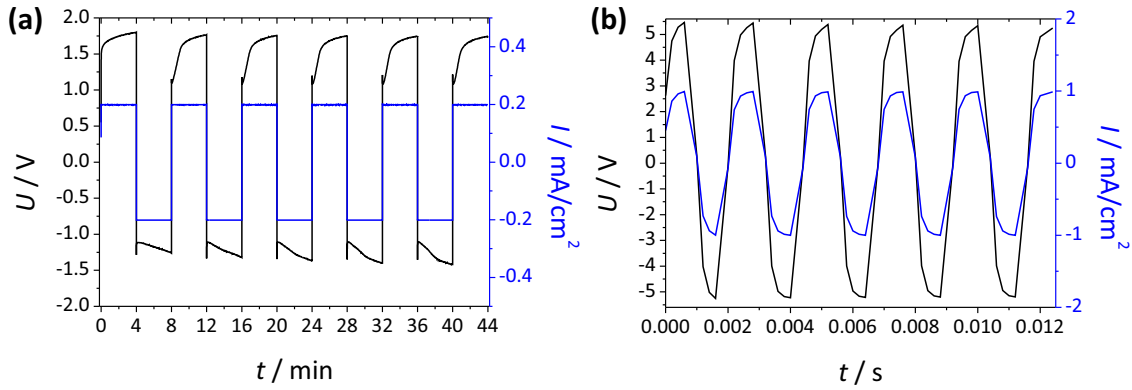


Figure 6.6: Cycling of a symmetric Li/LLZO/Li cell for current densities of 0.2 mA/cm² and 1 mA/cm² are shown in (a) and (b) at room temperature, respectively. An external pressure of 24 bar was applied.

Thus, the results clearly show that, without surface modification of the LLZO pellet, garnet type materials in principle show very poor interfacial properties, compared to β'' -alumina and LPS. The results in this section lead to the conclusion that the stability of the solid electrolyte does not automatically lead to sufficient interfacial properties.

6.5 Cycling across the interface alkali metal/solid electrolyte

In this section, the results of long time cycling are compared for β'' -alumina, NPS, LGPS and LPS. Fig. 6.7a and b show the cycling for β'' -alumina and NPS. For both, a constant pressure of 21 bar was applied. The current densities were set to 1 mA/cm² for β'' -alumina and 0.2 mA/cm² for NPS. Fig. 6.7a provides insight into the cycling stability of β'' -alumina, which lasted for more than 45 h at a constant level. Thus, the interface β'' -alumina/sodium metal could be cycled sufficiently at high current densities under application of mechanical pressure. Note that within 1 h a sodium metal electrolyte thickness of 9 μ m was dissolved and deposited, respectively.

Cycling for an hour with a current density of 0.2 mA/cm² for an NPS pellet is shown in Fig. 6.7b. The drawing of a smaller current compared to the experiment for β'' -alumina yielded a significantly higher voltage, which is in good agreement with the results in the previous sections. Furthermore, the voltage plateaus are increasing for every cycling step, which could either be explained by the still growing interphase or an electrochemically enhanced interphase growth. Clarification of this finding is extremely complex and mainly limited by the sample properties. It will be difficult to distinguish between the chemically induced and the electrochemically enhanced interphase growth. Detailed results on a more suitable material system will be discussed later in this section.

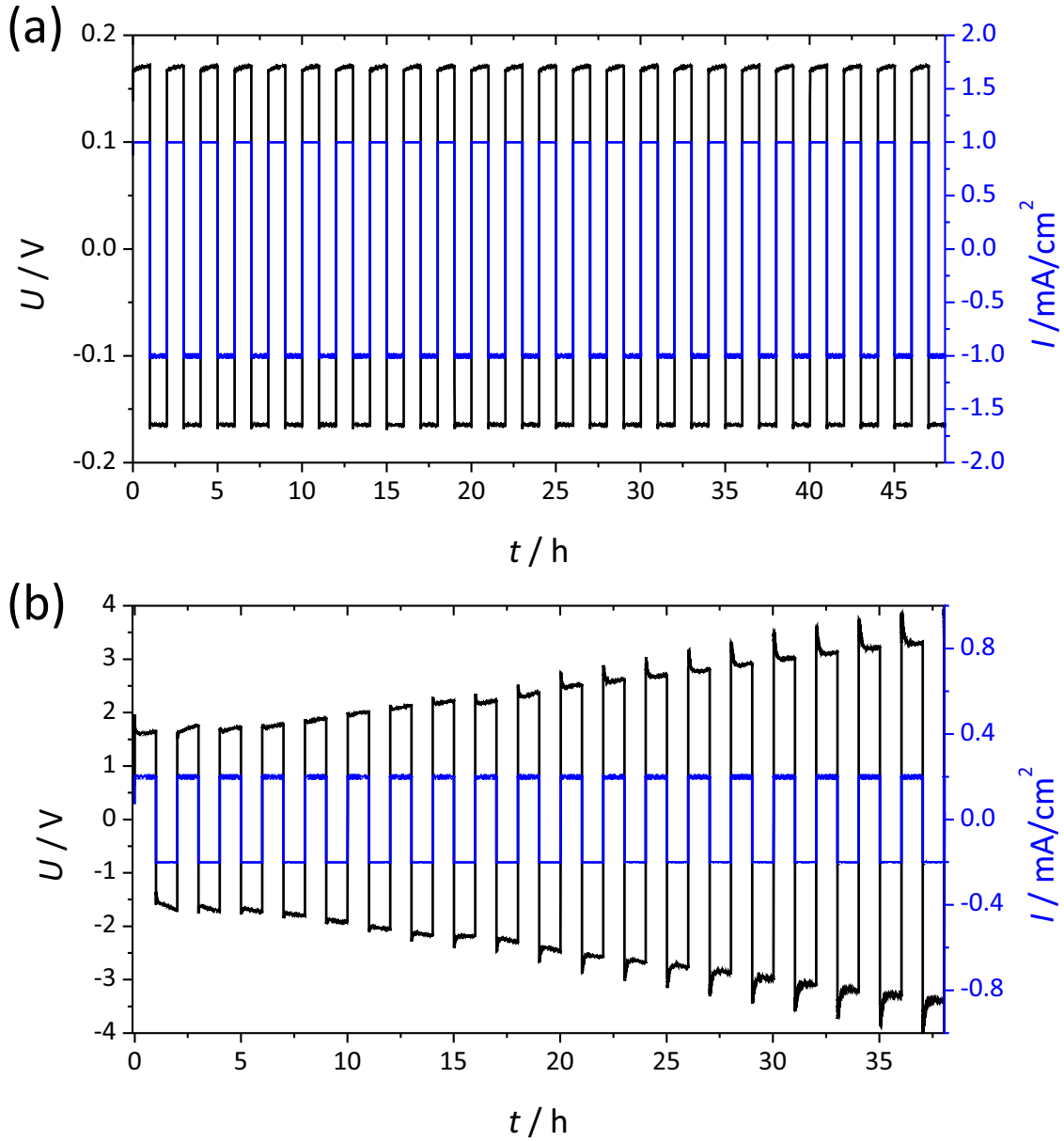


Figure 6.7: Cycling results for β'' -alumina and NPS are displayed in (a) and (b), respectively. Note that the current density for β'' -alumina was set to 1 mA/cm^2 , whereas for NPS a current density of 0.2 mA/cm^2 was chosen. For both a cycle time of 1 h and a mechanical pressure of 21 bar were selected.

NPS and LPS showed similar chemical instability against their parental alkali metals and consequently LPS would be a suitable system to investigate the electrochemically induced interphase growth, as the chemical interphase growth is limited. Unfortunately, the cycling shows a completely different behavior, which could be seen in Fig. 6.8a and b. In a, the cycling procedure is dominated by erratic fluctuations with irregular shape leading directly into short circuiting of the cell. Reproducing the results in Fig. 6.8a leads either to similar findings or to results comparable to those displayed in Fig. 6.8b. There, erratic fluctuations are observed, too, again leading to short circuiting after several hours (not shown). This is in accordance with the results discussed in this section. LPS appears to be prone to dendrite formation and short circuiting.

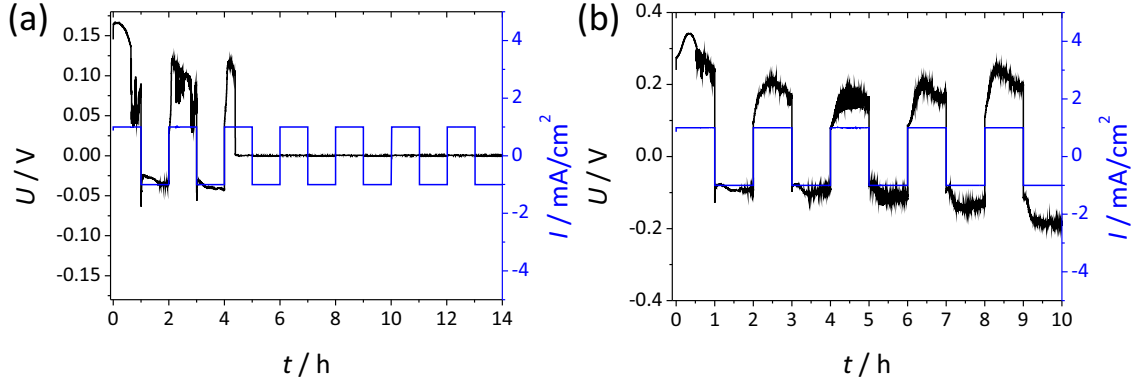


Figure 6.8: Typical cycling results for LPS are displayed in (a) and (b), respectively. A cycle time of 1 h, a current density of 1 mA/cm² and a mechanical pressure of 21 bar were selected.

Regarding the findings in this section, only β'' -alumina appears to be a solid electrolyte with a suitable interface and conductivity that could be cycled without increasing overvoltage. Generally, the application of mechanical pressure is crucial, as the pore formation and the resulting contact loss greatly influence the cycling performance. LPS was found to be prone to dendrite formation, which made it impossible to investigate the electrochemically enhanced interphase growth. A far more suitable system is LGPS, which is reported in the following section.

6.6 Electrochemically induced interphase growth

In order to provide insight into the electrochemically induced interphase growth, a symmetric Li/LGPS/Li cell was prepared and investigated by impedance spectroscopy during cycling. The obtained values are then compared to the results for the chemical degradation. Fig. 6.9a shows the cycling of a symmetric lithium metal/LGPS cell for a cycle time of 1 h, a mechanical pressure of 24 bar and a current density of 1 mA/cm². During cycling the voltage plateau increases from initially 1.3 V to more than 3 V after 45 h. As the reason for this voltage increase could not be the contact loss due to lithium metal dissolution, other effects might be responsible. The Nyquist plots for the initial cell, after 10 h, 20 h and 30 h are shown in Fig. 6.9b, showing that the overall resistance is strongly increasing, which might be attributed to the increasing interphase contribution of the resistance. By application of an equivalent circuit similar to those used for SEI formation in section 3.7, the interphase resistance can be determined. The results are displayed in Fig. 6.9c in comparison for the purely chemical degradation.

The initial value in Fig. 6.9b is in good agreement with the result obtained in section 3.7.2. After 10 h of waiting, the resistance value for the cell that was not cycled increased to approximately 200 Ωcm^2 , whereas the value for the cycled sample increased to approximately 700 Ωcm^2 . The effect after 20 h is even more pronounced, showing a difference of more than 1000 Ωcm^2 . Thus, cycling appears to increase the interphase growth. The reasons for this are still not clear. In literature, a few reports on enhanced growth rates during polarization were found^[175–177]. The application of an electric field influences the movement of charged species, which is a strong driving force^[175].

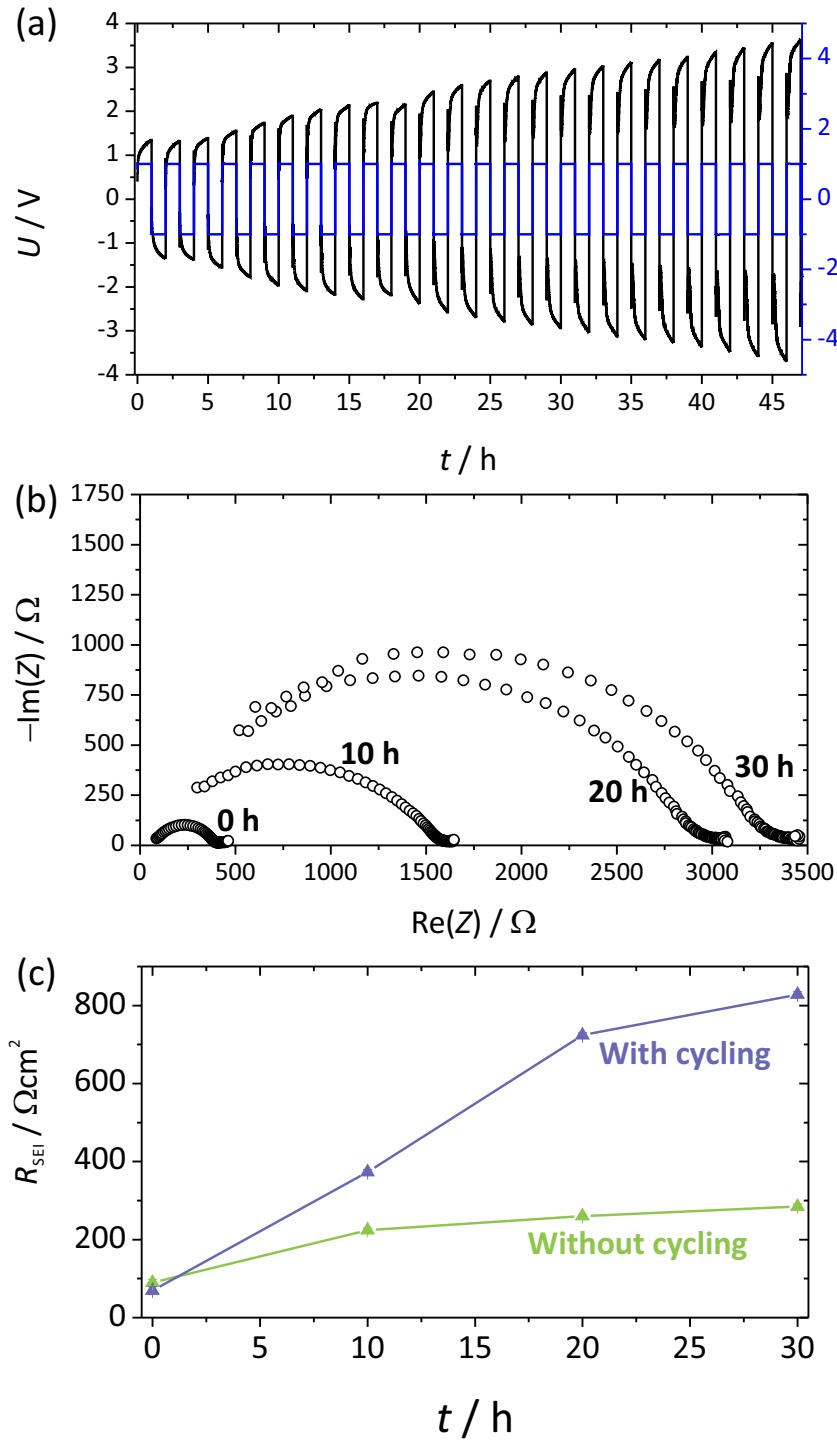


Figure 6.9: Cycling results for the symmetric cell Li/LGPS/Li with a current density of 1 mA/cm^2 , a cycle time of 1 h and a pressure of 24 bar are shown in (a). The Nyquist plots before the initial cycle, after 10 h, 20 h and 30 h are displayed in (b). A comparison of the chemical and electrochemical degradation of LGPS according to the results in section 3.7.2 and in (b), are illustrated in (c).

Local steps or spatial changes of the transference number may lead to metal deposition inside the solid electrolyte, corresponding to an internal electrolysis^[176]. Generally, the film growth is influenced by two terms, a chemical and a field term. For large product

film thicknesses, the field term is dominating, leading to linear film growth. For smaller thicknesses, the chemical term becomes more dominant and a parabolic behavior is observed^[177]. As the enhanced film growth in Fig. 6.9c shows an almost linear behavior, at least for 20 h, it can be assumed that the field term is dominating the reaction rate.

In the following, a model will be described that may explain the enhanced growth caused by cycling. Therefore, an SEI with the electrochemical properties of Li_2S on LGPS is assumed, which is a good approximation according to the results in section 3.7.2. The model is schematically illustrated in Fig. 6.10. LGPS exhibits an electronic and ionic conductivity of a few nS/cm and mS/cm, respectively, resulting in a transference number of 10^{-6} for electrons. The SEI (Li_2S) shows an electronic and ionic conductivity of 0.1 pS/cm and a few nS/cm, directly resulting in an electronic transference number of 10^{-4} , which is two orders of magnitude higher compared to the solid electrolyte. Assuming that a current of 1 mA is crossing the cell, the ionic current in the solid electrolyte will be approximately 1 mA (subtracted by 10^{-6} mA) and in the SEI approximately 1 mA (subtracted by 10^{-4} mA). The difference in the transference number of ions is two orders of magnitude, which will be compensated by electronic transfer. Thus, the chemical potential for lithium will grow at the interface between the SEI and the solid electrolyte until a certain limiting value is reached and lithium metal deposition occurs. In sodium ion conductors, this effect is well known and caused by small local changes of the transference number^[146,147].

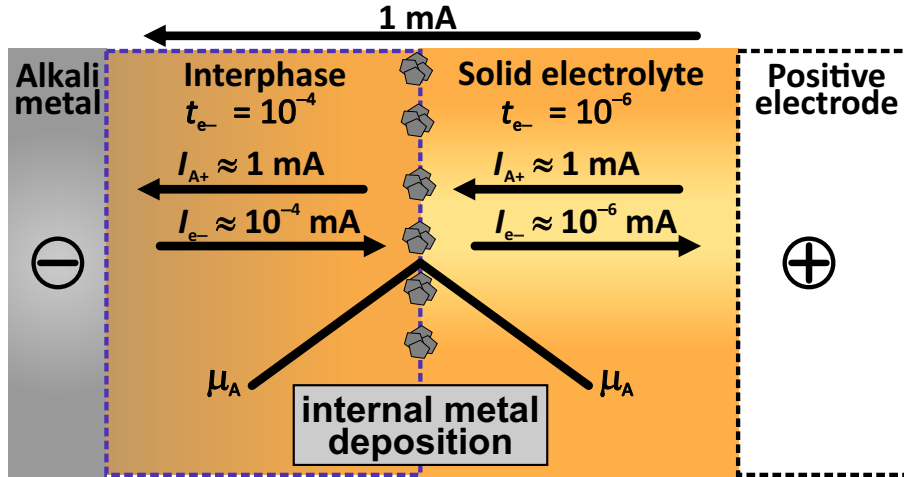


Figure 6.10: The concept of internal metal deposition of two mixed conducting solid electrolytes.

The freshly deposited and highly reactive alkali metal will then react with the solid electrolyte under formation of an SEI until the alkali metal is completely consumed or the reaction becomes diffusion controlled and is slowing down. As a consequence the interphase boundary moves towards the solid electrolyte and the SEI thickness is increased. Simulation according to the results of this section and Faraday's law are displayed in section 11.1.2. Thus, the interphase growth is electrochemically enhanced, which is in agreement with the findings of Sakuma et al.^[80] for lithium alloy electrodes. Fig. 6.9 and 11.3 hint that this effect might be dominating the interphase growth.

6.7 Summary and conclusion

The best way to give an overview of the interfacial behaviors of different solid electrolytes may be given by comparing the results of the transition current measurements, as these should be independent of non-linear effects e. g. oscillations and contact loss. The latter two are already described in section 5. A summary of the transition current density values is given in Fig. 6.11. Note that the IR-drop is already subtracted from the voltage values so that only the overvoltage remains, which is then only caused by interfacial and interphase contributions to the resistance. Regarding Fig. 6.11, β'' -alumina exhibits the smallest overvoltages for all solid electrolytes that were studied during this project. Surprisingly only small differences were found for LGPS and LPS. Both NPS and LLZO showed extremely high overvoltages and suffer from high interfacial and interphase resistances. Thus, the interface needs to be stabilized for LPS, LGPS and NPS and modified for LLZO. For the latter the surface decomposition products and small particles have to be removed. β'' -alumina was found to be the most effective and versatile solid electrolyte of all materials studied in this project.

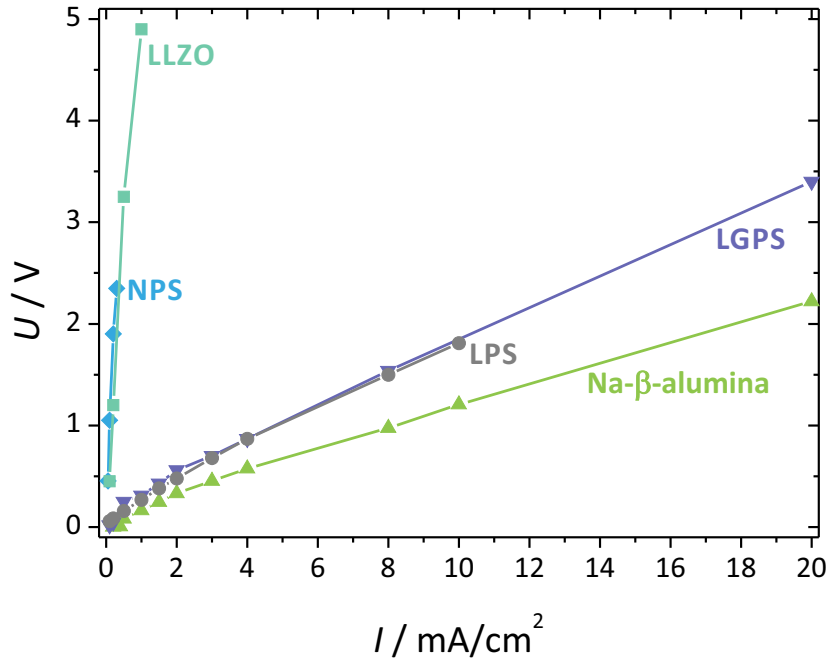


Figure 6.11: Summary of the results for the transition current experiments, including LLZO, NPS, LGPS, LPS and β'' -alumina. The IR-drop of the pellet is subtracted so that only the interface and interphase contributions are compared.

The interface between alkali metals and solid electrolytes was found to be influenced by the application of pressure. Again, higher current densities required the application of higher mechanical pressures. Lithium metal electrodes in general were in need of higher pressure, which is in good agreement with the higher Brinell hardness. Thus, the plastic formation starts at higher pressures compared to softer metal like sodium metal.

LGPS showed remarkable properties during the galvanostatic experiment, as short circuiting due to dendrite formation was seldom observed. In contrast to this, LPS suffered

from dendrite formation and resulting short circuits, which appeared independent of the current density and pressures (in this range). The interface alkali metal electrode and NPS or LLZO showed only negligible pressure dependence, as only low current densities could be established. Thus, the vacancy formation rate was significantly smaller compared to other experiments leading to nearly sufficient metal atom supply by diffusion processes. Beside the comparison of the interfacial properties, cycling experiments played an important role for the evaluation for a possible solid electrolyte application in combination with alkali metal electrodes. The results of this chapter and chapter 5 were used concerning the application of pressure to the interface and applicable current densities. β'' -alumina showed an overvoltage of approximately 0.15 V for a current density of 1 mA/cm², which represented the best performance of all studied interfaces. The cycling of LPS under similar conditions led to erratic deviations (oscillations) during the experiment and in most cases to short circuiting due to dendrite formation.

NPS showed an approximately ten times higher starting overvoltage for a current density of 0.2 mA/cm². The overvoltage increased up to approximately 3 V after 37 cycles (or hours) which might be caused by the ongoing fast interphase growth or electrochemical enhanced interphase growth. Applying a high pressure to the interface prevented the voltage increase caused by contact loss.

In order to investigate potentially enhanced interphase growth during cycling, LGPS experiments were performed under the application of high pressure. Impedance spectroscopy revealed a growth of the interphase contribution to the resistance of the Nyquist plots. Comparing the interphase resistance results obtained during cycling with the results in section 3.7.2 showed an obviously higher resistance increase that showed nearly linear behavior, which is in good agreement with results found in literature. This finding seems to be a unique effect for SEI forming materials. To find an explanation for this, the transference number of the SEI and the solid electrolyte were compared, resulting in possibility of internal metal deposition. For β'' -alumina, which is stable in contact with alkali metals this issue was already described for small gradients in the transference number. The SEI and LGPS exhibit a notably higher difference in the transference number.

Using this model, the interphase growth caused by electrochemical cycling experiments can be simulated using Faraday's law. Therewith, a significantly higher interphase growth during cycling was found for LPS compared to LGPS. Four hours galvanostatic cycling resulted in an interphase growth of less than 1 nm for LGPS and more than 1.5 nm for LPS³.

Thus, stable solid electrolytes with a favorable interface showed more promising results for the application of alkali metal electrodes in ASSBs. SEI forming materials showed a continuous degradation during cycling, which might be caused by a large gradient in the electronic transference number at the SEI/SE interface. Smaller gradients will weaken this effect.

³Assuming 8 nS/cm as SEI conductivity.

7 Summary, conclusion and outlook

The application of alkali metal as negative electrode material in all-solid-state batteries (ASSBs) or alkali metal ion batteries is often seen as the "holy grail" because of the exceptional high volumetric and gravimetric energy densities. This purpose is often prevented by safety issues, solid electrolyte interphase formation and morphological issues caused by the properties of the electrode material, e. g. dendrite formation. Thus, the question, whether the application of solid electrolytes will enable the use of alkali metal electrodes in ASSBs, was raised in the introduction. This thesis gave several arguments for and against it, which will be summarized in the following. After successful synthesis, the first issue found during the study of solid electrolyte/alkali metal interfaces, was the stability of solid electrolytes in contact with the respective alkali metal (lithium and sodium). In order to obtain experimental insight, a combined approach was developed, including time resolved impedance spectroscopy experiments and a new in situ photoelectron spectroscopy approach (developed during this project). This is schematically shown in Fig. 7.1, showing that the in situ XPS technique provided the identification of products and the time resolved impedance spectroscopy experiments gave kinetic information about the formation and growth of the decomposition film.

Due to the results obtained during this project, an interface/interphase classification was composed, which is again shown in Fig. 7.1. The three different interfaces/interphases were classified according to the properties of the reaction products. The stable interface did not show any decomposition during contacting, whereas the other two materials showed the formation of a mixed conducting (MCI) or a solid electrolyte interphase (SEI), which is a result of the thermodynamic instability (driving force) towards the decomposition products. The MCI formation resulted in a strongly increasing electronic conductivity causing the short circuiting of the cell/battery and a notably fast interphase growth, as a result of the mixed conducting character of the products. Examples for MCI forming materials are $\text{Li}_{0.35}\text{La}_{0.55}\text{TiO}_3$, $\text{Li}_{1+x}\text{Al}_x\text{Ti}_{2-x}(\text{PO}_4)_3$ and $\text{Li}_{3/8}\text{Sr}_{7/16}\text{Ta}_{3/4}\text{Zr}_{1/4}\text{O}_{12}$, where the transition metals titanium and tantalum (and to a certain extent zirconium) are reduced to lower oxidation states including the metal.

The formation of an SEI resulted in a resistance increase of the pellets due to the formation of less ion conducting materials like Li_2S and Li_3P . The more prominent solid electrolytes that are shown to form SEIs were $\text{Li}_7\text{P}_3\text{S}_{11}$ (LPS) and $\text{Li}_{10}\text{GeP}_2\text{S}_{12}$ (LGPS), leading to resistance increases up to approximately $25\ \Omega\text{cm}^2$ and $250\ \Omega\text{cm}^2$, that are still increasing. This finding was explained by the use of Wagner's model for tarnishing (as a classical model for solid state reactions), where the conductivity of the minor charge carriers, in this case the electronic conductivity, is limiting the interphase growth. According to this model, the growth should exhibit a parabolic growth behavior, which was actually observed in both cases and was used to determine the parabolic growth constants. Using the obtained values the interphase growth was simulated for a time span of 10 years, resulting in a strong resistance growth. Thus, the interfacial/interphase properties of the battery will obviously worsen the battery performance due to an elevated overvoltage (as the result of the resistance increase). For LGPS, a significantly higher SEI thickness and growth

rate was observed. This finding might be explained by the effect of germanium metal and/or germanium lithium alloy on the local transport coefficients. The verification of this hypothesis will be conducted by TEM measurements of the interphase cross section, but could not be included in this thesis for time reasons.

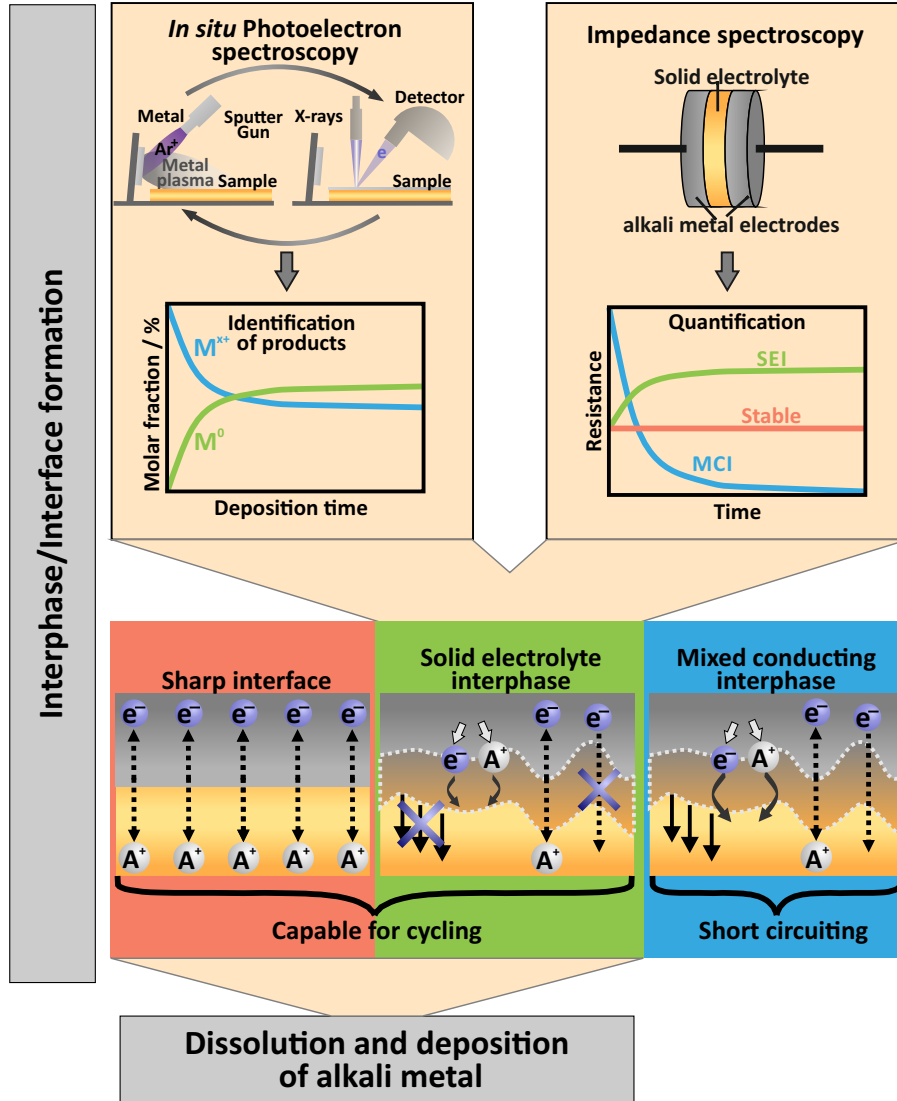


Figure 7.1: Schematic summary of the experiments and results obtained during this project are shown. Firstly, the two technical approaches are displayed, followed by the qualitatively illustration of results, leading to the interphase/interface classification.

Additionally, the interphase formation of $\text{Li}_6\text{PS}_5\text{Cl}$, $\text{Li}_5\text{La}_3\text{Ta}_2\text{O}_{12}$ and $\text{Na}_3\text{Zr}_2\text{Si}_2\text{PO}_{12}$ were investigated, too. The generation of strain due to interphase formation and the potential application of interface protection concepts were discussed.

Assuming a resistance of $0.1 \Omega\text{cm}^2$ (for a solid electrolyte with a conductivity of 1 mS/cm and a thickness of $1 \mu\text{m}$), the SEI resistance ($25 \Omega\text{cm}^2$) is obviously the major contribution to the overall resistance. Thus, stable solid electrolytes would be more favorable. Only

two materials were found to be stable in contact with lithium and sodium metal: the garnet type material $\text{Li}_7\text{La}_3\text{Zr}_2\text{O}_{12}:\text{Al}$ and β'' -aluminum oxide.

The stability is only one requirement for the application of solid electrolytes and alkali metals in ASSBs, another requirement will be the massive volume changes due to metal dissolution. During metal dissolution, vacancies are formed that can be extincted by alkali metal diffusion or by accumulation under pore formation as shown in Fig. 7.2, which will strongly decrease the contact area and therefore increase the voltage for the galvanostatic dissolution of metal. Generally, quite a few processes happen at the interface, including diffusion, adatom diffusion, relaxation of dislocations and the equilibration of pore sizes.

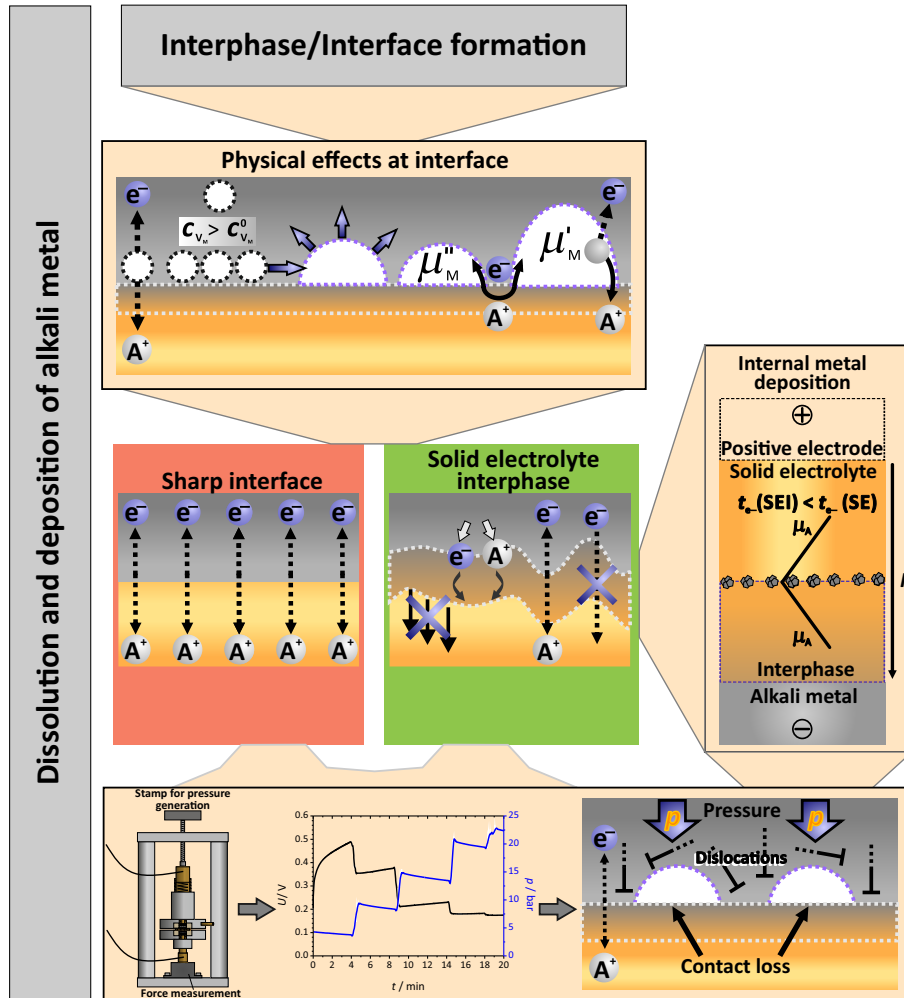


Figure 7.2: Graphical summary of the experiments and results concerning the interfacial effects under current load are displayed.

In order to study the impact of this effects, sodium metal electrodes and β'' -alumina were used. Using a symmetric cell setup, the voltage increase due to contact loss was observed and relaxation (by resting for several hours) was not sufficient to maintain the interfacial contact area for current densities in the range of $0.5 \text{ mA}/\text{cm}^2$ and $2 \text{ mA}/\text{cm}^2$. Thus, plastic deformation (by pressure application between 0 bar and 24 bar) was used, showing that this method is suitable to maintain the contact area. Increasing the pressure also resulted in proper cycling of the sodium metal electrode/ β'' -alumina interface with

current densities of 2 mA/cm² and even allowed the dissolution of a macroscopic sodium metal electrode without high voltages. The application of high pressures also led to the finding that the interface approached ohmic behavior. Freshly deposited sodium metal also showed a memory effect and was dissolved with lower overvoltage compared to the initial electrode. However, this effect weakened with time so that a self-healing of the cathodically deposited sodium metal was observed. Thus, only the application of pressures up to 20 bar guaranteed cycling without strongly increasing overvoltages.

A comparison of different solid electrolytes was conducted by transition current experiments. By removing the IR-drop, the comparison showed that β'' -alumina exhibited an at least two times lower voltage value compared to LPS or LGPS. This might completely be attributed to the effects caused by the interphase. NPS and LLZO exhibited an extremely high interphase or interfacial resistance. The pressure dependence was generally found to be stronger for sodium metal electrodes than for lithium metal, which is evidently caused by the ten times higher hardness of lithium. Cycling experiments of LPS proved that this material was extremely prone for dendrite formation and short circuits, whereas the cycling of LGPS revealed an increasing overvoltage value (even though the application of high pressures). Using impedance spectroscopy experiments during cycling an electrochemically increased interphase growth was found, again schematically shown in Fig. 7.2. Reason for this might be the large difference in the electronic transference number of the interphase and the solid electrolyte, leading to internal metal deposition. The freshly deposited alkali metal then may react with the solid electrolyte and increases the interphase thickness and resistance. This effect might be clarified and experimentally observed by the conception of model systems, containing a transference number gradient between two stable phases.

In order to settle the question, whether the application of solid electrolytes in ASSBs will enable the use of alkali metal electrodes, a few experiments revealed information. One of the most important issues is the stability of solid electrolytes in contact with alkali metal, which might lead to a strongly increased cell resistance and consumption of active material, as shown in this thesis. An exception for this might be LiPON, where the interphase products exhibit a higher conductivity than the initial material. The SEI formation additionally induces other effects, like internal metal deposition and electrochemically enhanced interphase growth or dendrite formation. Thus, stable solid electrolytes are favorable for the application of alkali metal electrodes. Cycling experiments revealed that the interfacial contact area is decreasing during metal dissolution, leading to a strong voltage increase. In order to prevent this effect, the application of pressures up to 24 bar showed magnificent results and allowed the dissolution of a macroscopic metal electrode without increasing overvoltage. Thus, the application of alkali metal electrodes in ASSBs is potentially achievable in combination with stable solid electrolytes or interphase forming materials like LiPON and the application of mechanical pressure. The insertion of interfacial protection layers also showed promising results. However, the prevention of internal metal deposition and dendrite formation are the most important issues that have to be clarified to enable the use of alkali metals in ASSBs.

8 Appendix 1 – Synthesis and characterization of solid electrolytes

In this section, the synthesis and characterization¹ of the solid electrolytes and one sacrificial layer compound are described. The chemicals are summarized in Tab. 8.1. The purpose of this section is to give details that are necessary to reproduce the synthesis of the used materials and to give guidance for further research on these materials.

Table 8.1: Supplier, purity and annealing parameters for the starting materials used for synthesis.

Material	Supplier	Purity / %	Remarks
Li ₂ CO ₃	Sigma Aldrich	99	
La ₂ O ₃	Chempur	99.999	Annealed for 12 h at 900 °C
ZrO ₂	Chempur	99.995	
TiO ₂	Chempur	99.99	
Ta ₂ O ₅	Chempur	99.99	
γ-Al ₂ O ₃	Chempur	99.999	
Al(OH) ₃	Chempur	99.9	
H ₃ PO ₄	Sigma Aldrich	99.99	85 wt% in H ₂ O
LiOH	Chempur	99	
Na ₂ CO ₃	Sigma Aldrich	99.999	
BaCO ₃	Sigma Aldrich	99.999	
GeS	Sigma Aldrich	99.99	Bought as GeS
Na ₂ S	Sigma Aldrich	99.99	
Li ₂ S	Sigma Aldrich	99.98	
P ₂ S ₅	Sigma Aldrich	99	
PCl ₅	Sigma Aldrich	98	
NH ₄ Cl	Sigma Aldrich	99.998	

For conductivity measurements blocking gold electrodes were used (and deposited by an in-house constructed vapor-deposition chamber) and impedance analysis was performed using a sp300 impedance analyzer (Biologic). Data fitting was carried out with the RelaxIS software package (rhd instruments) and the standardized (RQ)_{bulk}-(RQ)_{gb}-Q equivalent circuits (Q: constant phase element), describing the bulk and grain boundary contributions, respectively. A climate chamber (Weiss Klimatechnik) was used for the temperature dependent impedance measurements, in order to gain the activation energy. For the application of equivalent circuits and the fitting procedures, the error tolerance was set to the standard program values (less than 2 %). Note that the experimental error, caused by temperature changes, uncertainty of the contact area and pellet thickness and small

¹Rietveld refinements were carried out for all samples, but are not shown here, as the intention of this work is focused on the interface/interphase. The Rietveld refinements were partially carried out by Dr. Dominik Weber and the author himself. In all cases, the refinements prove the phase purity of the samples, especially for the triclinic LPS.

deviations in the cell geometry causes far higher errors. The electronic conductivity was determined via a DC technique by application of 1 V to a cell using blocking gold electrodes. For this, a Keithley 6430 sub-femtoamp source meter was used. After steady state polarization was attained, constant current values were achieved, which were used to calculate the electronic conductivity by Ohm's law. In order to prove the phase purity, x-ray diffraction was carried out. Therefore, stainless steel sample holders were used, which were sealed with an adhesive polyimide foil in the argon atmosphere of the glove box (MBraun). Measurements were carried out on a PANalytical Empyrean powder diffractometer with Cu K $_{\alpha}$ radiation² in Bragg-Brentano $\Theta - \Theta$ geometry, using a PIXcel detector with 255 measuring channels. Diffraction diagrams in a 2Θ range of 10° to 90° with a step size of 0.026° and a counting time of 270 s per step were recorded. A few measurements were carried out on a STOE Stadi-P diffractometer in Debye-Scherrer geometry, applying monochromatic Cu K $_{\alpha 1}$ radiation ($\lambda = 154.056$ pm) and a Mythen2 R 1K detector with 1280 strips (BELLA, KIT). Samples were sealed under argon in borosilicate glass capillaries (Hilgenberg) and the diffraction pattern were recorded in a 2Θ range of 10° to 80° with a step size of 0.012° and a counting time of 780 s per step^[78]. All synthesis steps were conducted in a Nabertherm oven for temperatures up to 1200°C . For temperatures between 1200°C and 1700°C a MoSi oven was used. Rough milling was conducted by using ZrO $_2$ balls with 5 mm diameter, and for fine milling and reaction milling, balls with 2 mm diameter were used (Fritsch Pulverisette 5 Premium line).

² $\lambda_1 = 154.056$ pm and $\lambda_2 = 154.539$ pm with $I(\lambda_2/\lambda_1) = 0.5$

8.1 Perovskites

The synthesis routes for $\text{Li}_{0.35}\text{La}_{0.55}\text{TiO}_3$ (LLTO) and $\text{Li}_{3/8}\text{Sr}_{5/8}\text{Ta}_{3/4}\text{Zr}_{1/4}\text{O}_3$ (LSTZO)³ are displayed in Fig. 8.1a and b, respectively.

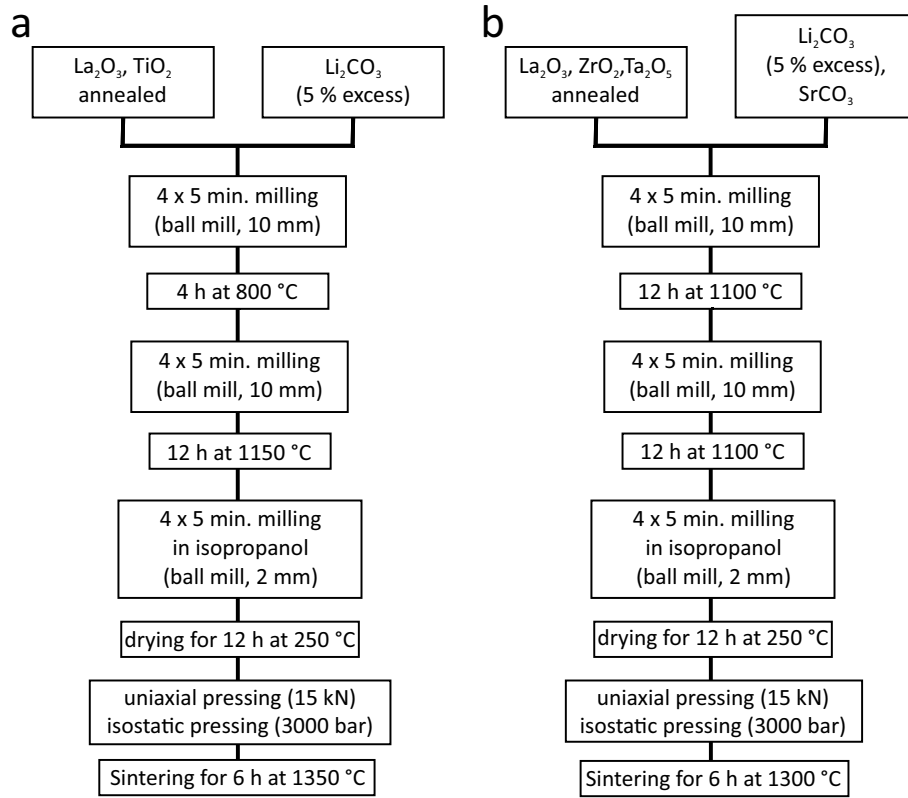


Figure 8.1: Synthesis route for LLTO and LSTZO are shown schematically in (a) and (b), respectively.

For this, high purity starting materials were used (see Tab. 8.1) and La_2O_3 was annealed before mixing to decompose $\text{La}(\text{OH})_3$ (which forms when La_2O_3 is in contact with air) and to guarantee an exact stoichiometry of the compounds. Synthesis was conducted according to the literature^[26,30].

To determine the activation energy of the compounds, temperature dependent impedance measurements were carried out, like described above. The results are shown in the Arrhenius plots in Fig. 8.2. The activation energies are then obtained by the slope of the fitted data and are summarized in Tab. 8.2, together with the electronic and ionic conductivities.

³LSTZO is described as $\text{Li}_{3/8}\text{Sr}_{5/8}\text{Ta}_{3/4}\text{Zr}_{1/4}\text{O}_3$ in the literature^[30] and the nomenclature is adopted.

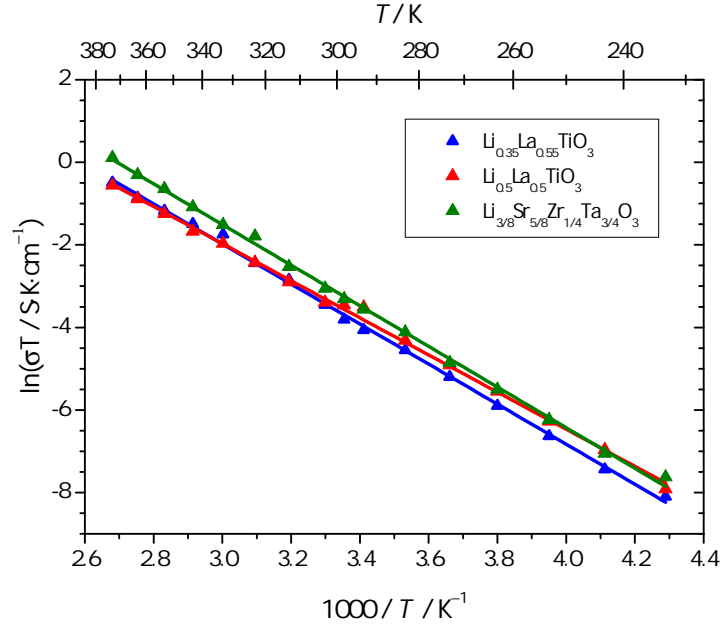


Figure 8.2: Arrhenius plots for the perovskite-type compound LSTZO, and two different LLTO compositions. The activation energies are summarized in Tab. 8.2.

Table 8.2: Summary of the activation energies, ionic and electronic partial conductivities of two compositions of LLTO and LSTZO at room temperature.

Material	E_A / kJ/mol	E_A / eV	σ_{ionic} / S/cm	σ_{electron} / S/cm
$\text{Li}_{0.35}\text{La}_{0.55}\text{TiO}_3$	40.3	0.42	$7.4 \cdot 10^{-5}$	$1.3 \cdot 10^{-11}$
$\text{Li}_{0.5}\text{La}_{0.5}\text{TiO}_3$	37.4	0.39	$1.1 \cdot 10^{-4}$	$1.5 \cdot 10^{-11}$
LSTZO	40.9	0.42	$1.2 \cdot 10^{-4}$	$6.0 \cdot 10^{-11}$

Tab. 8.2 shows that perovskite type compounds exhibit ionic conductivities up to approximately 0.1 mS/cm and electronic conductivities in range of 10 to 60 pS/cm. The ionic conductivities are in good agreement with literature values^[26,30], whereas the electronic partial conductivities were not reported so far.

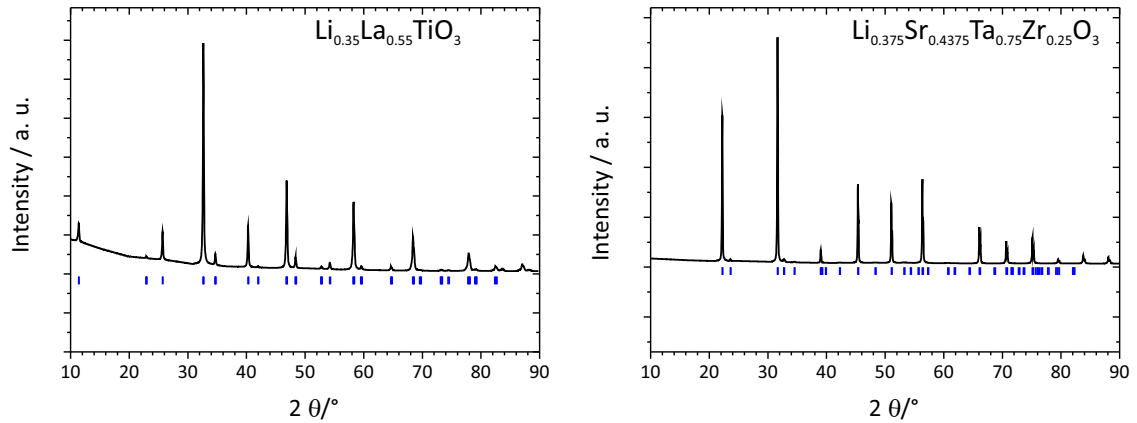


Figure 8.3: Diffraction diagrams of LLTO and LSTZO. The theoretical positions for the reflexes are marked in blue^[26,30].

The XRDs in Fig. 8.3 show the phase pure synthesis of the perovskite materials, except for $\text{Li}_{0.5}\text{La}_{0.5}\text{TiO}_3$, which has not been used in this work.

8.2 Garnet type materials

The synthesis route for garnet type materials^[33] is shown in Fig. 8.4, and the Arrhenius plots are shown in Fig. 8.5 and Fig. 8.6.

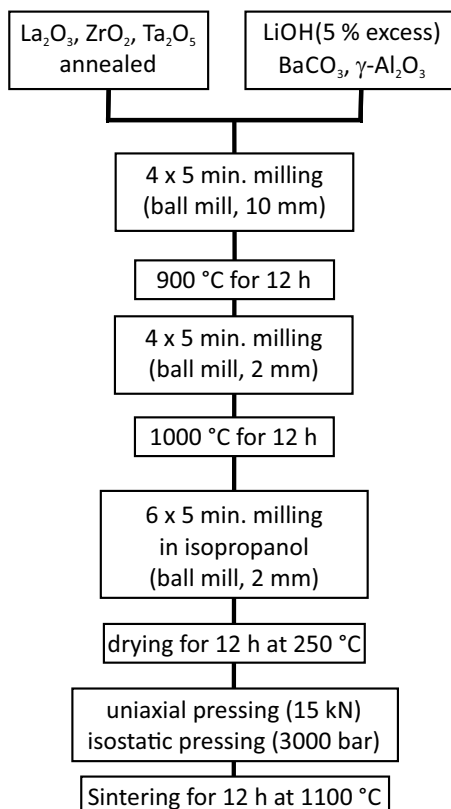


Figure 8.4: Synthesis route for the different compositions of the garnet type structures.

The resulting conductivities and the activation energies are summarized in Tab. 8.3, showing that the ionic conductivities for garnet type compounds range from 38 $\mu\text{S}/\text{cm}$ to 600 $\mu\text{S}/\text{cm}$. The electronic conductivities are low and in the range of a few pS/cm and the activation energies range from 0.41 to 0.56 eV. For the investigations in this work, only LLZO and LLTa₂O were used. This is mainly due to the insufficient intensities for XPS. The afore mentioned two compounds showed sufficient intensities for the Zr and Ta signals, respectively.

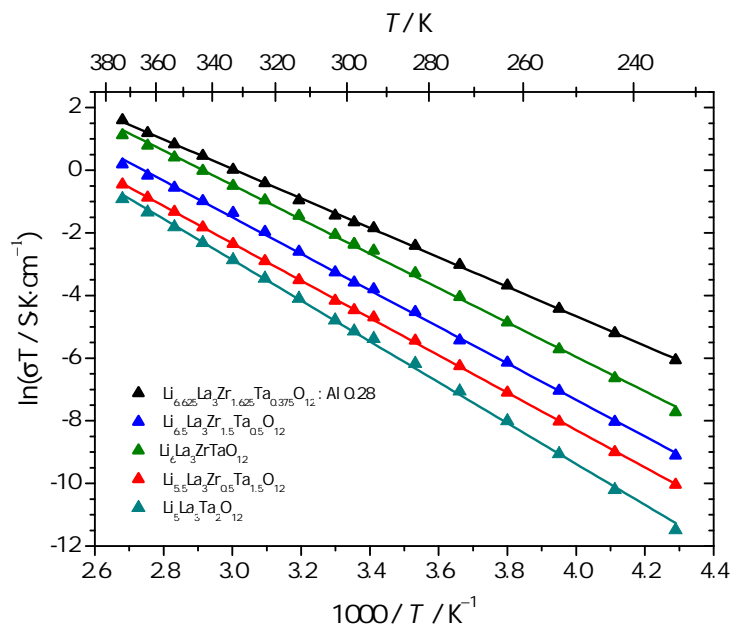


Figure 8.5: Arrhenius plots for the garnet type compounds. The activation energies are summarized in Tab. 8.3.

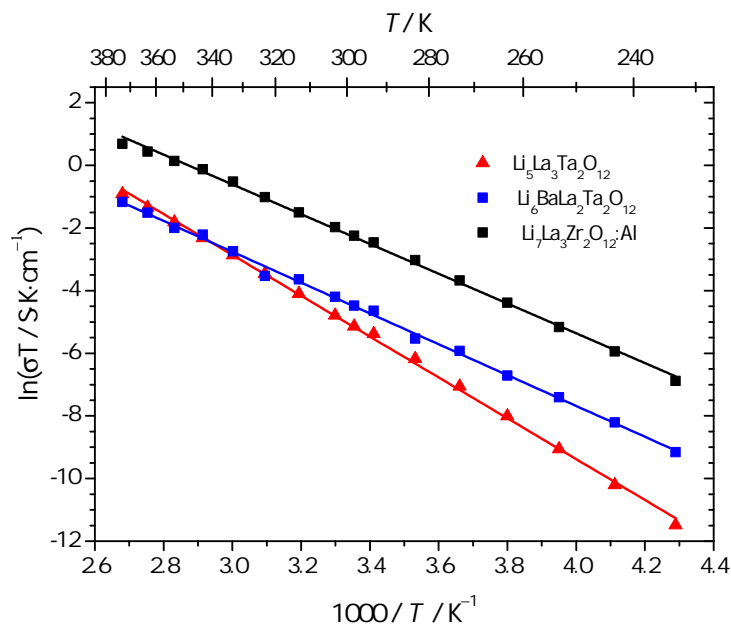


Figure 8.6: Arrhenius plots for the garnet type compounds. The activation energies are summarized in Tab. 8.3. LLTa₂O (Li₅La₃Ta₂O₁₂) is additionally shown in Fig. 8.5 to allow better comparison of the garnet type compounds.

Table 8.3: Summary of the activation energies, ionic and electronic partial conductivities for the garnet type compounds.

Material	E_A / eV	σ_{ionic} / S/cm	σ_{electron} / S/cm
$\text{Li}_{6.625}\text{La}_3\text{Zr}_{1.625}\text{Ta}_{0.325}\text{O}_{12}:\text{Al}$	0.41	$5.7 \cdot 10^{-4}$	$1.2 \cdot 10^{-11}$
$\text{Li}_{6.5}\text{La}_3\text{Zr}_{1.5}\text{Ta}_{0.5}\text{O}_{12}$	0.50	$8.8 \cdot 10^{-5}$	$3.0 \cdot 10^{-11}$
$\text{Li}_6\text{La}_3\text{ZrTaO}_{12}$	0.47	$2.7 \cdot 10^{-4}$	$8.9 \cdot 10^{-12}$
$\text{Li}_{5.5}\text{La}_3\text{Zr}_{0.5}\text{Ta}_{1.5}\text{O}_{12}$	0.51	$3.3 \cdot 10^{-5}$	$9.7 \cdot 10^{-12}$
$\text{Li}_5\text{La}_3\text{Ta}_2\text{O}_{12}$	0.56	$2.4 \cdot 10^{-5}$	$1.4 \cdot 10^{-11}$
$\text{Li}_6\text{BaLa}_2\text{Ta}_2\text{O}_{12}$	0.42	$3.8 \cdot 10^{-5}$	$9.2 \cdot 10^{-12}$
$\text{Li}_7\text{La}_3\text{Zr}_2\text{O}_{12}:\text{Al}$	0.41	$3.5 \cdot 10^{-4}$	$8.8 \cdot 10^{-12}$

The XRDs in Fig. 8.7 show that phase pure products were obtained by this synthesis route.

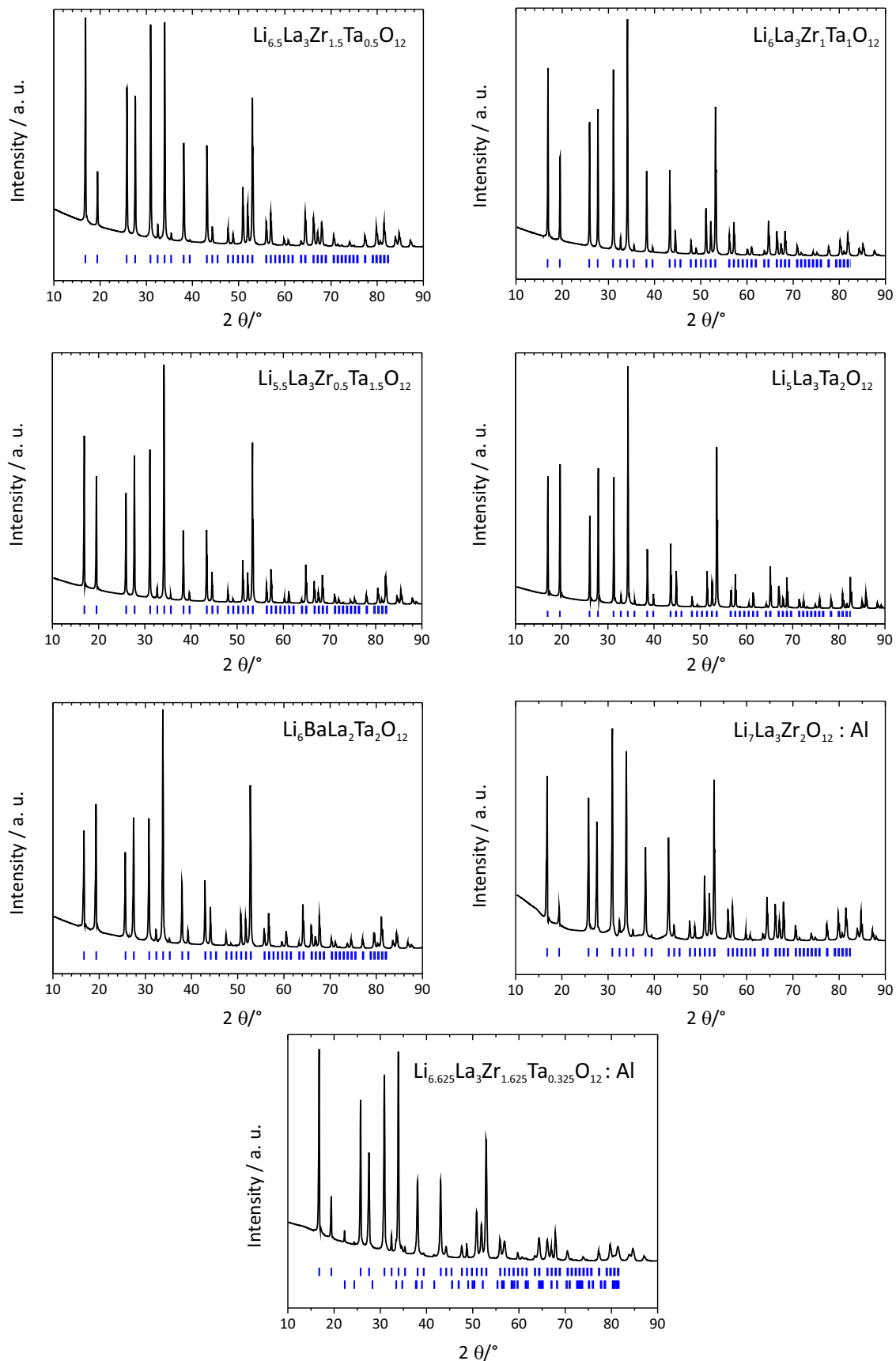


Figure 8.7: Diffraction diagrams of the garnet type compounds. The theoretical positions for the reflexes are marked in blue^[33]. The second phase for $\text{Li}_{6.625}\text{La}_3\text{Zr}_{1.625}\text{Ta}_{0.325}\text{O}_{12}:\text{Al}$ corresponds to LiAlO_2 , which fills pores between the LLTZO grains and hence increases the conductivity.

8.3 NASICON type materials – LATP

The synthesis route for the LATP compounds is schematically shown in Fig. 8.8. To prevent reactions of the carbonates with the phosphoric acid, the TiO_2 , $\text{Al}(\text{OH})_3$ and carbonate mixture was added slowly to the acid. In order to ease the grinding after drying the acid-solid mixture, citric acid was added to the solution, that decomposed during drying and strongly decreases the material density. After drying the material was easily grinded and pressed into a pellet.

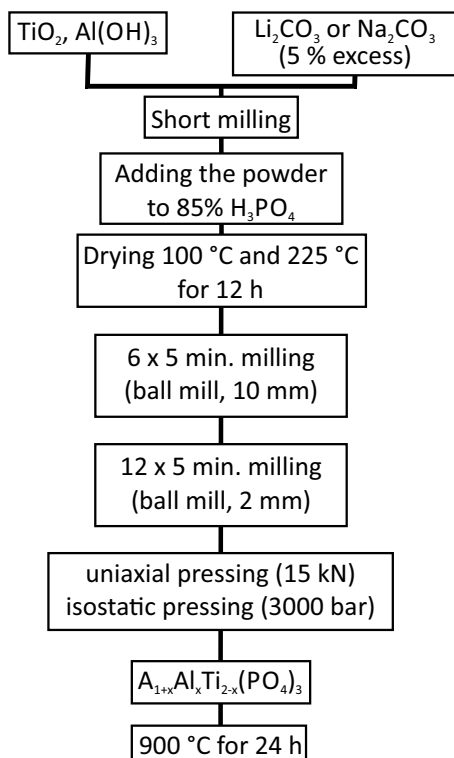


Figure 8.8: Synthesis route for the LATP compounds.

The Arrhenius plots are shown in Fig. 8.9 and the corresponding conductivity values and activation energies are summarized in Tab. 8.4, showing only small differences for the ionic and electronic conductivities. The conductivity of the NATP pellet was too small to be determined.

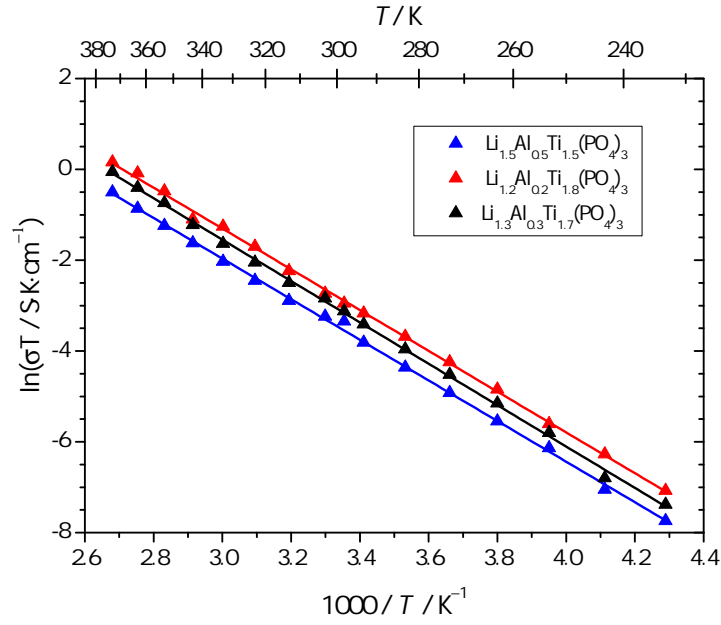


Figure 8.9: Arrhenius plots for the LATP compounds with three different compositions. The activation energies are summarized in Tab. 8.4.

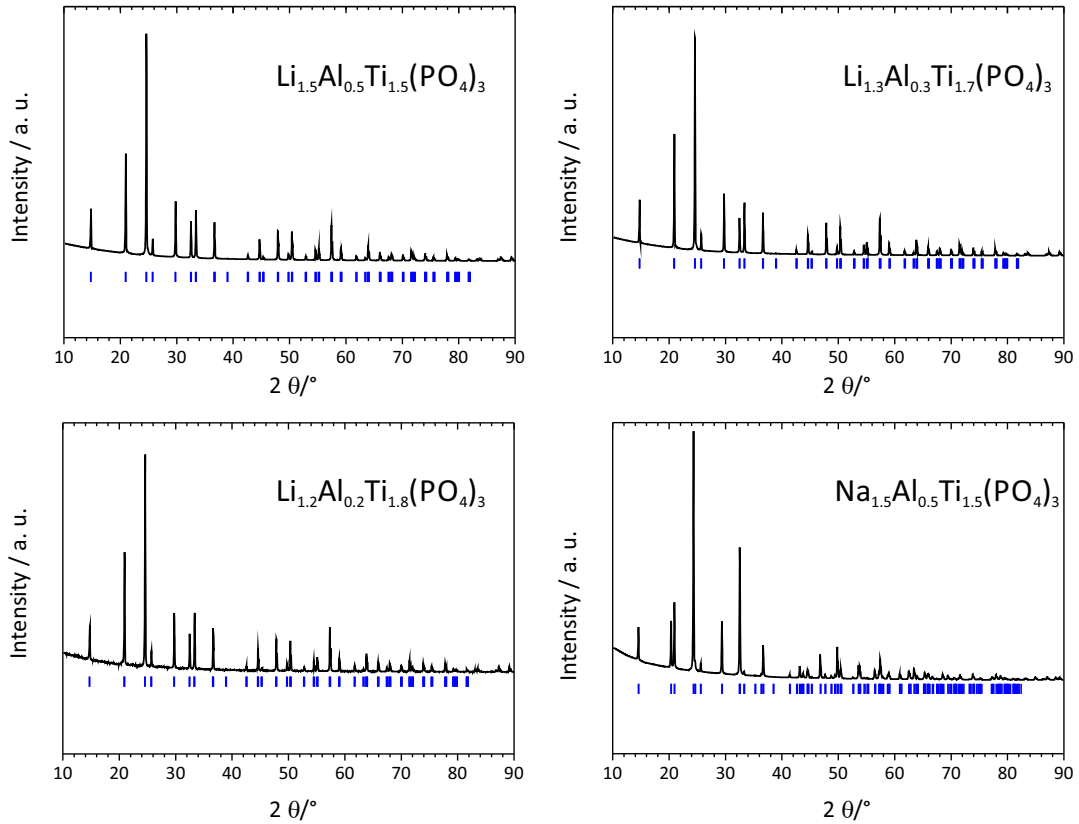


Figure 8.10: Diffraction diagrams of the LATP and NATP compounds. The theoretical reflex positions are marked in blue^[178].

The diffraction diagrams for the three different LATP compositions and for the NATP compounds (e. g. $\text{Na}_{1.5}\text{Al}_{0.5}\text{Ti}_{1.5}(\text{PO}_4)_3$) are shown in Fig. 8.10, proving the phase purity of the samples.

Table 8.4: Summary of the activation energies, ionic and electronic partial conductivities of three compositions of the LATP compounds.

Material	E_A / eV	σ_{ionic} / S/cm	σ_{electron} / S/cm
$\text{Li}_{1.5}\text{Al}_{0.5}\text{Ti}_{1.5}(\text{PO}_4)_3$	0.39	$1.2 \cdot 10^{-4}$	$2.3 \cdot 10^{-11}$
$\text{Li}_{1.3}\text{Al}_{0.3}\text{Ti}_{1.7}(\text{PO}_4)_3$	0.39	$1.5 \cdot 10^{-4}$	$2.5 \cdot 10^{-11}$
$\text{Li}_{1.2}\text{Al}_{0.2}\text{Ti}_{1.7}(\text{PO}_4)_3$	0.39	$1.7 \cdot 10^{-4}$	$2.1 \cdot 10^{-11}$

8.4 LPS, LGPS, NPS and beta-alumina

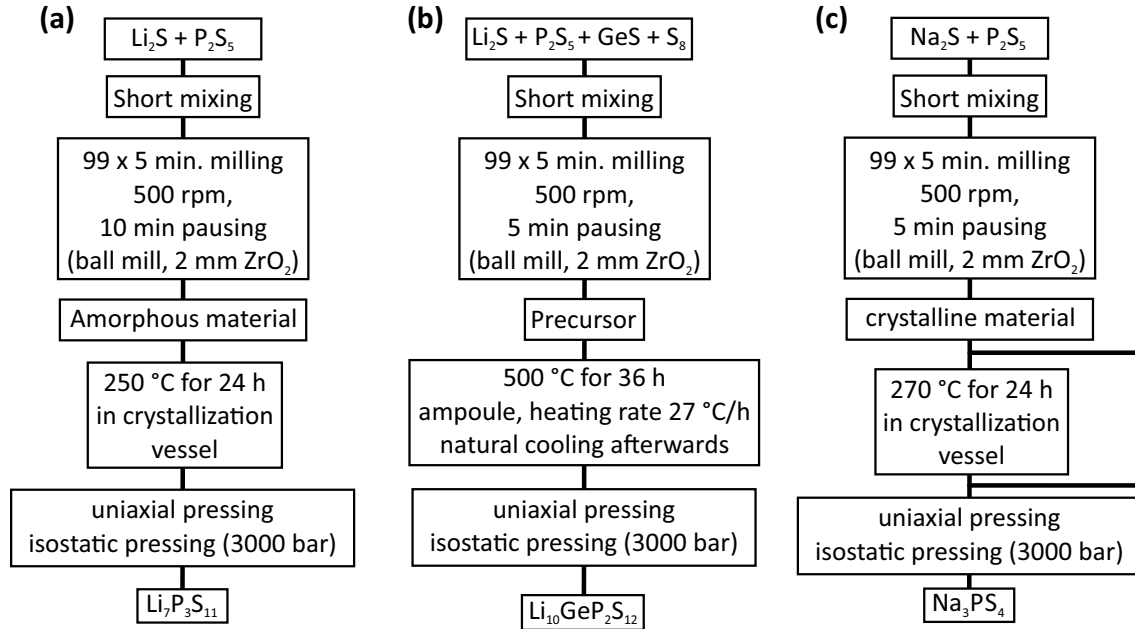


Figure 8.11: The synthesis routes for $\text{Li}_7\text{P}_3\text{S}_{11}$, $\text{Li}_{10}\text{GeP}_2\text{S}_{12}$ and Na_3PS_4 are displayed in (a), (b) and (c), respectively ^[12,16,20].

In the synthesis route for LPS and NPS, a crystallization vessel was used, consisting of a PTFE-sealed steel vessel, where the sample is placed in a borosilicate jar. The milled NPS compound showed reflexes for the cubic lattice after milling and reflex intensity could be increased by crystallization.

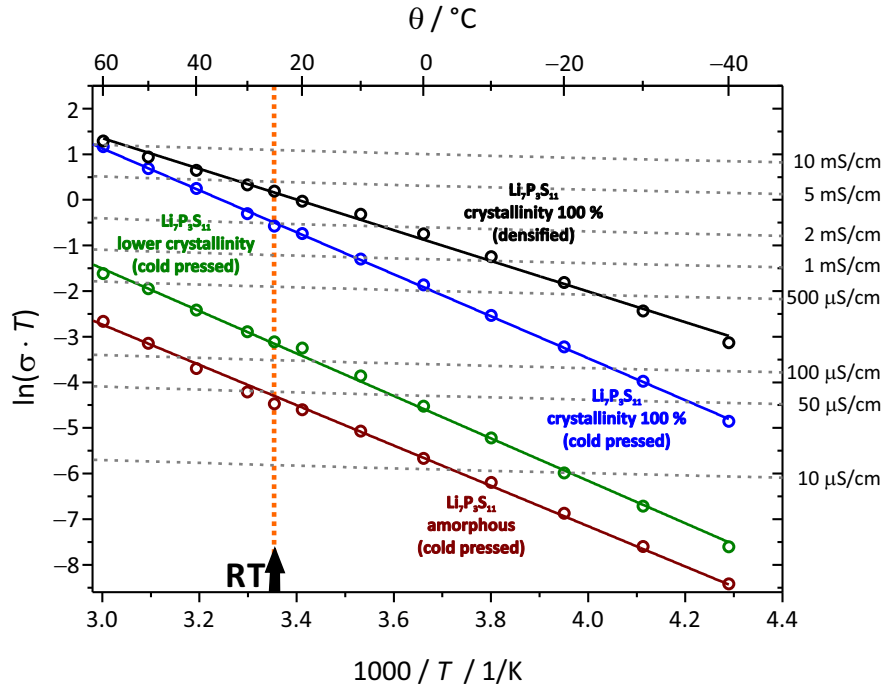


Figure 8.12: Arrhenius plots for LPS compounds, which were treated differently. Equi-conductivity lines are dotted gray to illustrate the conductivity values^[78].

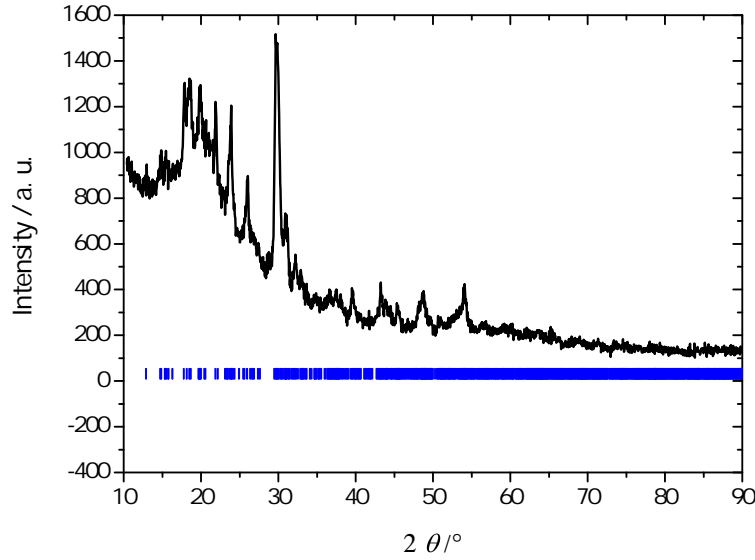


Figure 8.13: Diffraction pattern for the triclinic LPS. The theoretical reflex positions are marked in blue^[17].

The Arrhenius plot in Fig. 8.12 shows the data for differently treated samples. The amorphous material exhibits the highest slope (and therefore the highest activation energy) and the lowest conductivity. By crystallization, the conductivity and the activation energy are greatly influenced and exhibit higher σ and lower values E_A compared to the less crystalline materials, respectively. By densification of the sample (sintering) the grain boundary contribution, which seems to be the limiting factor, is decreased and the conductivity is increased. More information about the crystallinity values are reported by

Wenzel et al.^[78], where it is shown that the crystallinity yields 100 %. The diffraction pattern for LPS is shown in Fig. 8.13. The Rietveld refinements proved the phase purity of the samples^[78]. The enormous background is caused by the gas tight sample holder. The Arrhenius plot and the XRD for LGPS are shown in Fig. 8.14 and Fig. 8.15, respectively. The latter shows that the material is phase pure. The activation energy is given in Tab. 8.18.

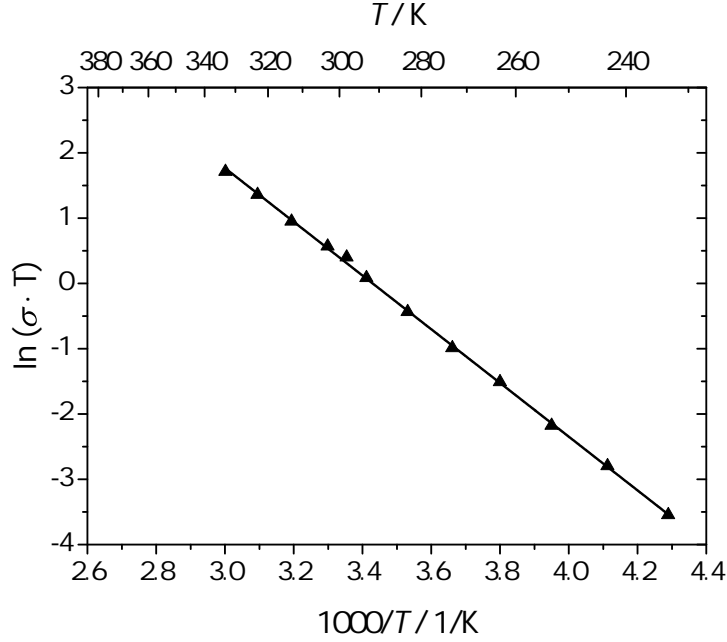


Figure 8.14: Arrhenius plot for LGPS^[82].

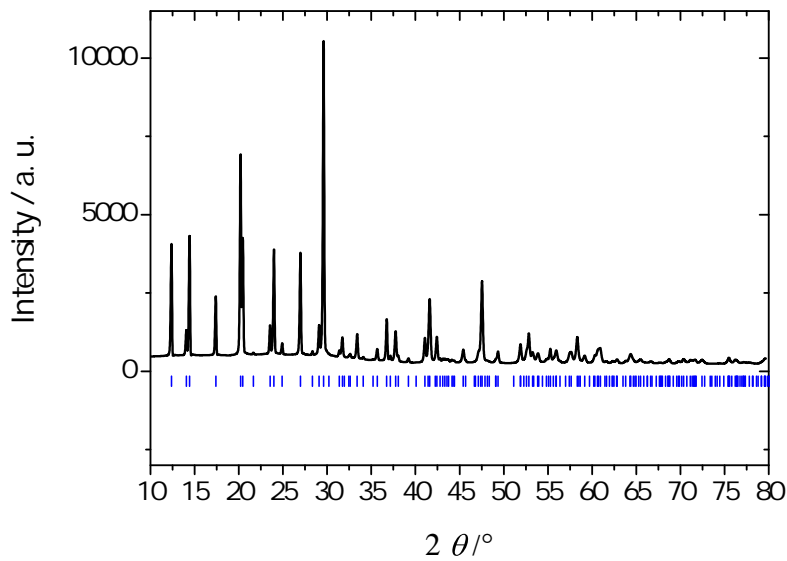


Figure 8.15: Diffraction pattern for LGPS. The theoretical reflex positions are marked in blue^[13].

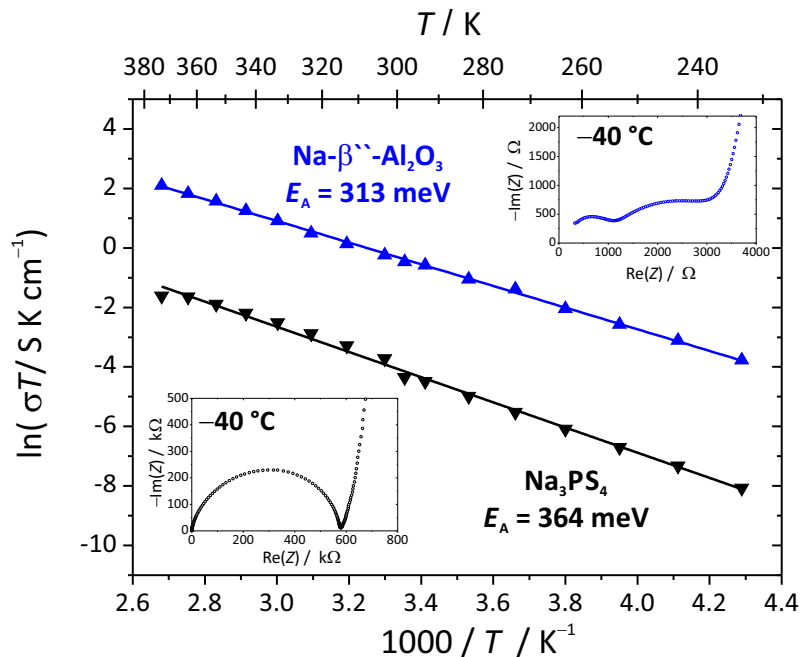


Figure 8.16: Arrhenius plots for Na_3PS_4 and β'' -alumina. The insets display sample Nyquist plots at -40°C for both compounds, respectively^[43].

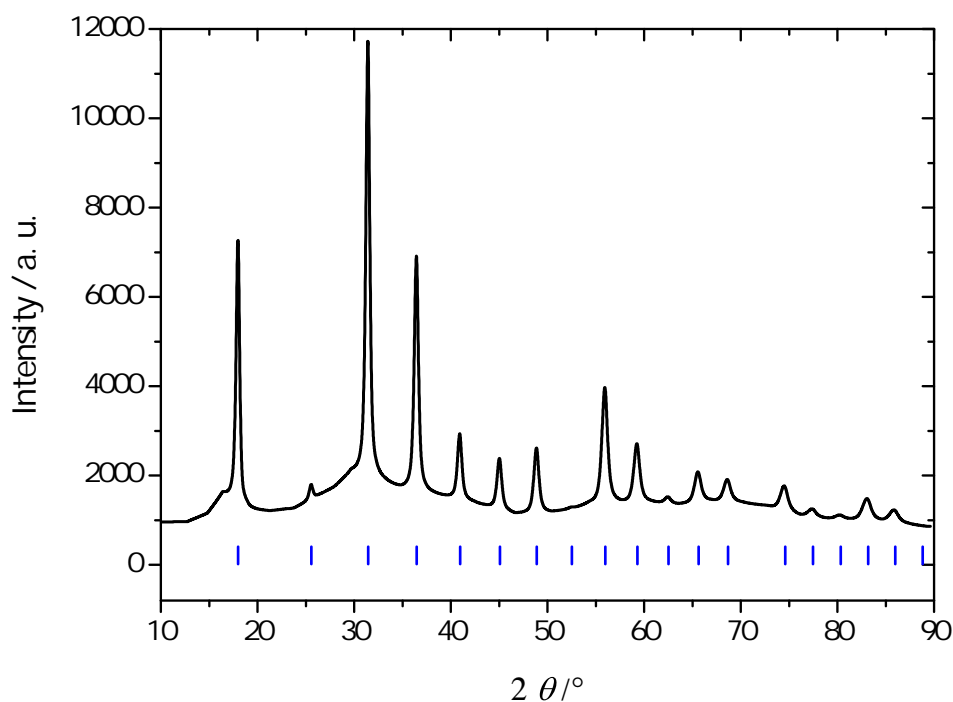


Figure 8.17: Diffraction pattern for NPS. The theoretical reflex positions are marked in blue^[21].

The Arrhenius plots for NPS and β'' -alumina are shown in Fig. 8.16. A summary of all

values is given in Tab. 8.5. Fig. 8.17 displays the diffraction pattern of NPS. The reflex positions are in good agreement with the theoretical values and hint that this material is phase pure. To the contrary, β'' -alumina, which was bought from Ionotec Ltd., showed a minor second phase, as seen in Fig. 8.18. The impurity does not seem to have a significant effect on the conductivity.

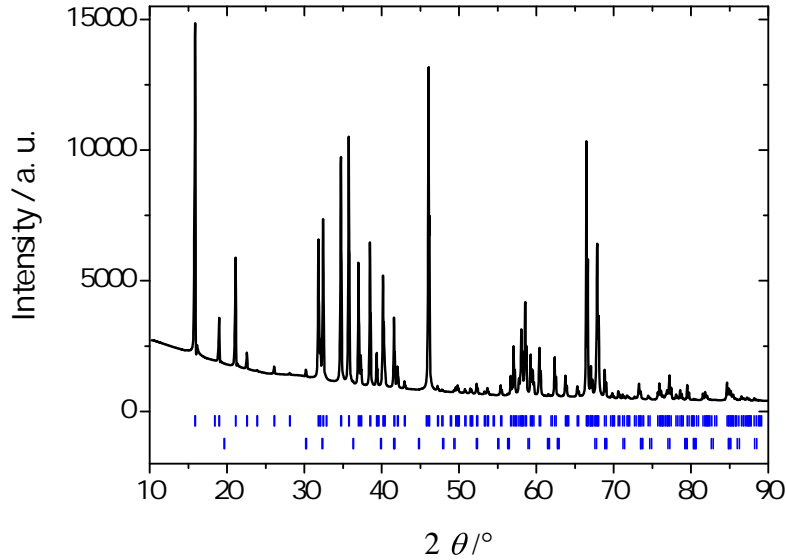


Figure 8.18: Diffraction pattern for β'' -alumina. The theoretical reflections positions for β'' -alumina (main component) and a second phase (NaAlH_4) are marked in blue.

The activation energies, the ionic and electronic partial conductivities are summarized in Tab. 8.5. All lithium ion conducting materials show values in the range of a few mS/cm for the ionic and several nS/cm for the electronic transport. NPS exhibits an ionic conductivity of 0.04 mS/cm and the value for the electronic conductivity shows a comparable value to the lithium containing compounds. The β'' -alumina (Ionotec Ltd.) exhibits a significantly smaller electronic conductivity of values less than $6.0 \cdot 10^{-12}$ S/cm. An ionic conductivity of 2 mS/cm is guaranteed by the manufacturer and often a value of 2.1 mS/cm is found.

Table 8.5: Summary of the activation energies, ionic and electronic partial conductivities for LGPS, NPS, LPS and densified LPS. The values for β'' -alumina (Ionotec Ltd.) are displayed, too.

Material	E_A / eV	σ_{ionic} / S/cm	σ_{electron} / S/cm
$\text{Li}_{10}\text{GeP}_2\text{S}_{12}$	0.35	$5.0 \cdot 10^{-3}$	$9.0 \cdot 10^{-9}$
Na_3PS_4	0.36	$4.0 \cdot 10^{-5}$	$2.5 \cdot 10^{-9}$
$\text{Li}_7\text{P}_3\text{S}_{11}$	0.39	$1.9 \cdot 10^{-3}$	$2.1 \cdot 10^{-9}$
$\text{Li}_7\text{P}_3\text{S}_{11}$ (densified)	0.29	$4.1 \cdot 10^{-3}$	$2.1 \cdot 10^{-9}$
Na- β'' -alumina	0.31	$2.1 \cdot 10^{-3}$	$6.0 \cdot 10^{-12}$

8.5 Argyrodite

The argyrodite compound was prepared by Dr. Stefan Sedlmaier (BELLA, Karlsruhe Institute of Technology) and was phase pure. The activation energy and ionic conductivity

are summarized in Tab. 8.6 and were provided (and determined) by Stefan Sedlmaier.

Table 8.6: Summary of the activation energies and ionic conductivities for the argyrodite compound.

Material	E_A / eV	σ_{ionic} / S/cm
Li ₆ PS ₅ Cl	0.32	$1.3 \cdot 10^{-3}$

8.6 Content classified by JLU

[REDACTED]

[REDACTED] \rightarrow [REDACTED] (8.1)

[REDACTED]	[REDACTED]	[REDACTED]
[REDACTED]	[REDACTED]	[REDACTED]
[REDACTED]	[REDACTED]	[REDACTED]
[REDACTED]	[REDACTED]	[REDACTED]
[REDACTED]	[REDACTED]	[REDACTED]
[REDACTED]	[REDACTED]	[REDACTED]

9 Appendix 2 - Technical approaches and in situ XPS

9.1 Technical approaches

9.1.1 DC resistance measurements

In this section, detailed information about the DC techniques are given. In order to determine the partial electronic conductivity a DC polarization technique was used. Therefore, a symmetric cell with blocking gold electrodes was prepared and polarized with 1 V. Thus, firstly the solid electrolyte is polarized and after the polarization process is finished, only electronic conduction is taking place. According to Ohm's law, the resistance is then calculated by dividing the voltage by the current and thus, the electronic conductivity is calculated by the resistance and cell constant^[33]. It should be noted that the resulting electronic partial conductivity is an average value for the applied voltage range. As no reference electrode is used, the results should only be taken as rough estimates.

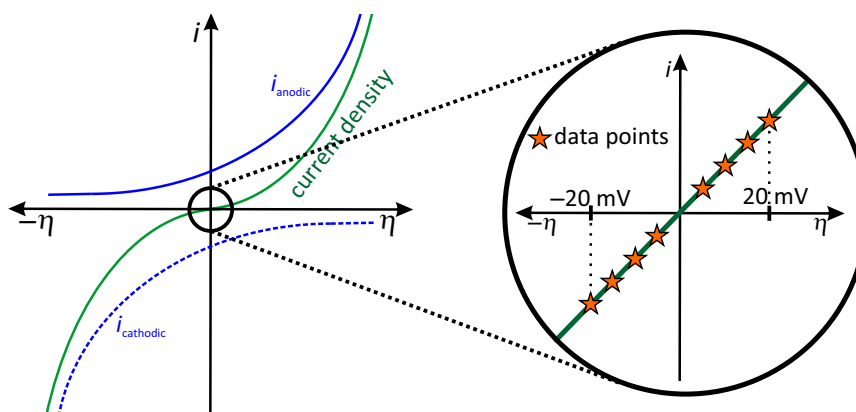


Figure 9.1: The typical Butler-Volmer plot is shown on the left side and the linear region at the origin is displayed on the right side. The data points are indicated with orange colored stars.

The second DC technique^[179,180] was used in order to gain information about the fast decomposition of MCI forming materials. As impedance spectroscopy is notably slow and one scan takes between 2 min and 15 min, depending on the resolution and number of data points, an alternative DC technique was used. For this, a symmetric cell using two alkali metal electrodes was prepared and voltages between -20 mV and 20 mV were applied and the current was recorded, according to the linear range of the Butler-Volmer kinetics^[104]. A sketch of this technique is displayed in Fig. 9.1. By application of this technique the overall cell resistance is determined, including the charge transfer, interphase

and solid electrolyte contributions (grain boundary and bulk). The resistance is then obtained by the inverse slope of the fitted data. The advantage of this technique is speed. The determination of one resistance value takes only a few seconds, as only defined values for the voltage are applied to the cell. However, voltage pulses are used which corresponds to a non-equilibrium technique and therefore leads to deviations compared to steady state techniques. Similarly, the overall resistance is the only information, except the resistance changes, that is obtained. Using impedance techniques, the separation of the resistance contribution is only possible for the first few hours (see section 3.5.4) and afterwards the relevant data cannot be recorded due to extremely low resistance values (time constants). Thus, the two electrode DC technique is suitable for the determination of resistance changes caused by MCI formation.

9.1.2 CV for determination of the polarization resistance

For SEI formation, DC techniques show valuable results. The cell setup in Fig. 9.2 was used for the determination of the polarization resistance. The technique is already described in section 3.5.3. Using a simple CV technique in the range of -20 mV to 20 mV, the polarization resistance is determined by the inverse slope, again according to the Butler-Volmer model.

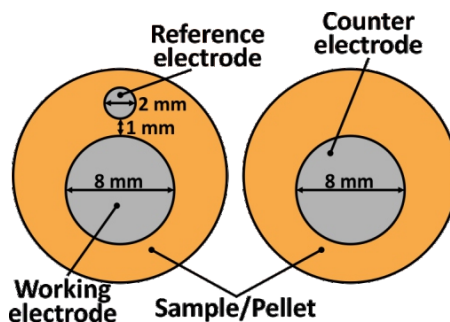


Figure 9.2: Schematical cell geometry for the determination of the polarization resistance by a CV technique^[82].

In order to separate the information content of impedance spectroscopy and the CV technique, Fig. 9.3 shows a schematic cross section of a cell and the respective resistance contributions. Using impedance spectroscopy four different resistance types can be obtained (but unfortunately not resolved in most cases): The charge transfer between electrode and interphase, the interphase resistance (bulk and grain boundary contributions), the charge transfer between the interphase and the solid electrolyte and the solid electrolyte resistance (bulk and grain boundary contributions), respectively. However, the different contributions are either not recorded which is often the case for solid electrolytes with high conductivities, or not resolved and thus cannot be separated. Therefore, the two resistance contributions of the solid electrolyte and interphase are combined, respectively. The charge transfer resistances are often found at very low frequencies and were not considered in this project¹.

¹Reasons for this are the low frequency range and the resulting temporal difficulties, leading to strong changes during the data recording.

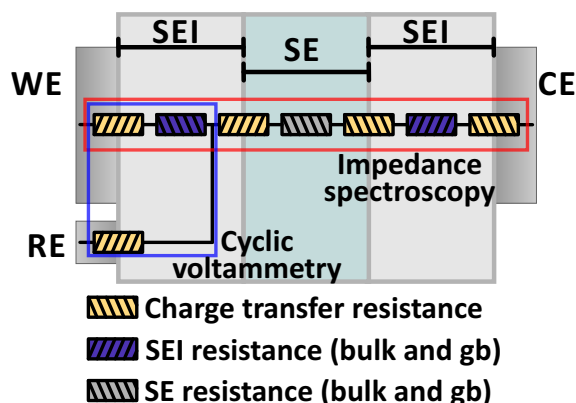


Figure 9.3: Theoretical resistance contributions of a cell that consists of alkali metal electrodes (working electrode WE, reference electrode RE and counter electrode CE) on a solid electrolyte pellet.

The CV method, by application of the reference electrode, operates comparably to a potential divider and therefore the counter electrode (CE) is not considered during data recording. Using this approach, the polarization resistance between electrode and interphase and the interphase resistance are summarized and obtained by the inverse slope of the linear voltage-current plot.

9.2 In situ XPS technique – additional information

In this section, additional information about the in situ XPS technique is provided. The setups are shown in Fig. 9.4. Fig. 9.4a shows the setup for angle resolved measurements. For this, the target holder is placed in the middle of the sample holder and the sputter position has to be adjusted according to the distance between the new and the initial target position. In Fig. 9.4b, the standard in situ XPS setup is shown and Fig. 9.4c shows the setup mounted on a XPS sample holder directly after deposition with an attached sample. The entire sample holder in Fig. 9.4d was constructed in order to directly polarize the solid electrolytes in the XPS chamber in order to determine the decomposition products at higher voltage. The sample holder was later used by Torben Krauskopf in his bachelor thesis^[181].

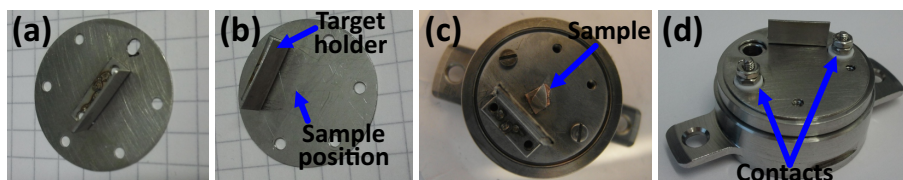


Figure 9.4: The in situ XPS setup is shown for angle resolved measurement in (a), the standard setup in (b) and the mounted setup after deposition in (c). The in situ sample holder with electronic contacts is shown in (d).

In order to determine the amount of deposited alkali metal, the intensity changes for lithium metal on a MgO single crystal and sodium metal on β'' -alumina were used. The following equation^[107] was applied in order to determine the deposition rate:

$$I = I_0 \cdot \exp\left(\frac{-d}{\lambda \cdot \cos(\alpha)}\right) \quad (9.1)$$

I is the peak intensity, I_0 the peak intensity at $t = 0$ s, d is the thickness, λ the effective attenuation length (EAL) and α the angle between the analyzer and the x-ray source. Rearrangement and insertion of $d = t \cdot r$ (t is the time, r the deposition rate) leads to equation 9.2:

$$\ln\left(\frac{I}{I_0}\right) = -\frac{t \cdot r}{\lambda \cdot \cos(\alpha)} \quad (9.2)$$

The natural logarithm of the ratio between the intensity and the initial intensity is plotted against the deposition time in Fig. 9.5. Then, the deposition rate is obtained by equation 9.3:

$$r = m \cdot \lambda \cdot \cos(\alpha) \quad (9.3)$$

The EALs for sodium and lithium metal were taken from the NIST EAL database^[107].

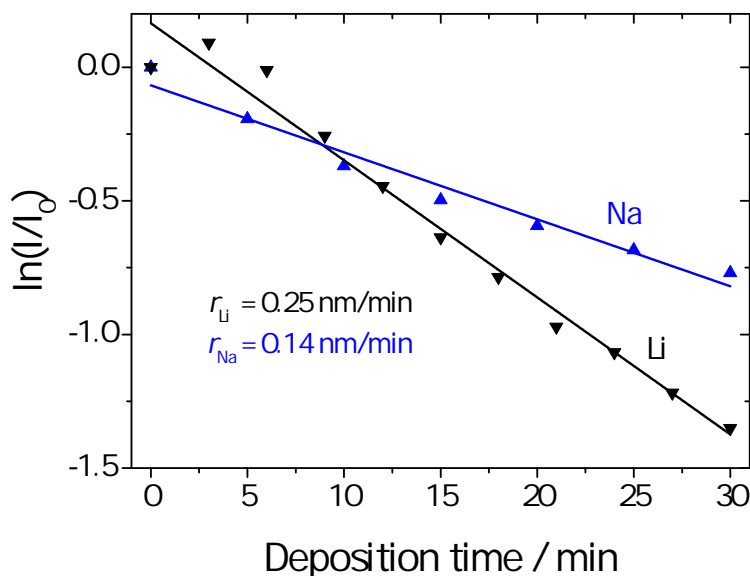


Figure 9.5: Plot of the natural logarithm of the ratio between the intensity and the initial intensity versus the deposition time for sodium and lithium metal, respectively. See equation 9.2.

In Fig. 9.6, the deposition profile of lithium metal on nickel metal is shown. As the nickel metal exhibits only small oxygen contents, due to nickel oxide at the surface, the lithium oxide growth during deposition can be observed. Fig. 9.6 shows that the oxide content is strongly increased during lithium metal deposition and approaches a ratio of 2:1 for lithium and oxygen, respectively. Thus, lithium oxide is formed during the deposition process of lithium metal due to oxygen traces in the UHV chamber and is only found at the surface and can be easily removed by depth profiling, leading again to lithium metal².

²During lithium deposition, the sample surface is protected from reactions with oxygen. After the deposition step, the formation of an oxide surface film is observed.

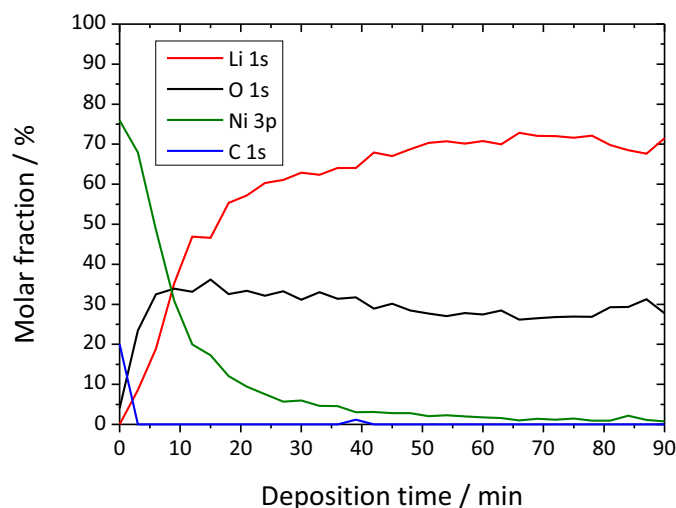


Figure 9.6: The changes of the element ratios of nickel, lithium, oxygen and carbon are shown during the deposition of lithium metal.

9.3 Additional information about interphase forming materials

The charge referencing was conducted via the signal for adventitious carbon at around 284.8 eV for every material. Sometimes, the signal of another stable compound, like the La 3s signal, was used together with the carbon signal.

9.3.1 LLTO

Fig. 9.7a shows a stacked plot of different deposition states for lithium metal on LLTO for the Ti 2p line, as a supplementation of the data shown in section 3.6.1.

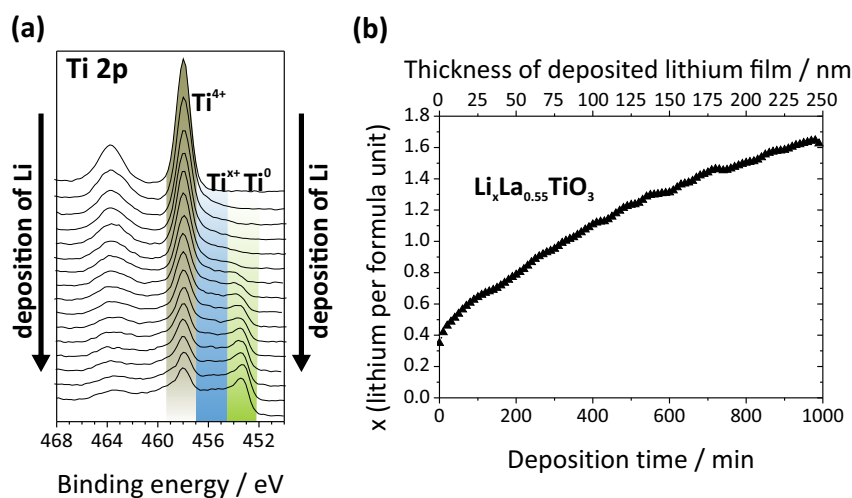


Figure 9.7: A stacked plot of the Ti 2p spectra for the lithium metal insertion into LLTO is shown in (a). In (b), the calculated fraction of inserted lithium metal is calculated with the data described in section 3.6.1^[61].

In Fig. 9.7b, the fraction of inserted lithium metal is displayed in dependence of the deposition time and the deposited lithium film thickness. The fraction starts at 0.35, which is the stoichiometric content of lithium in LLTO and increases to approximately the fourfold during deposition. Thus, a huge amount of lithium metal has been inserted into LLTO.

In the following the peak fit model for the Ti 2p line of LLTO is described. The FWHMs for Ti 2p_{3/2} were around 1.5 to 1.8 eV for all titanium signals, whereas the FWHMs for Ti 2p_{1/2} are generally broader compared to Ti 2p_{3/2}. Titanium metal exhibits a smaller FWHM of approximately 1.3 eV. For the fitting of the Ti⁴⁺, Ti³⁺ and Ti²⁺ signals a Gaussian-Lorentz line shape (GL(30)) was used. Ti⁰ is described by a Lorentzian asymmetric line shape with tail damping (LF(0.5,5,10,200)), due to coupling with conduction electrons. The areas of Ti 2p_{1/2} were fixed to half of the area of the Ti 2p_{3/2} signal, corresponding to the ratio of degeneracy. Detailed parameters for all titanium species are in good agreement with Biesinger et al.^[182] and given in Tab. 9.1.

Table 9.1: The XPS fitting parameters for the Ti 2p line of LLTO. Similar parameters were used for all titanium containing materials (e. g. LATP).

	2p _{3/2} ⁴⁺	2p _{1/2} ⁴⁺	2p _{3/2} ³⁺	2p _{1/2} ³⁺	2p _{3/2} ²⁺	2p _{1/2} ²⁺	2p _{3/2} ⁰	2p _{1/2} ⁰
Line shape	GL(30)	GL(30)	GL(30)	GL(30)	GL(30)	GL(30)	LF	LF
A constraint	/	· 0.5	/	· 0.5	/	· 0.5	/	· 0.5
FWHM	1.5	2.6	1.8	2.2	1.6	1.6	1.3	1.2
ΔFWHM	1.4 , 1.6	2 , 3	1 , 2	1 , 3	1 , 2	1 , 3	1 , 2	1 , 2
Position	458.9	464.6	457.2	462.8	455.7	461.4	454.2	460.4
P constraint	±0.2	+5.7	±0.2	+5.6	±0.2	+5.7	±0.2	+6.1

9.3.2 LSTZO

The spectra of the pristine and decomposed LSTZO material are shown in Fig. 9.8a and b, respectively. The pristine material exhibits only one oxidation state for tantalum (5+) and zirconium (4+). After lithium metal deposition, both are reduced to lower oxidation states, including the metal. By comparing the relative intensity of the metal species to the pristine species, it is concluded that tantalum is heavily reduced, whereas zirconium exhibits only small amounts of reduced species in relation to Zr⁴⁺.

Using the peak fit model that is summarized in Tab. 9.2 and displayed in Fig. 9.8a and b, the relative molar fractions for every deposition step can be obtained. The results are shown in Fig. 9.8c and d for zirconium and tantalum, respectively. Zirconium is reduced to suboxides at first and then the metal is formed. The fraction of metal and suboxides is generally low, compared to the Ta⁵⁺ fractions. For tantalum, reduced tantalum species are formed at the beginning and the tantalum metal formation starts after 120 min.

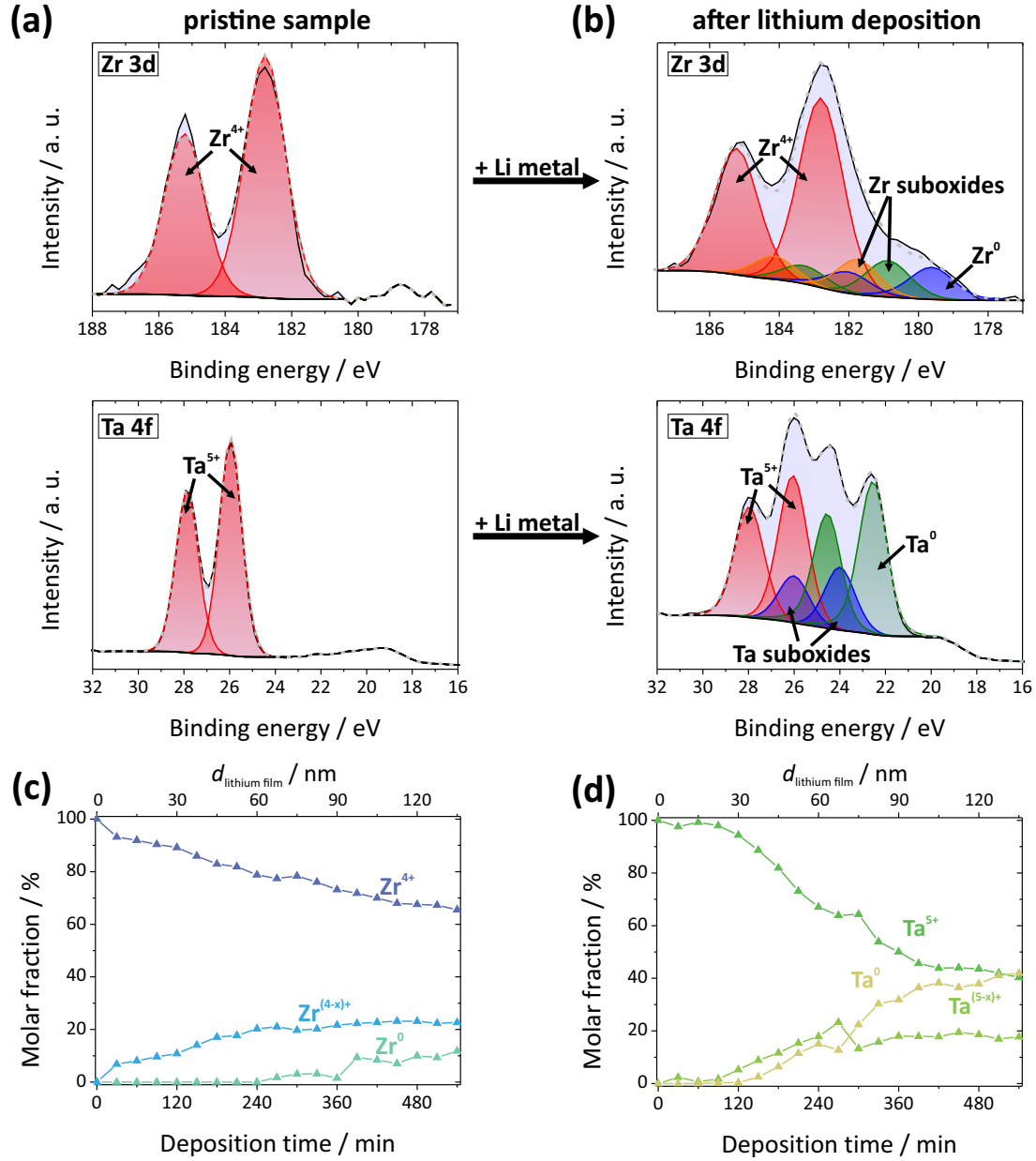


Figure 9.8: The peak fit models for the Zr 3d and Ta 4f signals for the pristine and deposited sample are shown in (a) and (b), respectively. The obtained deposition profiles for the different species are displayed in (c) for the Zr 3d and in (d) for Ta 4f species. Note that the relative molar fraction is only referring to one species.

Table 9.2: The XPS fitting parameters for the Ta 4f and Zr 3d line for LSTZO are summarized.

	$Ta^{5+} 4f_{7/2}$	$Ta^{n+} 4f_{7/2}$	$Ta^0 4f_{7/2}$
Binding energy / eV	26.1	23.9	22.5
FWHM / eV	1.52	1.56	1.42
Splitting / eV	1.9	2.0	2.0
	$Zr^{4+} 3d_{5/2}$	$Zr^{n+} 3d_{5/2}$	$Zr^0 3d_{5/2}$
Binding energy / eV	182.8	180.9 & 181.7	179.6
FWHM / eV	1.5	1.5	1.5
Splitting / eV	2.4	2.4	2.4

Using the profiles in Fig. 9.8c and d, a theoretical MCI thickness of 64 nm is calculated

after 540 min deposition. The resistance changes, recorded by the DC method described in section 9.1, for LSTZO are displayed in Fig. 9.9, showing a similar curve shape like LLTO and is, according to the resistance evolution and the in situ XPS results, assigned to an MCI forming material. The overall resistance in Fig. 9.9 approaches zero, comparable to LLTO. In the literature, this material is described as an inert compound in contact with lithium metal^[30]. The findings in this work are different. The results suggest that the MCI will lead to critical self-discharge of a battery after several hours.

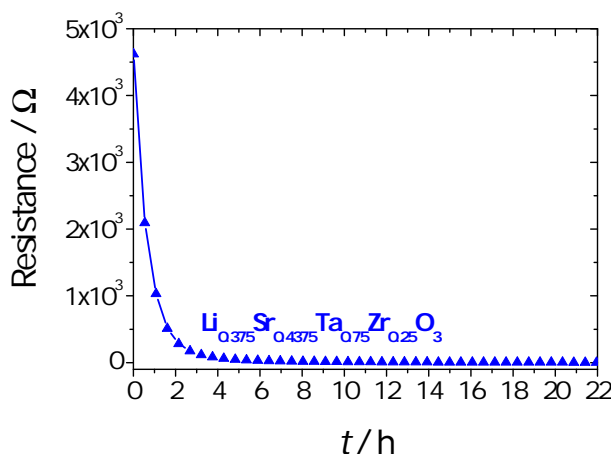


Figure 9.9: The resistance changes for a symmetric lithium metal/LSTZO cell, recorded by a DC technique.

9.3.3 LATP

The in situ XPS results for LATP are displayed in Fig. 9.10 and b for the pristine and the decomposed material, respectively. The pristine material exhibits only one oxidation state for titanium ($4+$). After lithium deposition, the material is heavily reduced and the major species is found to be Ti^{3+} . Small amounts of Ti^{2+} and Ti^0 are found, too. This finding is surprising, as for other titanium containing species, like LLTO, the major decomposition (reduced) species is titanium metal. The other species are only slightly affected. Aluminum is not reduced and the oxygen species only show the formation of lithium oxide species, which is mainly caused by the residual oxygen in the UHV chamber. Nevertheless, the P 2p line exhibits a new state around 126 eV that is assigned to Li_3P . It follows that some fraction of lithium oxide is formed by decomposition of phosphate. This finding is new, in the literature the decomposition of the phosphates in LATP type materials is not reported^[62].

Thus, the resistance changes might not be that strong compared to LSTZO and LLTO, as the fraction of formed metal is low. Other decomposition products were formed, too, that may not show high ionic or electronic conductivities, which will strongly influence (decrease) the resistance change. The deposition profile in Fig. 9.10e is obtained by applying the peak fit model in Fig. 9.10a and b to all spectra. Details of the peak fit model can be found in Tab. 9.1 (LLTO), as similar chemical species are formed. Only small binding energy and FWHM deviations (maximal 0.5 eV) were found, caused by the difference between oxide and phosphate.

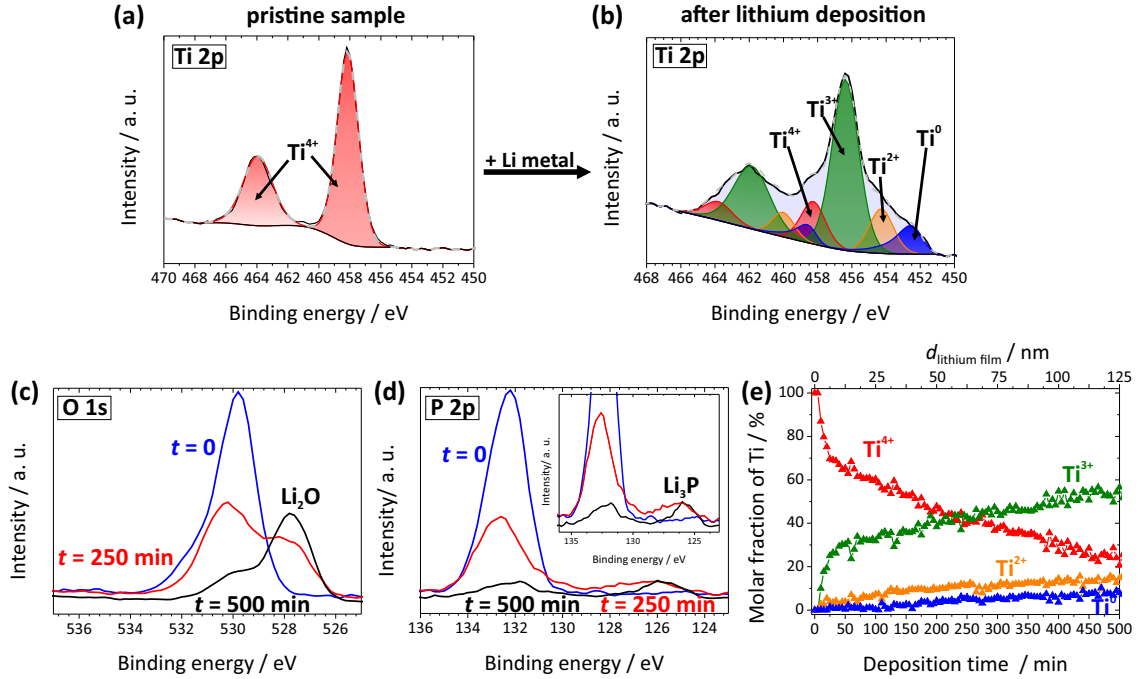


Figure 9.10: The photoelectron spectra for the pristine and decomposed titanium species of LATP are displayed in (a) and (b), respectively. The changes of the O 1s and P 2p line for three different deposition times are shown in (c) and (d), respectively. According to the peak fit model in (a) and (b), the molar fractions of the titanium species are obtained and displayed in (e).

Using the deposition profile in Fig. 9.10e, the MCI thickness is calculated to be 765 nm (only Ti is regarded). The resistance changes, again recorded by the DC technique, are depicted in Fig. 9.11. Here, the resistance is almost linearly decreasing, which is quite different to the findings for LLTO and LSTZO. This result might be explained by the formation of various decomposition products, which might be ionically insulating, as already stated above for the in situ XPS results. Thus, the overall conductivity is caused by a combination of ionic and electronic contributions.

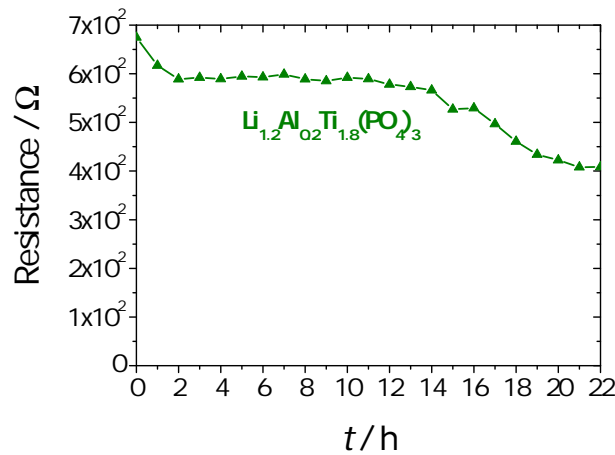


Figure 9.11: The resistance changes for a symmetric lithium metal/LATP cell, recorded by the DC technique.

9.3.4 LPS and LGPS

The peak fit model parameters for LPS are summarized in Tab. 9.3. A Gaussian-Lorentzian line shape (GL(30)) was used. The species were fitted using Shirley background correction. The $2p_{3/2}$ and the $2p_{1/2}$ area ratio was fixed to 0.5 according to the ratio of degeneracy; the FWHM values were constrained between 0.8 eV and 2 eV and were set to be equal for the corresponding $2p_{3/2}$ and the $2p_{1/2}$ peaks. For this material type (and LGPS, NPS and the argyrodites), the FWHMs are generally small.

Table 9.3: XPS fitting parameters for the pristine and the decomposed $\text{Li}_7\text{P}_3\text{S}_{11}$.

	S 2p P-S-P	S 2p P=S	S 2p P-S-Li	S 2p Li₂S
FWHM / eV	1.19	1.20	0.92	0.95
Position / eV	163	162.1	161.5	160
Position constraint (splitting) / eV	± 0.1 (1.4)	± 0.1 (1.4)	± 0.1 (1.22)	± 0.1 (1.1)
	P 2p P₂S₇⁴⁻	P 2p PS₄³⁻	P 2p Li₃P	P 2p reduced
FWHM / eV	0.98	1.25	1	1.6 & 1.5
Position / eV	131.9	132.9	126.7	130.2 & 127.7
Position constraint (splitting) / eV	± 0.1 (0.88)	± 0.1 (0.87)	± 0.1 (1.4)	± 0.1 (0.95 & 0.96)

The lithium metal formation on LPS is shown in Fig. 9.12 after the SEI formation is finished.

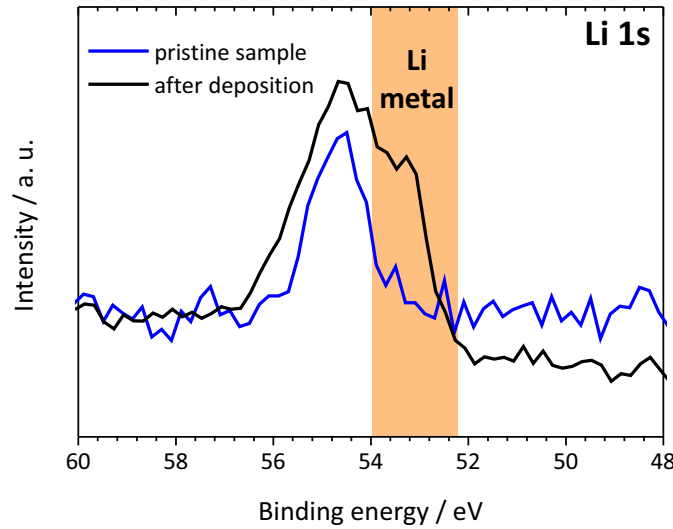


Figure 9.12: The Li 1s line before and after lithium metal deposition^[82].

Coupled fits were conducted by the following approach. The peak areas of Li_2O , Li_2S , Li_3P for the P 2p, O 1s and S 2p lines were coupled to the respective lithium signal. Therefore the following equation was used:

$$\frac{X_1}{X_2} = \frac{\frac{A_1}{RSF_1 \cdot T_1 \cdot MFP_1}}{\frac{A_2}{RSF_2 \cdot T_2 \cdot MFP_2}} \quad (9.4)$$

RSF is the relative sensitivity factor, T the transmission function, MFP the mean free path and A the peak area for component 1 and 2, respectively. The fraction X_1/X_2 is the nominal atomic ratio. By rearrangement, equation 9.5 is obtained, which is then used to calculate the area ratio of two atom types.

$$A_1 = A_2 \cdot \frac{X_1}{X_2} \frac{\frac{A_1}{RSF_1 \cdot T_1 \cdot MFP_1}}{\frac{A_2}{RSF_2 \cdot T_2 \cdot MFP_2}} = A_2 \cdot l \quad (9.5)$$

The transmission values were obtained by the CasaXPS software. The MFPs are regarded to be approximately the same for both components, which is a sufficient approach for main group elements. In principle, the MFP values can easily be calculated, but for real systems with an overlayer containing multiple compounds, the calculations are challenging and erroneous. By using this approach, the Li 1s and S 2p lines can be coupled, for example, and the fraction of Li of Li₂O, Li₂S, Li₃P etc. can be determined. Thus, the amount of reacted lithium metal can be determined, which then directly corresponds to the SEI thickness.

Fig. 9.13 shows a Bode diagram for the decomposition data of LPS in section 3.7.1. For high frequencies, the phase angle starts at negative values, which is often the case for ion conducting materials, as the capacitance of the electrodes is the major process. At lower frequencies, the phase angle approaches 0 and is hence corresponding to a pure resistive behavior. The resistance data for 0 h and 12 h show similar shapes, the latter exhibits distinctly higher values. Unfortunately, the resistance contributions of the solid electrolyte and the interphase could not be separated in the Bode plot, which is in good agreement with the results obtained by the Nyquist plots. The Bode plots do not provide additional information.

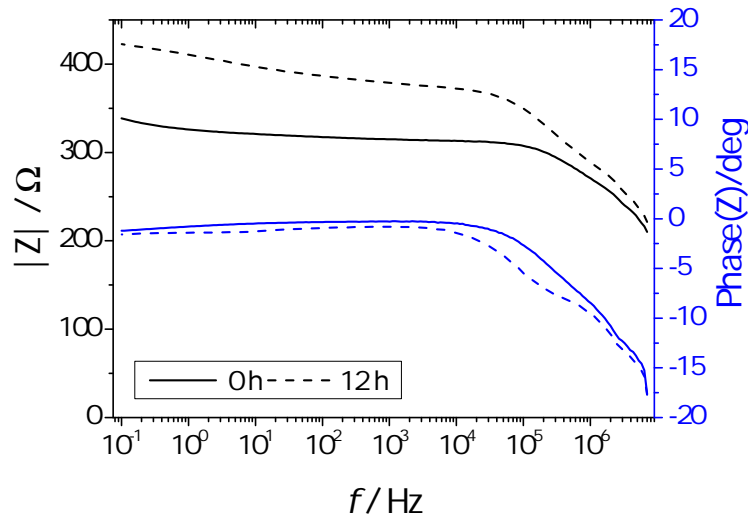


Figure 9.13: Bode plot for the decomposition of LPS (supporting information for section 3.7.1).

Stacked Nyquist diagrams for the decomposition of LPS and LGPS are shown in Fig. 9.14. For both, a resistance increase, that is larger for LGPS compared to LPS, is obviously seen.

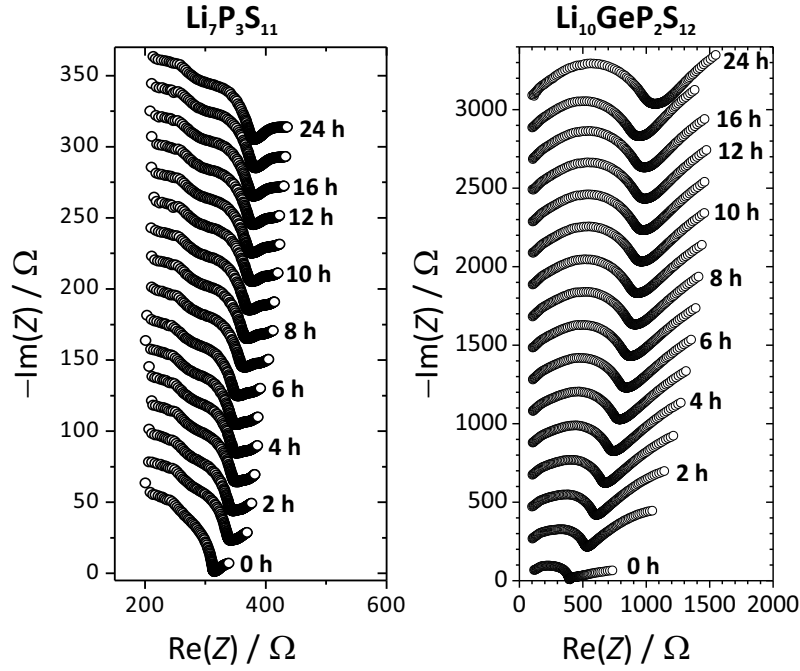


Figure 9.14: Stacked Nyquist plots for the decomposition of LPS and LGPS are displayed. The figure for LGPS is already published by Wenzel et al.^[82]. The data for LPS and LGPS are constantly stacked with 20 Ω and 200 Ω , respectively.

The Bode plot for LGPS is shown in Fig. 9.15 for contact times of 0 h and 12 h, respectively. This time, the resistance increase is drastically larger compared to LPS, which is in good accordance with the results in section 3.7.2. The phase angle exhibits a similar shape like found for LPS.

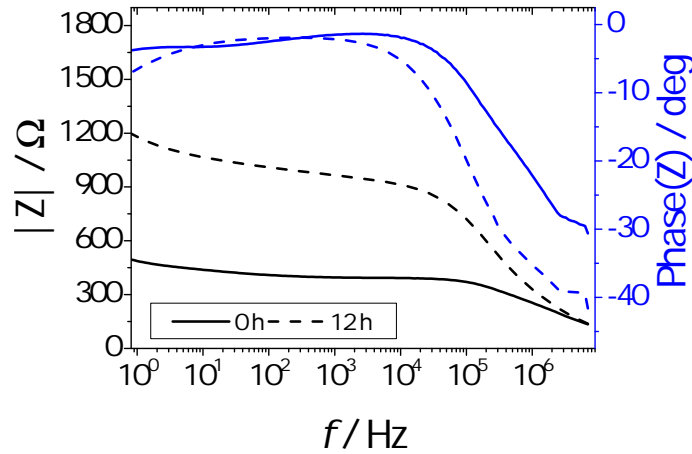


Figure 9.15: Bode plot for the decomposition of LGPS (supporting information for section 3.7.2). The figure is already published by Wenzel et al.^[82].

The fit parameters for LGPS are summarized in Tab. 9.4 and the fitting was conducted according to the experiences for LPS, so that the same conditions were applied to the LGPS spectra.

Table 9.4: Fit parameters for LGPS and its decomposition products. A Shirley background model was used.

	S 2p P=S	S 2p Ge/P-S-Li	P 2p PS ₄ ³⁻	Ge 3d of GeS ₄ ⁴⁻
Binding energy / eV	162	161.5	132	30.9
FWHM / eV	1	1.1	1.1	1.4
Splitting / eV	1.44	1.22	0.85	/
Ge 3d reduced	Ge 3d metal	S 2pLi ₂ S	P 2p Li ₃ P	P 2p reduced
28.6	27	160	126	130.5
1.5	1.5	1	1.1	1.05
/	/	1.2	0.85	0.9

9.3.5 Argyrodite

Beside LGPS and LPS, the material class of argyrodites shows promising properties. One example is the compound Li₆PS₅Cl, for which the stability and interphase formation in contact with lithium metal will be discussed in this section. The material was provided by Dr. Stefan Sedlmaier (KIT, BELLA) and the properties are already described in section 8 (again provided by Dr. Stefan Sedlmaier). Thus, the material showed a high ionic conductivity of 1.3 mS/cm, resulting in the assumption that the interphase might be the limiting factor for ASSB application (for thin films). To gain insight in the stability of the material, parts of the combined approach were used, namely the in situ XPS technique and time resolved impedance spectroscopy.

The deposition-state dependent XPS detail spectra are shown in Fig. 9.16 for S 2p, P 2p, O 1s, Cl 2p and Li 1s. The S 2p spectra show that a S²⁻ species is already found in the pristine compound. During deposition with lithium metal, more S²⁻ is formed. In the P 2p and O 1s spectra, the formation of Li₃P and Li₂O is observed. For Cl 2p no changes were found and in the Li 1s spectra, the formation of lithium metal is observed.

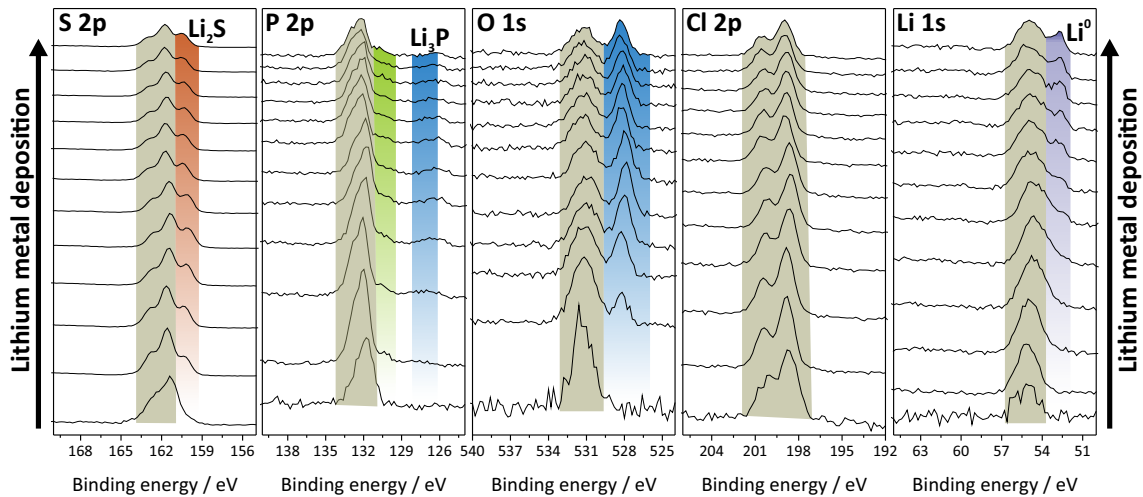


Figure 9.16: Deposition state dependent photoelectron detail spectra for the S 2p, P 2p, O 1s, Cl 2p and Li 1s signals of the LPSCl sample.

The peak fit models for Cl 2p, P 2p and S 2p are shown in Fig. 9.17 and the parameters are given in Tab. 9.5.

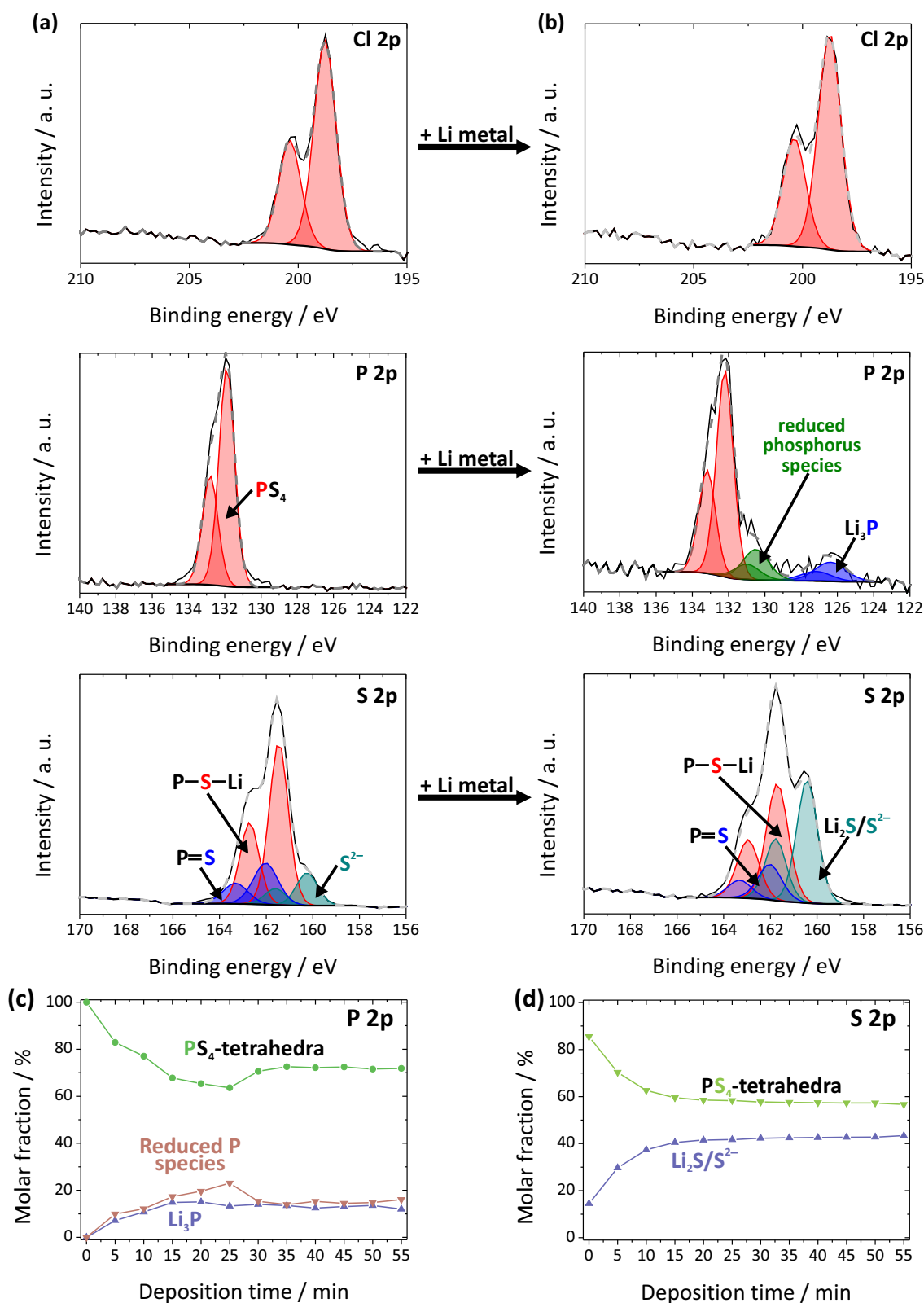


Figure 9.17: The photoelectron detail spectra of the pristine and the reacted samples including the peak fit model for the Cl 2p, P 2p and S 2p signal are shown in (a) and (b). (c) and (d) show the evolution of the decomposition products.

A detailed look at the spectra of the pristine and reacted samples in Fig. 9.17a and b clearly

shows that the Cl 2p species are unchanged during lithium metal deposition. For P 2p spectra, the decomposition of the pristine PS₄-tetrahedra (in a) to reduced phosphorus species (again fitted with an average peak) and Li₃P is seen in b. As the pristine sample already contains of S²⁻, the evolution of Li₂S could only be judged by the growth of the Li₂S/ S²⁻ signal. The initial S²⁻ signal and the unchanged chlorine signal are matching well with the structural model of the systems, as S²⁻ and Cl⁻ ions are incorporated in the structure in the ratio 1:1. The composition of the pristine sample does not match with the theoretical values, as the amount for incorporated S²⁻ of 0.22 is smaller than (in relation to the species of the sulfur species of the PS₄-tetrahedra) 1/3. The ratio of the P–S–Li and P=S groups is 3:1, which matches with the theoretical values. By quantification, an elevated chlorine content is found, which should be 16.7 mol.% in relation to the sulfur species but yields 19.2 mol.%.

Using the peak fit model in Fig. 9.17a and b, the evolution of the decomposition products can be determined as a function of the amount of lithium metal being deposited. The results for the phosphorus and sulfur species are shown in Fig. 9.17a and b, respectively. For the phosphorus compounds, small fractions were found which is in good agreement with results for LPS and LGPS (see section 3.7). The ratio of Li₂S/S²⁻ starts at elevated values due to the S²⁻- motive in the structure. By lithium metal deposition, the amount of Li₂S/S²⁻ is increasing, which is attributed to the formation of Li₂S, and approached a limiting value that is comparable to LPS.

Table 9.5: XPS fitting parameters for the pristine and the decomposed Li₆PS₅Cl.

	Cl 2p	S 2p P=S	S 2p P-S-Li	S 2p Li ₂ S	P 2p PS ₄ ³⁻	P 2p Li ₃ P	P 2p r
BE / eV	198.8	162	161.5	160.2	132.2	126.4	130.5
FWHM / eV	1.2	1.2	1	1.1	1.1	2	1.7
Splitting / eV	1.6	1.3	1.3	1.3	1	0.9	0.5

The results for the impedance measurements are shown in Fig. 9.18. Nyquist plots directly after contacting and 12 h of contact are displayed in Fig 9.18a, showing that the resistance is slightly increased. Unfortunately, the grain boundary and bulk contributions to the material resistance are not resolved, which is often the case for highly conducting solid electrolytes. The knowledge about the initial resistance of the material was used to separate the material and SEI contributions for the early contact states (0 h to 4 h). Afterwards, the SEI resistances could clearly be separated from the material resistances. The results in Fig. 9.18 show a parabolic behavior of the SEI resistance evolution, that exhibits values comparable to LPS, but slightly lower. Again the growth rate is decreasing. Thus, the resistance is increased, which will affect the battery performance and cyclability. Using the resistance values in Fig. 9.18b and the information that Li₂S is the main decomposition product, the SEI thickness could be calculated and plotted against the square root of the time, resulting in the parabolic growth constant. This is shown in section 3.7.4 in comparison to LGPS and LPS (for more information see section 3.7.4). Thus, the argyrodite compounds are reacting with lithium metal under formation of a resistance increasing SEI, comparable to LPS.

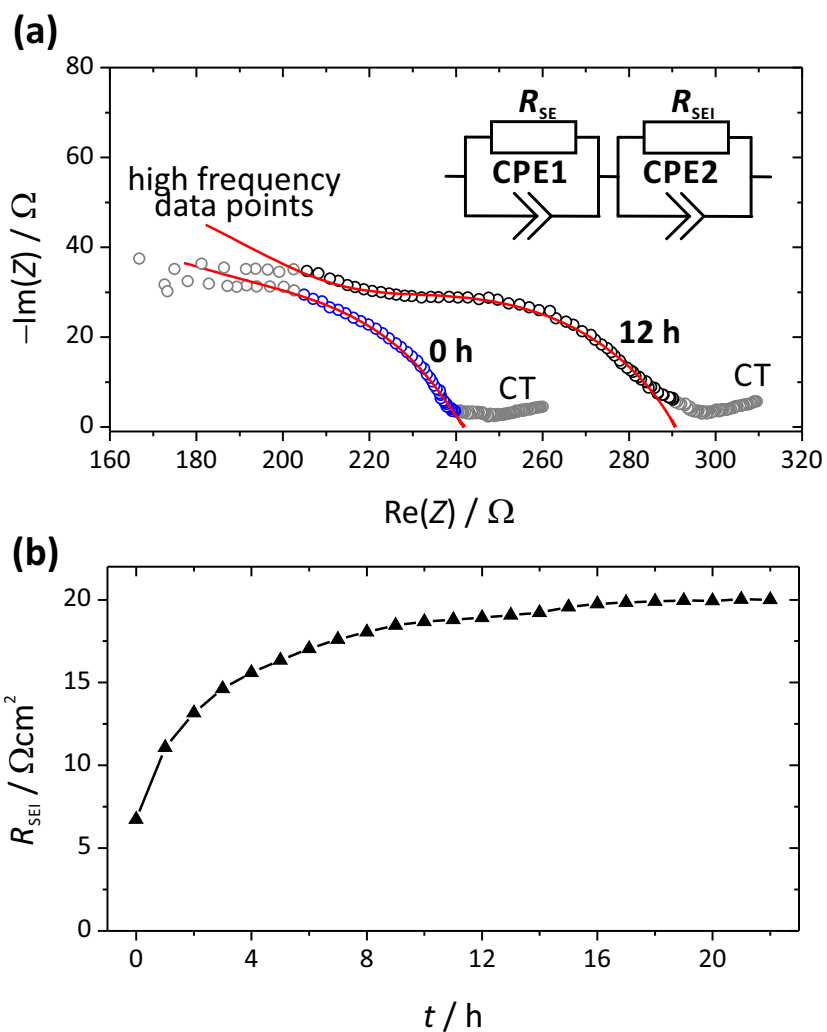


Figure 9.18: Nyquist plots and the fits directly after contacting and after 12 h of contact are displayed in (a), the equivalent circuit is shown as an inset. The fit results are then shown in (b) for 22 h. Note that the SEI resistance refers to one electrode.

9.3.6 NPS

Stacked Nyquist plots for the decomposition of Na_3PS_4 are displayed in Fig. 9.19. The plots already hint at a linear resistance increase of the interphase.

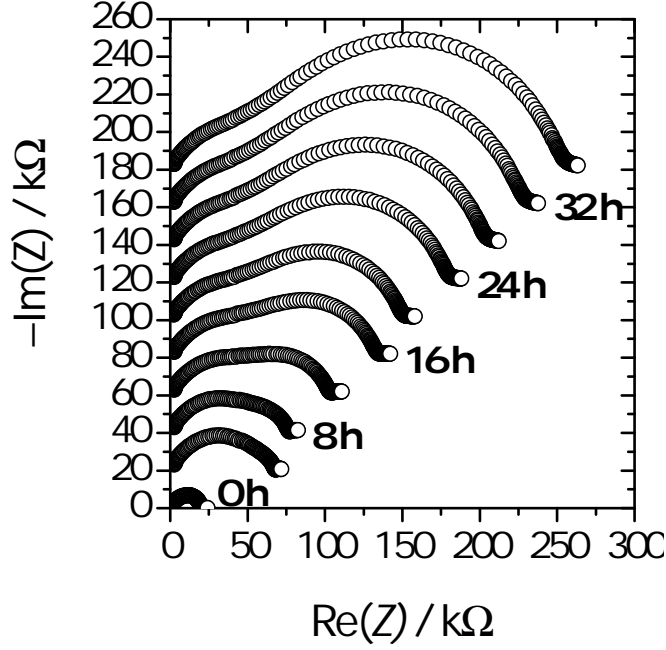


Figure 9.19: Stacked Nyquist plots for the decomposition of NPS are displayed^[43]. The plots are constantly stacked with 20 kΩ.

The Bode plots directly after contacting and after 12 h are shown in Fig. 9.20. The phase angle for the high frequency range shows an even more capacitance-like behavior compared to LGPS and LPS, as the conductivity of the material is lower.

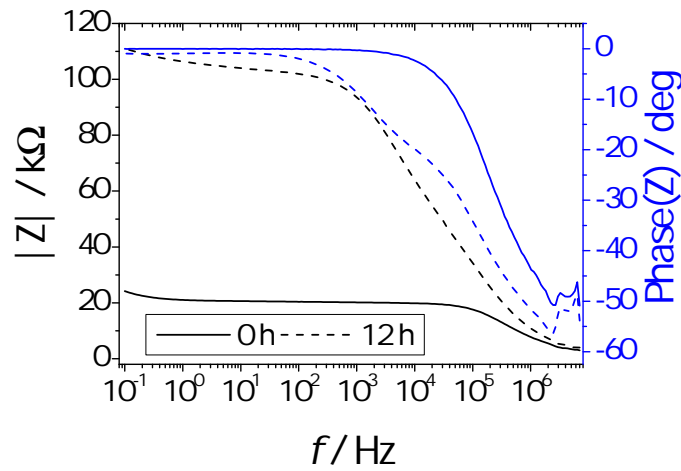


Figure 9.20: Bode plot for the decomposition of NPS (supporting information for section 3.7.3)^[43].

The peak fit model parameters for NPS are summarized in Tab. 9.6 and are comparable

to those found for LPS or LGPS. Due to different bond length and composition, small deviations were found.

Table 9.6: Fit parameters for NPS and its decomposition products. A Shirley background model was used. BE is the abbreviation for binding energy and red. for reduced, respectively.

	S 2p P=S	S 2p P-S-Na	P 2p PS ₄ ³⁻	S 2p Na ₂ S	P 2p Na ₃ P	P 2p red.
BE / eV	161	160	131	158.7	125	126.5 & 129
FWHM / eV	1	1	1.6	1	1.3	1.8
Splitting / eV	1.3	1.2	0.9	1.1	0.9	/

9.3.7 Tantalum containing garnet type structures

Fig. 9.21a shows the oxygen species of the pristine sample and after lithium metal deposition. At the beginning the O 1s line for the pristine material is dominant, but also a small amount of lithium oxide is found. After lithium metal deposition, the ratio has turned and more lithium oxide is found.

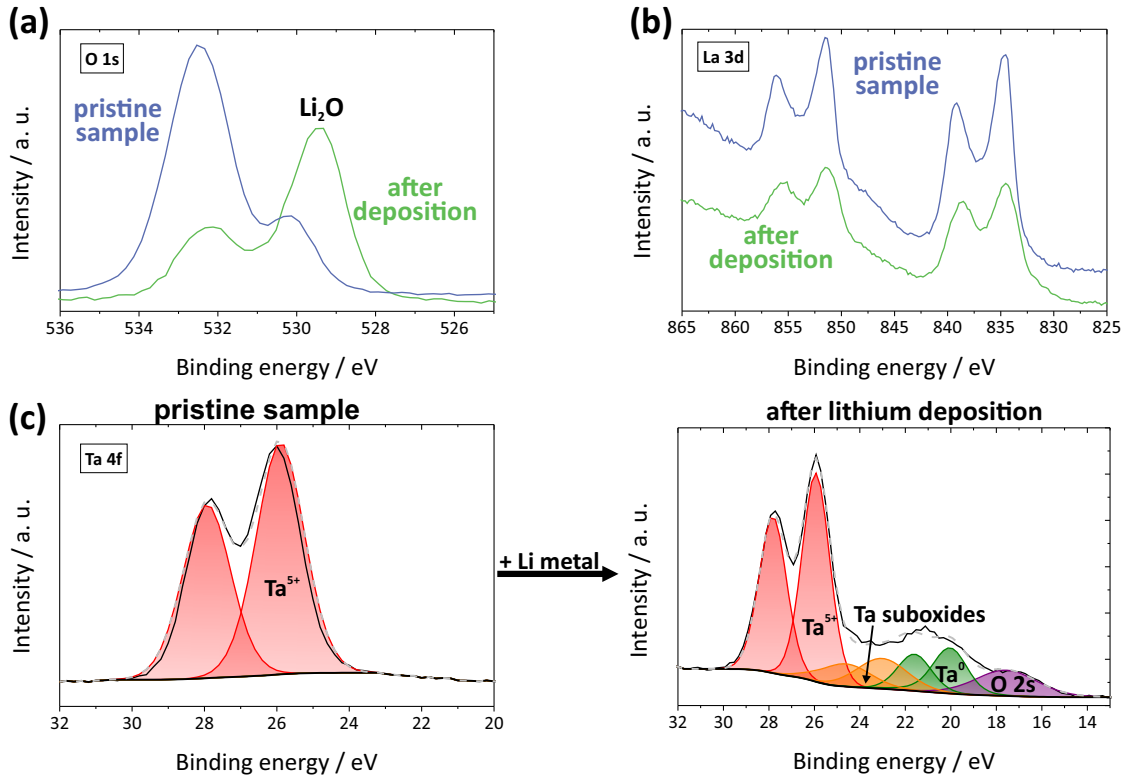


Figure 9.21: Photoelectron spectra for the O 1s and La 3d line of the pristine sample and after lithium deposition are displayed in (a) and (b), respectively. The peak fit model for the Ta 4f line of the pristine and deposited sample are shown in (c).

This might be either caused by material decomposition or a reaction of lithium metal and the residual oxygen content in the UHV chamber. The La 3d signal is mostly unaffected by metal deposition except for signal intensity damping, which is in good agreement with the results for LLTO (see section 3.6.1). According to previous results for tantalum containing materials, the reduction of Ta⁵⁺ to lower oxidation states, including the metal, should occur. This is shown in Fig. 9.21c for the pristine material and after lithium metal

deposition. Only one oxidation state (5+) is found for the pristine sample. After lithium metal deposition, the reduction to several reduced tantalum species and tantalum metal is observed. The reduced tantalum species are fitted with two average signals, due to missing information about the exact positions. Thus, the formation of highly conductive metal is observed. Using this peak fit model, a deposition profile is obtained and shown in Fig. 9.22a. Remarkably, the fraction of reduced species is very small compared to the results for LLTO, LSTZO or LATP. Peak fit model parameters are already described for LSTZO and were adopted with small deviations.

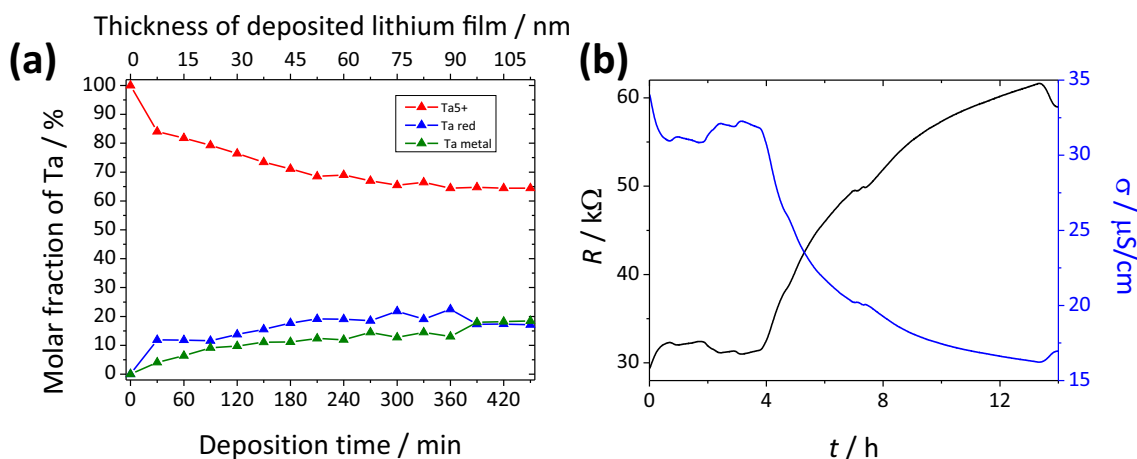


Figure 9.22: Deposition profile of LLTa_2O ($\text{Li}_5\text{La}_3\text{Ta}_2\text{O}_{12}$) according to the peak fit model in Fig. 9.21c and Tab. 9.2 is shown in (a). The results of the DC decomposition measurements are shown in (b).

According to the classification in section 3.2, this material should be prone to MCI formation, as reduced and metal species are formed. Nevertheless, the resistance data in Fig. 9.22b, obtained by the DC technique, show an strong resistance increase. This is unexpected, as reduced tantalum species are formed. In fact, the relative small fraction of reduced species compared to insulating compounds seems to stabilize the interphase at a certain extent. This might be completely controlled by the microstructure of the interphase.

9.3.8 NaSICON – NZSPO

The NaSICON samples with a composition of $\text{Na}_3\text{Zr}_2\text{Si}_2\text{PO}_4$ were delivered by Zhizhen Zhang³ and were reported to be phase pure. In order to study the stability against sodium metal, in situ XPS experiments were conducted. The results are displayed in Fig. 9.23a for the pristine and in b for the reacted sample. For zirconium the reduction to suboxides is observed, the formation of metal can be excluded. In general the reduction of metals in the highest oxidation to lower valent states is characteristic for MCI formation. However, the evolution of sodium metal and the constant ratio between Zr^{4+} and Zr^{4-x+} in Fig. 9.23b state that further growth of the interphase is prevented. The fit model described in section 9.3.2 was adopted.

³Key Laboratory for Renewable Energy (E01) Institute of Physics, Chinese Academy of Sciences, Beijing.

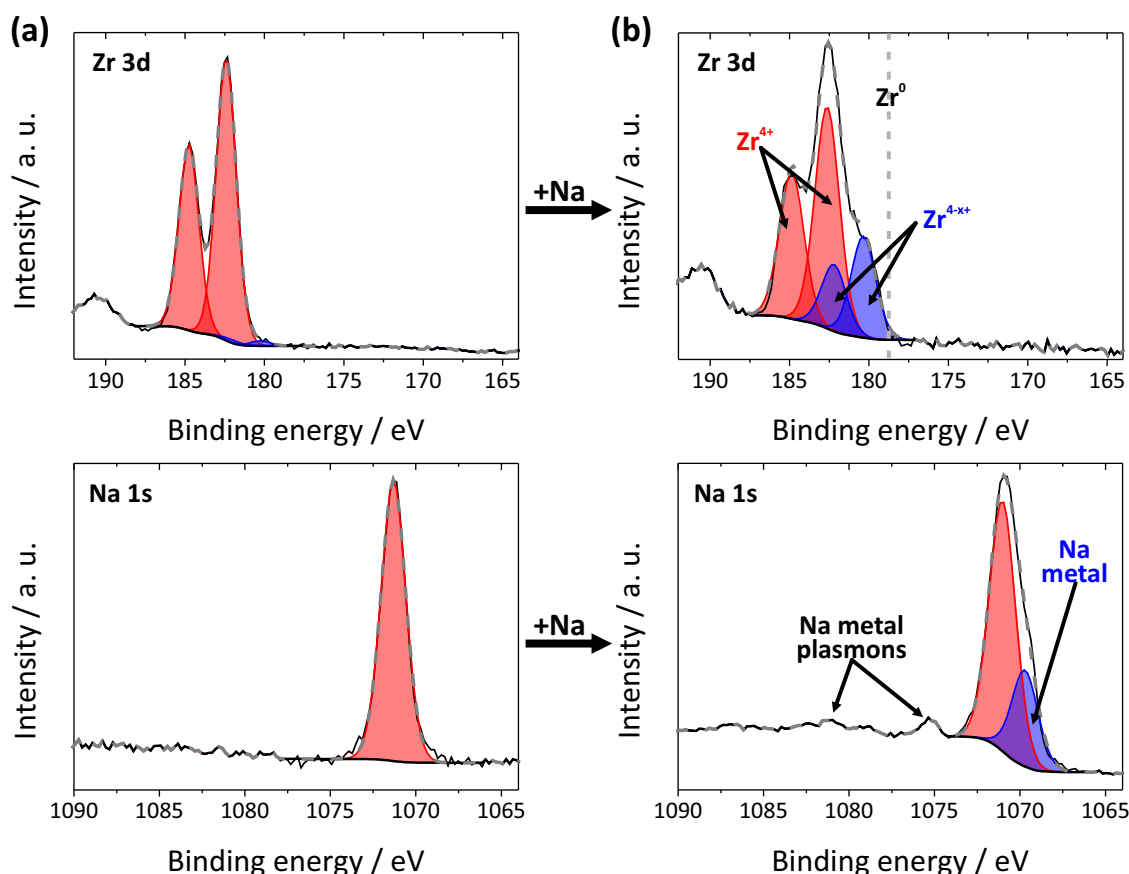


Figure 9.23: Photoelectron detail spectra of Zr 3d and Na 1s for the pristine and reacted sample are displayed in (a) and (b), respectively. The fit model was prepared according to the parameters in section 9.3.2.

The changes for the oxygen, silicon and phosphors signals are shown in Fig. 9.24a, b and c, respectively. As sodium Auger lines are interfering with the O 1s signal it is hard to extract any changes in the photoelectron spectra. In the Si 2p signal only small changes were observed, according to a reduction of Si^{4+} to lower oxidation states. The P 2p signal in Fig. 9.24c exhibits unchanged spectra before and after sodium metal deposition.

In order to determine the changes in the O 1s signal, non-chromatized Mg x-ray radiation was used to shift the sodium Auger lines, which depend on the excitation wavelength. This is illustrated in Fig. 9.25 for the pristine and the reacted sample. The results clearly show that the oxygen species are unaffected by the reaction with sodium metal.

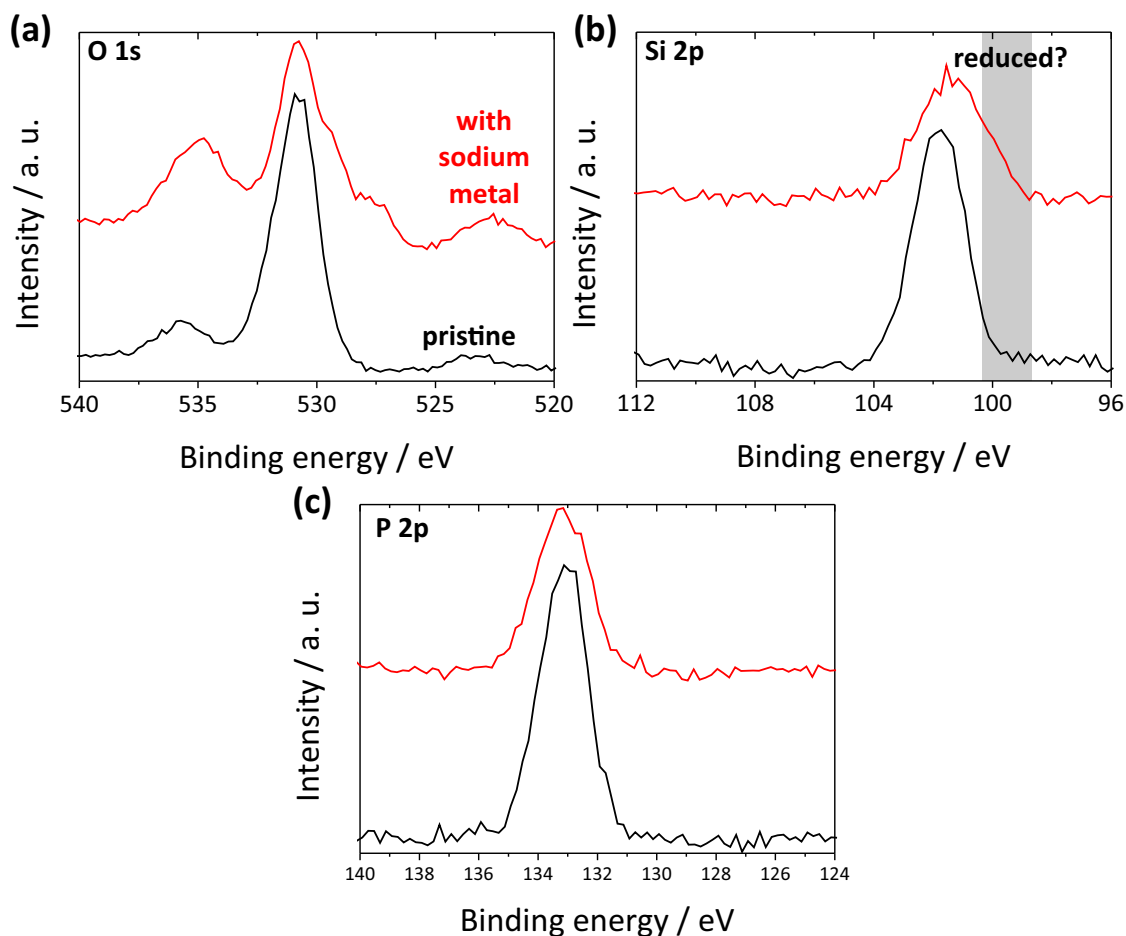


Figure 9.24: Photoelectron detail spectra for the O 1s, Si 2p and P 2p signals before and after sodium metal deposition are displayed in (a), (b) and (c), respectively.

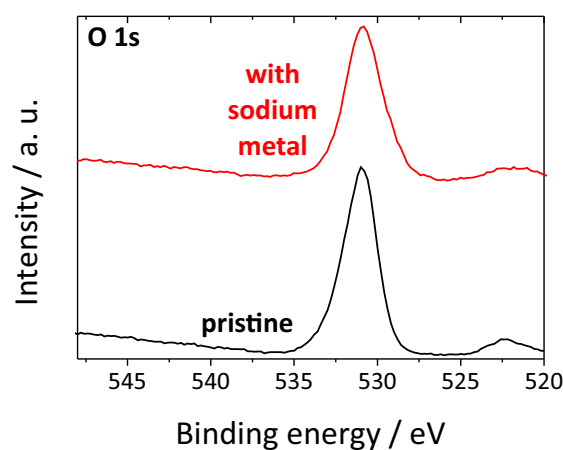


Figure 9.25: Photoelectron spectra for the pristine and reacted sample of O 1s signal are shown, recorded under usage of Mg radiation.

Thus, the material shows the reduction of zirconium (most likely Zr^{3+}) and silicon (most likely Si^{3+}) to suboxide states by sodium metal deposition. The interphase growth and further reduction reactions are stopped after a few deposition cycles, which is characteristic

for SEI formation and comparable to the findings for LLTa_2O . Thus, $\text{Na}_3\text{Zr}_2\text{Si}_2\text{PO}_4$ most likely forms an SEI.

10 Appendix 3 – Supporting results on the interface of sodium metal and beta-alumina

10.1 Interface preparation via hot pressing

In order to obtain a proper contact between β'' -alumina and sodium metal, both were heated up to 85 °C. Afterwards, the sodium metal electrode surfaces were mechanically cleaned to remove surface contaminants (e. g. oxides), directly attached to the solid electrolyte and fixed in the cell setup. To ensure proper contacting, the mechanical pressure on the interface was set to values between 20 bar and 24 bar and left constant during the natural cooling process, leading to an easily manufactured solid electrolyte/electrode interface with reasonable contact properties.

10.2 Limitation of SEM techniques

SEM images were obtained before and after galvanostatic experiments with current densities of 4 mA/cm² (for Fig. 10.1a and b) and 2 mA/cm² (for Fig. 10.1d). The results are displayed in Fig. 10.1, where a and b show dendritic shaped structures that grew at the edge of the sodium metal electrode during deposition. Quite a few dendrites could be observed.

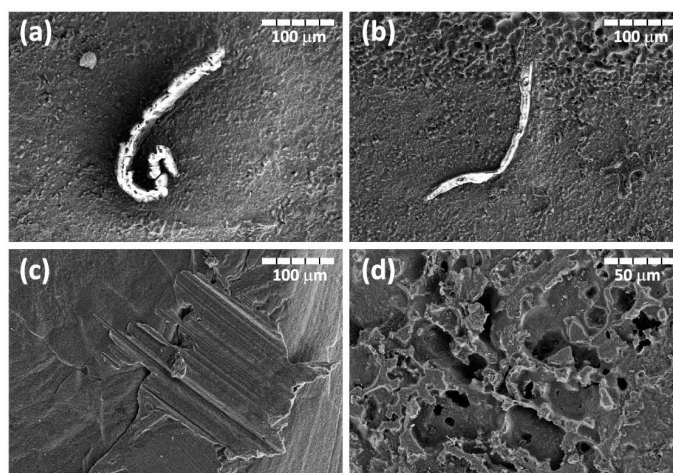


Figure 10.1: SEM figures of electrochemically deposited sodium metal are shown in (a) and (b). (c) displays a pristine sodium metal electrode and (d) a sodium electrode after the dissolution process.

Fig. 10.1c shows a freshly prepared sodium metal electrode¹. After cycling with 2 mA/cm², the morphology changed, which is shown in Fig. 10.1d. The surface was roughened and transformed to a canyon-like structure with large holes in between. Parts of the structure will surely be caused by templating of the solid electrolyte surface. The rest may result from the dissolution process, which is hard to distinguish for not ideally flat solid electrolytes.

10.3 IR-drop determination

The IR-drop was determined via finite element method (FEM) by Dr. Boris Mogwitz. Using the cell geometry and the properties of the solid electrolyte, the voltage drop between the reference and working electrode was determined; the resulting contour plot is illustrated in Fig. 10.2 for the cell setup displayed in Fig. 9.2.

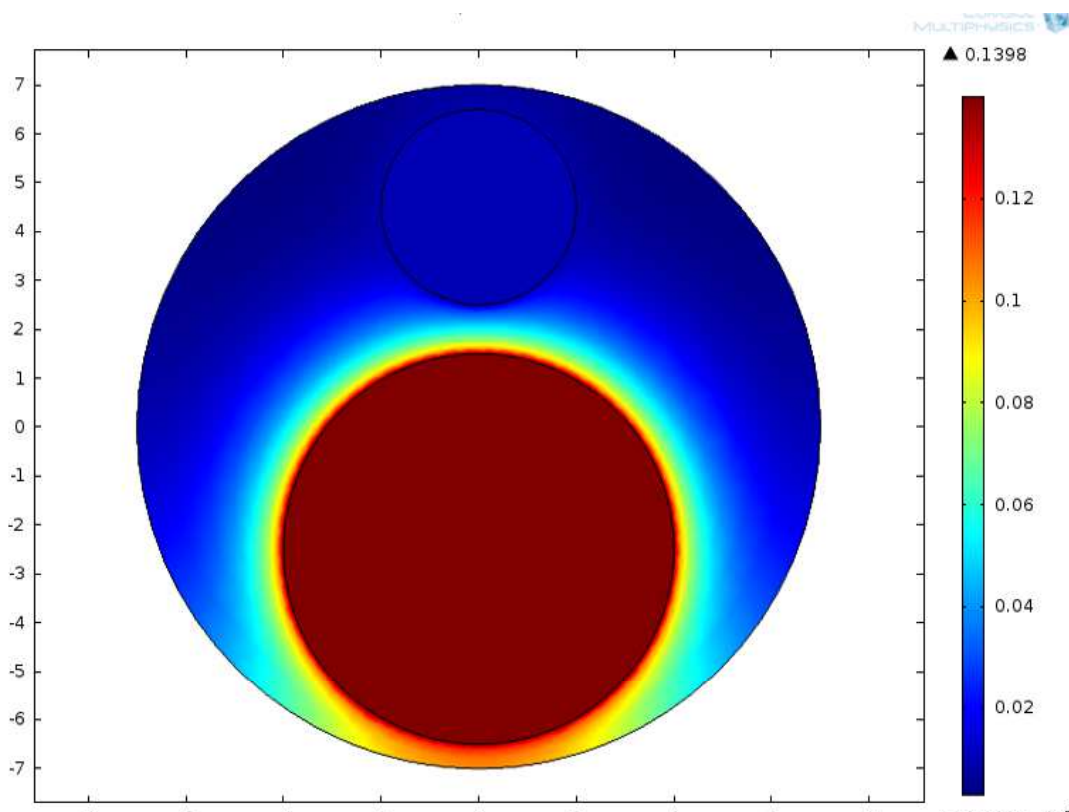


Figure 10.2: Contour plot of the potential behavior for the cell used to determine the IR-drop between reference and working electrode.

Using the potential difference between the working and the reference electrode, calculated for a current of 1 mA, the resistance difference between both electrodes can be obtained, which is then directly used to calculate the IR-drop. The CV data in section 5.5 are corrected accordingly.

¹Electrodes were prepared from a sodium metal ingot by rolling.

10.4 Pressure dependence of the conductivity

To exclude the possibility that the mechanical pressure on the electrode and the solid electrolyte also influences the conductivity of the solid electrolyte by lattice compression, impedance spectroscopy experiments were conducted with a cell using blocking gold electrodes (prepared by vapor deposition). Gradually increasing the pressure resulted in no visible changes of the Nyquist plot, which is shown in Fig. 10.3. Similar results were found for all solid electrolytes studied during this project. The thio-phosphate compounds showed a different behavior at pressures above 20 bar, caused by mechanic destruction of the pellet.

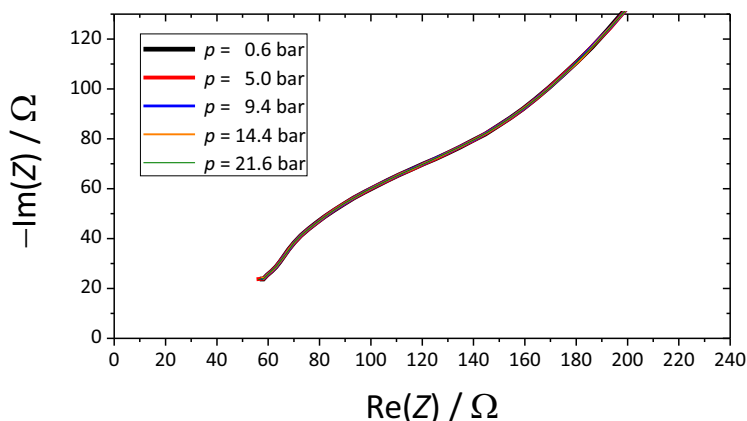


Figure 10.3: Nyquist plots of a symmetric Au/ β'' -alumina/Au cell for different mechanical pressures are shown.

10.5 Interface relaxation

Relaxation processes play an important role for cycling of alkali metal electrodes. Here it is shown that natural relaxation (resting) is not sufficient for high current density applications. At the beginning, a freshly prepared symmetric sodium metal/ β'' -alumina cell was galvanostatically cycled and afterwards rested for 2 h, which is shown in Fig. 10.4a and b. Fig. 10.4a displays the resistance development determined by impedance spectroscopy for different steps and b the results for the galvanostatic dissolution of sodium metal directly after resting. After the initial deposition step, the overall resistance increased to approximately 1800 Ω and decreased again to 800 Ω after resting for 2 h. Restarting the dissolution process (in Fig. 10.4b) leads to a rapid voltage increase and the termination of the experiment, as the boundary values are rapidly reached. Impedance analysis yields an overall resistance of more than 1000 Ω . Resting for 4 h and 10 h leads to a decreased overall resistance (approximately 700 Ω and 620 Ω) but the galvanostatic experiment rapidly reaches the boundary conditions again.

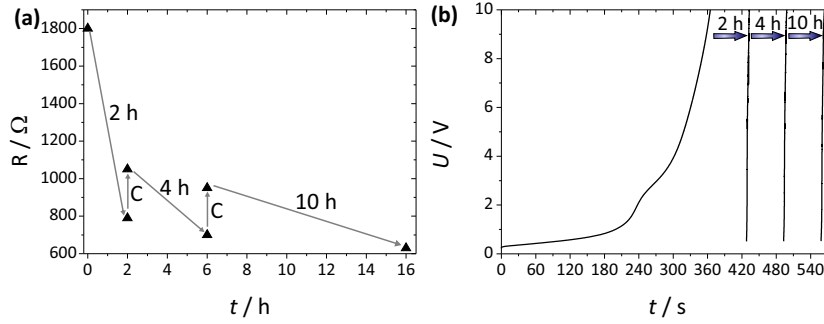


Figure 10.4: The resistance changes for the resting experiment are displayed in (a), resting periods are denoted with the resting time and cycling periods with C. In (b), the corresponding results for the galvanostatic experiments are shown.

Thus, resting will only slightly compensate the consequences of cycling and is therefore an insufficient technique for maintaining the interfacial contact. Reason for this might be the electrochemical Ostwald ripening^[144]. Lithium ions and electrons are formed and transported through the solid electrolyte and the metal and deposited again, so that the surface energy is decreased and the contact area increased.

10.6 Galvanostatic experiments for higher current densities

A current density of 10 mA/cm^2 led to the results shown in Fig. 10.5. Increasing the pressure up to 9.1 bar increased the time until the voltage increased strongly and slightly decreased the overvoltage.

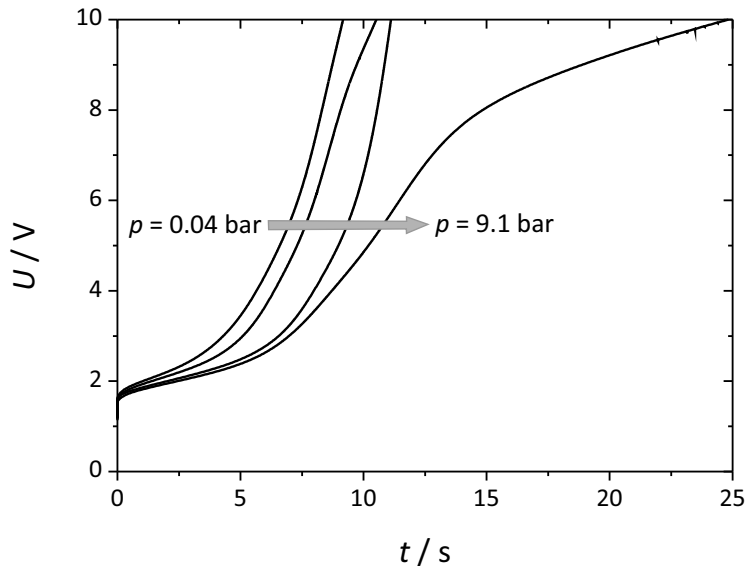


Figure 10.5: Result of the pressure dependent galvanostatic experiments for a current density of 10 mA/cm^2 are displayed.

The most prominent problem at high current densities were mossy structures that grow around the solid electrolyte and lead to short circuiting². This process is even more pronounced with increasing pressure, so that only experiments up to 9.1 bar could be realized.

10.7 Additional information on the pressure dependent contact loss model

Fig. 10.6a shows the average voltage slope (dU/dt) that approaches the boundary value of 0 V/min. For higher current densities, the pressure at which the average slope approaches zero, is higher compared to lower current densities. In Fig. 10.6b, the development of the overvoltage (corrected by the IR-drop of the solid electrolyte), in dependence of the pressure, is displayed. Again, a boundary value is approached that is approximately the same as the IR-drop for the solid electrolyte.

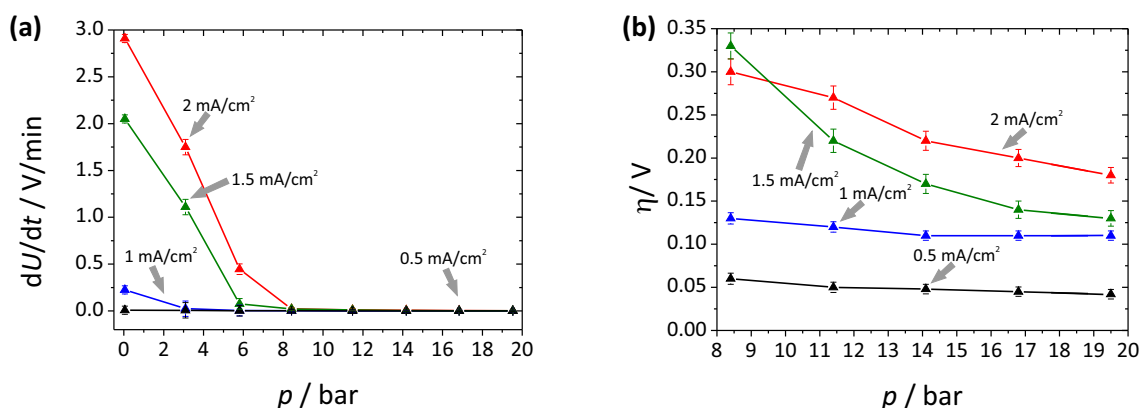


Figure 10.6: Pressure dependence of the average voltage slope and of the overvoltage are shown in (a) and (b), respectively.

10.8 Oscillation of the interface sodium metal/beta-alumina

The oscillation of the interface sodium metal/ β'' -alumina is shown in Fig. 10.7 for a current density of 0.2 mA/cm². In order to observe this oscillation, lower current densities than studied in section 5 are required and the pressure has to be set to 0 bar (corresponding to zero externally applied pressure). Then, oscillations with a time constant of less than 1 h are observed, like those shown in Fig. 10.7. The peaks exhibit a more complex fine structure, but the temporal resolution of the analyzers is generally too low to resolve this. Reproduction of the results was challenging, as the parameter for obtaining oscillations strongly depended on the interface formation and the ambient conditions.

²Unfortunately, the mossy structures were strongly changing in the SEM and were extremely sensitive to oxygen and water traces in the glove boxes.

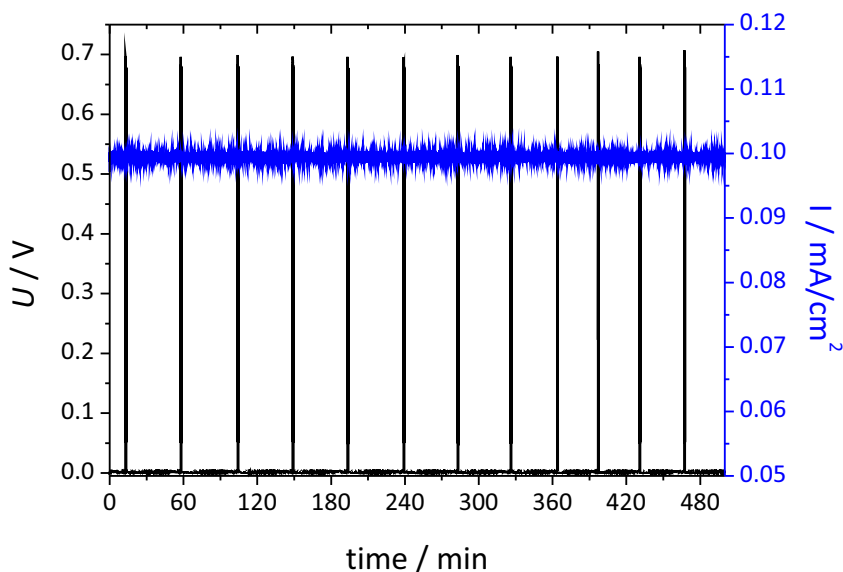


Figure 10.7: Galvanostatic oscillation of the overvoltage at the interface between sodium metal electrode and the solid electrolyte β'' -alumina at room temperature.

10.9 Reversion of polarity

A simple experiment was conducted to show the voltage drop due to the reversion of polarity.

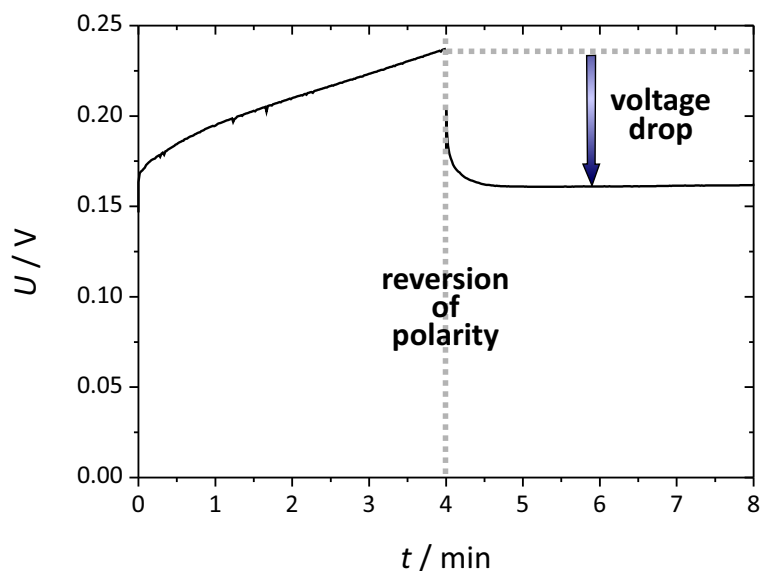


Figure 10.8: Results of the dissolution of freshly deposited sodium metal at room temperature, without external pressure.

Sodium metal was dissolved for 4 min and afterwards the polarity was changed, leading to a decreased voltage, which is shown in Fig. 10.8. Additionally to this finding, it was observed that the voltage-time curve is ideally flat, with virtually no slope. Thus, the

freshly deposited sodium metal was dissolved with a smaller overvoltage compared to the pristine electrode.

10.10 Dislocation relaxation process

As mentioned in section 5, plastic deformation often occurs by dislocation motion^[183]. One mechanism is the constant supply of sodium metal by relaxation of dislocations, shown in Fig. 10.9. Firstly, the electrode preparation process leads to dislocation formation (rolling), which are further produced and forced to the surface by the application of pressure. The relaxation then happens by gliding of the dislocated plane in direction of the interfacial pores.

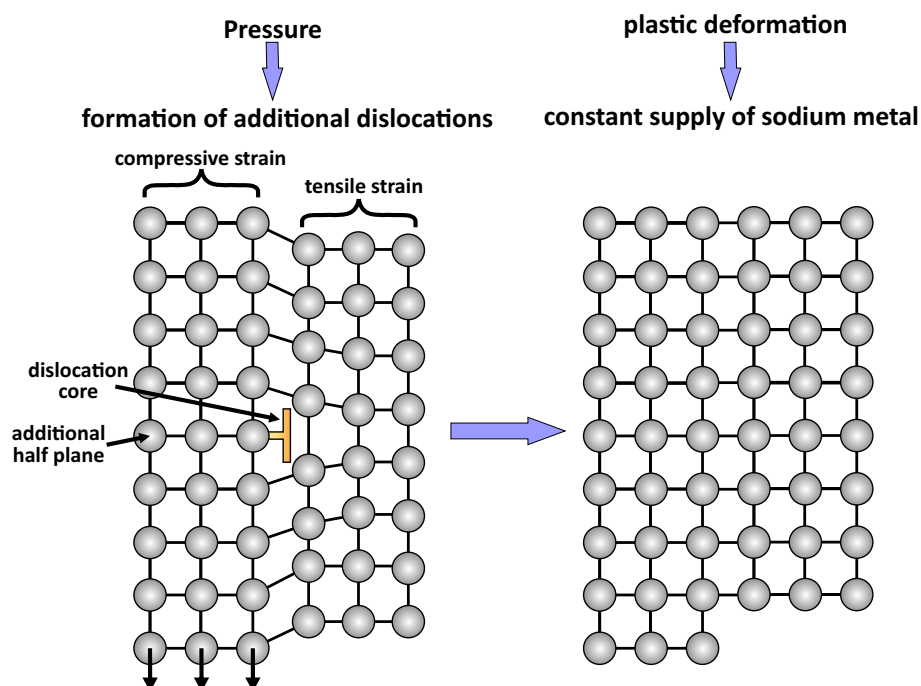


Figure 10.9: The mechanism of dislocation movement (gliding), caused by pressure application to the sodium metal electrode.

11 Appendix 4 – Supporting results on the interface of lithium metal and solid electrolytes

11.1 Cycling of lithium metal electrodes on LPS

In Fig. 11.1, cycling experiments at different pressures and current densities are shown. Fig. 11.1a displays the pressureless cycling with a current density of 1 mA/cm². Again the cathodically deposited lithium metal could be dissolved with negligible overvoltage, but the amount of initially dissolved lithium metal is larger compared to the amount dissolved at smaller overvoltages. Thus, some kind of other processes, e. g. degradation might occur. The experimental results in Fig. 11.1 starts with anodic dissolution of alkali metal and proceeds with cathodic deposition in the second step. Note that, according to the results in section 5.3, the anodic process is limiting and thus mostly a two electrode setup was used.

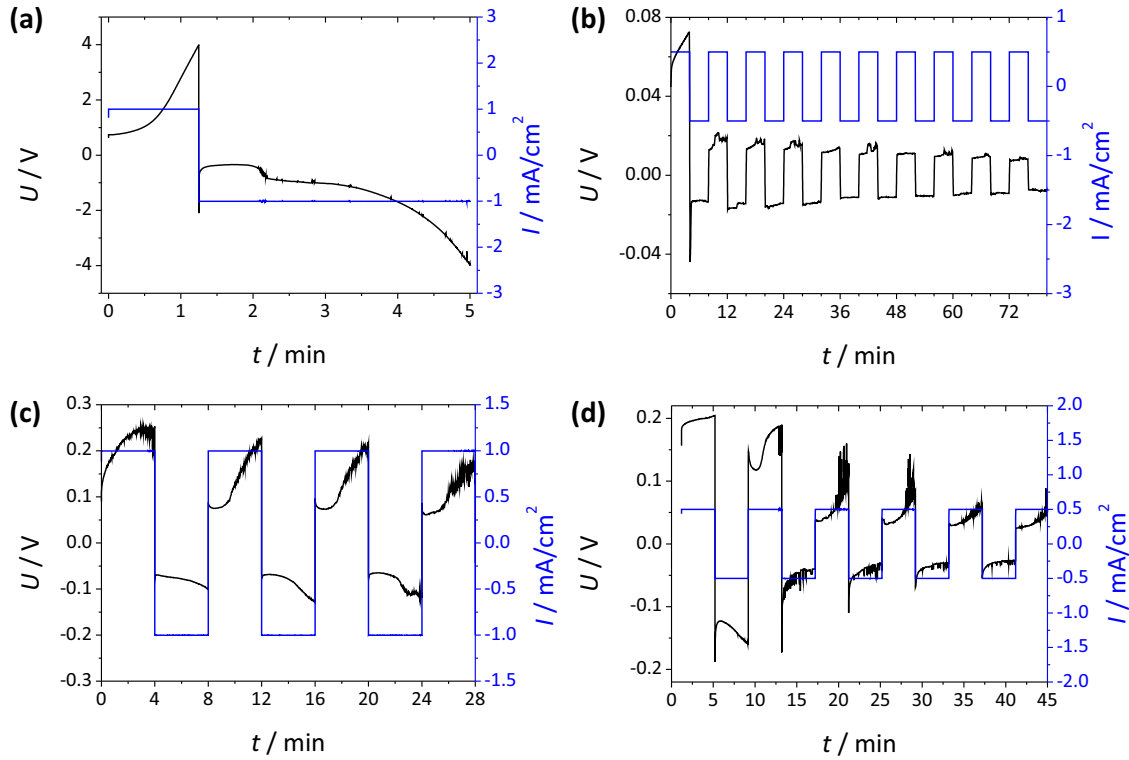


Figure 11.1: Additional examples on cycling experiments of lithium metal electrodes on LPS are shown for different current densities. In (a), (b), (c), and (d) the pressure values were set to 0 bar, 3 bar, 19 bar and 24 bar, respectively.

In Fig. 11.1b, a current density of 0.5 mA/cm^2 was applied without additional mechanical pressure. The results show that the freshly deposited lithium metal can be easily dissolved, which is in good agreement with the results in chapter 5. Again erratic deviations (oscillations) are observed. Fig. 11.1c shows the results for a current density of 1 mA/cm^2 and a pressure of 19 bar, again resulting in an unreproducible voltage profile. By increasing the pressure to 24 bar and decreasing the current density to 0.5 mA/cm^2 , more erratic oscillations are observed in Fig. 11.1d. The findings are in accordance with the results in section 6 and in good agreement with the statement that lithium metal electrodes could not be cycled properly in contact with the solid electrolyte LPS.

11.1.1 Cycling of sodium metal electrodes on NPS

Fig. 11.2 shows a representative cycling result for sodium metal electrodes on NPS for a current density of 0.2 mA/cm^2 and a pressure of 16 bar. There, a characteristic spike at the beginning of the metal deposition process is observed that is attributed to the initial deposition step, like already described in section 5. Surprisingly, the voltage then decreases again, which is sometimes seen in experiments for LPS, too (see previous section).

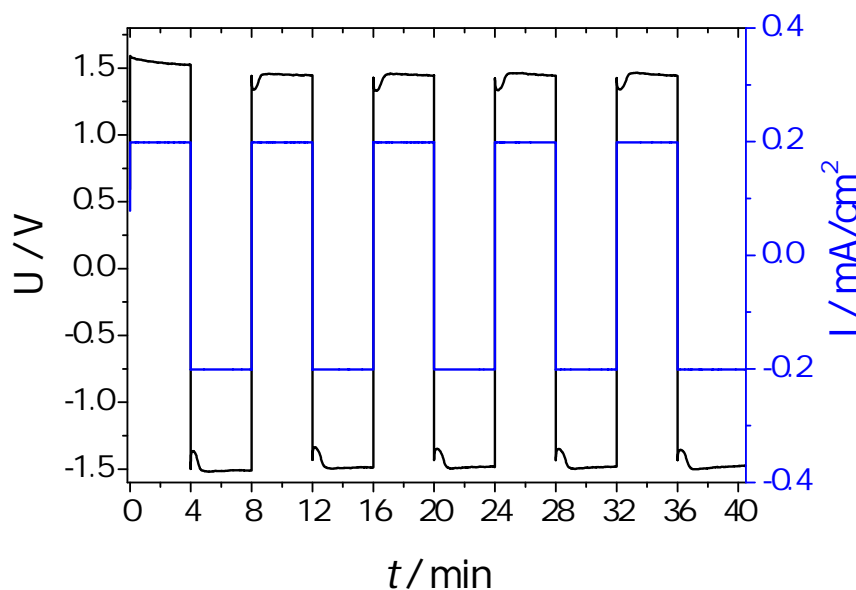


Figure 11.2: The result of a cycling experiment with a Na metal/NPS/Na metal cell setup.

In this current density and pressure range the cell could be cycled without increasing overvoltages. Nevertheless, the cycling time is relatively small leading only to a very small effect that is hardly seen.

11.1.2 Simulation of the enhanced interphase growth

Using Faraday's law and assuming that the lithium metal deposition starts without delay, the electrochemically enhanced interphase growth is displayed in Fig. 11.3, according to the results in section 6.6. Under the given assumption that this model is valid, an

interphase growth of 1.5 nm and 0.8 nm after four hours for LPS and LGPS could be simulated, calculated for a current density of 1 mA/cm².

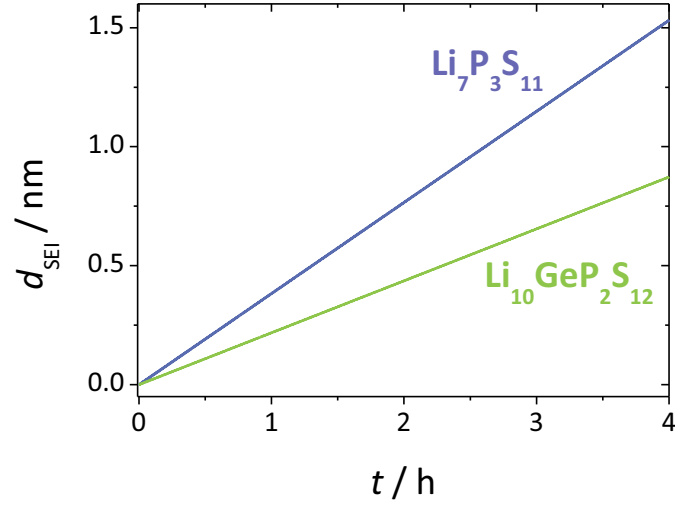


Figure 11.3: Simulation of the interphase growth during cycling.

12 Appendix 5

12.1 List of abbreviations

ASSB	All-solid-state battery
beta-alumina	Sodium- β "-aluminum oxide
BE	Binding energy
β "-alumina-alumina	Sodium- β "-aluminum oxide
CE	Counter electrode
CT	Charge transfer
CV	Cyclic voltammetry
DC	Direct current
EAL	Effective attenuation length
EDX	Energy dispersive x-ray spectroscopy
FEM	Finite element method
FWHM	Full Width at half maximum
LBLTO	$\text{Li}_6\text{BaLa}_2\text{Ta}_2\text{O}_{12}$
LGPS	$\text{Li}_{10}\text{GeP}_2\text{S}_{12}$
LIB	Lithium ion battery
LiPON	Lithium phosphorous oxy-nitride
LLTa ₂ O	$\text{Li}_6\text{La}_3\text{Ta}_2\text{O}_{12}$
LLTO	$\text{Li}_{0.35}\text{La}_{0.55}\text{TiO}_3$
LLZO	$\text{Li}_7\text{La}_3\text{Zr}_2\text{O}_{12}$, aluminum doped
LPS	$\text{Li}_7\text{P}_3\text{S}_{11}$
LPSCl	$\text{Li}_6\text{PS}_5\text{Cl}$
LSTZO	$\text{Li}_{3/8}\text{Sr}_{5/8}\text{Ta}_{3/4}\text{Zr}_{1/4}\text{O}_{12}$
LSV	Linear sweep voltammetry
MCI	Mixed conducting interphase
NPS	Na_3PS_4
OCV	Open circuit voltage

PEEK	Polyether ether ketone
r	Reduced
RE	Reference electrode
SEI	Solid electrolyte interphase
SEM	Scanning electron microscopy
TEM	Transmission electron microscopy
TM	Transition metal
UHV	Ultra high vacuum
WE	Working electrode
XPS	X-ray photoelectron spectroscopy
XRD	X-ray diffraction

12.2 List of symbols

σ_{el}	Electronic conductivity in S/cm
σ_{ion}	Ionic conductivity in S/cm
$\nabla\mu_i$	Chemical potential gradient of component i
M	Molar mass in g/mol
d or ξ	Thickness (of SEI) in nm or cm
x	Stoichiometric factor (see reaction equation)
ρ	Density in g/cm ³
W_{EC}	Electrochemical stability window in V
F	Faraday constant
L_i	Transport coefficient of mobile component i
μ_i^0	Standard chemical potential of i in kJ/mol
a_i	Activity of component i
T	Temperature in °C or K
j_i	Molar flux of component i
A	Area in cm ²
R_{p}	Polarization resistance in Ω/cm^2
j	Current density in mA/cm ²
j_{V_M} or j_{I}	Flux of metal vacancies or interstitial
j_{M}	Flux of metal ions or atoms
$\xi_{\text{structural}}$	Structural relaxation zone
$\xi_{\text{M}}^{\text{relax}}$	Defect relaxation zone in the metal
$\xi_{\text{SE}}^{\text{relax}}$	Defect relaxation zone in the metal
η	Overvoltage in V
β	Angle between target and plasma beam in °
h_{b}	Height difference between sputter impact position and holder surface in cm
b	Distance between target and measurement position in cm
I	Signal intensity (XPS)
I_0	Initial signal intensity (XPS)
λ	Effective attenuation length in nm

t	Time in s or min
α	Angle between analyzer and x-ray source (XPS)
r	Deposition rate (in situ XPS) in nm/min
m	Slope
X	Fraction of the nominal atomic ratio (coupled fits)
A	Area (peak or electrode)
RSF	Relative sensitivity factor (XPS)
MFP	Mean free path (XPS)
T	Transmission function (XPS)
Z	Impedance
$R_{or}R_a$	Resistance or area resistance in Ωcm^2
f	Frequency in Hz
$-\text{Im}(Z)$	Imaginary part of the impedance in Ω
$\text{Re}(Z)$	Real part of the impedance Ω
R_{SE}	Resistance of the solid electrolyte
R_{SEI}	Resistance of the SEI
R_{gb}	Grain boundary resistance
R_{bulk}	Resistance of the bulk material
CPE	Constant phase element

12.3 List of conference contributions

Posters:

- S. Wenzel, T. Leichtweiss, D. Weber, J. Sann and J. Janek, "Interphase Formation between Lithium Metal and Lithium Solid Ion Conductors Studied by In Situ XPS", *Material Research Society Fall Meeting*, Boston, USA, **2015**.
- S. Wenzel, T. Leichtweiss, D. Weber, J. Sann and J. Janek, "Interphase Formation on Lithium Solid Electrolytes – A Simple Approach to Study Interfacial Reactions In Situ by Photoelectron Spectroscopy", *Material Research Society Fall Meeting*, Boston, USA, **2015**.

12.4 List of publications

- S. Wenzel, T. Hara, J. Janek, P. Adelhelm, "Room-temperature sodium-ion batteries: Improving the rate capability of carbon anode materials by templating strategies", *Energy Environ. Sci.*, **2011**, 4, 3342-3345.
- S. Wenzel, H. Metelmann, C. Raiss, A. K. Duerr, J. Janek, P. Adelhelm, "Thermodynamics and cell chemistry of room temperature sodium/sulfur cells with liquid and liquid/solid electrolyte", *J. Power Sources*, **2013**, 243, 758-765.
- S. Darmawi, S. Burkhardt, T. Leichtweiss, D. A. Weber, S. Wenzel, J. Janek, M. T. Elm, P. J. Klar, "Correlation of electrochromic properties and oxidation states in nanocrystalline tungsten trioxide", *Phys. Chem. Chem. Phys.*, **2015**, 17, 15903-15911.
- S. Wenzel, T. Leichtweiss, D. Krueger, J. Sann, J. Janek, "Interphase formation on lithium solid electrolytes – An in situ approach to study interfacial reactions by photoelectron spectroscopy", *Solid State Ionics*, **2015**, 278, 98-105.
- S. Wenzel, D. A. Weber, T. Leichtweiss, M. R. Busche, J. Sann, J. Janek, "Interphase formation and degradation of charge transfer kinetics between a lithium metal anode and highly crystalline $\text{Li}_7\text{P}_3\text{S}_{11}$ solid electrolyte", *Solid State Ionics*, **2016**, 286, 24-33.
- S. Wenzel, S. Randau, T. Leichtweiss, D. A. Weber, J. Sann, W. G. Zeier and J. Janek, "Direct Observation of the Interfacial Instability of the Fast Ionic Conductor $\text{Li}_{10}\text{GeP}_2\text{S}_{12}$ at the Lithium Metal Anode", *Chem. Mater.*, **2016**, acs.chemmater.6b00610.
- S. Wenzel, T. Leichtweiss, D. A. Weber, J. Sann, W. G. Zeier and J. Janek, "Interfacial reactivity of the sodium ion conductor Na_3PS_4 : A case for β -alumina in protected sodium metal anodes and sodium all-solid-state batteries", to be submitted.

List of Figures

1.1	Summary of the specific and volumetric energy densities of different battery systems (taken with modifications from Tarascon et al. ^[4]).	2
2.1	Summary of the temperature dependence of the ionic conductivities for different solid and liquid electrolytes. The data for LGPS ^[12] , LPS ^[18] , LLTO ^[27] , LPSCl ^[23] , LLZO ^[34] , LLTa ₂ O ^[33] , LSTZO ^[30] , NPS ^[20] , LiPON ^[40] (all SEs), DOL:DME:LITFSI 1M ^[41] , EC:DMC:LiPF ₆ 1M ^[42] and EC:PC:LiPF ₆ 1M ^[42] (LEs) were taken from literature. LiPON is mostly used in thin-film ASSBs and is drawn as reference. For β'' -alumina the data reported in this thesis and by Wenzel et al. ^[43] were used.	9
2.2	Illustration of the two different ASSB cell concepts, in (a) the thin film and the scheme of a battery package ^[47] and in (b) the thick-film (powder) ASSB ^[46] are displayed.	11
3.1	The three different interphase/interface types between alkali metal and a solid alkali ion conductor. (a) Thermodynamically stable interface; (b) a reactive and mixed-conducting interphase (MCI); (c) metastable, kinetically stabilized solid electrolyte interphase (SEI). Figure from ^[61] .	14
3.2	The schematic band structure for a solid electrolyte that is stable in contact with the positive electrode material and alkali metal is shown in (a). In (b), the unstable solid electrolyte is shown, which reacts with both electrodes.	18
3.3	Sketch of Wagner's model for tarnishing is displayed in (a). (b) Interface-controlled reaction, the chemical potential difference forms the driving force for the interface transfer. (c) Diffusion controlled growth of SEI.	20
3.4	Schematic progression of the film thickness for a solid state reaction, showing the transition from an interface to a diffusion controlled reaction.	22
3.5	Limited and connecting percolation pathways are schematically displayed in (a). The potential drop caused by limited percolating species, with high conductivity compared to the interphase, is shown in (b).	23
3.6	Cyclic voltammetry data for a few well-known solid electrolytes, using alkali metal electrodes. The black, blue and green data correspond to the stable, SEI and MCI forming solid electrolytes, respectively. Li ₅ La ₃ Ta ₂ O ₁₂ is a special case and therefore marked in red. (Unpublished data).	24
3.7	The three parts of the combined approach are schematically displayed. The experimental setups and schematic sample data are shown to exemplify the information gained by the respective method. Parts of this figure are already published by Wenzel et al. ^[83] .	25
3.8	The expectations for a stable material and materials which are forming mixed-conducting (MCI) or solid electrolyte interphases (SEI) for the electrochemical techniques ^[43,83] .	28

3.9	Experimental results for a stable, an MCI and an SEI forming solid electrolyte. The resistance change, example Nyquist plots, the CV data and the polarization resistance are shown in (a), (b), (c) and (d), respectively ^[83] .	29
3.10	The scheme of the in situ XPS technique, the procedure is shown in (a) and involves sequential analysis and deposition steps. The geometrical figure is drawn in (b). ^[61]	30
3.11	XPS spectra of an MgO single crystal deposited with lithium metal. The intensities of the yellow and red colored Mg 2p and Li 1s signals are decreasing and increasing, respectively ^[61] .	31
3.12	Photoelectron spectra for the pristine sample and for deposition times of 300, 600 and 900 minutes for the Ti 2p, La 3d and O 1s signals are shown, respectively (Wenzel et al. ^[61]).	33
3.13	XPS fits of the pristine (a) and deposited sample (b) for the Ti 2p signal. Using this peak fit model, the fraction of the titanium oxidation states are displayed in (c) (Wenzel et al. ^[61]).	34
3.14	Resistance and conductivity changes of an LLTO pellet in contact with lithium metal electrodes (Wenzel et al. ^[61]).	35
3.15	Stacked photoelectron spectra for the S 2p and P 2p signals for several lithium metal deposition steps onto LPS. The reaction products are marked and labeled ^[78] .	36
3.16	The peak fit models for the pristine and the reacted LPS sample are shown in (a) and (b), respectively. In (c) and (d), the resulting molar fractions for the sulfur and phosphorus species are displayed, according to the peak fit model in (a) and (b) ^[78] .	37
3.17	Two Nyquist plots directly after contacting and after 12 h hours for a symmetric Li metal electrode/LPS cell are shown in (a). In addition, the fit and the equivalent circuit are displayed. The obtained resistance change for one electrode is then monitored in (b). Modified version of an already published figure (Wenzel et al.) ^[78] .	38
3.18	Time-resolved photoelectron spectra for S 2p, O 1s and P 2p signals are shown in (a). Depth profiling to remove the interphase was then conducted and the obtained detail spectra are displayed in (b) for the S 2p, O 1s and P 2p signals (Wenzel et al.) ^[78] .	40
3.19	Photoelectron detail spectra for S 2p, Ge 3d and P 2p for several lithium metal deposition states. Some products are colored and labeled directly in the figure ^[82] .	41
3.20	The peak fit models for the Ge 3d, P 2p and S 2p signals for the pristine and deposited sample are shown in (a) and (b), respectively. The obtained deposition profiles for the different species are displayed in (c) for the Ge 3d and S 2p species and in d for P 2p species (Wenzel et al.) ^[82] .	42
3.21	Two Nyquist plots, directly after contacting and after 12 h hours for a symmetric Li metal electrode/LGPS cell, are shown in (a). In addition, the fit and the equivalent circuit are displayed. The obtained resistance change for one electrode is then monitored in (b) and the CV data in (c). The inset in (c) displays the polarization resistance evolution ^[82] . Again, the capacities are in the range of 10^{-9} F, comparable to Peled et al. ^[90,95]	44
3.22	Sketch of the SEI between lithium metal and LGPS to illustrate the formation of partial percolating subnetworks ^[82] .	45

3.23	Deposition state dependent photoelectron detail spectra for the P 2p, Na 1s and S 2p signals of the NPS sample ^[43]	46
3.24	The detail spectra of the pristine and the reacted samples including the fit model for the S 2p and the P 2p signal are shown in (a) and (b). (c) and (d) show the evolution of the decomposition products ^[43]	47
3.25	Two Nyquist plots directly after contacting and after 12 h hours for a symmetric Na metal electrode/NPS cell are shown in (a). The obtained resistance change is then monitored in (b). In addition, the fit and the equivalent circuit are displayed in (a) and (b), respectively. The CV data are shown in (c) and the thereof determined polarization resistance is plotted in (d) ^[43]	48
3.26	Theoretical growth rate of the interphase of Li metal and LPS as a function of the interphase thickness d_{SEI} . Different electronic conductivities were used for the theoretical simulations. The results are compared to the data derived in section 3.7.1 ^[78]	50
3.27	The interphase thickness in dependence of the square root of the time is displayed in (a). The parabolic behavior proves the diffusion-controlled growth mechanism. The fit results are summarized in Tab. 3.1 ^[82] . (b) shows the resistance increase, which was directly obtained by equation 3.26 and the SEI resistance. The fit results are summarized in Tab. 3.2.	51
3.28	Simulated interphase thickness (a) and resistance increase (b) for LGPS, LPS and LPSCl for a battery lifetime of ten years, using the parameter in Tab. 3.1 and 3.2.	52
3.29	Deposition state dependent photoelectron detail spectra for the Al 2p, Na 1s and O 1s signals of the β'' -alumina sample ^[43]	53
3.30	Nyquist plots for 0 h and 12 h after contacting the beta-alumina pellet with two sodium metal electrodes are displayed in (a). The CV data are shown in (b) ^[43]	54
3.31	Deposition state dependent photoelectron spectra for the La 3d, Zr 3d and Li 1s signals of the LLZO sample are displayed in (a). Note that the data are stacked with a constant value to improve the clarity. The results for the time-resolved impedance and CV analysis are shown in (b) and (c), respectively. Unpublished data.	54
3.32	The Gibbs free energies for the decomposition of substitution materials are sketched in a diagram to illustrate the stability. All values are normed to the reduction of one mol of elements. For example the reduction of Ta_2O_5 is normalized to the value for the reduction of one Ta^{5+} to Ta^0 . Unpublished data.	56
3.33	The model cases for the volume increase are shown in (a) and (b). A more realistic picture of the interphase is displayed in (c).	58
3.34	The different materials are classified according to the type of interphase/interface that is formed. LiPON is marked with an asterisk, as it is not shown in this work but is nevertheless one of the most prominent ion conductors. $\text{Na}_3\text{Zr}_2\text{Si}_2\text{PO}_{12}$ and $\text{Li}_5\text{La}_3\text{Ta}_2\text{O}_{12}$ are special cases that might be assigned to SEI forming materials.	60
4.1	The pristine LLTO pellet is shown in (a), after LiPON deposition in (b), with lithium metal in (c) and a reacted sample in (d).	63
4.2	Content classified by JLU	65
4.3	Stability window gap diagram. The stability data were taken from Zhu et al. ^[76]	66

5.1	Schematic figure to illustrate the interface between a parent metal M and the M^+ conducting solid electrolyte is shown in (a). The concentration gradients are drawn in blue and denoted with C and indices according to the Kroeger-Vink notation. ξ_{relax} denotes the relaxation zones. Modified figure according to Janek and coworkers ^[130] . (b) and (c) show the behavior of the fluxes lines before and upon pore (vacancy accumulation) formation, respectively	69
5.2	Summary of the processes at the interface of a metal and a solid electrolyte during galvanostatic dissolution process. According to Janek et al. ^[143]	71
5.3	The two failure modes for liquid sodium/ β'' -alumina interfaces according to Virkar and Ansell ^[146,147] are illustrated.	72
5.4	Galvanostatic experiment for a symmetric Na metal/solid electrolyte cell with application of a reference electrode is shown. External pressure was not applied and a current density of 1 mA/cm ² was chosen.	74
5.5	The setup for the pressure dependence of galvanostatic plating and stripping of alkali metal electrodes is displayed. The inset shows a magnification of the cell housing.	75
5.6	The current/voltage curves for cells with differently prepared electrode-electrolyte contacts are shown in (a). In (b), the Nyquist plots of a solid electrolyte with gold and sodium electrodes are displayed for comparison. All data were recorded without externally applied pressure and at room temperature.	77
5.7	The results for pressure dependent galvanostatic measurement (at room temperature) for current densities of 0.5 mA/cm ² , 1 mA/cm ² , 1.5 mA/cm ² and 2 mA/cm ² are displayed in (a), (b), (c) and (d), respectively. The theoretical voltage drop caused by the pellet resistance is shown in dashed gray and the pressure in blue.	78
5.8	The pressure dependent galvanostatic measurements and the corresponding Nyquist plots before and after the measurement are displayed for current densities of 0.5 mA/cm ² , 1 mA/cm ² , 1.5 mA/cm ² and 2 mA/cm ² in (a), (b), (c) and (d), respectively. For 1.5 mA/cm ² and 2 mA/cm ² , the initial resistances and values for high pressures are showing similar behavior as for 1 mA/cm ² , but are hidden due to the excessively high resistance after the pressureless experiment.	80
5.9	The calculated area changes in dependence of the pressure are shown without and with the fit results in (a) and (b), respectively. In (c), the response range value b is plotted against the current density and the slopes are directly given in the figure. According to the results in (c) the current density dependence of the pressure that is required to maintain 95 % of the contact area is drawn in (d).	82
5.10	The pressure dependent LSV measurements and the simulation of ohmic behavior are displayed for comparison.	83
5.11	The results of the transition current experiment are displayed in (a) and (b) shows the fit of the data obtained for this technique.	84
5.12	Cycling (at room temperature) of a symmetric Na/ β'' -alumina/Na cell without (a) and with (14 bar) (b) the application of pressure is displayed. In (c) the cell rested for 2 h between the cycles.	85

5.13	Pressure dependent dissolution of initially deposited sodium metal is displayed. The initially deposited amount of sodium metal is marked with gray.	86
5.14	The dissolution of a 500 μm thick sodium metal electrode by application of a pressure of 16 bar and a current density of 1 mA/cm^2 at room temperature.	87
5.15	Schematic summary of the effects during dissolution at the interface between alkali metal and solid electrolyte is shown according to the results in this chapter and the literature survey in section 5.2.	89
6.1	Results of the pressure dynamic galvanostatic experiment for a symmetric Li metal/LGPS cell are shown in (a) and (b) for current densities of 0.5 mA/cm^2 and 1 mA/cm^2 , respectively.	92
6.2	The transition current experiment results are displayed in (a) and the pressure dependent LSV data together with the theoretic ohmic behavior in (b). The results of the pressure dynamic galvanostatic experiments are shown in (c) and (d) for current densities of 0.5 mA/cm^2 and 1 mA/cm^2 , respectively.	93
6.3	Results of the pressure dynamic galvanostatic experiments for a symmetric Li metal/LPS cell are shown in (a) and (b) for current densities of 0.5 mA/cm^2 and 1 mA/cm^2 , respectively. The results of the galvanostatic experiment for different pressures are shown in (c) and (d). The transition current experiment results are displayed in (e) and the pressure dependent LSV data together with the theoretic ohmic behavior in (f).	94
6.4	The results for the pressure dependent galvanostatic and galvanostatic measurements for three different pressures are shown in (a) and (b) for a current density of 0.1 mA/cm^2 , respectively. In (c) and (d), the transition current measurement and the LSV for three different pressures are displayed.	96
6.5	The results for the pressure dependent galvanostatic measurements are shown in (a) for a current density of 0.2 mA/cm^2 . In (b) and (c), the LSV data for three different pressures (including the simulated ohmic behavior) and the transition current measurements are displayed. (d) shows a representative voltage profile for a current density of 0.4 mA/cm^2 leading to short circuiting.	97
6.6	Cycling of a symmetric Li/LLZO/Li cell for current densities of 0.2 mA/cm^2 and 1 mA/cm^2 are shown in (a) and (b) at room temperature, respectively. An external pressure of 24 bar was applied.	98
6.7	Cycling results for β'' -alumina and NPS are displayed in (a) and (b), respectively. Note that the current density for β'' -alumina was set to 1 mA/cm^2 , whereas for NPS a current density of 0.2 mA/cm^2 was chosen. For both a cycle time of 1 h and a mechanical pressure of 21 bar were selected.	99
6.8	Typical cycling results for LPS are displayed in (a) and (b), respectively. A cycle time of 1 h, a current density of 1 mA/cm^2 and a mechanical pressure of 21 bar were selected.	100
6.9	Cycling results for the symmetric cell Li/LGPS/Li with a current density of 1 mA/cm^2 , a cycle time of 1 h and a pressure of 24 bar are shown in (a). The Nyquist plots before the initial cycle, after 10 h, 20 h and 30 h are displayed in (b). A comparison of the chemical and electrochemical degradation of LGPS according to the results in section 3.7.2 and in (b), are illustrated in (c).	101
6.10	The concept of internal metal deposition of two mixed conducting solid electrolytes.	102

6.11	Summary of the results for the transition current experiments, including LLZO, NPS, LGPS, LPS and β'' -alumina. The IR-drop of the pellet is subtracted so that only the interface and interphase contributions are compared.	103
7.1	Schematic summary of the experiments and results obtained during this project are shown. Firstly, the two technical approaches are displayed, followed by the qualitatively illustration of results, leading to the interphase/interface classification.	106
7.2	Graphical summary of the experiments and results concerning the interfacial effects under current load are displayed.	107
8.1	Synthesis route for LLTO and LSTZO are shown schematically in (a) and (b), respectively.	111
8.2	Arrhenius plots for the perovskite-type compound LSTZO, and two different LLTO compositions. The activation energies are summarized in Tab. 8.2. .	112
8.3	Diffraction diagrams of LLTO and LSTZO. The theoretical positions for the reflexes are marked in blue ^[26,30]	112
8.4	Synthesis route for the different compositions of the garnet type structures.	113
8.5	Arrhenius plots for the garnet type compounds. The activation energies are summarized in Tab. 8.3.	114
8.6	Arrhenius plots for the garnet type compounds. The activation energies are summarized in Tab. 8.3. LLTa ₂ O (Li ₅ La ₃ Ta ₂ O ₁₂) is additionally shown in Fig. 8.5 to allow better comparison of the garnet type compounds.	114
8.7	Diffraction diagrams of the garnet type compounds. The theoretical positions for the reflexes are marked in blue ^[33] . The second phase for Li _{6.635} La ₃ Zr _{1.625} -Ta _{0.325} O ₁₂ :Al corresponds to LiAlO ₂ , which fills pores between the LLTZO grains and hence increases the conductivity.	116
8.8	Synthesis route for the LATP compounds.	117
8.9	Arrhenius plots for the LATP compounds with three different compositions. The activation energies are summarized in Tab. 8.4.	118
8.10	Diffraction diagrams of the LATP and NATP compounds. The theoretical reflex positions are marked in blue ^[178]	118
8.11	The synthesis routes for Li ₇ P ₃ S ₁₁ , Li ₁₀ GeP ₂ S ₁₂ and Na ₃ PS ₄ are displayed in (a), (b) and (c), respectively ^[12,16,20]	119
8.12	Arrhenius plots for LPS compounds, which were treated differently. Equi-conductivity lines are dotted gray to illustrate the conductivity values ^[78] . .	120
8.13	Diffraction pattern for the triclinic LPS. The theoretical reflex positions are marked in blue ^[17]	120
8.14	Arrhenius plot for LGPS ^[82]	121
8.15	Diffraction pattern for LGPS. The theoretical reflex positions are marked in blue ^[13]	121
8.16	Arrhenius plots for Na ₃ PS ₄ and β'' -alumina. The insets display sample Nyquist plots at -40 °C for both compounds, respectively ^[43]	122
8.17	Diffraction pattern for NPS. The theoretical reflex positions are marked in blue ^[21]	122
8.18	Diffraction pattern for β'' -alumina. The theoretical reflections positions for β'' -alumina (main component) and a second phase (NaAlH ₄) are marked in blue.	123

9.1	The typical Butler-Volmer plot is shown on the left side and the linear region at the origin is displayed on the right side. The data points are indicated with orange colored stars.	125
9.2	Schematical cell geometry for the determination of the polarization resistance by a CV technique ^[82]	126
9.3	Theoretical resistance contributions of a cell that consists of alkali metal electrodes (working electrode WE, reference electrode RE and counter electrode CE) on a solid electrolyte pellet.	127
9.4	The in situ XPS setup is shown for angle resolved measurement in (a), the standard setup in (b) and the mounted setup after deposition in (c). The in situ sample holder with electronic contacts is shown in (d).	127
9.5	Plot of the natural logarithm of the ratio between the intensity and the initial intensity versus the deposition time for sodium and lithium metal, respectively. See equation 9.2.	128
9.6	The changes of the element ratios of nickel, lithium, oxygen and carbon are shown during the deposition of lithium metal.	129
9.7	A stacked plot of the Ti 2p spectra for the lithium metal insertion into LLTO is shown in (a). In (b), the calculated fraction of inserted lithium metal is calculated with the data described in section 3.6.1 ^[61]	129
9.8	The peak fit models for the Zr 3d and Ta 4f signals for the pristine and deposited sample are shown in (a) and (b), respectively. The obtained deposition profiles for the different species are displayed in (c) for the Zr 3d and in (d) for Ta 4f species. Note that the relative molar fraction is only referring to one species.	131
9.9	The resistance changes for a symmetric lithium metal/LSTZO cell, recorded by a DC technique.	132
9.10	The photoelectron spectra for the pristine and decomposed titanium species of LATP are displayed in (a) and (b), respectively. The changes of the O 1s and P 2p line for three different deposition times are shown in (c) and (d), respectively. According to the peak fit model in (a) and (b), the molar fractions of the titanium species are obtained and displayed in (e).	133
9.11	The resistance changes for a symmetric lithium metal/LATP cell, recorded by the DC technique.	133
9.12	The Li 1s line before and after lithium metal deposition ^[82]	134
9.13	Bode plot for the decomposition of LPS (supporting information for section 3.7.1).	135
9.14	Stacked Nyquist plots for the decomposition of LPS and LGPS are displayed. The figure for LGPS is already published by Wenzel et al. ^[82] . The data for LPS and LGPS are constantly stacked with 20 Ω and 200 Ω , respectively.	136
9.15	Bode plot for the decomposition of LGPS (supporting information for section 3.7.2). The figure is already published by Wenzel et al. ^[82]	136
9.16	Deposition state dependent photoelectron detail spectra for the S 2p, P 2p, O 1s, Cl 2p and Li 1s signals of the LPSCl sample.	137
9.17	The photoelectron detail spectra of the pristine and the reacted samples including the peak fit model for the Cl 2p, P 2p and S 2p signal are shown in (a) and (b). (c) and (d) show the evolution of the decomposition products.	138

9.18	Nyquist plots and the fits directly after contacting and after 12 h of contact are displayed in (a), the equivalent circuit is shown as an inset. The fit results are then shown in (b) for 22 h. Note that the SEI resistance refers to one electrode.	140
9.19	Stacked Nyquist plots for the decomposition of NPS are displayed ^[43] . The plots are constantly stacked with 20 k Ω	141
9.20	Bode plot for the decomposition of NPS (supporting information for section 3.7.3) ^[43]	141
9.21	Photoelectron spectra for the O 1s and La 3d line of the pristine sample and after lithium deposition are displayed in (a) and (b), respectively. The peak fit model for the Ta 4f line of the pristine and deposited sample are shown in (c).	142
9.22	Deposition profile of LLTa ₂ O (Li ₅ La ₃ Ta ₂ O ₁₂) according to the peak fit model in Fig. 9.21c and Tab. 9.2 is shown in (a). The results of the DC decomposition measurements are shown in (b).	143
9.23	Photoelectron detail spectra of Zr 3d and Na 1s for the pristine and reacted sample are displayed in (a) and (b), respectively. The fit model was prepared according to the parameters in section 9.3.2.	144
9.24	Photoelectron detail spectra for the O 1s, Si 2p and P 2p signals before and after sodium metal deposition are displayed in (a), (b) and (c), respectively.	145
9.25	Photoelectron spectra for the pristine and reacted sample of O 1s signal are shown, recorded under usage of Mg radiation.	145
10.1	SEM figures of electrochemically deposited sodium metal are shown in (a) and (b). (c) displays a pristine sodium metal electrode and (d) a sodium electrode after the dissolution process.	147
10.2	Contour plot of the potential behavior for the cell used to determine the IR-drop between reference and working electrode.	148
10.3	Nyquist plots of a symmetric Au/ β "-alumina/Au cell for different mechanical pressures are shown.	149
10.4	The resistance changes for the resting experiment are displayed in (a), resting periods are denoted with the resting time and cycling periods with C. In (b), the corresponding results for the galvanostatic experiments are shown.	150
10.5	Result of the pressure dependent galvanostatic experiments for a current density of 10 mA/cm ² are displayed.	150
10.6	Pressure dependence of the average voltage slope and of the overvoltage are shown in (a) and (b), respectively.	151
10.7	Galvanostatic oscillation of the overvoltage at the interface between sodium metal electrode and the solid electrolyte β "-alumina at room temperature.	152
10.8	Results of the dissolution of freshly deposited sodium metal at room temperature, without external pressure.	152
10.9	The mechanism of dislocation movement (gliding), caused by pressure application to the sodium metal electrode.	153
11.1	Additional examples on cycling experiments of lithium metal electrodes on LPS are shown for different current densities. In (a), (b), (c), and (d) the pressure values were set to 0 bar, 3 bar, 19 bar and 24 bar, respectively.	155
11.2	The result of a cycling experiment with a Na metal/NPS/Na metal cell setup.	156
11.3	Simulation of the interphase growth during cycling.	157

List of Tables

3.1	The slope (parabolic rate constant k) and d -intercept for the fits in Fig. 3.27 for LPS, LGPS and LPSCl.	50
3.2	The slope (parabolic resistance rate constant k') and d -intercept for the fits in Fig. 3.27b for LPS, LGPS and LPSCl.	51
8.1	Supplier, purity and annealing parameters for the starting materials used for synthesis.	109
8.2	Summary of the activation energies, ionic and electronic partial conductivities of two compositions of LLTO and LSTZO at room temperature.	112
8.3	Summary of the activation energies, ionic and electronic partial conductivities for the garnet type compounds.	115
8.4	Summary of the activation energies, ionic and electronic partial conductivities of three compositions of the LATP compounds.	119
8.5	Summary of the activation energies, ionic and electronic partial conductivities for LGPS, NPS, LPS and densified LPS. The values for β'' -alumina (Ionotec Ltd.) are displayed, too.	123
8.6	Summary of the activation energies and ionic conductivities for the argyrodite compound.	124
9.1	The XPS fitting parameters for the Ti 2p line of LLTO. Similar parameters were used for all titanium containing materials (e. g. LATP).	130
9.2	The XPS fitting parameters for the Ta 4f and Zr 3d line for LSTZO are summarized.	131
9.3	XPS fitting parameters for the pristine and the decomposed $\text{Li}_7\text{P}_3\text{S}_{11}$	134
9.4	Fit parameters for LGPS and its decomposition products. A Shirley background model was used.	137
9.5	XPS fitting parameters for the pristine and the decomposed $\text{Li}_6\text{PS}_5\text{Cl}$	139
9.6	Fit parameters for NPS and its decomposition products. A Shirley background model was used. BE is the abbreviation for binding energy and red. for reduced, respectively.	142

13 Bibliography

- [1] B. Scrosati, *J. Solid State Electrochem.*, **2011**, 15, 1623-1630.
- [2] P. Hockenos, *Die ZEIT*, **2012**, 47.
- [3] R. Garcia-Valle and J. A. Pecas Lopes, "Electric Vehicle Integration into Modern Power Networks", Springer-Verlag, Heidelberg **2013**.
- [4] J.-M. Tarascon and M. Armand, *Nature*, **2001**, 414, 359-367.
- [5] T. Yamada, S. Ito, R. Omoda, T. Watanabe, Y. Aihara, M. Agostini, U. Ullissi, J. Hassoun and B. Scrosati, *J. Electrochem. Soc.*, **2015**, 162, A646-A651.
- [6] J. Maier, "Physical Chemistry of Ionic Materials: Ions and Electrons in Solids", Wiley, Weinheim **2004**.
- [7] G. C. Farrington and J. L. Briant, *Science*, **1979**, 204, 1371-1379.
- [8] Y. Wang, W. D. Richards, S. P. Ong, L. J. Miara, J. C. Kim, Y. Mo and G. Ceder, *Nat. Mater.*, **2015**, 14, 1026-1031.
- [9] W. Li, G. Wu, Z. Xiong, Y. P. Feng and P. Chen, *Phys. Chem. Chem. Phys.*, **2012**, 14, 1596-1606.
- [10] U. von Alpen, M. F. Bell and T. Gladden, *Electrochim. Acta*, **1979**, 24, 741-744.
- [11] I. Kishida, F. Oba, Y. Koyama, A. Kuwabara and I. Tanaka, *Phys. Rev. B*, **2009**, 80, 024116.
- [12] N. Kamaya, K. Homma, Y. Yamakawa, M. Hirayama, R. Kanno, M. Yonemura, T. Kamiyama, Y. Kato, S. Hama and K. Kawamoto, *Nat. Mater.*, **2011**, 10, 682-686.
- [13] S. Adams and R. Prasada Rao, *J. Mater. Chem.*, **2012**, 22, 7687-7691.
- [14] C. Cao, Z. Li, X. Wang, X. Zhao and W. Han, *Front. Energy Res.*, **2014**, 2, 1-10.
- [15] H. Eckert, Z. Zhang and J. H. Kennedy, *Chem. Mater.*, **1990**, 2, 273-279.
- [16] A. Hayashi, K. Minami, S. Ujiie and M. Tatsumisago, *J. Non. Cryst. Solids*, **2010**, 356, 2670-2673.
- [17] H. Yamane, M. Shibata, Y. Shimane, T. Junke, Y. Seino, S. Adams, K. Minami, A. Hayashi and M. Tatsumisago, *Solid State Ionics*, **2007**, 178, 1163-1167.
- [18] K. Minami, A. Hayashi and M. Tatsumisago, *J. Ceram. Soc. Japan*, **2010**, 118, 305-308.
- [19] K. Xiong, R. C. Longo, Santosh. KC, W. Wang and K. Cho, *Comput. Mater. Sci.*, **2014**, 90, 44-49.
- [20] A. Hayashi, K. Noi, N. Tanibata, M. Nagao and M. Tatsumisago, *J. Power Sources*, **2014**, 258, 420-423.
- [21] N. Tanibata, K. Noi, A. Hayashi, N. Kitamura, Y. Idemoto and M. Tatsumisago, *ChemElectroChem*, **2014**, 1, 1130-1132.
- [22] Z. Nagamedianova and E. Sanchez, *Solid State Ionics*, **2006**, 177, 3259-3265.
- [23] S. Boulinau, M. Courty, J.-M. Tarascon and V. Viallet, *Solid State Ionics*, **2012**, 221, 1-5.
- [24] H. J. Deiseroth, S. T. Kong, H. Eckert, J. Vannahme, C. Reiner, T. Zaiss and M. Schlosser, *Angew. Chemie - Int. Ed.*, **2008**, 47, 755-758.
- [25] T. Ohtomo, A. Hayashi, M. Tatsumisago and K. Kawamoto, *J. Mater. Sci.*, **2013**, 48, 4137-4142.
- [26] Y. Inaguma, C. Liqun, M. Itoh, T. Nakamura, T. Uchida, H. Ikuta and M. Wakihara, *Solid State Commun.*, **1993**, 86, 689-693.
- [27] C. H. Chen and K. Amine, *Solid State Ionics*, **2001**, 144, 51-57.
- [28] V. Thangadurai and W. Weppner, *Ionics*, **2000**, 6, 70-77.
- [29] C. Ma, K. Chen, C. Liang, C.-W. Nan, R. Ishikawa, K. More and M. Chi, *Energy Environ. Sci.*, **2014**, 7, 1638-1642.
- [30] C. Chen, S. Xie, E. Sperling, A. S. Yang, G. Henriksen and K. Amine, *Solid State Ionics*, **2004**, 167, 263-272.

- [31] W. G. Zeier, *Dalton Trans.*, **2014**, 43, 16133-16138.
- [32] V. Thangadurai, S. Narayanan and D. Pinzaru, *Chem. Soc. Rev.*, **2014**, 43, 4714-4727.
- [33] H. Buschmann, S. Berendts, B. Mogwitz and J. Janek, *J. Power Sources*, **2012**, 206, 236-244.
- [34] H. Buschmann, J. Doelle, S. Berendts, A. Kuhn, P. Bottke, M. Wilkening, P. Heitjans, A. Senyshyn, H. Ehrenberg, A. Lotnyk, et al., *Phys. Chem. Chem. Phys.*, **2011**, 13, 19378-19392.
- [35] S. Duluard, A. Paillasa, L. Puech, P. Vinatier, V. Turq, P. Rozier, P. Lenormand, P. Taberna, P. Simon and F. Ansart, *J. Eur. Ceram. Soc.*, **2013**, 33, 1145-1153.
- [36] M. Guin and F. Tietz, *J. Power Sources*, **2015**, 273, 1056-1064.
- [37] N. Anantharamulu, K. Koteswara Rao, G. Rambabu, B. Vijaya Kumar, V. Radha and M. Vithal, *J. Mater. Sci.*, **2011**, 46, 2821-2837.
- [38] T. Oshima, M. Kajita and A. Okuno, *Int. J. Appl. Ceram. Technol.*, **2004**, 1, 269-276.
- [39] X. Lu, B. W. Kirby, W. Xu, G. Li, J. Y. Kim, J. P. Lemmon, V. L. Sprenkle and Z. Yang, *Energy Environ. Sci.*, **2013**, 6, 299-306.
- [40] Y. Su, J. Falgenhauer, A. Polity, T. Leichtweiss, A. Kronenberger, J. Obel, S. Zhou, D. Schlettwein, J. Janek and B. K. Meyer, *Solid State Ionics*, **2015**, 282, 63-69.
- [41] M. R. Busche, personal communication, unpublished data.
- [42] P. E. Stallworth, J. J. Fontanella, M. C. Wintersgill, C. D. Scheidler, J. J. Immel, S. G. Greenbaum and A. S. Gozdz, *J. Power Sources*, **1999**, 81-82, 739-747.
- [43] S. Wenzel, T. Leichtweiss, D. A. Weber, J. Sann, W. G. Zeier and J. Janek, "Interfacial reactivity of the sodium ion conductor Na₃PS₄: A case for β -alumina in protected sodium metal anodes and sodium all-solid-state batteries", to be submitted.
- [44] J. Li, C. Ma, M. Chi, C. Liang and N. J. Dudney, *Adv. Energy Mater.*, **2015**, 5, 1401408.
- [45] Y. J. Nam, S. J. Cho, D. Y. Oh, J. M. Lim, S. Y. Kim, J. H. Song, Y. G. Lee, S. Y. Lee and Y. S. Jung, *Nano Lett.*, **2015**, 15, 3317-3323.
- [46] M. Tatsumisago and A. Hayashi, *Int. J. Appl. Glas. Sci.*, **2014**, 5, 226-235.
- [47] Y. Kato, K. Kawamoto, R. Kanno and M. Hirayama, *Electrochemistry*, **2012**, 80, 749-751.
- [48] A. Sakuda, A. Hayashi and M. Tatsumisago, *Chem. Mater.*, **2010**, 22, 949-956.
- [49] B. R. Shin, Y. J. Nam, D. Y. Oh, D. H. Kim, J. W. Kim and Y. S. Jung, *Electrochim. Acta*, **2014**, 146, 395-402.
- [50] S. Boulineau, J.-M. Tarascon, J.-B. Leriche and V. Viallet, *Solid State Ionics*, **2013**, 242, 45-48.
- [51] F. Han, T. Gao, Y. Zhu, K. J. Gaskell and C. Wang, *Adv. Mater.*, **2015**, 27, 3473-3483.
- [52] M. Kotobuki and K. Kanamura, *Ceram. Int.*, **2013**, 39, 6481-6487.
- [53] J. Heine, S. Krueger, C. Hartnig, U. Wietelmann, M. Winter and P. Bieker, *Adv. Energy Mater.*, **2014**, 4, 1300815.
- [54] W. Luo and L. Hu, *ACS Cent. Sci.*, **2015**, 1, 420-422.
- [55] N.-W. Li, Y.-X. Yin, C.-P. Yang and Y.-G. Guo, *Adv. Mater.*, **2015**, 28, 1853-1858.
- [56] D. Santhanagopalan, D. Qian, T. McGilvray, Z. Wang, F. Wang, F. Camino, J. Graetz, N. Dudney and Y. S. Meng, *J. Phys. Chem. Lett.*, **2014**, 5, 298-303.
- [57] A. C. Luntz, J. Voss and K. Reuter, *J. Phys. Chem. Lett.*, **2015**, 6, 4599-4604.
- [58] S. Lupart, "Research and Application Challenges of Solid Electrolytes for next Generation Automotive Batteries", *MRS Fall Meeting (Boston)*, **2015**.
- [59] Y. Tao, S. Chen, D. Liu, G. Peng, X. Yao and X. Xu, *J. Electrochem. Soc.*, **2016**, 163, A96-A101.
- [60] K. Yang, J. Dong, L. Zhang, Y. Li and L. Wang, *J. Am. Ceram. Soc.*, **2015**, 98, 3831-3835.
- [61] S. Wenzel, T. Leichtweiss, D. Krueger, J. Sann and J. Janek, *Solid State Ionics*, **2015**, 278, 98-105.
- [62] P. Hartmann, T. Leichtweiss, M. R. Busche, M. Schneider, M. Reich, J. Sann, P. Adelhelm and J. Janek, *J. Phys. Chem. C*, **2013**, 117, 21064-21074.
- [63] J. M. Whiteley, J. H. Woo, E. Hu, K.-W. Nam and S.-H. Lee, *J. Electrochem. Soc.*, **2014**, 161, A1812-A1817.

- [64] C. Hua, X. Fang, Z. Wang and L. Chen, *Electrochem. Commun.*, **2013**, 32, 5-8.
- [65] P. Birke, S. Scharner, R. A. Huggins and W. Weppner, *J. Electrochem. Soc.*, **1997**, 144, 167-169.
- [66] M. Nakayama, T. Usui, Y. Uchimoto, M. Wakihara and M. Yamamoto, *J. Phys. Chem. B*, **2005**, 109, 4135-4143.
- [67] O. Bohnke, C. Bohnke and J. L. Fourquet, *Solid State Ionics*, **1996**, 91, 21-31.
- [68] K.-Y. Yang, I.-C. Leu, K.-Z. Fung, M.-H. Hon, M.-C. Hsu, Y.-J. Hsiao and M.-C. Wang, *J. Mater. Res.*, **2008**, 23, 1813-1825.
- [69] Y. Inaguma, C. Liqun, M. Itoh, T. Nakamura, T. Uchida, H. Ikuta and M. Wakihara, *Solid State Commun.*, **1993**, 86, 689-693.
- [70] C. Chen and K. Amine, *Solid State Ionics*, **2001**, 144, 51-57.
- [71] S. Stramare, V. Thangadurai and W. Weppner, *Chem. Mater.*, **2003**, 15, 3974-3990.
- [72] Y. Zhu, X. He and Y. Mo, *J. Mater. Chem. A*, **2016**, 4, 3253-3266.
- [73] R. J. Lauf and J. H. DeVan, *J. Electrochem. Soc.*, **1992**, 139, 2087-2091.
- [74] A. Schwoebel, R. Hausbrand and W. Jaegermann, *Solid State Ionics*, **2015**, 273, 51-54.
- [75] A. Hayashi, S. Hama, F. Mizuno, K. Tadanaga, T. Minami and M. Tatsumisago, *Solid State Ionics*, **2004**, 175, 683-686.
- [76] Y. Zhu, X. He and Y. Mo, *ACS Appl. Mater. Interfaces*, **2015**, 7, 23685-23693.
- [77] W. D. Richards, L. J. Miara, Y. Wang, J. C. Kim and G. Ceder, *Chem. Mater.*, **2015**, 28, 266-273.
- [78] S. Wenzel, D. A. Weber, T. Leichtweiss, M. R. Busche, J. Sann and J. Janek, *Solid State Ionics*, **2016**, 286, 24-33.
- [79] Y. S. Jung, D. Y. Oh, Y. J. Nam and K. H. Park, *Isr. J. Chem.*, **2015**, 55, 472-485.
- [80] M. Sakuma, K. Suzuki, M. Hirayama and R. Kanno, *Solid State Ionics*, **2016**, 285, 101-105.
- [81] S. P. Ong, Y. Mo, W. D. Richards, L. Miara, H. S. Lee and G. Ceder, *Energy Environ. Sci.*, **2013**, 6, 148-156.
- [82] S. Wenzel, S. Randau, T. Leichtweiss, D. A. Weber, J. Sann, W. G. Zeier and J. Janek, *Chem. Mater.*, **2016**, 28, 2400-2407.
- [83] S. Wenzel, W. G. Zeier and J. Janek, "Solid electrolytes: Stable or not?", in preparation.
- [84] J. Wolfenstine, J. L. Allen, J. Read and J. Sakamoto, *J. Mater. Sci.*, **2013**, 48, 5846-5851.
- [85] K. Ishiguro, Y. Nakata, M. Matsui, I. Uechi, Y. Takeda, O. Yamamoto and N. Imanishi, *J. Electrochem. Soc.*, **2013**, 160, A1690-A1693.
- [86] Z. Zhang and J. T. Yates, *Chem. Rev.*, **2012**, 112, 5520-5551.
- [87] A. Schwoebel, W. Jaegermann and R. Hausbrand, *Solid State Ionics*, **2016**, 10-14.
- [88] J. Haruyama, K. Sodeyama, L. Han, K. Takada and Y. Tateyama, *Chem. Mater.*, **2014**, 26, 4248-4255.
- [89] L. Zhang, K. Yang, J. Mi, L. Lu, L. Zhao, L. Wang, Y. Li and H. Zeng, *Adv. Energy Mater.*, **2015**, 5.
- [90] E. Peled, D. Golodnitsky, G. Ardel and V. Eshkenazy, *Electrochim. Acta*, **1995**, 40, 2197-2204.
- [91] C. Xu, B. Sun, T. Gustafsson, K. Edström, D. Brandell and M. Hahlin, *J. Mater. Chem. A*, **2014**, 2, 7256-7264.
- [92] K. A. Murugesamoorthi and J. R. Owen, *Br. Polym. J.*, **1988**, 20, 227-231.
- [93] D. Fauteux, *Solid State Ionics*, **1985**, 17, 133-138.
- [94] I. Ismail, A. Noda, A. Nishimoto and M. Watanabe, *Electrochim. Acta*, **2001**, 46, 1595-1603.
- [95] E. Peled, *J. Electrochem. Soc.*, **1979**, 126, 2047-2051.
- [96] H. Schmalzried, "Chemical Kinetics of Solids", Wiley-VCH, Weinheim **1995**.
- [97] H. Schmalzried, "Solid state reactions", Wiley-VCH, Weinheim **1981**.
- [98] C. Wagner, *Z. Phys. Chem. B*, **1933**, 21, 25-41.
- [99] T. P. Hoar and L. E. Price, *Trans. Faraday Soc.*, **1938**, 34, 867-872.
- [100] H. Schmalzried and J. Janek, *Ber. der Bunsenges. Phys. Chem.*, **1998**, 102, 127-143.

- [101] S. Kirkpatrick, *Rev. Mod. Phys.*, **1973**, 45, 574-588.
- [102] K. Peppler, C. Reitz and J. Janek, *Appl. Phys. Lett.*, **2008**, 93, 074104.
- [103] A. Brazier, L. Dupont, L. Dantras-Laffont, N. Kuwata, J. Kawamura and J. Tarascon, *Chem. Mater.*, **2008**, 20, 2352-2359.
- [104] A. J. Bard and L. R. Faulkner, "Electrochemical Methods: Fundamentals and Applications", John Wiley & Sons, **2001**.
- [105] P. L. J. Gunter, J. W. Niemantsverdriet, *Appl. Surf. Sci.*, **1995**, 89, 69-76.
- [106] P. Marcus, C. Hinnen, D. Imbert and J. M. Siffre, *Surf. Interface Anal.*, **1995**, 19, 127-132.
- [107] C. J. Powell and A. Jablonski, "The NIST Electron Effective-Attenuation-Length Database", Version 1.3, **2002**.
- [108] A. Jablonski, *J. Electron Spectros. Relat. Phenomena*, **2012**, 185, 498-508.
- [109] F. Altorfer, W. Buehrer, I. Anderson, O. Schaerpf, H. Bill, P. L. Carron and H. G. Smith, *Phys. B Condens. Matter*, **1992**, 180-181, 795-797.
- [110] H. G. Von Schnering and W. Hoenle, *Chem. Rev.*, **1988**, 88, 243-273.
- [111] C. S. Fuller and J. C. Severiens, *Phys. Rev.*, 1954, 96, 21-24.
- [112] P. R. Abel, A. M. Chockla, Y.-M. Lin, V. C. Holmberg, J. T. Harris, B. A. Korgel, A. Heller and C. B. Mullins, *ACS Nano*, **2013**, 7, 2249-2257.
- [113] G. Nazri, *Solid State Ionics*, **1989**, 34, 97-102.
- [114] L. Wu, D. Bresser, D. Buchholz, G. Giffin, C. R. Castro, A. Ochel and S. Passerini, *Adv. Energy Mater.*, **2014**, 5, 1401142.
- [115] M. B. Pinson and M. Z. Bazant, *J. Electrochem. Soc.*, **2013**, 160, A243-A250.
- [116] J. Christensen and J. Newman, *J. Electrochem. Soc.*, **2004**, 151, A1977-A1988.
- [117] M. Tang, S. Lu and J. Newman, *J. Electrochem. Soc.*, **2012**, 159, A1775-A1785.
- [118] Y. Kato, S. Hori, T. Saito, K. Suzuki, M. Hirayama, A. Mitsui, M. Yonemura, H. Iba and R. Kanno, *Nat. Energy*, **2016**, DOI: 10.1038/nenergy.2016.30
- [119] S. Wenzel, "On the stability of NaSICON materials in contact with sodium metal", *Analysis report*, **2016**.
- [120] X. Chunhua and G. Wei, *Mat. Res. Innov.*, **2000**, 3, 231-235.
- [121] H. Wang, D. Im, D. J. Lee, M. Matsui, Y. Takeda, O. Yamamoto and N. Imanishi, *J. Electrochem. Soc.*, **2013**, 160, A728-A733.
- [122] N. Imanishi, S. Hasegawa, T. Zhang, A. Hirano, Y. Takeda and O. Yamamoto, *J. Power Sources*, **2008**, 185, 1392-1397.
- [123] J. Reinacher, S. Berendts and J. Janek, *Solid State Ionics*, **2014**, 258, 1-7.
- [124] S. J. Visco and Y. S. Nimon, "Protected lithium electrodes having tape cast ceramic and glass-ceramic membranes", patent, US 20120219842.
- [125] W. Schnick and J. Luecke, *Solid State Ionics*, **1990**, 38, 271-273.
- [126] W. Schnick and U. Berger, *Angew. Chem. Int. Ed.*, **1991**, 30, 830-831.
- [127] J. Christensen, P. Albertus, R. S. Sanchez-Carrera, T. Lohmann, B. Kozinsky, R. Liedtke, J. Ahmed and A. Kojic, *J. Electrochem. Soc.*, **2012**, 159, R1-R30.
- [128] E. Peled, D. Golodnitsky, H. Mazor, M. Goor and S. Avshalomov, *J. Power Sources*, **2011**, 196, 6835-6840.
- [129] J. Janek, *Habilitation*, "Zum Ladungsdurchtritt an Phasengrenzen in Festkoerpern", Hannover **1997**.
- [130] J. Janek, *Solid State Ionics*, **2000**, 131, 129-142.
- [131] H. Fischbach, *Zeitschrift fuer Metallkunde*, **1980**, 71, 115-119.
- [132] J. Janek and S. Majoni, *Ber. der Bunsenges. Phys. Chem.*, **1995**, 99, 14-20.
- [133] S. Majoni and J. Janek, *Ber. der Bunsenges. Phys. Chem.*, **1998**, 102, 756-762.
- [134] M. Rohnke, C. Rosenkranz and J. Janek, *Solid State Ionics*, **2006**, 177, 447-456.
- [135] R. D. Armstrong, T. Dickinson, H. R. Thirsk, R. Whitfield, *J. Electroanal. Chem.*, **1971**, 29, 301-307.

- [136] R. M. Guseinov and N. G. Bukun, *Sov. Electrochem.*, **1978**, 14, 1226.
- [137] M. Rohnke, T. Best and J. Janek, *J. Solid State Electrochem.*, **2005**, 9, 239-243.
- [138] J. Corish and C. O'Briain, *J. Cryst. Growth*, **1972**, 13-14, 62-67.
- [139] A. Spangenberg, J. Fleig and J. Maier, *Adv. Mater.*, **2001**, 13, 1466-1468.
- [140] K. Peppler and J. Janek, *Solid State Ionics*, **2006**, 177, 1643-1648.
- [141] K. Hsu, P. Ferreira and N. Fang, *Appl. Phys. Lett.*, **2010**, 96, 024101.
- [142] C. Rosenkranz, Dissertation, " Zur oszillierenden Elektrodenkinetik an der fest/fest-Phasengrenze Me/AgX", Hannover **1997**.
- [143] J. Janek, S. Majoni, *Defect Diffus. Forum*, **1996**, 129-130, 243-252.
- [144] A. Schroeder, J. Fleig, D. Gryaznov, J. Maier and W. Sitte, *J. Phys. Chem. B*, **2006**, 110, 12274-12280.
- [145] J. T. Kummer and N. Weber, *SAE Trans.*, **1968**, 1003-1007.
- [146] A. V. Virkar, *J. Mater. Sci.*, **1981**, 16, 1142-1150.
- [147] R. O. Ansell, *J. Mater. Sci.*, **1986**, 21, 365-379.
- [148] R. N. Singh and N. Lewis, *Solid State Ionics*, **1983**, 10, 159-164.
- [149] R. D. Armstrong, T. Dickinson and J. Turner, *Electroanal. Chem. Interfacial Electrochem.*, **1973**, 44, 157-167.
- [150] M. H. Braga, J. A. Ferreira, V. Stockhausen, J. E. Oliveira and A. El-Azab, *J. Mater. Chem. A*, **2014**, 2, 5470-5480.
- [151] M. Nagao, A. Hayashi and M. Tatsumisago, *Electrochem. commun.*, **2012**, 22, 177-180.
- [152] E. Rangasamy, Z. Liu, M. Gobet, K. Pilar, G. Sahu, W. Zhou, H. Wu, S. Greenbaum and C. Liang, *J. Am. Chem. Soc.*, **2015**, 137, 1384-1387.
- [153] L. Cheng, E. J. Crumlin, W. Chen, R. Qiao, H. Hou, S. Franz Lux, V. Zorba, R. Russo, R. Kostecki, Z. Liu, et al., *Phys. Chem. Chem. Phys.*, **2014**, 16, 18294-18300.
- [154] L. Cheng, J. S. Park, H. Hou, V. Zorba, G. Chen, T. Richardson, J. Cabana, R. Russo and M. Doeff, *J. Mater. Chem. A*, **2014**, 2, 172-181.
- [155] U. von Alpen and M. Bell, *Solid State Ionics*, **1981**, 4, 259-262.
- [156] M. Motoyama, M. Ejiri and Y. Iriyama, *Electrochemistry*, **2014**, 82, 364-368.
- [157] B. L. Mehdi, J. Qian, E. Nasybulin, C. Park, D. A. Welch, R. Faller, H. Mehta, W. A. Henderson, W. Xu, C. M. Wang, et al., *Nano Lett.*, **2015**, 15, 2168-2173.
- [158] F. Sagane, K. Ikeda, K. Okita, H. Sano, H. Sakaebe and Y. Iriyama, *J. Power Sources*, **2013**, 233, 34-42.
- [159] M. Nagao, A. Hayashi, M. Tatsumisago, T. Kanetsuku, T. Tsuda and S. Kuwabata, *Phys. Chem. Chem. Phys.*, **2013**, 15, 18600-18606.
- [160] D. Devaux, K. J. Harry, D. Y. Parkinson, R. Yuan, D. T. Hallinan, A. A. MacDowell and N. P. Balsara, *J. Electrochem. Soc.*, **2015**, 162, A1301-A1309.
- [161] T. R. Jow and C. Liang, *J. Electrochem. Soc.*, **1983**, 130, 737-740.
- [162] T. R. Jow and C. Liang, *Solid State Ionics*, **1983**, 10, 695-698.
- [163] M. Meyer, H. Rickert und U. Schwaitzer, *Solid State Ionics*, **1983**, 10, 689-694.
- [164] Q. Chen, K. Geng and K. Sieradzki, *J. Electrochem. Soc.*, **2015**, 162, A2004-A2007.
- [165] C. Monroe, J. Newman, *J. Electrochem. Soc.*, **2005**, 152, A396-A404.
- [166] G. M. Stone, S. A. Mullin, A. A. Teran, D. T. Hallinan, A. M. Minor, A. Hexemer and N. P. Balsara, *J. Electrochem. Soc.*, **2012**, 159, A222-A227.
- [167] Y. Ren, Y. Shen, Y. Lin and C. W. Nan, *Electrochem. commun.*, **2015**, 57, 27-30.
- [168] R. Sudo, Y. Nakata, K. Ishiguro, M. Matsui, A. Hirano, Y. Takeda, O. Yamamoto and N. Imanishi, *Solid State Ionics*, **2014**, 262, 151-154.
- [169] M. Kotobuki, H. Munakata, K. Kanamura, Y. Sato and T. Yoshida, *J. Electrochem. Soc.*, **2010**, 157, A1076-A1079.

- [170] Y. Suzuki, K. Kami, K. Watanabe, A. Watanabe, N. Saito, T. Ohnishi, K. Takada, R. Sudo and N. Imanishi, *Solid State Ionics*, **2015**, 278, 172-176.
- [171] S. F. Pugh, *Philos. Mag. Ser. 7*, **1954**, 45, 823-843.
- [172] J. S. Koehler, *Phys. Rev.*, **1941**, 60, 397-410.
- [173] M. Butzin, personal communication.
- [174] D. Gourier, J. Barret and D. Vivien, *Solid State Ionics*, **1989**, 31, 301-311.
- [175] M. T. Johnson, H. Schmalzried and C. B. Cartera, *Solid State Ionics*, **1997**, 103, 1327-1333.
- [176] U. Stilknebohmer and H. Schmalzried, *phys. stat. sol.*, **1994**, 146, 31-41.
- [177] C. Korte, *Habilitation*, "Zur Wechselwirkung von Ionentransport und Mikrostruktur in inneren Grenzflaechen", Giessen **2009**.
- [178] X. Xu, Z. Wen, X. Yang, J. Zhang and Z. Gu, *Solid State Ionics*, **2006**, 177, 2611-2615.
- [179] C. Wagner, *Prog. Solid State Chem.*, **1975**, 10, 3-16.
- [180] H. Poepke, E. Mutoro, B. Luerssen and J. Janek, *Catal. Today*, **2013**, 202, 12-19.
- [181] T. Krauskopf, *Bachelor thesis*, "In-situ Polarisationsmessungen an Duennschicht-Batteriematerialien in einem Roentgenphotoelektronenspektrometer", Justus Liebig University Giessen **2015**.
- [182] M. C. Biesinger, L. W. M. Lau, A. R. Gerson and R. S. C. Smart, *Appl. Surf. Sci.*, **2010**, 257, 887-898.
- [183] William D. Callister, "Materials Science and Engineering - An Introduction", Wiley, New York **2007**.